Structure and dynamics of single living cells : comparison of non intrusive coherent microscopicmethods and AFM indentation experiments

Cristina Martinez Torres

Université Claude Bernard Lyon 1

Lab PHYS ENS de LYON

UNIVERSITÉ DE LYON

No. ordre 168-2015

Année 2015

THESE DE L'UNIVERSITE DE LYON
Specialité Physique

Délivrée par

L'UNIVERSITE CLAUDE BERNARD LYON 1

ECOLE DOCTORALE DE PHYSIQUE ET ASTROPHYSIQUE

DIPLOME DE DOCTORAT

(arrêté du 7 août 2006)

soutenue publiquement le 25 septembre 2015

par

Mlle. Cristina E. MARTINEZ TORRES

Structure and dynamics of single living cells: comparison of non intrusive coherent microscopic methods and AFM indentation experiments

---

Directeur de thèse: Mme. Françoise ARGOUL

Devant le jury composé de

M. Jean-Pierre ANTOINE	Président du jury
Mme. Françoise ARGOUL	Directrice de thèse
M. Atef ASNACIOS	Rapporteur
M. Serge MONNERET	Rapporteur
M. Jean-Paul RIEU	Examinateur

“When I am working on a problem, I never think about beauty but when I have finished, if the solution is not beautiful, I know it’s wrong."

Buckminster Fuller

Acknowledgements

Je remercie d'abord aux membres de mon jury de thèse d'avoir accepté d'en faire partie et de juger mes travaux, cela a été un vrai honneur de compter avec ce jury interdisciplinaire. En particulier, merci à Atef Asnacios et Serge Monneret qui ont rapporté le manuscrit, et dont les conseils et remarques ont été très utiles pour améliorer ce travail. Merci également à Jean-Pierre Antoine qui a accepté bien en avance de participer au jury, même si le temps d'attente était long et le sujet de thèse semblait-il un peu eloigné, s'agissant de la biophysique et pas des mathématiques. En fin, merci à Jean-Paul Rieu pour sa patience ainsi que pour les mots d'encouragement.

Un grand merci à ma directrice de thèse, Françoise Argoul, pour son encadrement et soutien tout au long de ma thèse. Merci pour ta disponibilité, qu'il s'agissait d'une minute pour répondre à mes questions, ou des quelques heures pour réflechir ensemble sur les casse-têtes que nous avons rencontré, tu as été toujours là pour me guider et me motiver (voire *me pousser dans l'eau*). J'ai beaucoup apprecié travailler avec toi ces trois années dans un projet qui a été toujours passionnant, autant pour les résultats et peut-être surtout, pour les difficultées. Je te remercie aussi pour m'avoir permis d'explorer et developper mes compétences, même si cela n'a jamais été facile en essayant de faire de l'experimentation, programmation, et même un peu de théorie ou des simulations, c'était très enrichissant et je dois l'admettre, amusant.

Un merci spécial à Lotfi Berguiga, qui a partagé son expertise et qui a été toujours au secours face aux problèmes rencontrés, particulièrement pour le montage du systeme optique. Merci pour ta patience et le temps que tu as dedié à m'expliquer ‹‹ comment ça marche ››. Je tiens à remercier Alain Arneodo pour les nombreuses discussions scientifiques, ses explications simplifiées des choses qui n'étaient pas evidentes à comprendre et surtout pour les conseils et le soutien pour la fin de la thèse. Je voudrais remercier également à Bastien Laperrousaz pour son investissement et sa disponibilité qui ont été une grande aide dans ce projet. Ce travail de thèse en effet suit celui realisé par Bastien concernant l'étude des cellules leucémiques. Merci aussi à nos collaborateurs Pierre Argoul, Juan Elezgaray, Laurent Schaeffer et Véronique Maguer-Satta.

J'ai eu la fortune de partager de très bons moments avec mes co-bureaux et l'ensemble de l'équipe. Merci pour ces trois années pleins de beaux souvenirs et pour faire le jour à jour au labo une vèritable joie. Merci Elise pour être si accueillante, spècialement au dèbut, même avec les difficultées que nous avions pour nous communiquer (d'accord, il est encore difficile

mais au moins on y arrive). Grâce à toi la vie en France avait l'air d'être très facile. Laura, *do you know atomic force microscopy?*, phrase inoubliable et qui represente tous les moments (parfois bizarres) que nous avons passé ensemble. Je vais jamais oublier les conversations scientifiques que nous avons eu dans des endroits les plus improbables (surtout chez M). Guèno, merci pour supporter mes questions et commentaires les plus insignifiants du monde (desolée pour tous les spoilers de GoT). Je te souhaite tout le bonheur avec cette nouvelle étape que tu viens de commencer. J'aimerais dire un merci particulier à ma co-bureau, chère coloc, and my favorite mathematician, Rasha. Thanks for all the laughs, tous les mails que tu m'as aidé à composer, the constant verification on the insignificant details that we care too much about (- *tu penses que c'est bien aligné? - no, ça se voit tout suite, il est 0.01 mm á droite*) ... bref, I could write a lot of things, but you get the point.

Merci également aux membres passées et présentes du laboratoire de Physique et du laboratoire Joliot-Curie, dans le désordre et de manière non-exhaustive: Benjamin, Simona, Evgenia, Qiong-Xu, Hanna, Pascale, Arezki, Léna, Johan, Xavier, Julien, Christophe, Ludovic, Stéphane, Thierry.

Pour bien finir, un énorme merci à ma famille. Sé que la distancia no ha hecho las cosas nada fáciles, pero siempre han encontrado la manera de motivarme y de ofrecerme un apoyo inquebrantable a lo largo de estos tres años y medio. No tengo palabras para expresar cuánto me ha alegrado que hayan podido estar presentes el día de mi defensa de tesis. Unas cuantas líneas nunca bastarán para agradecerles por todo, así que sólo diré: de todo corazón, gracias.

Abstract

Living cells undergo a series of active and passive processes occurring in a wide range of temporal scales. From the dynamics of single macromolecules (micro to milliseconds) and up to the cell cycle (hours), cells perform a temporal integration of all their internal processes. One example that illustrates this interplay across the spatio-temporal scales, is mechanotransduction, that is, how cells translate the mechanical properties of their environment into biochemical signals. Since the mechanical properties of cells confer to them the ability to respond temporally and spatially to their environment, we consider here the cell mechanics as an essential factor to explain their regulation and modification in pathological situations. We have developed a methodology that paves a broad frequency spectrum. It is based on two techniques suited to study single-cell mechanics: Diffraction Phase Microscopy (DPM) and Atomic Force Microscopy (AFM). DPM is a non-intrusive optical technique that quantifies the optical phase of the object, proportional to the product of its refractive index and thickness. We complement DPM, that covers a range of frequency from the microHz to kHz, with AFM, that offers a greater spatial resolution with a frequency range from mHz to MHz, allowing also to evaluate the cell response to a local mechanical perturbation.

In the first chapter of this thesis I discuss the importance of spatial and temporal scales in living systems, and I review the main components involved in the mechanical response of living cells. After this introductory chapter, the second one is dedicated to evaluating the mechanical response of single-cells with AFM, and in particular, its dynamical aspect. I present the analysis of force-indentation curves without any assumption on the linearity of the system, contrary to more typical analysis based on Sneddon's or Hertz models. Then, I propose an alternative method to study the cell rheology based on the multi-frequency excitation of the cantilever by thermal noise. DPM is discussed on chapter three. I revisit the phase recovery method using the 2D wavelet transform, and I show how DPM can be used to characterise the temporal fluctuations and the morphology of different types of blood cells and adherent cells. Finally, chapter four is a conclusion chapter where I summarise our results by comparing healthy and pathological immature blood cells. For instance I show that, in comparison to healthy cells, leukaemic cells undergo morphological changes that are accompanied by a stiffer and more elastic behaviour. Altogether, our results indicate that this cell transformation involves the whole cytoskeleton and its coupling to the nucleus rather than simply the cell cortex.

Résumé

Une cellule vivante présente une série de processus actifs et passifs qui ont lieu sur une large gamme d'échelles temporelles. En commençant par la dynamique de macromolécules (allant de la micro à la milliseconde) et jusqu'au cycle cellulaire (heures), la cellule réalise une intégration temporelle de tous ses processus internes. Un exemple qui illustre cette interaction entre les différentes échelles spatio-temporelles, est celui de la mécanotransduction. C'est à dire, comment la cellule traduit les propriétés mécaniques de l'environment aux signaux biochimiques. Étant donné que les propietés mécaniques d'une cellule lui permettent de répondre temporellement et spatialement à son environment, nous considérons la mécanique cellulaire comme un facteur essentiel pour expliquer leur régulation et modification dans des situations pathologiques. Dans cette étude, nous avons developé une méthodologie permettant de couvrir une large gamme de fréquences temporelles. Cette méthode est basée sur deux techniques adaptées pour l'étude de la mécanique des cellules uniques: la microscopie de diffraction de phase (DPM en anglais) et la microscopie à force atomique (AFM). La DPM est une technique non-intrusive qui quantifie la phase optique de l'objet, proportionelle à son indice de refraction et son épaisseur. Nous complémentons la DPM, qui permet d'étudier des dynamiques dans la gamme de fréquence [μHz, kHz], avec l'AFM. Cette dernière offre une meilleure résolution spatiale avec un spectre de fréquence entre les mHz et les MHz, et permet en autre d'évaluer ainsi la réponse cellulaire suite à une perturbation mécanique.

Le premier chapitre de cette thèse traite de l'importance des échelles temporelles et spatiales dans le contexte des systèmes vivants. J'y décris également les principaux composants de la réponse mécanique des cellules vivantes. Après ce chapitre introductif, le deuxième chapitre est dédié à la réponse mécanique des cellules évaluée avec l'AFM et en particulier, son aspect dynamique. Je présente d'abord l'analyse des courbes force-indentation, puis je propose une méthode alternative pour l'étude de la rhéologie cellulaire qui est basée sur l'excitation multi-fréquence du levier par bruit thermique. La DPM est l'objet du troisième chapitre où je revisite la méthode d'extraction de phase en utilisant la transformation en ondelette à deux dimensions. Ensuite je montre comment la DPM peut être utilisée pour caracteriser les fluctuations temporelles et la morphologie de différents types de cellules du sang et de cellules adhérentes. Finalement, le chapitre quatre est un chapitre de conclusion où je fais une synthèse des résultats obtenus. Par exemple, je montre que, en comparaison avec des cellules saines, les cellules leucémiques subissent des changements morphologiques qui sont accompagnés par un comportement mécanique plus rigide et plus élastique. Cela indique que dans cet exemple la transformation cellulaire n'est pas seulement donnée par son cortex mais aussi par son cytosquelette et son couplage avec le noyau.

Table of Contents

Acknowledgements iii

Abstract v

Table of Contents vii

List of Figures x

List of Tables xiii

1 Complexity of living systems: from scaling laws to single-cell mechanics 5
1.1 Biological systems and complexity . . . 5
1.1.1 Scaling laws in biology . . . 7
1.2 Spatio-temporal description of a living cell . . . 8
1.2.1 Nucleus . . . 8
1.2.2 Cytoskeleton . . . 10
1.2.2.a Intermediate filaments . . . 10
1.2.2.b Microtubules . . . 11
1.2.2.c Actin filaments . . . 12
1.2.3 Cell membrane . . . 14
1.3 Single-cell mechanics . . . 16
1.3.1 Cell microenvironment . . . 18
1.3.2 Mechanotransduction . . . 18
1.3.2.a Sensing the microenvironment properties . . . 18
1.3.2.b Integration of mechanical signals and cell response . . . 19
Summary . . . 20

2 Stress-strain response of single-cells under AFM indentation 21
2.1 Mechanical properties of viscoelastic materials . . . 21
2.1.1 Low deformation regime: Linear elastic materials . . . 21
2.1.2 Viscoelasticity and the time dependence . . . 21
2.1.2.a Maxwell model . . . 22
2.1.2.b Kelvin-Voigt model . . . 23
2.1.2.c Generalised Maxwell model . . . 23
2.1.3 Viscoelastic models for living cells . . . 24
2.1.3.a Fractional scaling laws in cellular rheology . . . 25

2.2 Principles of Atomic Force Microscopy . . . 27
2.2.1 Experimental setup and operation modes . . . 27
2.2.2 Estimation of the cantilever spring constant . . . 28
2.3 Materials and Methods . . . 29
2.3.1 TF1 cell line and culture conditions . . . 29
2.3.2 Force indentation curves . . . 30
2.3.2.a Data recording on the TF1 cell line . . . 30
2.3.2.b Wavelet Transform Analysis of force-indentation Curves . . . 30
2.3.3 Thermally excited AFM . . . 31
2.3.3.a Signal recording of cantilever fluctuations . . . 31
2.3.3.b Data analysis . . . 32
2.4 Quasi-static measurement of cell stiffness with atomic force microscopy . . . 32
2.4.1 Large distance cell indentations with atomic force microscopy on living cells . . . 33
2.4.2 Tracking the scaling-laws of AFM force-indentation curves . . . 35
2.4.2.a Actin cortex stiffening as signature of leukaemic cells . . . 38
2.5 Temporal survey of the cell mechanical fluctuations . . . 40
2.5.1 Cantilever dynamics and thermal noise . . . 41
2.5.1.a Parametrisation of experimental curves . . . 43
2.5.2 Dynamics of healthy and leukaemic HSCs . . . 45
2.5.2.a From fluctuation signals to cell mechanics . . . 50
Summary . . . 54

3 Diffraction Phase Microscopy **55**
3.1 Principles of DPM . . . 55
3.1.1 Phase objects . . . 55
3.1.2 Theoretical background . . . 56
3.1.3 Design considerations . . . 58
3.2 DPM setup characterisation and phase extraction method . . . 59
3.2.1 Spatial filter . . . 59
3.2.2 DPM setup resolution . . . 61
3.2.3 Revisiting the phase extraction method with the 2D wavelet transform . . . 62
3.2.4 Homogeneity in the field of view . . . 65
3.3 Materials and methods: cell culture and sample preparation . . . 69
3.3.1 Cell culture . . . 69
3.3.2 Microbeads and polymer layers . . . 70
3.4 Imaging of model systems . . . 70
3.4.1 PMMA layers . . . 71
3.4.2 Polystyrene beads . . . 75
3.5 Characterisation of living cells . . . 78
3.5.1 Geometrical parameters . . . 79
3.5.2 Composition and refractive index . . . 80
3.5.3 Optical path depth . . . 82
3.6 Methods for the characterisation of the cell structure . . . 83
3.6.1 Image segmentation for object identification . . . 83

3.6.2 Multi-sphere boundary model: phase isocontours . . . 85
3.6.2.a One-dimensional case: Isotropic structures . . . 85
3.6.2.b Phase profiles on 2D . . . 90
3.6.2.c Application of the multi-shell model to single cells. . . . 93
3.6.3 Wavelet transform maxima chains . . . 95
3.6.3.a 2D Gaussian derivative WT and local maxima detection . . . 97
3.6.3.b Application of the WTMM method to single cells . . . 102
3.7 Cell morphology characterisation . . . 105
3.7.1 Red Blood Cells . . . 105
3.7.2 Primary CD34+ cells . . . 108
3.7.3 TF1 cell line: transformation induced by an oncogene and adherence . . . 111
3.7.3.a Intracellular structure characterisation . . . 115
3.7.4 Adherent cells: Myoblasts C2C12 and hepatocytes HepG2 . . . 116
3.8 Living cell dynamics . . . 119
3.8.1 Healthy and leukaemic Red Blood Cells . . . 119
3.8.2 TF1 cell line: round-shaped cells with a complex internal structure . . . 123
Summary . . . 130

4 Conclusions and prospects **131**

Appendices **156**
A. Multi-scale analysis of AFM force-indentation curves. . . . 157
B. Passive cell rheology with thermally excited AFM. . . . 175
C. Wavelet-based analysis to retrieve the phase from DPM images . . . 183
D. Detection of internal boundaries from optical path difference gradients. . . . 195

List of Figures

1.1 Biological processes in space and time . . . 6
1.2 Nuclear envelope structure . . . 9
1.3 Intermediate filaments assembly . . . 11
1.4 Microtubules polymerisation and localisation . . . 13
1.5 Actin filaments organisation . . . 14
1.6 Experimental techniques to probe single-cell mechanics . . . 17
1.7 Temporal mechanical response of a cell . . . 19

2.1 Types of stress applied to deform a material. . . . 22
2.2 Vsicoelastic models for living cells. . . . 25
2.3 Atomic Force Microscopy. . . . 28
2.4 Scheme of the first three symmetric modes for a rectangular cantilever. . . . 29
2.5 Power spectral density of the thermal-excited fluctuations of a rectangular cantilever in air. . . . 30
2.6 Shear modulus extraction from AFM force curves on immature hematopoietic TF1 cells. . . . 34
2.7 Illustration of the computation of the scaling exponent α from three model force-indentation curves corresponding to three different α exponents. . . . 37
2.8 Force indentation curve analysis of control and cancer TF1 cell lines, in adherent conditions . . . 39
2.9 AFM cantilever as a damped spring-mass system. . . . 42
2.10 Oscillations from a clamped-free rectangular cantilever. . . . 43
2.11 PSD comparison of v-shaped cantilevers oscillating free in air or in water. . . . 44
2.12 AFM topography image of an adherent TF1-BCR-ABL cell. . . . 45
2.13 Positioning of the AFM cantilever tip on TF1-GFP cells. . . . 46
2.14 AFM vertical deflection from a cantilever in contact with an TF1-GFP cell. . . . 47
2.15 TF1-GFP cell dynamics extracted from the cantilever torsion signal . . . 48
2.16 Wavelet transform for the detection of the cell response in the deflection signal of TF1-GFP cells. . . . 49
2.17 Positioning of the AFM cantilever tip on TF1-BCR-ABL cells. . . . 49
2.18 TF1-BCR-ABL cell dynamics extracted from the cantilever deflection signal . . . 50
2.19 Comparison of periodograms and wavelet spectra $E_z(\omega)$ of cantilever fluctuations when placed in contact with a TF1-GFP cell. . . . 52
2.20 Comparison of periodograms and wavelet spectra $E_z(\omega)$ of cantilever fluctuations when placed in contact with a TF1-BCR-ABL cell. . . . 52

3.1 Wavefront deformation induced by a phase object. 56
3.2 Diffraction Phase Microscopy (DPM) setup 57
3.3 Evaluation of the filtered image with different pinholes. 60
3.4 2d anisotropic Morlet wavelet 63
3.5 Wavelet transform modulus maxima detection 64
3.6 Phase extraction methods comparison 66
3.7 Homogeneity in a liquid chamber 67
3.8 Values distribution for a liquid chamber. 68
3.9 Imaging of PMMA layers 72
3.10 OPD maps of PMMA layers 73
3.11 Thickness distribution from a PMMA layer. 74
3.12 PMMA layer thickness measured by AFM. 74
3.13 Imaging of small polystyrene beads. 75
3.14 Intensity and phase profiles of a cross section from a small bead. 76
3.15 OPD image of a 10 μm polystyrene bead. 77
3.16 Imaging of 10 μm polystyrene beads aggregates. 78
3.17 Geometrical description of living cells. 79
3.18 Cell composition and refractivity. 81
3.19 Characterisation based on the Optical Path Depth. 82
3.20 Image segmentation method for object identification. 86
3.21 3D representation of the isotropic multilayer model structures. 87
3.22 OPD profile and OPD distribution for the radial section of a solid sphere. 88
3.23 OPD profile and OPD distribution for the radial section of a cortex filled with a denser medium. 88
3.24 OPD profile for the radial section of an empty cortex. 89
3.25 OPD distribution for the radial section of an empty cortex. 90
3.26 OPD distributions from two-dimensional OPD maps. 91
3.27 OPD map and OPD distribution of a multi-sphere structure. 92
3.28 OPD distribution of an asymmetric multi-shell structure. 93
3.29 Phase isocontours of a living cell. 94
3.30 OPD profiles from model spheres with radial RI profiles. 97
3.31 OPD profiles from model spheres with non-monotonous radial RI profiles. 98
3.32 2D Gaussian derivative wavelet 98
3.33 Wavelet transform argument for a spheroid and an ellipsoid contour. 100
3.34 WTMM chain detection from the OPD profile of a noisy RI spherical model. . . . 101
3.35 WTMM chain detection on a living red blood cell. 103
3.36 WTMM chain detection on a living CD34+ primary cell. 104
3.37 Changes in shape of a human erythrocyte and flicker activity 106
3.38 OPD images of living red blood cells. 107
3.39 Morphological parameters of RBCs. 108
3.40 OPD images of living CD34+ primary cells. 109
3.41 Morphological parameters of CD34+ cells. 110
3.42 OPD images of living TF1-GFP cells. 111
3.43 Morphological parameters of non-adherent TF1-GFP vs. TF1-BA cells. 112
3.44 OPD images of TF1-BA cells clearly transformed by the oncogene. 112

3.45 Morphological parameters of adherent TF1-GFP vs. TF1-BA cells. 113
3.46 OPD images of adherent TF1-GFP vs. TF1-BA cells clearly transformed by the oncogene. 114
3.47 Cell segmentation of healthy and cancer TF1 cells based on isophase contours. . 115
3.48 Statistical analysis of cell structural parameters from the WTMM analysis of control and cancer TF1 cells. 116
3.49 OPD images of living myoblasts. 117
3.50 Morphological parameters of adherent C2C12 myoblasts. 118
3.51 OPD images of living hepatocytes. 119
3.52 Temporal evolution of the cell position of healthy and leukaemic RBCs. 120
3.53 Deformation of a healthy RBC 121
3.54 Deformation of a leaukaemic RBC 121
3.55 Spatial distribution of the OPD scaling exponent for a healthy RBC. 122
3.56 Spatial distribution of the scaling exponents of a CML RBC. 123
3.57 Temporal evolution of the cell position of TF1-GFP cells. 124
3.58 Deformation of TF1-GFP cells. 125
3.59 OPD scaling exponent for a TF1-GFP cells. 126
3.60 Spatial distribution of the scaling exponents of TF1-GFP cells at different frequency ranges. 127
3.61 Spatial distribution of the scaling exponents of TF1-GFP cells. 127
3.62 TF1-BA cell dynamics measured by DPM. 129

4.1 BCR-ABL induces an alteration of F-actin distribution in TF1 cells 134
4.2 TF1 cell transformation by the oncogene BCR-ABL. 136

List of Tables

2.1 Theoretical values of the correction factor β_n for a rectangular and a triangular cantilever 29
2.2 Parametrisation of the experimental curves obtained from a clamped-free rectangular cantilever. 44

3.1 DPM setup parameters determining the spatial resolution of the system 61
3.2 Parameters used for the characterisation of living cells 84

Preamble

Experimental and theoretical studies on single cells have been the focus of cellular biological and biophysical research during the past two decades. Being the simplest form of life, a living cell provides the necessary information to understand the link between higher levels of organisation and molecular events. However, a single cell is highly complex in both space and time, with emergent properties that will depend on the scale of study. A clear example of this spatio-temporal dependence is the cell mechanical properties. They are related to the organisation and dynamics of the cell structure, and they confer to the cell its ability to respond and adapt in real time to intra-/extra stimuli. Indeed, one of the most active fields of research in biophysics is the characterisation of cell mechanics. Generally, a living cell is considered as a viscoelastic material with nonlinear dynamics. Beyond the questions that can arise regarding the biomolecular nature of this behaviour, the mechanical description at the whole-cell level remains a theoretical and experimental challenge.

There is an increasing number of mechanical models that aim to relate, using elastic and/or viscous parameters, the cell response to an external stimuli. Given that we are working at nano- and micro-metric scales, the thermal fluctuations become an important component of the system. One of the main difficulties then encountered, is the evaluation of the contribution from active and passive processes to the total cell response. For relatively simple cells such as Red Blood Cells (RBCs), the separation of passive and active fluctuations has been broadly studied. The homogeneous structure and well-defined geometry of RBCs permit to model the membrane fluctuations due to thermal noise and to ATP, as well as to estimate the range of frequencies where each type of response can be observed. In physiological conditions, the model predictions are in good agreement with experimental data, but small differences start to appear when cells are not in optimal conditions (ageing, solution tonicity, pathologies...).

Most cell types, however, possess a more complex and dynamical structure, leading to very interesting physical phenomena. For instance, the cell cytoskeleton and the plasma membrane, that is, two of the main cell structural components, are systems far from equilibrium with structural rearrangements and nonlinear dynamics principally driven by ATP. The fast development of experimental tools suited to study the sub-/cellular structures, has offered the possibility to measure the cell mechanical properties with an outstanding amount of temporal and spatial resolutions. It is possible, for example, to apply a local mechanical stimuli using atomic force microscopy or magnetic/optical tweezers; impose a mechanical constraint at the whole-cell level using substrate stretching, microplates or microfluidic devices; follow

the cytoskeleton rearrangements with fluorescence microscopy; or to passively study the cell structure and deformation with non-intrusive optical techniques. With the vast amount of information that can be accessed experimentally, it is now important to address the compatibility between results, and mainly, how they can be integrated to describe and understand the cell behaviour. In the last decade, a consensus between techniques and cell types has started to consolidate. Rather than assuming an *a priori* structure or mechanical model to retrieve values of viscoelastic variables, such as the Young's or shear modulus, the focus has been directed to investigate the type of hierarchical structure that will best describe the observed cell response.

The current thesis work aims to characterise the structure and dynamics of living cells using two complementary techniques: on the one side an intrusive mechanical nanoscale deformation method (atomic force microscopy - AFM) and on the other side a non intrusive optical interferometry method (diffraction phase microscopy - DPM). AFM allows to evaluate the cell response to a precise mechanical stimuli with great spatial and temporal resolution, however its high localization limits the field of observation to sub-micron regions and can hardly provide a spatial map of the cellular response at a reasonable speed. DPM on the contrary, is a wide-field coherent optical technique that permits a non-intrusive quantification of the optical phase of the object, proportional to the product of its thickness and refractive index. When its coupled to high speed cameras (kHz acquisition rate) it is possible to rapidly evaluate the structure of a large set of cells, and to perform longer time recordings with an acquisition speed limited only by the camera. However, the interpretation of a phase map extracted from a single image is quite complex and challenging.

When I started my PhD work, I could have access to a commercial AFM and the DPM optical bench was not yet assembled and tested. Even if the AFM system was already providing acquisition and analysis softwares, these data which were already filtered and transformed by the manufacturer were not suited for our spectral analysis. We had to add another raw data capture system and to develop our own analysis softwares to validate the calibration of the nanocantilevers and to check the stability of the recorded signals. Concerning the optical system, it took us about one year to have the correct filtering and illumination systems after several trials and error and special fabrication by an external company. The recovery of the phase images from the raw interferometry images could not be performed with standard Hilbert transform methods. Therefore, we tested different filtering methods and we finally ended on the wavelet transform modulus method as the most efficient tool. Finally, after more than one year of efforts we could finally test these two systems on calibrated samples (polymer layers in air and in liquid for the AFM, and polymer and glass microparticles for the DPM). These steps were also helpful for me to master the physical and technical principles of these two methods. I could not describe in much details all these technical steps in this document to let more space for the discussion of experiments with living cells.

The chapter 1 of this thesis introduces the context of this study. I start discussing the complexity found in living systems, emphasising the importance of the spatio-temporal scales. Next, I describe the main structural cell components that contribute to its mechanical and dynamical behaviour: the nucleus, the cytoskeleton and the cell membrane. Rather than describing

the biochemical composition of each component, I focus on their structural and temporal organisation as well as their mechanical properties. I follow up with a synthesis of the current progress in cell mechanics and the main questions being tackled: what type of material are we dealing with? how well do the current mechanical models explain the cell response? how does the intracellular structure dictates the cell mechanics? The chapter ends with a brief description of mechanotransduction, i.e., how the cell translates mechanical to biochemical signals to adapt to its environment, exemplifying the coupling of processes across spatio-temporal scales.

The evaluation of the response of living cells under AFM indentation is presented in chapter 2. The characterisation of the cell mechanical response relies on its ability to deform under the application of a given load. Therefore, the stress-strain response of single cells is a fundamental step in their characterisation. I recall the basic concepts of viscoelastic materials, such as the Young's and the shear modulus, and their time dependence due to viscosity. After describing simple spring-dashpot models, such as the Maxwell model or the Kevin-Voigt model, I review briefly some of the continuum viscoelastic models for living cells, pointing out strengths and weakness of each of them. One of the main reasons of the high variability between reported values for the elastic modulus of cells in similar experimental conditions, is the 'blind' use of common mechanical models to fit experimental data. A majority of studies analysing the force-indentation curves obtained with AFM, assumes that the cells behave as linear and elastic systems, which is generally true only at very small indentations. Even if the validation of such assumption is a crucial point on the analysis of force-indentation curves, it is often ignored. Differently from other research groups working with force-indentation curves, we have decided to make no hypothesis on the underlying mechanical model and to rather use statistical and signal analysis tools (Fourier filtering and time-frequency decompositions) to recover the local shear modulus and its potential variation during an AFM indentation experiment. Considering the highly dynamic nature of living cells, we focus also on the dynamics of these cells under constant load. One difficulty that arises on dynamic AFM measurements, is the excitation of the cantilever by thermal noise, its correct choice and calibration is therefore crucial. We used a standard spring-dashpot model to describe the thermal excitation of the cantilever, and I discuss several aspects that need to be considered on the cantilever choice. Two type of experiments were performed with AFM on living cells: i) large amplitude strain-to-stress response obtained for a fixed velocity of indentation, and ii) small amplitude deformations driven by thermal noise for a fixed load. The first approach allows us to follow in real time how a living cell responds to a large deformation and possibly to follow the modification of its shear modulus depending on the depth of penetration of the cantilever. The second approach remains a very local measure where the cantilever is pressed inside the cell and maintained at a given load; in that case we record the thermal fluctuations of the tip of the cantilever whose autocorrelation functions are shown to be related to the local shear modulus $G(\omega)$ of the material, thanks to the fluctuation dissipation theorem (FDT). We apply both of these methods to compare the mechanical properties of hematopoietic stem cells and their transformation by transduction with the chronic myelogeneous leukaemia oncogene BCR-ABL

On chapter 3, I present the implementation of a DPM setup to study the structure of living

cells. This non-intrusive interferometric technique introduced by Popescu *et al.* in 2006 relies on a common-path interferometer, providing a stable compact configuration with fast image acquisition. I start by introducing the theory behind such technique and mainly, I discuss the design principles of the setup, i.e., the diffraction grating and the spatial filter. I report first the characterisation of calibrated systems, such as PMMA layers and polystyrene microbeads, to validate the experimental setup. To retrieve the optical phase from the recorded interferograms, we use a two-dimensional filtering method based on anisotropic two-dimensional wavelet transforms (Morlet). By applying this method to numerical models of microbeads, and to experimental data, we show its ability to retrieve the phase even when there is a step phase gradient and/or intensity variations, surpassing more traditional methods as the ones based on the Hilbert transform or a simple Fourier filtering. I discuss the difficulties that arise from the interpretation of the phase images, both for the cell contour and for the intracellular regions where the refractive index of the medium is integrated all along the cell thickness, coupling both quantities. We then image different types of cells, such as RBCs, non-adherent blood cells (primary cells, TF1 cell line characterised on the previous chapter), and adherent cells (myoblasts C2C12 cell line, hepatocytes HepG2). We study the cell structure at the whole-cell level via the characterisation of their contour and their internal structures. For the later case, it was necessary to develop an analytical tool capable of retrieving the contours about intra-cellular domains. We implemented a wavelet based contour detection method for that purpose. This method identifies the cell regions where the OPD gradient is locally maximum, thus, serving to characterise how complex or inhomogeneous is the intracellular structure. We then apply the methodology presented with DPM to assess the optical properties of TF1 cells and their possible alteration when they are transformed with the chronic myelogenous leukemia oncogene BCR-ABL. This characterisation is based on a statistical measure of the cell morphology, i.e., geometrical parameters associated to the cell contour, estimation of the cell refractive index thanks to their spherical geometry, and the evaluation of the homogeneity of the cell internal structure. Finally, I show some examples and preliminary results on the temporal recordings of DPM. I analyse the cell movement on the x-y plane, the cell contour deformation and the variations in the optical phase of the cell.

The last chapter, 4, is a conclusion chapter that summarises the results presented on this thesis work, both on the experimental and analytical aspects, as well as their application to the mechanics and dynamics of living cells, for instance hematopoietic stem cells and their transformation by the oncogene of chronic myelogeneous leukaemia. I discuss the coherence of the results obtained with both techniques, and how they are positioned in reference to what has been reported in literature. The final part outlines the perspectives and the possible research topics that could be addressed with the present methodology.

Chapter 1

Complexity of living systems: from scaling laws to single-cell mechanics

Biological processes span over several scales of space and time, covering more than 10 orders of magnitude in length and up to 30 orders of magnitude in time. Traditionally, each level of organisation has been studied in a separate and independent way from each other, having different sub-disciplines devoted to them (Fig.1.1) . The fast development and increased amount of information obtained at the cellular and molecular level have led to an integrative vision of biology, pointing out the interplay and communication across spatio-temporal scales, as well as the need to extend our frame of observation of a given process. For instance, a living cell performs a spatio-temporal integration of mechanical signals to respond and adapt to its environment. Indeed, the mechanical properties of cells are crucial for their regulation and their adaptation to their environment. When these properties are altered, pathological behaviours may occur. In recent years, the multi-scale approach of living systems has gained a lot of interest, introducing 'scaling' or scale invariance to characterise their behaviour across scales.

1.1 Biological systems and complexity

A living system can be described throughout several orders of magnitude. For example, a human being (10^0 m) is composed at the elementary level by molecules (10^{-9} m), involving processes ranging from the $\sim 10^{-12}$ s (associated to molecular vibrations) up to 10^9 s (a lifetime). Furthermore, most of these processes are somehow coupled. A single heartbeat, for example, is the result of a series of signalling mechanisms happening at multiple levels of organisation: a single ionic channel will open and close randomly at sub-milliseconds time scales, eventually leading to the opening of a group of channels and a collective flux of calcium within a pulse during tenths of milliseconds; at a whole cell scale, the electrical stimulation will produce an action potential resulting on an electrical impulse propagating from the heart atrium to the ventricles, causing synchronised contractions each second [5, 6]. Probably one of the most fascinating examples of multi-scale functionality is illustrated in circadian rhythms, that is, the oscillations in biological processes with a 24 hour period. The mammalian circadian

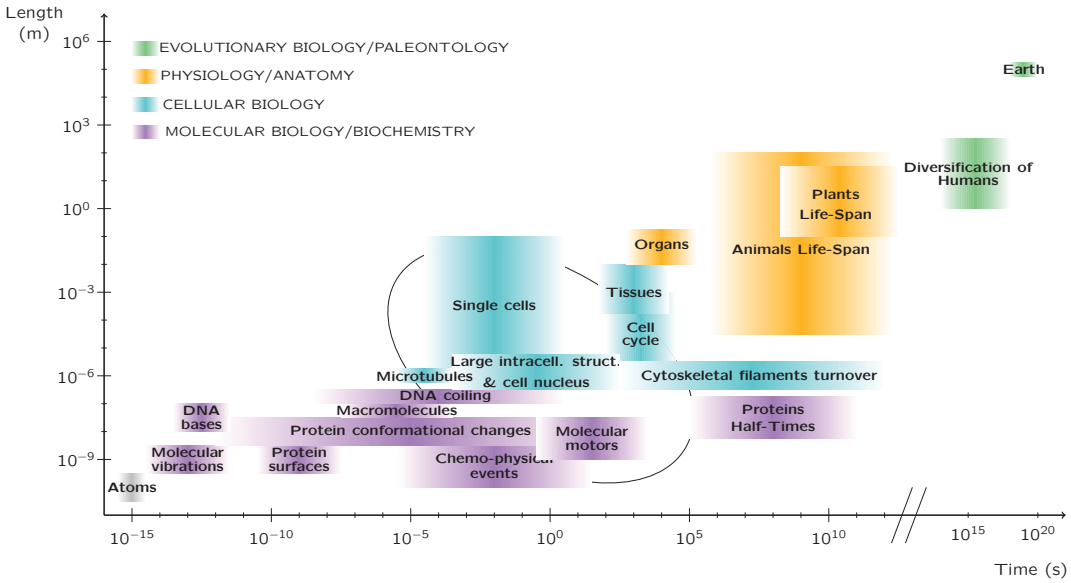

Figure 1.1 – **Biological processes in space and time.** Spatio-temporal distribution of some examples of biological processes. The colours highlight different groups of events accordingly to the sub-discipline studying them. The oval encloses the range of scales and/or processes that are considered in our study. Adapted from [1–4].

clock regulates essential functions such as metabolism, cell cycle and body temperature. An alteration on the circadian clock will have an impact on diverse mood, sleep and neurodegenerative disorders, as well as cancer [6–9] . The circadian peacemaker is localised in the suprachiasmatic nuclei (SCN) of the hypothalamus where nearly 20 000 neurones interact and synchronise together with environmental cycles (particularly stimulated by light), each one going through interlocked feedback loops in transcription and post-translational modifications that generate oscillations on the core clock proteins. This integration and communication between different scales is also present in pathologies. Consider the case of cancer, which may start from genetic mutations triggered by environmental factors. These mutations are likely to produce modifications at a cellular level, which will may later form a malignant cell population. This mass of cells will produce biochemical signals that affect the process of creation of blood vessels, to in turn increase the blood supply for the tumour [10].

The structural and temporal complexity found on living systems can, under certain circumstances, be studied under the framework of the physics of complex systems. A complex system is made up of a large number of simple elements interacting with each other. It should also be thermodynamically open and most importantly, the system possesses emergent properties that cannot be explained solely by summing the individual properties [11, 12]. One remarkable property in living systems is self-organisation, the spontaneous emergence of a non-equilibrium structural organisation from self-driven active parts consuming energy usually produced by metabolism. Such structural organisation can be either spatial, temporal, or both [13, 14]. As the emergent properties of the system are dependent on the scale of study, it becomes necessary to observe what happens at different scales [15]. For example, if we want to understand how the mechanical properties of a biological structure arise from its building

parts, we need to describe a living dynamic structure that covers a range of time scales from the milliseconds (molecular motors) up to several days (development of an organism) [3, 16].

1.1.1 Scaling laws in biology

Let's consider the following function:

$$g(x) = Ax^{\alpha} \tag{1.1}$$

where A and α are real constants, with $\alpha \leq 0$, and x is a variable (the measured parameter). When we represent eq.(1.1) in a log-log plot, this type of function follows a characteristic straight line of slope α. From a mathematical point of view, this power-law or scaling exponent α can have different interpretations: it can determine the long-range dependence, the regularity or the self-similarity of a signal [17]. One of the oldest scaling behaviour reported in biological systems refers to the one of allometric relations. We can find, for example, that the basal metabolism, life span and heart-rate (Y) are related to the mass (M) of an organism by allometric equations of the form $Y = aM^b$ [18–20].

There are numerous systems that follow a scale-invariant behaviour, in other words, they stay quite the same no matter the scale we are looking at, as they have patterns repeating themselves on a whole range of scales [21]. For instance, fractals are geometrical patterns with geometrical and topographical features that are repeated in miniature on smaller and smaller length-scales. Such repetition independent of size or refinement level is called self-similarity [22]. Self-similarity can go from the spatial branching of certain cardiac muscles, the lungs, up to the dynamics of the human heart beat. The temporal recordings of heartbeats is one of the most studied systems [23–26]. It has proven to be a system far from equilibrium presenting a nonlinear complexity that involves coupled cascades of feedback loops. Another example is the one of human gait dynamics [27]. The gait phenomenon refers to the step to step fluctuations in human walking rhythm [23]. The scaling behaviour of these fluctuations becomes more pronounced when the subject needs to adopt a different period than his own, with an increase on the randomness of the fluctuations for children and elderly people. The scaling behaviour of the dynamics of the heartbeat and human gait has proven to be an important parameter on the characterisation of pathologies, providing an alternative way of diagnosis.

At the sub-cellular level, scaling laws have been suggested from experimental data for the secondary structure of rRNA [28], the nuclear organisation of chromatin [29], and in the coding sequence of DNA [30], among others [31]. The scaling behaviour of the membrane flickering of Red Blood Cells (RBCs) [32–34] has revealed differences between different morphological states of erythrocytes, mainly between the discocyte shape and spherocytes. This difference on the scaling behaviour of the membrane fluctuations with time has been related to a low deformability of the membrane and hence, a higher stiffness assumed to be dependent on cellular ATP. In a recent study, the fractal dimension of the cell membrane has proven to be efficient in distinguishing cancer cells from their healthy counterparts [22], providing a marker-free diagnosis tool.

1.2 Spatio-temporal description of a living cell

Single cells are often termed the building blocks of living organisms, positioning the study of living cells as a key stage for understanding how molecular events can affect higher levels of organisation. Even if we can consider single cells as the simplest form of life, they posses a highly complex structure, both spatially and temporally. Furthermore, there is a remarkable amount of molecules and proteins constantly interacting and responding to biochemical, electromagnetical and mechanical signals, conferring to the cell its ability to respond to external stimuli from its environment. In the present work we consider the mechanical properties of the cells as a crucial factor to explain their regulation and alteration in pathological situations. Therefore, in the following I will generally describe the structure of living cells considering only the main components involved on its mechanical behaviour. Furthermore, this description will focus on the structural and material properties of each component, rather than on its biochemical composition, with the objective of sketching the underlying basis and principles of cell mechanics.

1.2.1 Nucleus

The nucleus is the biggest and stiffest cellular organelle. It encloses the genetic information of the cell, separating the chromatin from the cytoplasm with a double lipid bilayer, known as the nuclear envelope (NE). The NE is composed by an inner and an outer membrane, separated by a gap of ~ 50 nm, in contact only at nuclear pore complexes, where molecules under ~ 40 kDa will freely diffuse from/to the cytoplasm, and the bigger ones will be actively transported [35] (Fig.1.2). The outer nuclear membrane is an extension of the endoplasmic reticulum, both structurally and functionally, whereas the inner membrane adheres to the nuclear lamina (NL), an underlying mesh structure of intermediate filaments [36].

The nucleus behaves as a viscoelastic material with very different mechanical properties from those from the cytoplasm, suggesting that the nucleus may be the main contributor to the inhomogeneity of the cell [37, 38]. The main techniques used to study the nuclear mechanics include micropipette aspiration (MPA), atomic force microscopy (AFM), microplate compression and particle tracking. Interestingly, MPA experiments on isolated nuclei have revealed a power-law rheology for the apparent elasticity $E(t)$ of the nucleus and its components [39]:

$$E(t) = B\left(\frac{t}{sec}\right)^{-\alpha} \tag{1.2}$$

where t is the time variable, B is a pre-factor in units of kPa and α is the scaling exponent with values between 0.19-0.32, depending on the swallow state of the nucleus. This could account for the ability of the nucleus to respond differently on a broad range of timescales: at short times the nucleus behaves as a stiffer structure protecting the nuclear interior from brief alterations, and preventing any modification of the gene expression by sudden mechanical changes; whereas at long timescales the lower stiffness allows nuclear deformation, hence affecting the gene expression, and potentially cell spreading and crawling. Although the details of how the mechanical forces sensed by the nucleus affect gene expression will be discussed in section 1.3.2, it is important to say that the integrity and shape of the nuclear lamina is

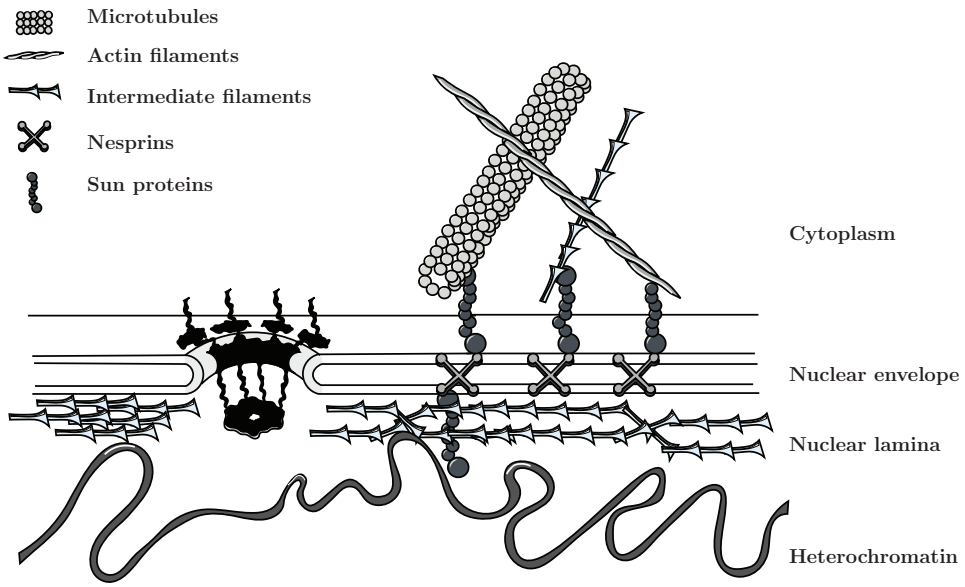

Figure 1.2 – **Nuclear envelope structure.** Scheme of the interacting proteins at the nuclear envelope. The inner and outer membrane are connected at nuclear pore complexes (shown in black). The cytoskeleton is anchored to the nucleus via the LINC complexes, composed by nesprins and sun proteins, while on the intranuclear side, the heterochromatin enters in contact at some points with the nuclear lamina.

crucial for the peripheral positioning of certain genome loci, as some mutations of lamina A and lamina B, two of the main proteins of the NL perturb the intranuclear positioning and compaction of chromosomes, altering the gene expression [40]. In fact, the nuclear lamina is a stiff elastic network and a crucial element of the nuclear mechanics, as it contributes to its stiffness and stability. There are more than 450 diseases associated to lamina mutations or laminopathies, which are often related to highly tissue-specific disorders. It has been speculated that the fact that laminopathies are found at a tissue level reflects the damage caused in single cells who have a weak nuclear envelope [41], affecting the tissue-specific gene expression.

One can question, however, the relevance of the results found on isolated nuclei, as they are unlikely to reflect a physiological situation since isolation techniques very often alter the nuclear mechanical properties. Indeed, at the cellular level shear stress affects the nucleus, its positioning and its substructure, evidencing the existing connection between the nucleus and the cytoskeleton. This coupling occurs via two main families of proteins of the nuclear envelope: sun proteins and nesprins (Fig.1.2), which are part of the LINC complexes (Linkers of Nucleoskeleton and Cytoskeleton) [42]. The interaction between the cytoskeleton and the nucleus is central to regulate the nuclear positioning and shape, with the nucleus maintained in a prestressed state by the cytoskeleton [43–45]. For example, a recent study used micropatterned PDMS covered with fibronectin, imposing geometrical constraints that revealed the

relation between nuclear deformation and density and positioning of actin stress fibres [46].

1.2.2 Cytoskeleton

The cytoskeleton (CSK) is a network composed by several accessory and regulatory proteins, and mainly, from three types of filaments: actin filaments, microtubules (MTs), and intermediate filaments (IFs). The highly dynamic nature of the cytoskeletal structure confers the cell its ability to adapt and respond in real-time to several intra-/extracellular stimuli.

There are two essential processes responsible for the structural reorganisation of the cytoskeleton: the de-/polymerisation of actin filaments and MTs by the hydrolysis of ATP/GTP to ADP/GDP, and the dynamic cross-linking of filaments by ATP driven molecular complexes [47]. In mammalian cells, the actin filament turnover and the dynamics of molecular motors can account for half of the ATP cell consumption. Furthermore, it is the energy consumption, or GTP-'chemical switch' that makes the cytoskeleton a system far from equilibrium, being crucial to explain the dynamic instability of MTs observed experimentally [48]. For instance, it has been shown that in a 3-component *in vitro* CSK model, the non-equilibrium motor activity controls the mechanical properties of the network [49]. Another study suggests the ATP-dependence, and more precisely, the dependence on acto-myosin, of the spontaneous structural rearrangements of the CSK, as observed by the positively correlated dynamics of a bead moving inside the cell characterised by periods of confinement punctuated by hops [50, 51].

Another interesting feature of the cytoskeleton is its emergent mechanical properties. On one side, there is the dramatical influence of filament cross-linking on the cytoskeleton mechanics [52], and on the other, there is recent theoretical evidence of a qualitatively and quantitative difference between the collective behaviour of several filaments and that of a single filament, with the ATP/GTP dynamics playing a central role [48].

1.2.2.a Intermediate filaments

The intermediate filaments (IFs) are the most heterogeneous class of the large cytoskeletal structures. They are encoded by more than 65 genes in humans, with a high cell-type and differentiation-stage specificity [53]. As stated before, IFs form part of the nuclear lamina, but they are also localised at cellular junctions (both cell-cell and cell-matrix junctions), where they interact with multiple supramolecular complexes that are part of the mechanotransduction signalling pathways [54]. They are important to maintain cellular integrity and intercellular connectivity, and they are thought to have a main part on the coordination of mechanical forces in specific tissues during embryogenic development. Diseases associated to mutations on IF proteins are often characterised by the structural disruption or malfunction of tissues. Besides the laminopathies mentioned in section 1.2.1, we can find, among others, the desminopathies, a result of mutations of a muscle-specific IF protein called desmin. The most common desminopathies are the ones affecting the skeletal muscle, and those related to cardiac diseases [55].

Generally, the intermediate filaments are composed of rod-shaped subunits that assemble

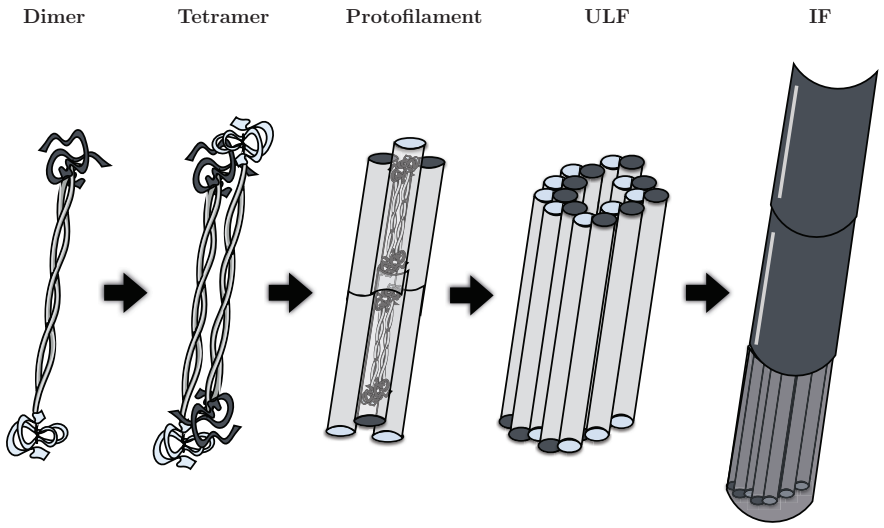

Figure 1.3 – **Intermediate filaments assembly.** Scheme of the intermediate states in IFs assembly. The anti-parallel association of tetramers into protofilaments cause apolar structures. After a fast assembly of unit length filaments (ULFs), the diameter is reduced in a slower phase to form IFs.

into parallel dimers (Fig.1.3). These dimers are highly stable, specially when compared to microtubules or actin filaments, resisting to non-optimal conditions as lower temperature and different salt concentrations. The cytoplasmic filaments are first assembled into full-width ~ 60 nm filaments, by a mechanism of lateral association. This form of assembly is rather quick and can be completed in a few seconds. After a slower phase involving molecular rearrangements of these long filaments, there is an essential cooperative step where the filaments diameter is reduced [56]. The mechanical properties of IFs are then given by the dimers and the cohesive forces between them. As a result, the intermediate filaments network is a highly flexible and nearly unbreakable structure, enabling the cells to support large deformations. For instance, an AFM study on single IFs showed that they can resist strains up to 300 % [57]. Moreover, the association of IFs with microtubules and actin filaments has been shown to reinforce the whole cytoskeletal network [58, 59].

1.2.2.b Microtubules

Microtubules (MTs) are polar polymers composed typically of 13 protofilaments with an α-β heterodimer of the globular protein tubulin, all assembled into a tubular structure with variable lengths but with a rather constant outer diameter of ~ 25 nm and a wall thickness of ~ 4 nm [60]. They are involved in vesicle trafficking and transport, organelle positioning, cell shape maintenance and in chromosome segregation. The MTs are found, for instance, as part of mitotic spindles, which is the structure that forms in the mitosis process. At the spindle mid-zone, MTs can be either linked to each other or bounded to chromosomes [61], called kinetochore MTs (Fig.1.4B). It is thought that during anaphase shrinking kinetochore MTs generate pulling forces that help to segregate chromosomes, as it is known that the poly-

merisation of MTs causes pushing forces whereas pulling forces are a consequence of depolymerisation [60].

It has been shown that the mechanical stability of the microtubule cytoplasmic network is partially due to the MT curvature, or bending, resulting from large non thermal force fluctuations, such as the ones produced by myosin contractility or other ATP-driven motors that affect the directionality of MT growth [62]. Nevertheless, probably the most interesting behaviour of MTs are the so-called dynamical instability and catastrophes (Fig.1.4A). The dynamical instability refers to the constant stochastic switching between growing and shortening states of MTs, probably allowing them to explore rapidly a variety of arrangements and choosing the ones that protect them against depolymerysation [63]. A catastrophe refers to the abrupt transition between the growing state and the shortening one. Interestingly, the force-induced catastrophes are an intrinsic property of microtubules. It has been shown that compressive forces increase the catastrophe frequency while decreasing the MTs growth velocity [64], suggesting a possible local regulation mechanism of MTs dynamics at the cell cortex. Additionally, a recent study observed that the microtubule dynamics are also affected by the different conformations of $\alpha\beta$ tubulin (curved, straight or helicoidal) as there will be a selective interaction of other regulatory proteins that will affect the rate of GTP hydrolysis [65].

Finally, it is important to mention that the microtubules have a highly variable stiffness, with an average value of at least three orders of magnitude more than actin filaments [47]. Moreover, contrary to what has been proposed with theoretical models [48], *in vitro* experiments have found that the force of MT bundles increases linearly with the number of microtubules present [66]. Perhaps such contradictory results arise from the different conditions considered, such as the GTP hydrolysis, filament cross-linking and/or isolated MTs.

1.2.2.c Actin filaments

Actin filaments play a crucial role in cell shape dynamics, as they are a key element to produce contractile forces in the cell. The globular protein actin, or G-actin, is the building block of the double-stranded helical actin filament, or F-actin. In a similar way to microtubules assembly, actin polymerisation is driven by ATP hydrolysis in a head-to-tail manner, producing polar structures. Depending on the function and the cell structure where they are found, the filaments can be organised into different architectures (Fig.1.5): branched/cross-linked networks (lamellipodiums/membrane cortex), and anti-/parallel bundles (stress fibres/filopodium) [67].

The mechanical properties of F-actin and the actin dynamics are often studied *in vitro*, using simple models of the actin network that consist of actin filaments, a cross-linker, and a molecular motor. Actin filaments assemble into a stable network of stiff and rigid bundles in the presence of the cross-linking molecule, whereas the addition of ATP and molecular motors can result in a highly dynamic structure. The activity of such heterogeneous system will depend on its connectivity in order to molecular motors to produce force [68]. Actin filaments

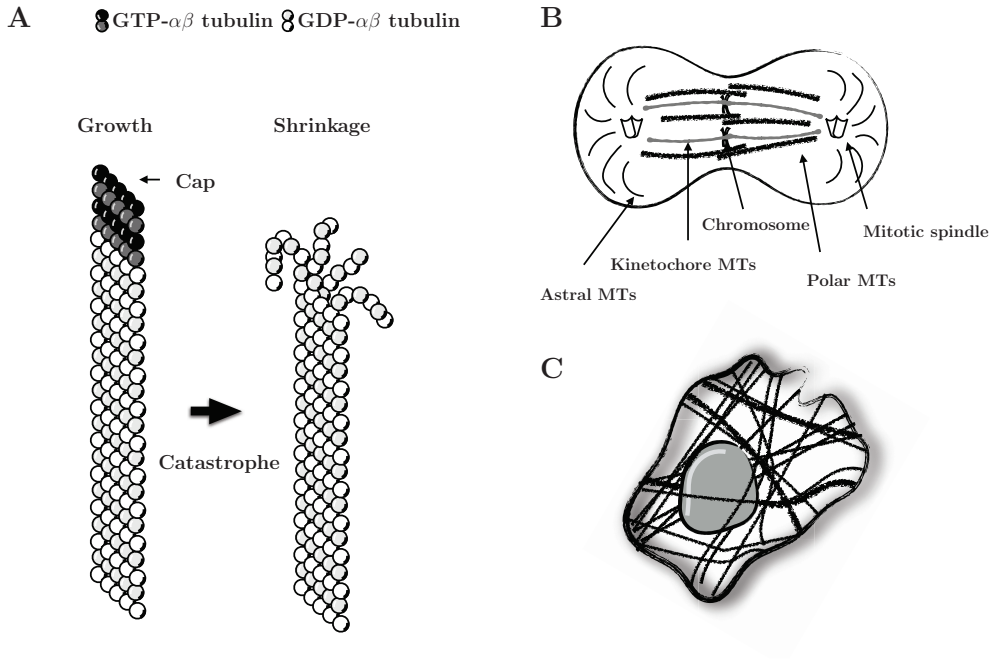

Figure 1.4 – **Microtubules polymerisation and localisation.** (A) MTs are polymerised into tubular structures from GTP-$\alpha\beta$-tubulin heterodimers. Microtubules play an important role in mitosis (B) and in maintaining the cell structure (C).

are usually coupled to myosin, a molecular motor that uses ATP to produce pulling forces on actin filaments. When there are enough cross-linkers in the actin network, that is, when the network has a sufficient level of connectivity, the forces exerted by molecular motors produce contraction. According to the way actin filaments are anchored to the membrane cortex, this contraction can result in changes on the cell shape and cortex remodelling [69, 70]. The actin network contractility is specially important for cell adhesion, migration and during mitosis.

In interphase, cells undergo a structural remodelling where the actin network is rapidly dismantled and reorganised, conferring the cell its round shape. Moreover, the separation of centrosomes is dependent on the cortical flow of actin and the myosin activity [71]. At the end of mitosis, actin is again rearranged into a structure known as the contractile ring that constricts the cell membrane to separate the daughter cells. The formation of the contractile ring requires a group of cross-linking proteins called septins, which are involved in the 'circularisation' of actin bundles [72]. In cell adhesion, actomyosin bundles are coupled to the extracellular matrix via focal adhesions, producing a force-transducing slip-stick friction between the actin filaments and the extracellular matrix [73]. Adherent cells present an interesting phenomenon of actin dynamics consisting of travelling waves. Wave-like actin patterns are found on spreading, migrating and stationary cells, each one presenting different dynamics and extending across subcellular domains [74, 75]. For example, a recent study has found that in geometrically regulated cells, a type of actin waves called circular dorsal ruffles present 'breathing' modes and wave annihilation upon collision of wavefronts [76].

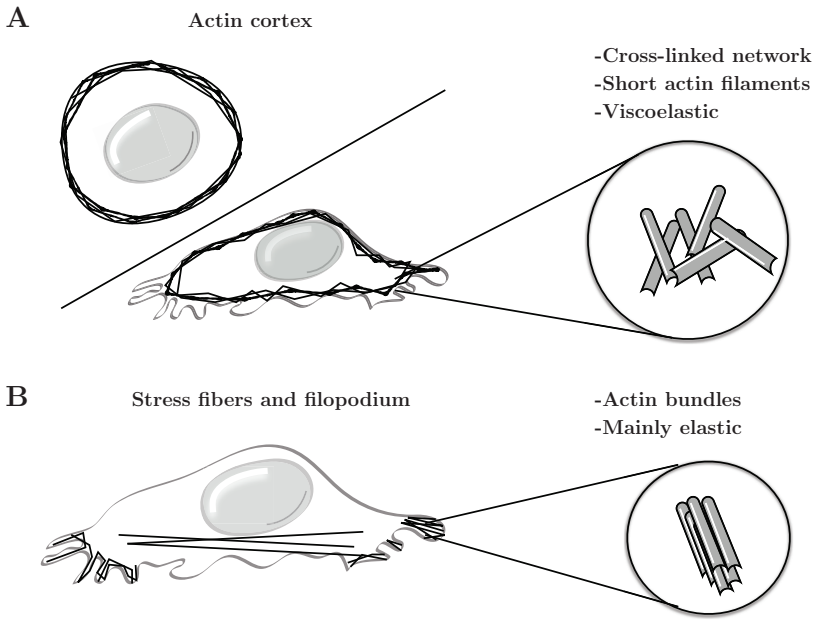

Figure 1.5 – **Actin filaments organisation**. Actin filaments can organise into different structures with distinct mechanical properties. The predominant architectures are cross-linked networks (A) and parallel or anti-parallel bundles (B).

The force generated by actin filaments has been measured on the order of picoNewtons using an optical trap-based method [77]. Surprisingly, it was also found that small actin bundles were similar to single F-actin, suggesting that there is no cooperation between the separate filaments in the bundle to generate forces. It has been shown that the actin bundles establish a mechanical feedback with microtubules *in vitro*: actin bundles can capture and guide MT growth, while microtubules can determinate the F-actin spatial organisation, as they can pull, stretch and bundle single actin filaments [78].

1.2.3 Cell membrane

The plasma membrane separates the cell interior from the environment, allowing the cells to selectively control the import and export of ions and polar molecules. According to the fluid mosaic model [79], the cell membrane can be though of as a two-dimensional liquid in which lipids and proteins diffuse and interact, and as such, it cannot resist shear stresses in the membrane plane, but it will resist normal stress or isotropic tension in the plane [80]. It is composed of a bilayer of phospholipids with some embedded proteins. Furthermore, it is highly heterogeneous with disordered and ordered phases, also known as lipid rafts, characterised mainly by the presence of cholesterol, which is used to adjust the rigidity and structure of the ordered domain. The line tension at the boundary of these domains plays a major role in maintaining the non-spherical shape observed in some cell types. It has been shown that

the bilayer stretching elasticity and chemical composition determine the order-disorder transition, the length of the boundary and the bending rigidities in both phases [81]. Indeed, the membrane deformation, or curvature, is controlled by the proteins and lipids within, as either the shape of the molecules themselves, or the differences in the two monolayers will result in the membrane spontaneous curvature. Interestingly, this curvature induces the reorganisation and remodelling of the ordered/disordered phases, guiding the spatial organisation of proteins and lipids, thus, establishing a continuous feedback between both processes [82, 83].

An animal cell often deals with changes in the osmolarity of the external fluid which is reflected on pressure differences between the cell interior and the outside. Given that the plasma membrane is quite thin and fragile, the cell stores some excess membrane in reservoirs, allowing the cell to increase its surface area by a factor of 3 to 10 times, hence, controlling the membrane tension to avoid breakage. This becomes particularly necessary in hypotonic solutions, as the cells swell due to the influx of water [84, 85]. It has been found that the hydrostatic pressure is non equilibrated along the plasma membrane of blebbing cells [86]. Blebs are almost spherical protrusions with a typical size of $\sim 2\ \mu$m that appear momentarily from the surface of the cell, reappearing elsewhere in a repetitive asynchronous manner. They originate from the detachment of the actin cortex from the membrane, which once a critical threshold tension is reached, grows by filling up with cytosol and without any cytoskeletal structure, in a process that lasts a couple of tenths of seconds. In the ~2 min shrinking step, the bleb passes from being a membrane similar to that of erythrocytes, to a membrane that is coated with an actin cortex [87]. Given that the actin cortex plays a crucial role in blebbing, it has been proposed that by modelling the cortex as an active elastic material, the main characteristics of the bleb can be predicted [88].

One remarkable feature of cell membranes is that they are out-of-equilibrium structures. Indeed, since ionic channels are active proteins that diffuse around in the membrane, there are ATP-driven force fluctuations that become a source of non-thermal noise, producing interesting membrane dynamics [89]. A recent study proposes a hydrodynamic theory based on the forcing of a membrane by a fluid with motile elements, showing that the essential mechanism lies in the interaction of the membrane with the cytoskeleton, driven by ATP [90]. In fact, one of the most debated topics concerns the origin of the cell membrane fluctuations, and in particular, to which extend they are caused by thermal fluctuations. It is often assumed that rapid spontaneous oscillations are related to passive thermal fluctuations, such as the flickering of erythrocytes or even oscillations in lymphocytes, happening at ~ 1 kHz and ~ 0.2-30 Hz frequency, respectively [91]. The slower membrane deformations, however, are often related to an underlying cytoskeleton mechanism driven by ATP, and thought to be crucial for the cell adhesion and motility [91–95].

To end this section, I will briefly mention two of the least studied properties of cell membranes: its roughness, and the effect of electrostatic charges on its mechanical properties. The membrane roughness can be a very sensitive marker of cell health, however, due to its challenging characterisation and experiment-dependent measurement, it has not been well exploited. In spite of that, experiments performed with AFM have proven to be successful when a proper data analysis is involved [96, 97], perhaps fractal analysis being the most promising

analysing tool. On the other hand, electromechanics of cell membranes have gain some recent attention, acknowledging that the membrane potential and the negative charge on the cytoplasmic side can induce modifications on the mechanical properties of the membrane [98, 99].

1.3 Single-cell mechanics

The study of the mechanical properties of living cells imposes several challenges, both experimentally and theoretically. With single cells being a highly complex material whose structure is constantly remodelling in order to adapt to its environment, the key question is: how can we measure the mechanical properties of an object if it reacts to the measurement tools? Furthermore, there is still an uncertainty about what is the most adequate manner of describing the cell mechanical behaviour as it is unclear what kind of material we are dealing with. In general, a living cell can be considered as a viscoelastic object with nonlinear dynamics. However, the details and mechanisms of this behaviour as well as its validity across temporal scales remain elusive.

The central point for the characterisation of the cell mechanical properties is the deformation or resistance to deform of cellular and intracelullar structures when they are subjected to external forces [100, 101]. There are numerous experimental tools that have been developed with this purpose, presenting a large choice of applied forces and spatial resolution: uni-/biaxial tension or compression, pure shear, hydrostatic pressure, bending, twisting, and any combination of them either in a local or global manner with an observation of the intra-/extracellular structure (Fig.1.6). The vast set of experimental conditions and properties measured leads to a big variability on the results and what is more, on the interpretation of such results. In spite of that, there seems to be a general agreement on some characteristics of cell mechanics: it is mainly dictated by spatio-temporal organisation of the cytoskeleton, and it depends greatly on the cell microenvironment. As a result, the cell mechanical properties will be different during cell cycle [102], cell differentiation [103, 104], and they will impact the ability for the cell to spread and/or migrate [105, 106].

There are several models that have been proposed to explain the mechanical behaviour of living cells. The simplest models are perhaps those associated with a spring-dashpot system, either arranged in series or in parallel. However, even if they do predict to some extent the cell viscoelastic properties, they are very limited in what refers to the cell dynamics [107, 108]. In the last decade or so, there have been two models who have gained a lot of attention, particularly for their non-linear mechanical aspect: tensegrity and soft glassy materials. In the tensegrity model the stability of the structures relies on the interaction of elements in tension, such as the stress fibres, with those elements who are under compression, as is the case of microtubules. This balance of forces makes the structure extremely reactive to any outside perturbation: when the structure is deformed the individual elements will reorient, while the local force can result in an integrated structural response [109, 110]. Nevertheless, the increased amount of results finding a power-law behaviour or scale-invariance of the cell viscoelasticity have put the spotlight on soft glassy materials (SGM) [111–117]. The SGM model

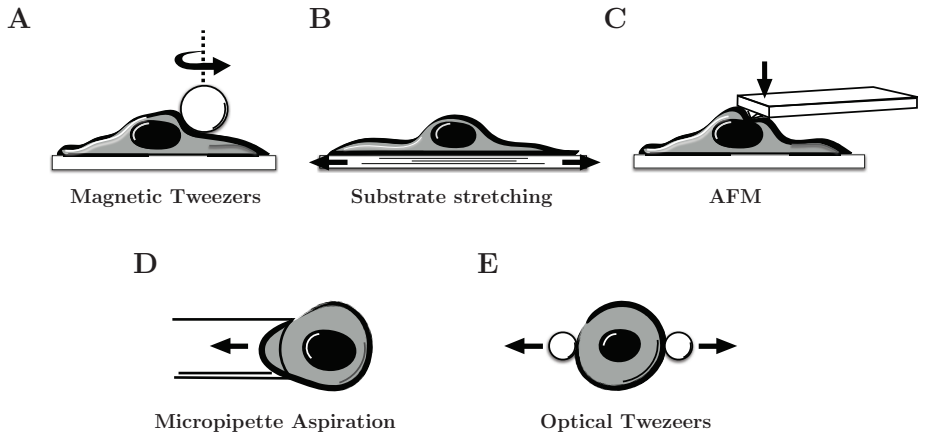

Figure 1.6 – **Experimental techniques to probe single-cell mechanics.** Examples of the most frequently used experimental approaches to asses the mechanical properties of single cells. The forces are applied either at a whole cell level (B,D), with a local probe (C), or at an intermediate scale (A,E).

describes the cell cytoskeleton as a material close to a glass transition, in other words, as a soft elastic solid with some relaxation processes driven by non-thermal stress fluctuations. This implicates that the main features of the cell mechanical behaviour are a dynamical interplay of structural disorder and rearrangements. A slight modification of SGM known as the Glassy Wormlike Model (SWM) includes the retardation of filament relaxation due to sticky interactions, and it has been proposed to explain the active tuning of cell stress stiffening and fluidisation in response to large external forces [118].

With a general vision of the cell mechanical behaviour getting clearer, the questions currently tackled refer to the detail mechanisms of this behaviour. Two of the most challenging research axes include the measurement of intracellular forces at localised sub-cellular structures, and the temporal evolution of the cell response to mechanical stimuli. The measurement of intracellular forces requires experimental tools with high spatial resolution that do not disrupt the intra-cellular structures. One of the most successful techniques is perhaps the study of cells lying on a substrate conformed by flexible micropilars [119]. Depending on the chemical composition of the surface and the stiffness of the micropilars, the cell will attach and exert forces causing the deflection of the pre-calibrated posts. Another recent approach consists on using FRET based sensors that have been genetically inserted in the cytoskeleton cross-linking proteins, demonstrating that the changes in the intracellular tension are mediated by myosin [120]. In what respects to the dynamical measurements, the difficulty lies in the limited temporal scales that can be accessed experimentally, thus requiring novel techniques and methodologies to be developed. For instance, by implementing a two-parallel plate system where one of them is flexible and capable of tuning in real time the effective stiffness experienced by a cell, it has been shown that there is a fast response happening at sub-seconds time scales, likely implying a purely mechanic response [121].

1.3.1 Cell microenvironment

The main cell microenvironment is the extracellular matrix (ECM). It provides the scaffold that gives physical support to cells and regulates the intracellular signalling. Cells are constantly evaluating their environment and respond accordingly, producing intracellular forces that act on the ECM. The extracellular matrix is a dynamic structure whose molecular components include collagens, ellastins and fibronectins, among others [122]. It is known that the rigidity of the ECM determines the cell proliferation and drives cell differentiation into different lineages [103]. Additionally, the matrix elasticity is important for cell contraction, migration and spatial organisation via a force feedback depending on actomyosin. It has been shown that the cells apply higher forces on stiffer substrates [123], and that the cell-induced deformation of the ECM propagates a certain depth into the matrix [124].

1.3.2 Mechanotransduction

Mechanotransduction refers to the process in which the cells sense their physical environment, translating mechanical properties into biochemical signals. In a general sense, the mechanical feedback that the cell establishes with its environment can be simplified into three main stages: cells probe the physical properties of its environment by constantly applying forces and evaluating its ability to deform; depending on the mechanical input that the cell gets, a biochemical signalling pathway is triggered; as a consequence, the cell adapts and reacts to its environment in real-time. Although most of the molecular components involved in each of these steps are known, it is still unclear how they interact and what is their precise role within the feedback.

1.3.2.a Sensing the microenvironment properties

It has been proposed that the cell senses mechanical forces via two types of protein complexes: stretch-induced ion channels, and integrins. In the former, the stress applied to the cell membrane will result on a protein conformational change, switching between open and closed states and causing a rapid increase on the intracellular calcium used as a second messenger in diverse signalling pathways [125]. Integrins, on the other hand, are transmembranal proteins that allow the interaction between the cytoskeleton and the ECM at focal adhesions (FAs). The integrins sensing mechanism is dictated by four key parameters: the strength of integrin binding to ECM ligands, the force, the speed of cell retractions and the sensitivity of associated mechanosensors [126]. There is no actual evidence of a direct binding between integrins and the cytoskeleton, instead it is assumed that they recruit and anchor a protein complex that connects to actin. Furthermore, it is likely that this complex will be responsible for the transformation of the mechanical force into a biochemical signal, as there are numerous signalling proteins localised at FAs [127].

Focal adhesion sites are several microns long and structurally polarised. They evolve from small dot-like adhesions that are continuously formed, eventually maturating into FAs, which grow and extend centripetally and concomitantly with the formation of actin stress fibres [128]. The formation and maintenance of FAs depends on the continuous application of local

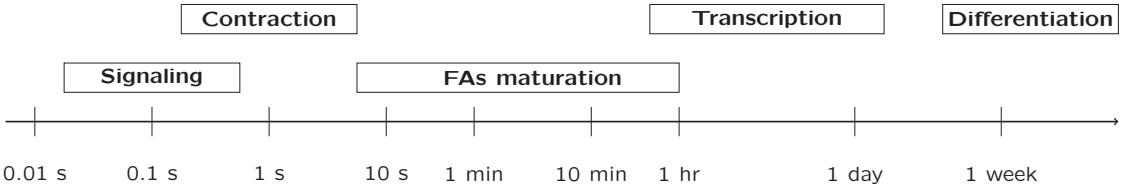

Figure 1.7 – **Temporal mechanical response of a cell.** Different active cell responses to mechanical stimuli occur over a wide range of timescales from the moment the perturbation was made. Adapted from [136].

force. Indeed, it has been shown that tension reinforces focal adhesions, with the direction of the force applied correlating with the elongation axis of the FAs [129]. A recent study proposed that the substrate rigidity regulates the loading rate of cell-substrate forces via the recruitment of more integrins into FAs [130]. The recruitment of new bonds is in turn driven by cytoskeletal movements, resulting in a dynamical process of bond loading, dissosiation and formation [93].

In recent years, the role of actomyosin contractility has been recognised to be crucial for rigidity sensing [131]. The actin-mediated mechanosensing depends on the myosine contractile stress, the speed of actin treadmilling, the elastic modulus and viscoelastic relaxation time of the cortex, and implies that the system can tune its efficiency without altering its behaviour [132].

1.3.2.b Integration of mechanical signals and cell response

One of the main advantages of cell regulation and adaptation depending on mechanical forces is the ability to respond rapidly. Forces can propagate through a wave-like mechanism across the cell body in a few microseconds as they travel at a velocity of several meters per second, with the signal transduction networks activating on several seconds [122]. One of the most intriguing parts of mechanotransduction is how the biomechanical signals are integrated at a nuclear level. It is known that there are several genes that are affected by mechanical cell perturbations, although the mechanisms of force-regulated gene expression remain elusive. One possibility is that the nuclear deformation can directly alter the positioning of heterochromatin, normally anchored to the nuclear lamina, modifying the genomic structure and its accessibility [133]. Interestingly, even though it has been proposed that the perinuclear actin cap connected to the nucleus through LINC complexes is important for the fast mechanotransduction [134], it has also been demonstrated that the LINC complexes are not absolutely necessary to activate the mechanosensitive genes upon a mechanical stimuli, suggesting that stretch forces could also act directly on nuclear pore complexes affecting the nuclear transport [135].

Summary

Biological systems present an outstanding structural and temporal complexity. Not only are the biological processes spanned over a wide range of scales, but they are also integrated and coupled in feedback loops. A key point to understand the spatio-temporal integration from molecules to tissues and their alteration in pathologies is the mechanical behaviour of living cells. The mechanical properties of a single-cell are dictated by the organisation and dynamics of its structure, with the cytoskeleton filaments being a central component in cell mechanical responses. The study of emergent properties and scaling laws has proven to be a complementary and useful tool to understand the underlying mechanisms of the cell structural remodelling and its adaptation to the environment.

Chapter 2

Stress-strain response of single-cells under AFM indentation

2.1 Mechanical properties of viscoelastic materials

2.1.1 Low deformation regime: Linear elastic materials

When the deformation is small, most materials deform elastically in a linear way. Typically, the ability for a material to deform is described by a 'stiffness' modulus, defined as the ratio between the stress and the strain. The Young's modulus (E), for instance, is a measure of stiffness in simple extension or compression, (Fig.2.1A) :

$$E = \frac{\sigma}{\epsilon} \tag{2.1}$$

with the stress σ and the strain ϵ given by

$$\sigma = \frac{F}{A_0} \quad , \quad \epsilon = \frac{\Delta l}{L_0} \tag{2.2}$$

where F is the force applied to the object cross area A_0, producing a change Δl on its total length L_0. A second type of stress, called shear stress, occurs when the deformation of a solid is caused by a force parallel to one of its surfaces while its opposite face experiences an opposing force (such as friction) (Fig.2.1B). The shear modulus G is then defined as the ratio between the shear stress and the shear strain (in Fig.2.1B, $\epsilon = \Delta l_x / L_y$). In the case of isotropic materials, the Young's modulus E and the shear modulus G are related by the expression

$$G = \frac{E}{2(1+\nu)} \tag{2.3}$$

with ν being the Poisson's ratio of the material [137].

2.1.2 Viscoelasticity and the time dependence

Unlike pure elastic materials, where the strain is proportional to the stress, the viscous material response will also introduce temporal dissipation during the deformation or strain-rate

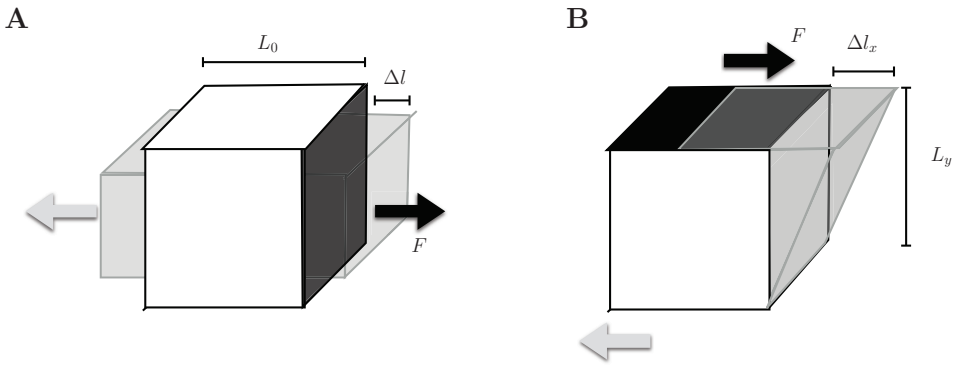

Figure 2.1 – **Types of stress applied to deform a material.** (A) Tensile stress. A force F is applied perpendicular to the object cross area A_0 (highlighted in dark grey), producing a change Δl_0 on its total length L_0. (B) Shear stress. The force F is applied parallel to one of the object surfaces, producing a shear strain $\epsilon = \Delta l_x / L_y$.

effects [138]. There are three major ways of describing viscoelastic behaviour: (i) the integral representation, based on the Boltzmann superposition principle, (ii) the differential representation, described by an assembly of Hookean springs and Newtonian dashpots, and (iii) the molecular description [137]. We will focus on the differential representation, which is perhaps the most intuitive approach for biological systems.

The elastic response is described by a spring of elastic constant E

$$\sigma_s = E\epsilon_s \tag{2.4}$$

and the viscous response is described by a dashpot element of viscosity η

$$\sigma_d = \eta \frac{\mathrm{d}\epsilon_d}{\mathrm{d}t} \tag{2.5}$$

The total response of the system is therefore given by the combination of spring and dashpot elements, arranged either in series (Maxwell model), in parallel (Kelvin-Voigt model), or in a mixture of both (standard linear solid model).

2.1.2.a Maxwell model

In the Maxwell model, the same force is transmitted from the spring to the dashpot. The force transmitted to the two mechanical elements is constant and the energy is shared into the elastic and viscous components. As the two elements are in series, the total strain ϵ_T is the sum of ϵ_s and ϵ_d:

$$\frac{\mathrm{d}\epsilon_T}{\mathrm{d}t} = \frac{\mathrm{d}\epsilon_s}{\mathrm{d}t} + \frac{\mathrm{d}\epsilon_d}{\mathrm{d}t} = \frac{\mathrm{d}\sigma}{\mathrm{d}t}\frac{1}{E} + \frac{\sigma}{\eta} \tag{2.6}$$

In a stress-relaxation experiment, the material is subjected to a sudden strain that is kept constant over the duration of the test, and the stress is measured over time. Then, with $\mathrm{d}\epsilon_T/\mathrm{d}t = 0$, we can write eq.(2.6) as

$$\frac{\mathrm{d}\sigma}{\mathrm{d}t} = -\frac{E}{\eta}\sigma \tag{2.7}$$

Defining $t = 0$ as the starting point of the experiment, with $\sigma = \sigma_0$ the initial stress, by a straightforward integration of eq.(2.6), we get

$$\sigma(t) = \sigma_0 e^{-\frac{E}{\eta}t} = \sigma_0 e^{-t/\tau} \tag{2.8}$$

meaning that the stress required to hold the material at a constant deformation fades away with time, due to the viscous effect of the material: the stress decays exponentially with a characteristic time constant $\tau = \eta/E$.

While the Maxwell model works well for the stress-relaxation experiments, it is of no use for modelling creep. The creep test is another transient experiment performed on viscoelastic materials, where the material is loaded and the change of deformation with time is recorded. The Maxwell model on these constant-stress conditions predicts that the strain will increase linearly with time, in disagreement with experimental observations.

2.1.2.b Kelvin-Voigt model

The Kelvin-Voigt model connects a Newtonian dashpot and a Hookean spring in parallel, such that the stress is distributed at each time into the two mechanical components

$$\sigma_T = E\epsilon_s + \eta\frac{\mathrm{d}\epsilon_d}{\mathrm{d}t} \tag{2.9}$$

For the creep experiment described earlier, we obtain

$$\epsilon(t) = \epsilon_\infty\left(1 - e^{-t/\tau}\right) \tag{2.10}$$

Upon application of a constant stress, the material deforms at a decreasing rate, asymptotically approaching the steady-state strain ϵ_∞.

As for the Maxwell model, the Kelvin-Voigt model has a limited application. It fails to predict stress-relaxation experiments, since under such conditions the model behaves as an elastic solid.

2.1.2.c Generalised Maxwell model

It is possible to obtain a frequency decomposition of the temporal strain-stress response (the spectrum of characteristic times) by combining a number of Maxwell (or Voigt) elements. Indeed, the relaxation spectrum is an important measure of viscoelastic behaviour, as it gives an idea of the number of relaxation processes involved in the stress relaxation. Furthermore, the relaxation spectrum can be derived from different types of experiments allowing comparisons between results.

Consider a number n of Maxwell elements joined in parallel. In the case of a stress-relaxation experiment, the strain is constant and the total stress of the system is simply the sum of the

individual stresses

$$\sigma(t) = \epsilon \sum_{i=1}^{n} E_i e^{-t/\tau_i} \tag{2.11}$$

where E_i and τ_i are respectively the stiffness and the relaxation time of the ith element. Equivalently, we can write eq.(2.11) as

$$\sigma(t) = [G_r \epsilon] + \epsilon \int_0^\infty f(\tau) e^{-t/\tau} d\tau \tag{2.12}$$

with $G_r\epsilon$ refers to the instantaneous stress. The function $f(\tau)d\tau$ replaces E_n and defines the concentration of Maxwell elements with relaxation times between τ and $(\tau + d\tau)$. The relaxation modulus is then given by

$$G(t) = G_r + \int_0^\infty f(\tau) e^{-t/\tau} d\tau \tag{2.13}$$

Therefore, the modulus at time t after the strain is imposed, is the sum of the initial modulus and the relaxation function that describes how the material stores the deformation in a viscous way to achieve the deformation at time t.

2.1.3 Viscoelastic models for living cells

There are several mechanical models that have been developed to characterise living cells based on experimental observations [139]. We will review here in a non-exhaustive manner the continuum mechanical models. The continuum approach is suited to study the mechanical response at the level of a cell, as it treats the cell as the combination of continuum mechanical elements at the expense of local molecular dynamics involved in the cell deformation.

- **Linear viscoelastic solid model.** Upon small strain deformation, the cell is assumed as an homogeneous viscoelastic material, disregarding any structural organisation (Fig.2.2A). Although initially developed for leukocytes, the model has proven to be more useful on several types of anchorage-dependent cells including endothelial cells, fibroblasts and chondrocytes.

- **Maxwell liquid drop model.** The cell is assumed as a pre-stressed cortical shell containing a Maxwell fluid (Fig.2.2B). This model explains the initial jump during micropipette aspiration (MPA), the fast recoil of the projection inside the pipette upon unloading (Fig.1.6 in section 1.3) and the initial rapid elastic rebound. However, upon a large strain-deformation it fails to explain the experimental data.

- **Newtonian liquid drop model.** Unlike the Maxwell liquid drop model, the Newtonian model assumes that the cell interior is a homogeneous viscous liquid, with measured viscosity on the order of 100-200 Pa s. On the other hand, the cell cortex is taken as an anisotropic viscous fluid layer with a static tension but without bending resistance (Fig.2.2C). The membrane tension has been measured as 0.02-0.04 $\cdot 10^{-3}$ N/m. This model cannot predict the elastic phenomena obtained with a Maxwell liquid drop model and observed in MPA.

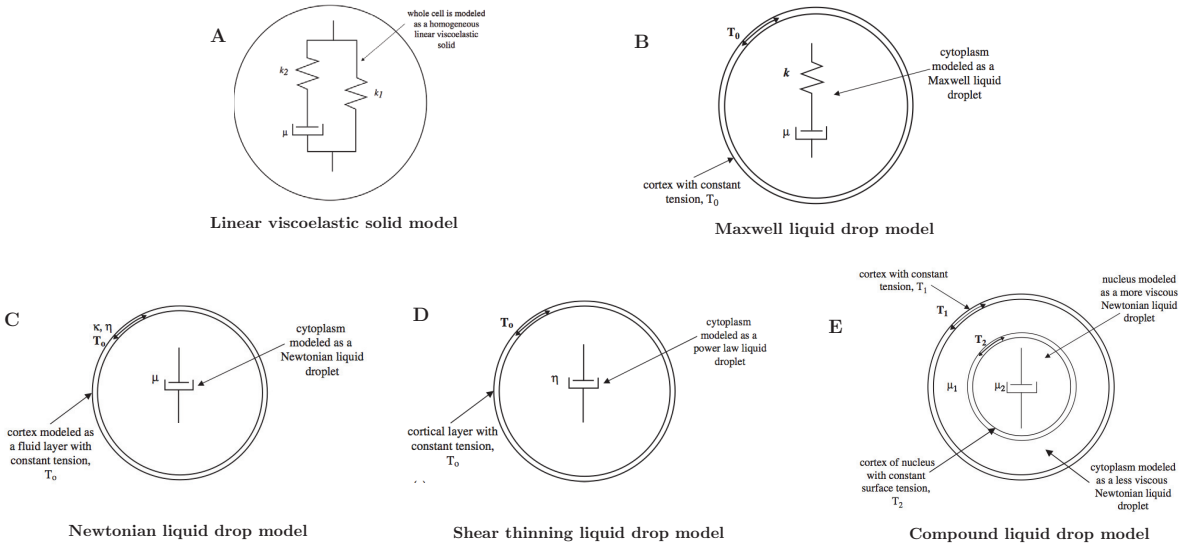

Figure 2.2 – **Viscoelastic models for living cells** [139] .

- **Shear thinning liquid drop model.** It has been observed that several biological materials present shear thinning, in other words, their viscosity decreases with an increasing rate of shear stress. The shear thinning liquid drop model adds a power-law constitutive relation to the cortical shell liquid core model: a positive feedback is established such that an increase in shear rate will lead to a decrease in viscosity (Fig.2.2D). It is more suited to model the large deformations than the small strain deformations.

- **Compound Newtonian liquid drop model.** The cell is modelled as a multilayered structure: (i) the plasma membrane and the ectoplasm compose the outer layer with a thickness >100 nm, (ii) the middle layer is composed by the endoplasm, which is fluid like and the softest region of the cell, (iii) the nuclear envelope is a cortex with constant tension and (iv) the core layer is composed by the condensed region of the nucleus (Fig.2.2E). It is perhaps the model that best describes the cell behaviour in transient experiments[1]. The respective elastic/viscosity ratio of each layer leads to different time scales that can explain the viscoelastic phenomena under small and large deformation. Although it can explain some nonlinear experimental phenomena, different parameters result in the same rheological behaviour, due to the impossibility to observe experimentally each layer separately.

2.1.3.a Fractional scaling laws in cellular rheology

Recent studies of the microrheology of the intracellular medium have highlighted the fact that this viscoelastic medium is complex and cannot be modeled by the association of a finite set of elastic and viscous elements as reported above, despite it is a very common approach in mechanical engineering [140, 141]. Actually, the viscoelastic complex modulus of the cell body exhibits a weak power-law behavior over a wide frequency range.

[1] Transient experiments usually involve following the cell response upon deformation, for example, creep or stress-relaxation experiments.

Cell cortex rheology.
Using magnetic twisting cytometry (MTC) coupled to an optical detection of the motion of a bead coupled to membrane RGD receptor, Fabry *et al.* [111, 142] succeeded in probing the cell surface dynamics in the frequency range from 0.01 Hz to 1 kHz. During the bead displacement on the cell surface (forced by a twisting magnetic field), the cell responds with an opposing torque that reflects the cell mechanical strength. The ratio of the complex torque $\tilde{T}$ to the complex bead displacement $\tilde{d}$ in Fourier space is defined as the elastic modulus $\tilde{G}(\omega)$:

$$G(\omega) = f_g \frac{T(\omega)}{d(\omega)} \ , \tag{2.14}$$

where the proportionality geometrical factor f_g depends on the shape, thickness of the cell and the degree of embedding of the bead in the cell cortex; $G(\omega) = G'(\omega) + iG''(\omega)$, where G' is the storage modulus and G'' the loss modulus. The range of stress and deformation used in this study was limited to the linear response regime for the cell. These authors found for five types of adherent cell models that both G' and G'' increase with excitation frequency as a weak power-law over the whole frequency range. These power-law dependences of G' and G'' on frequency was also observed by other groups [50, 113, 143–146] and with other methods, such as atomic force microscopy [112, 147]. Except for a small additive viscous term that emerges from this power-law regime at high frequencies, the mechanical responses collected from the cell surface did not appear to be tied to any specific frequency and in that respect was considered as (time) scale-invariant.

When a power-law behaviour emerges in the rheological response of a cell, a whole range of frequencies is required to bring the experimental demonstration of the existence of scale invariance. Actually, given this finite range of frequencies, the apparent power-law could still be parametrised by a combination of a large (but finite) number of viscoelastic elements, as a crossover between two distinct viscoelastic regimes. The most impressive result of the above studies is the fact that all the curves captured from different cells of various types could be collapsed to single master curves typical of soft glassy materials (SGM) [141, 148], demonstrating the universality of this behaviour [145, 149]. This universality law can be written as

$$G(\omega) = G'(\omega) + iG''(\omega) = G_0 \left(i \frac{\omega}{\omega_0} \right)^{x-1} + i\mu\omega \ , \tag{2.15}$$

where x is a unifying parameter, G_0 and ω_0 are cell type dependent scaling factors for stiffness and frequency, and μ is an additive Newtonian viscosity term that is negligible for frequencies lower than 30 Hz. This equation tells us that (below 30 Hz) the phase angle ϕ of $G(\omega)$,

$$\phi = \tan^{-1} \left(\frac{G''(\omega)}{G'(\omega)} \right) = \frac{\pi}{2}(x-1) \ , \tag{2.16}$$

is independent of the forcing frequency. This unifying parameter x depends on the cell state: x decreases to 1 when the cell approaches an ideal elastic material (for instance by increasing its contraction) whereas x increases towards 2 (limit of a Newtonian viscous fluid) when the cell prestress is diminished (*e.g.* by disrupting the actin CSK). The common and generic features of SGMs are due to the fact that they are composed of discrete, numerous elements

which are inter-connected in a random way via weak interactions. These materials are out-of-equilibrium metastable systems, very much like living cells.

Cytoplasm rheology.
Microparticles embedded inside living cells have been used as tracers of the internal cellular activity [150–152]. Two different regimes of transport have been observed: on the one hand passive fluctuations (local movements of the tracers) related to the local viscosity of the cytoplasm and on the other hand active trajectories which are driven by molecular motors such as kinesins and dyneins along microtubules. The same type of experiments was also performed more recently by nanoparticule tracing and manipulation inside A7 melanoma, MCF-10A and MCF-7 cells [153] with optical tweezers leading again to the conclusion that the elastic modulus follows a power-law: $| G(\omega) | \sim \omega^{\beta}$. These optical tweezer measurements confirmed the rubber-like elastic properties of the cytoplasm of these cells in two-dimensional adherent conditions.

2.2 Principles of Atomic Force Microscopy

2.2.1 Experimental setup and operation modes

The Atomic Force Microscope (AFM) introduced in 1986 by Binnig *et al.* [154] has become a powerful tool in biology, with applications going from topography of DNA [155] to the measurement of elasticity in thin tissues [156]. The principle of its operation is to measure forces as small as picoNewtons by monitoring the elastic deformation of a flexible cantilever beam. At the free end of the cantilever there is a tip that serves as a probe, interacting with the object of study (Fig.2.3A). The tip-sample contact forces produce the cantilever bending, and this deformation is captured with a position sensitive photodiode via a laser beam reflected on the top of the cantilever (Fig.2.3B). The distance between the cantilever and the sample surface or support, that is, the vertical position of the cantilever, is controlled using a piezoelectric motor, while the (optional) scanning in the x-y plane is usually performed with a motorised microscope stage.

Different operation modes exist depending on the feedback stablished between the cantilever deflection and the vertical position, or height. Among them we can find

- **Contact mode.** The cantilever is in constant contact with the surface of the sample. The feedback loop adjusts the height to maintain a constant cantilever deflection. The topography image is obtained from the feedback loop signal while scanning in the x-y plane. It is possible to obtain a measure of friction by monitoring the torsion signal of the cantilever.

- **Tapping mode.** The cantilever is in intermittent contact with the surface. The intermittency is obtained by exciting the cantilever at frequency close to its resonant frequency. This mode is particularly suited to image very soft samples, as the force applied is very small, keeping a low sample deformation. The feedback loop maintains the amplitude of oscillation constant.

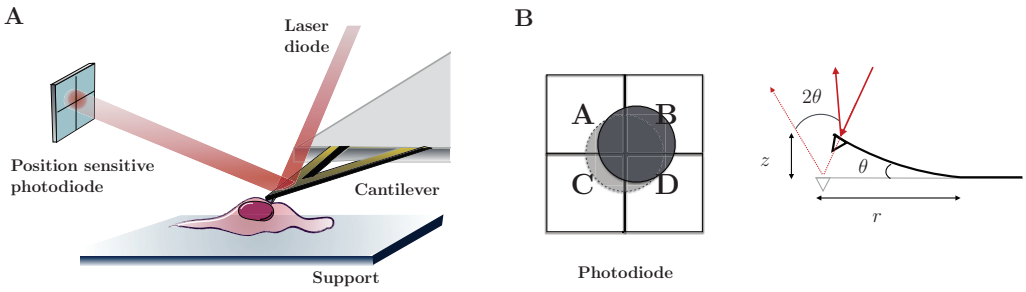

Figure 2.3 – **Atomic Force Microscopy.** (A) Diagram of the basic setup of an Atomic Force Microscope. A position sensitive photodiode registers the cantilever deflection via a laser diode that is reflected on the top of the cantilever. (B) Scheme of the measured deflection. The photodiode is segmented in four quadrants A, B, C, and D. The 'zero' position of the laser corresponds to the centre of the photodiode (light grey circle). The cantilever deflection z deviates the laser spot (dark grey circle) by an angle 2θ=$2z/r$. For a clamped-free beam, $r = 2L/3$, with L being the cantilever length.

- **Dynamic AFM.** This mode is similar to tapping mode, but without establishing contact with the surface. The cantilever is excited at its resonant frequency, and changes in the frequency, amplitude of oscillation and phase are monitored as the cantilever is kept close to the surface.
- **Multi-harmonic AFM.** This is a variant of dynamic AFM and/or tapping mode. The cantilever is excited at multiple resonant frequencies and the signal is recorded simultaneously. The higher-harmonics signals can reveal more details about the sample, particularly when imaging in liquid.

2.2.2 Estimation of the cantilever spring constant

The cantilever spring constant k_c can be calculated from the total cantilever deflection (Δz) due to thermal fluctuations [157]. If the cantilever is modelled as a harmonic oscillator in thermodynamic equilibrium, the mean-square displacement of the cantilever tip from its neutral position is described by [158]

$$\langle \Delta z^2 \rangle = \frac{k_B T}{k_c} \tag{2.17}$$

with k_B the Boltzmann constant, and T the temperature. Since several vibration modes are possible due to the geometry of the cantilever (Fig.2.4), to obtain the mean square deflection of one mode $\langle \Delta z_n^2 \rangle$(often the first), one should use a correction factor β_n,

$$\langle \Delta z_n^2 \rangle = \frac{k_B T}{k_c} \beta_n \tag{2.18}$$

Usually, the deflection is detected using the optical lever technique, which in reality, is a measure of the inclination instead of the deflection. Therefore, if we are interested in the forces acting at the end of the beam, another correction factor β_n^* should be introduced [159], and

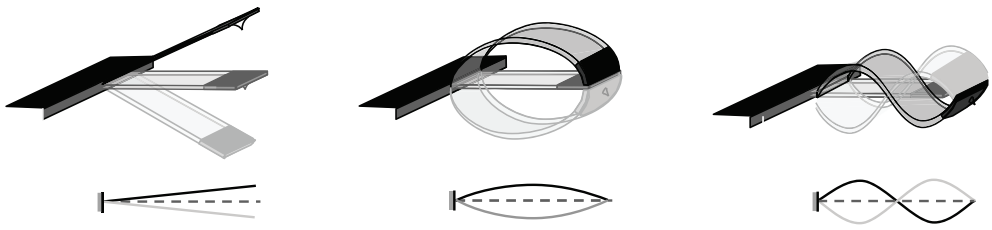

Figure 2.4 – **Scheme of the first three symmetric modes for a rectangular cantilever**

Mode n	ω_n/ω_1 (rect.)	β_n^* (rect.)	ω_n/ω_1 (V-shape)	β_n^* (V-shape)
1	1	0.8175	1	0.76
2	6.22	0.2511	5.23	0.297
3	17.55	0.0863	14.05	0.096
4	34.39	0.0441	27.16	0.06

Table 2.1 – **Theoretical values of the correction factor β_n for a free rectangular (rect.) and a V-shaped cantilever** [158, 159]. Only the symmetric modes are considered, with ω the resonant frequency.

k_c is finally given by

$$k_c = \frac{\beta_n^* k_B T}{\langle \Delta z_n^{*^2} \rangle} \tag{2.19}$$

where z_n^* is the effective deflection measured with the instrument.

In practice, we record the effective cantilever deflection when it is oscillating far from the surface, and we compute the power spectral density (PSD) of the temporal signal, obtaining the resonant modes of the thermally-excited cantilever (Fig.2.5a). Then, we fit the first resonant peak using a lorentzian function (Fig.2.5b), and we compute the area under the curve, which is equivalent to $\langle \Delta z_n^{*^2} \rangle$, and we estimate the cantilever spring constant k_c using eq.(2.19), with the correction factor β_n^* corresponding to the cantilever geometry.

2.3 Materials and Methods

2.3.1 TF1 cell line and culture conditions

The TF1 cell line (ATCC CRL-2003) was maintained at 1x10^5 cells/mL in RPMI-1640 medium, 10% FCS and granulocyte macrophage colony-stimulating factor (GM-CSF, 10ng/mL) (Sandoz Pharmaceuticals). Engineered TF1-GFP and TF1-BCR-ABL-GFP cell lines were obtained by transduction with an MSCV-based retroviral vector encoding either the enhanced green fluorescent protein cDNA alone (EGFP) as a control or the BCR/ABL-cDNA upstream from an IRES-eGFP sequence [160]. EGFP+ TF1 cells were sorted using a Becton Dickinson FACSAria. Before force curve recording, cells were seeded at the concentration 5x10^5 cells/mL and incubated for 24 hours. Adherent cells were prepared by letting non adherent cells adhere on glass cover slips coated with fibronectin (Sigma) in culture treated plates (BD Biosciences/Falcon)

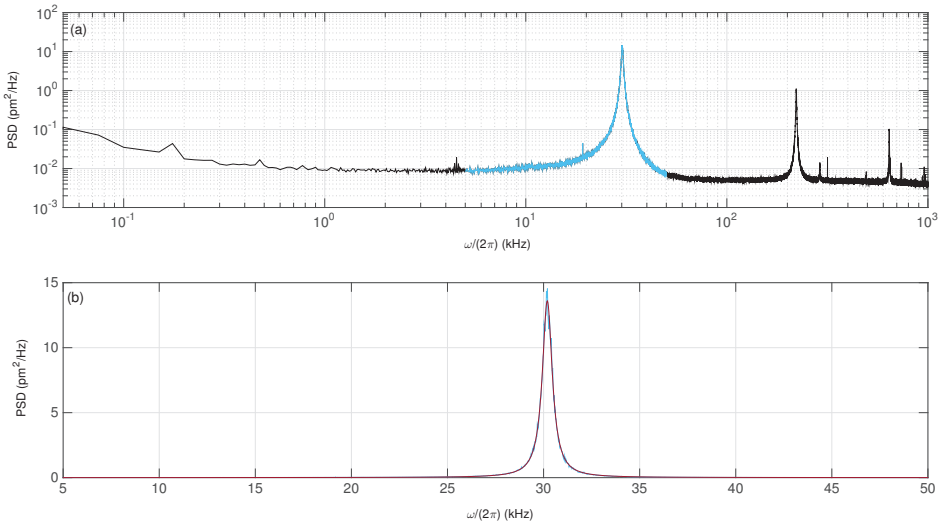

Figure 2.5 – **Power spectral density of the thermal-excited fluctuations of a rectangular cantilever in air.** (a) The first resonant peak (in blue) is selected from the whole PSD data (black curve). (b) The selected data (blue curve) is fitted using a lorentzian function (in red). Nominal $k_c = 0.12 N/m$.

for 1 hour at 37^{o}C, before removal of the non-adherent fraction. Finally, the glass coverslip was mounted on the AFM stage and the cells were kept in their culture medium at room temperature (24^{o}C). We thank Bastien Laperrousaz and Véronique Maguer-Satta from the Centre de Recherche en Cancerologie de Lyon for providing the cell samples.

2.3.2 Force indentation curves

2.3.2.a Data recording on the TF1 cell line

Force curves were recorded at z scan velocity 1 μm.s^{-1}. Prior to each experiment, the deflection sensitivity of the cantilever was estimated on fused silica and the cantilever spring constant was calibrated by the thermal noise method, the deflection set-point and feedback control gains were chosen for optimum signal to noise ratio. Indentation was carried out at the centre of each cell within 2 hours after removing cells from the incubator. In all the experiments, cell sizes were evaluated from their microscopic images.

The experiments on section 2.4 were performed with an AFM/STM 5500 (Agilent Technologies distributed by Scientec, Les Ulis, France) mounted on an inverted microscope (IX71 Olympus) and with pyramidal shape tip cantilevers (SNL-10, Bruker) having a nominal spring constant of 0.06 N.m^{-1}. The experiments on section 2.5 were performed with a CellHesion 200 AFM system (JPK Instruments). Transparent pyramidal tip cantilevers with rectangular section (qp-Cont from Nanosensors, Neufchatel, Switzerland) with a nominative spring constant 0.1 N.m^{-1} were used.

2.3.2.b Wavelet Transform Analysis of force-indentation Curves

Within the norm $\mathscr{L}^1$, the one-dimensional WT of a signal $F(x)$ reads:

$$W_\psi[F](b,s) = \frac{1}{s}\int_{-\infty}^{\infty} F(x)\psi^*(\frac{x-b}{s})dx\,, \tag{2.20}$$

where b is a position and s (>0) a scale parameter. A typical analyzing wavelet $\psi(x)$, that is admissible (of null integral) is the second derivative of a Gaussian $g^{(0)}(x) = e^{-x^2/2}$, also called the Mexican hat wavelet:

$$g^{(2)}(x) = -\frac{d^2}{dx^2}g^{(0)}(x) = e^{-x^2/2}(1-x^2)\,. \tag{2.21}$$

Via two integrations by part, we get that the WT of F with the second derivative of a Gaussian wavelet $W_{g^{(2)}}[F](b,s)$ at scale s is nothing but (up to a multiplicative coefficient s^2) the second derivative of $W_{g^{(0)}}[F](b,s)$, *i. e.* a smoothed version of F by a Gaussian function at scale s:

$$W_{g^{(2)}}[F](b,s) = s^2\frac{d^2}{db^2}W_{g^{(0)}}[F](b,s)\,. \tag{2.22}$$

Note that we can derive a similar relation with the first derivative of F. Given that $g^{(1)}(x) = \frac{d}{dx}g^{(0)}(x) = -xe^{-x^2/2}$ [30, 161, 162]:

$$W_{g^{(1)}}[F](b,s) = s\frac{d}{db}W_{g^{(0)}}[F](b,s)\,. \tag{2.23}$$

Let us point out that the validity of the WT definition (Eq. (2.33)) was further proved on distributions including Dirac distributions and derivatives [162, 163].

The advantage of the WT method is to use the same smoothing function to filter out the experimental background noise and to compute first-order and second-order derivatives with the same smoothing characteristic scale. In this study, we used modified versions of the definition (Eq. (2.33)) of the WT:

$$T_{g^{(0)}}[F](b,s) = W_{g^{(0)}}[F](b,s)\,, \tag{2.24}$$
$$T_{g^{(1)}}[F](b,s) = \tfrac{1}{s}W_{g^{(1)}}[F](b,s)\,, \tag{2.25}$$
$$T_{g^{(2)}}[F](b,s) = \tfrac{1}{s^2}W_{g^{(2)}}[F](b,s)\,, \tag{2.26}$$

These formulae give directly a measure of F in nN, dF/dZ in nN/nm and d^2F/dz^2 in Pascal$\cdot 10^{-9}$ smoothed by a Gaussian window of width s. For more details on the wavelet-based analysis of AFM force-indentation curves, please refer to the paper of Digiuni *et. al* [164] included in Appendix A.

2.3.3 Thermally excited AFM

2.3.3.a Signal recording of cantilever fluctuations

A JPK CellHesion 200 system was used. The deflection sensitivity was estimated by performing force curves on the surface of an empty petri dish. The temporal signals were obtained by recording the deflection and the torsion signals using a high-speed module of acquisition, at a frequency of 2.5 MHz in segments of 2 s, repeating once for the recordings on the cells, and five times for a total length of 10 s on the other cases. In the low frequency acquisition, we

recorded at 100 kHz during approx. 300 seconds. For measurements in liquid, 2 ml of liquid (distilled water or culture medium) are added in small sized petri dishes. Once the cantilever reaches the loading force contact with the sample, its fluctuations are recorded after a time delay of 5 *s* to avoid instabilities related to the cantilever movement of approach to the sample surface. The experiments on living cells where performed at a constant load of F= 2 nN. After the fluctuations signals were recorded, a series of 20 force-indentation curves were performed on the cell to estimate the shear modulus. The tip velocity was set to 1μm/s, and the setpoint to 2nN.

2.3.3.b Data analysis

Spectral densities

The power spectral density (PSD) for the free oscillations of the cantilever was computed using the Fast Fourier Transform (FFT) and averaging over 16 segments of a signal fraction corresponding to 2^{20} points, without overlapping (or sliding window). The PSD for the fluctuation signals of the cantilever in contact with the cells was computed for the total length of the signal (2^{22} points) later filtering the PSD curve in loglog scale over frequency windows $\Delta \log_{10} \omega = 0.03$. Recently we have computed wavelet spectra of the fluctuation signals using Cauchy wavelet transforms. This work has been written for a publication this summer, and a preprint has been added at the end of this manuscript (Appendix B) for those interested in the rigorous equations for wavelet spectral decompositions.

Wavelet Transform of the fluctuation signals

The one-dimensional WT of the deflection signal $z^*(t)$ was computed using Eq.(2.33) given in the section 2.4.2. The time-scale map for the detection of the change in dynamics of cantilever was computed using the first derivative of a gaussian as a mother wavelet, for a range of scales between [0.2 s: 1 s:10 s]. The filtering of the deflection signal was performed using a gaussian window of 2 s width.

2.4 Quasi-static measurement of cell stiffness with atomic force microscopy

As emerging in the late 1990s from scanning tunneling microscopy (STM) technologies, atomic force microscopy (AFM) was early recognized as providing a unique opportunity to investigate the structure, morphology, micromechanical properties and biochemical signaling activity of cells under physiological environment, and this with high temporal and spatial resolutions [154, 165]. The principle of AFM is to bring directly in soft (or hard) contact a sharp tip cantilever probe over a cell surface and to capture with piconewton sensitivity the interaction force of the tip with the cell surface. AFM is a very powerful technique that has been used to detect single biomolecules (receptors, lipids) on single cell surface without the need for fixation or staining. AFM has such a sensitivity that it can be used to measure interaction between and within single biomolecules [166–168]. Beyond its preliminary application for imaging the topography of biological objects [169–171], AFM has become a multitask scanning probe versatile tool (antigen recognition, molecular and membrane flexibility, single molecule, gel, cell and tissue elasticity, electric current, conductance, near field electromagnetic field) [172, 173].

AFM force spectroscopy can be applied to probe the elastic properties of a cell, either adherent or confined in a narrow chamber [174–177]. Its unique ability to detect and to map the cellular elasticity of living cells with a few tens of nanometres resolution definitely outmatches the performance of other techniques such as magnetic or optical tweezers. However it has as a main limitation that it cannot probe cell internal structure without crossing before the cell cortex. This difficulty has been partly overcome recently thanks to a singular space-scale analysis of force-distance curves to disentangle the viscoelastic moduli of the cell cortex and of the underlying CSK [164]. Interestingly, two-dimensional mapping of mean elastic modulus on a large variety of cells [174, 175, 178–181] were reconstructed, revealing for the first time intracellular interplay of mechanical forces in living cells.

2.4.1 Large distance cell indentations with atomic force microscopy on living cells

Unlike AFM based microrheology measurements [112, 147] discussed in chapter 1, which were limited to very small deformations (nanometer in scale), we consider now much larger deformations (more than 1/10 of the cell size) and their temporal and/or frequency decomposition [182]. A majority of previous studies of force-indentation responses of living cells (performed at constant tip velocity) assumed that the cells behave as stationary visco-elastic systems [174, 181], mainly because they operated in the limit of very small deformations ($\delta L/L < 0.01$, where L is the characteristic size of the cell). This assumption allowed the use of either the Hertz model [183] (for a spherical indenter), the Sneddon model [184] (for a pyramidal indenter) or a combination of these two models for blunted pyramidal tips [185].

The Sneddon's variation of the Hertz model describes the evolution of the force F with the indentation $\delta_z = z - z_c$, for the case of a pyramidal (or conical) and non-adhesive cantilever tip [184]:

$$F(\delta_z) = \frac{2\tan\theta E}{\pi(1-\nu^2)}\delta_z^2 = \frac{4\tan\theta G}{\pi(1-\nu)}\delta_z^2 \tag{2.27}$$

where θ is the half angle of the indenter, $E = 2G(1+\nu)$. This Hertz-Sneddon model assumes that the tested material is at equilibrium and does not change with the deformation, it gives therefore an estimation of the static Young's modulus E, or equivalently the shear modulus G. When the sample visco-elasticity is not stationary (typical of an active material), differential operators must be used in Eq.(2.27). Starting with the cantilever at rest position, $z(t) = 0$, for $t < 0$, and moving at constant rate, $z(t) = v_0 t$ for $t \geq 0$, the force-indentation relationship becomes [186]:

$$F(t) = \frac{8v_0^2\tan\theta}{\pi(1-\nu)}\int_0^t G(t')(t-t')dt' \tag{2.28}$$

$G(t)$ is the time-dependent shear modulus of the material. Taking the second derivative of $F(t)$ with respect to t, we obtain

$$\frac{\mathrm{d}^2F(t)}{\mathrm{d}t^2} = \frac{8v_0^2\tan\theta}{\pi(1-\nu)}G(t) \tag{2.29}$$

Therefore, from a fixed velocity deformation experiment we can retrieve the shear modulus

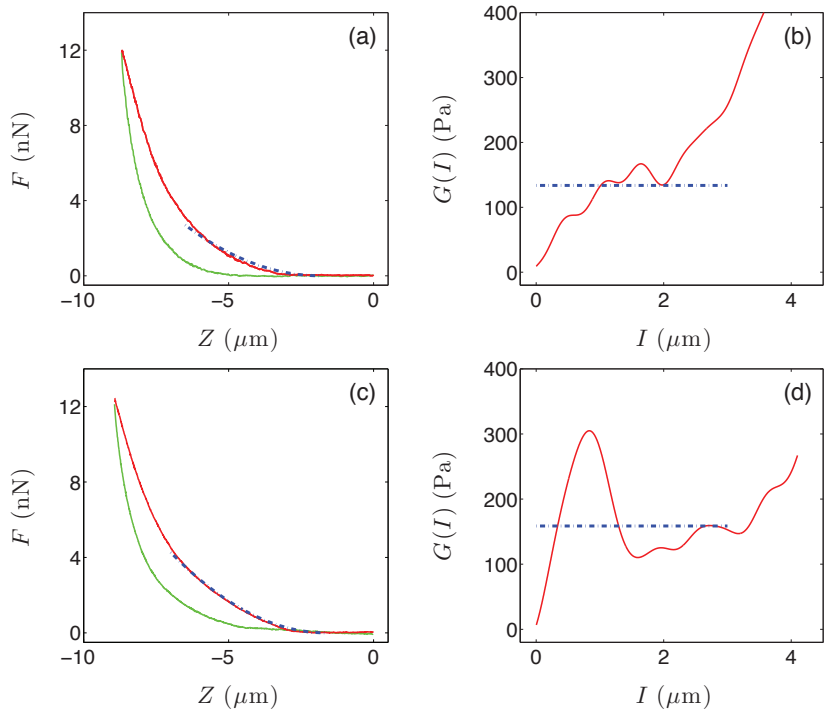

Figure 2.6 – **Shear modulus extraction from AFM force curves on immature hematopoietic TF1 cells.** (a) Approach (red) and retract (green) curves on a suspended cell. The blue dashed line corresponds to a parametrisation of F(Z) with a parabolic function (Eq. (2.27)). (b) G(I=δ_z) curve computed from the second derivative of the force curve (Eq. (2.29)), obtained with a fixed size (width 400 nm) second-order analysing wavelet (Eq. (3)). (c) and (d) are the same curves obtained for an adherent cell. (adapted from Laperrousaz *et al.* [160])

$G(t)$ by knowing the second order derivative of the applied force [2].

Figure 2.6 compares the temporal response of two immature hematopoietic TF1 cells. Fig.2.6(a) and (c) shows the approach (red) and retract (green) force curves recorded from respectively, a suspended and an adherent cell. The left-most curves are not treated or filtered, however reaching low noise force-indentation curves without additional filtering (to keep the sensitivity of this apparatus in force (a few pN)) requires a correct cantilever calibration (with the thermal noise method [187]) and a fine tuning of the laser beam reflected on the cantilever tip and collected on the photodiode detecting its flexural movements. In Fig.2.6(a,c) we use the Sneddon model (eq.2.27) to parametrise the approach force curve with a parabolic function with constant G (blue dashed line) within 3 μm indentation range. In Fig.2.6(b,d) we estimate the local curvature of the force curve (eq.2.29) using a second derivative of a Gaussian (width 400 nm) as analysing wavelet. For the suspended TF1 cell (Fig.2.6a,b) the transition to contact is smooth and the variation of $G(\delta_z)$ is very progressive, reaching a plateau around 120 Pa that lasts about 2 μm, before an ultimate sharp increase. For the adherent TF1 cell, the slope of the approach curve presents a discontinuity (from nearly zero to a finite value) when

[2] Changing the variable t for z, and using eq.(2.3), we obtain the more traditional form $\frac{d^2F}{dz^2} = \frac{4\tan\theta}{\pi(1-\nu^2)}E(z)$.

the cantilever tip comes in contact with the cell (Fig.2.6c). This discontinuity of the derivative of F appears as a hump in G of size given by the width of the analysing wavelet (Fig.2.6d). At larger indentation I, the $G(I)$ curve reaches a plateau around 160 Pa that lasts over 2 μm before increasing again. The last part of the $G(I)$ curves corresponds to the interaction of the cantilever tip with the nucleus, that appears to be stiffer than the surrounding cytoskeleton. Even though the values of $G(I)$ are not very different on the plateaus before the nucleus deformation, the way the suspended and adherent cells respond to the mechanical stress is very different. The former responds as a volume body with a viscoelasticity that increases progressively with the deformation (Fig.2.6b), analogous to the linear viscoelastic solid model (Fig.2.2A). The later responds as a stiffer cortex impeding the penetration of the cantilever tip (Fig.2.6d), similar to the response of the Maxwell liquid drop model (Fig.2.2B). These robust observations of change in local curvature of the force curves (*i.e.* in the local shear modulus G) put into light the need of revisiting the analysis of the cell mechanical response.

2.4.2 Tracking the scaling-laws of AFM force-indentation curves

To investigate the larger indentation depth regime ($0.01 < \delta L/L < 0.1$), we cannot make an assumption on the invariance of the shear modulus of the material during the indentation. For exemple, if $G(z) \sim \delta_z^{\zeta}$, we would expect a force curve with fractional power law behaviour for $F(z)$:

$$F(\delta_z) \sim z^{2+\zeta} \,. \tag{2.30}$$

Actually, as described in section 2.1.3 the cell is made of several structures (the extra-cellular membrane, the actin cortex, the cytoskeleton, the endoplasmic reticulum, the Golgi apparatus, the mitochondrial network, the nuclear membrane and cortex, the nucleus territories, the DNA and chromatin), separated or/not separated with a lipidic membrane, and each of this internal structure may have its own mechanical response. We treated the force curves with an empirical power-law equation, with an unknown exponent h:

$$F(\delta_z) = A_0 \left[\frac{\delta_z}{\delta_{z_0}} \right]^h \,, \tag{2.31}$$

in a given range of indentation $\delta_z = z - z_c$, with z_c the position where the cantilever comes in contact with the cell (that we estimated at the z-value where both the slope and the curvature of the force curve emerge from the background noise[3]). The pre-factor A_0 has the dimension of a force; it corresponds to the amount of force required to deform the cell by $\delta_{z_0} \simeq 150$ nm, that we have fixed to this value for reasons. The first reason is that the tip of the cantilever is usually rounded or friction-weared on several tens of nanometers which impacts the force curve on distances of about 100 nm, the second reason is that this value corresponds to the characteristic thickness of the actin cortex ($\sim 100 - 200$ nm). We do not therefore expect to have a very fine an local (3D) characterization of the cell cortex, but a rather global response. In particular, if it stiffness is larger than underlying cytoskeleton, this will appear in the force curve as a bump in the curvature of $F(\delta_z)$, typical of a cortical shell [188].

[3]For more details on the method to detect the contact point, please refer to the article of Digiuni *et. al* in Appendix A.

The exponent h in eq.(2.31) is now considered as a variable quantity. Consistent with the dynamical recording of AFM force-indentation curves, we are preferred to analyze the slope of these curves because not only it could help us get rid of linear trends and also the force curve derivatives were straightforwardly corrected for the stiffness of the cantilever. We assume that the first derivative of F takes the following general power-law form:

$$F^{(1)}(\delta_z) = \frac{\partial F(\delta_z)}{\partial \delta_z} = T \left[\frac{\delta_z}{\delta_{z_0}} \right]^{\alpha} , \tag{2.32}$$

$\alpha = h-1$ (eq.(2.32)), and $T = A_0 h/\delta_{z_0}$ is a pre-factor that has the unit of a tension (nN/μm) and which is proportional to the Young's modulus. Here we do not assume any *a priori* scaling-law exponent for cell strain-to-stress response [139] and we consider the exponent α as characterising how the cell reacts and adapts itself to the external stress via its cortex and cytoskeleton mechanical properties. If the cell responds as a linear elastic material (like a soft ball), we get $\alpha = 1$, according to the Sneddon's model (Eq.2.27) [184]. If instead the cell responds as an elastic shell like cortex [188], we expect that $\alpha = 0$ and in that case, A_0/δ_{z_0} is proportional to the shell cortex stretching modulus $K_S = W_C E/(1-\nu^2)$, where W_C is the shell thickness, E is the Yound modulus of the cortex (3D). Note that if we fix $\delta_{z_0} \sim W_C$, we get $A_0 \sim E W_C^2$.

From a practical point of view, a reliable estimate of the power-law exponent α and pre-factor T (eq. (2.32)) from experimental force-indentation curves requires an accurate determination of the contact point z_c. This detection was performed by computing both the first and the second derivative of the force curve and by defining thresholds on the force, its first order and its second order derivatives comparatively to their standard deviations far from the contact point. The elaboration of this original method required first a full wavelet-based decomposition of the force curves (see section 2.3.2.b and Appendix A for details).

Within the norm $\mathscr{L}^1$, the one-dimensional WT of a signal $F(x)$ reads:

$$W_\psi[F](b,s) = \frac{1}{s}\int_{-\infty}^{\infty} F(x)\psi^*\left(\frac{x-b}{s}\right)dx\,, \tag{2.33}$$

where b is a position and s (>0) a scale parameter. A typical analyzing wavelet $\psi(x)$, that is admissible (of null integral) is the second derivative of a Gaussian $g^{(0)}(x) = e^{-x^2/2}$, also called the Mexican hat wavelet:

$$g^{(2)}(x) = -\frac{d^2}{dx^2} g^{(0)}(x) = e^{-x^2/2}(1-x^2)\,. \tag{2.34}$$

For a given width of the analysing wavelet, we compute the smoothed functions F and $F^{(1)}$ and we estimate the contact position Z_c for a given threshold of F and F^1. To fix these thresholds, we look for a compromise in between a too strong smoothing of the derivative that would wipe out the non contact - contact transition and a too mild smoothing that would still suffer from a noisy estimation of the contact point. Once defined a range of indentation I values where the power-law scaling is expected to apply (Eq. (2.32)), the α exponent is estimated from a linear regression fit of $F^{(1)}(I)$ in a logarithmic representation [189].

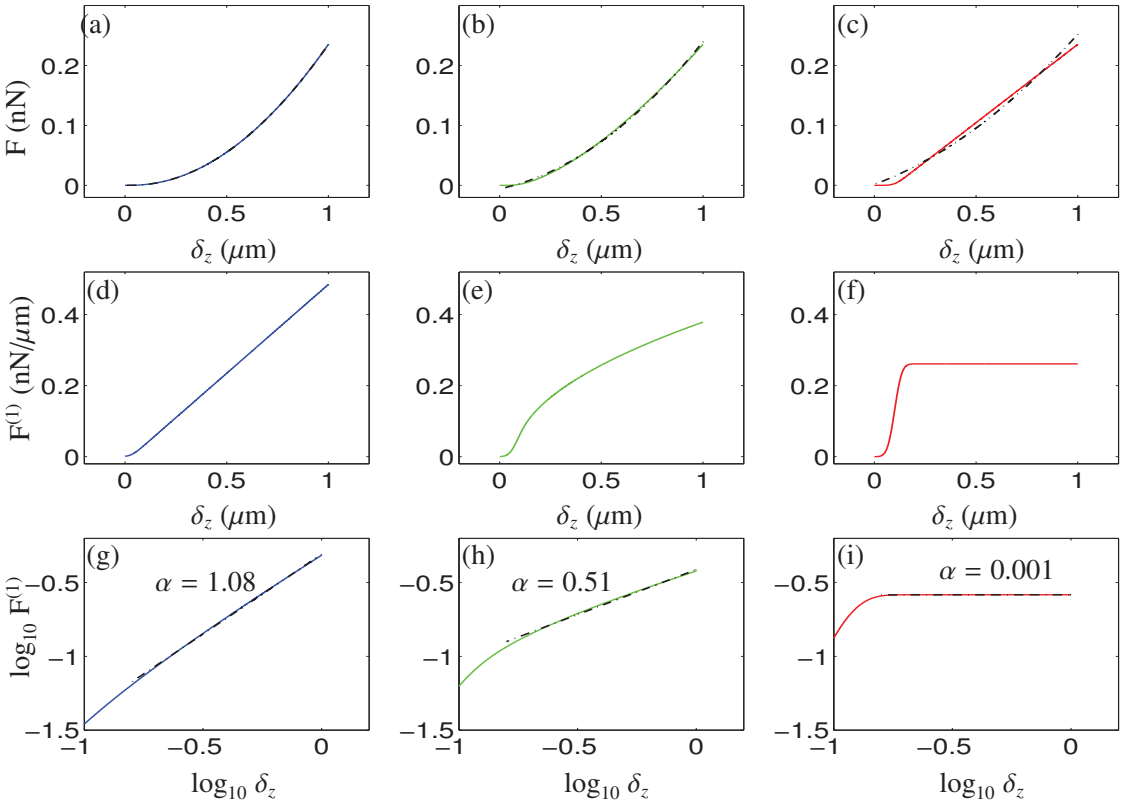

Figure 2.7 – **Illustration of the computation of the scaling exponent α from three model force-indentation curves corresponding to three different α exponents.** (a-c) Force indentation curves $F(\delta_z)$. (d-f) Derivatives of the force curves $F^{(1)}(\delta_z)$. (g-i) $\log_{10} F^{(1)}(\delta_z)$ vs $\log_{10}(\delta_z)$. The blue curves correspond to $\alpha = 1$, the green curves correspond to $\alpha = 0.5$, the red curves correspond to $\alpha = 0$. On panels (a-c) we have performed a quadratic fit of the force curves assuming that the Sneddon's model (Eq. (2.35)) [184] is correct. On panels (g-i) we have performed a linear regression of $F^{(1)}(\delta_z)$ in a logarithmic representation. The slopes of these dotted-dashed lines give the reported estimates of the scaling exponent α.

The performance of our method is illustrated in Fig.2.7, comparatively to standard fitting methods like the Sneddon's quadratic force model [184]. We report three model force curves corresponding to three different values of the α exponents (Eq.2.32), namely $\alpha = 1$ (Fig.2.7a), $\alpha = 0.5$ (Fig.2.7b) and $\alpha = 0$ (Fig.2.7c), such that the force curves at the end of a deformation of 1 μm reach the same value (2.35 nN). We have also smoothed the force curves with a smoothing window of 100 nm to reproduce the experimental situation, this smoothing may change slightly the exponent close to the contact point. As commonly done in the literature, let us first parametrise the three force curves with a Sneddon quadratic function (plotted with dotted-dashed lines in Fig. 2.7a-c):

$$F(\delta_z) = \gamma E \delta_z^h \text{ with } \gamma = \frac{2\tan\theta}{\pi(1-\nu^2)} \sim 0.31 \ , \tag{2.35}$$

where θ is the half tip angle ($\sim 20^o$) and $h = 2$.

The parametrisation of the three curves gives respectively $E = 800 \pm 10$ Pa for $\alpha = 1$, $E = 560 \pm 20$ Pa for $\alpha = 0.5$, $E = 400 \pm 40$ Pa for $\alpha = 0$. We note that the fitting of the force curve for $\alpha = 1$ is very good, but that it gets worse when α decreases. With this curve parametrisation, we should be tempted to conclude that the green force curve ($\alpha = 0.5$) in Fig. 2.7b gives a softer response than the blue curve ($\alpha = 1$) in Fig. 2.7a, since E is reduced by a factor of 0.7, and the red force curve($\alpha = 0$) in Fig. 2.7c gives an even softer response, since E is now reduced by a factor 0.5. Within a Sneddon model parametrisation of these theoretical force curves, we would have concluded that the smaller $\alpha = 0$ force curve (in red) would correspond to the softer situation. This conclusion is indeed completely misleading since by a simple visual inspection of the force curves in Fig. 2.7d-f, we realise that the red force curve increases much faster at low indentations than the blue force curve, meaning that it costs more strength to deform the cell. When investigating the derivative $F^{(1)}(\delta_z)$ of the force curves, we realise that the three situations correspond to three different power law behaviours. From a linear regression fit of $F^{(1)}(\delta_z)$ in a logarithmic representation (Fig. 2.7g-i) over the range of scales [150 nm; 1000 nm], as in the experiments, we get the following estimates for α: 1.08 ± 0.02 ($\alpha = 1$), 0.51 ± 0.02 ($\alpha = 0.5$) and 0.001 ± 0.01 ($\alpha = 0$). The pre-factors T estimated at $\delta_{z_0} = 150$ nm are respectively: $T = 0.07$ nN/μm ($\alpha = 1$) leading to $E \sim T * (1-0.5^2)/I_0 \sim 330$ Pa, $T = 0.13$ nN/μm ($\alpha = 0.5$) giving $E \sim 630$ Pa and $T = 0.26$ nN/μm ($\alpha = 0$) giving $E \sim 1300$ Pa. Comparing these pre-factors leads to the conclusion that the $\alpha = 0$ force curve model indeed corresponds to a stiffer system (amplification by a factor of 3.85) than the $\alpha = 1$ force curve model, in better agreement with the faster increase of the force curve when $\alpha = 0$.

These estimations are summarised in the following table:

α	1	0.5	0
$h = \alpha + 1$	2	1.5	1
E (Pa) (Sneddon)	800	560	400
E (Pa) (T pre-factor)	330	630	1300

These numerical examples show that one has to be careful when using blindly standard parametrising methods to fit AFM force-indentation curves. As illustrated in Fig. 2.7, the conclusions from the parametrisation by Sneddon's model (Eq. (2.35)) may be completely misleading.

2.4.2.a Actin cortex stiffening as signature of leukaemic cells

In a recent study [189, 190] we have used a unique model of human immature Chronic Myelogeneous Leukaemia (CML) cells (TF1 cell line, transduced with the BCR-ABL oncogene) that reproduces early steps of stem cell transformation [160] to question the possible modifications of mechanical properties of immature hematopoietic cells upon oncogene expression. Interestingly, in transformed cells, BCR-ABL was shown to bind actin filaments (F-actin) [191], a major determinant of the cell mechanical behaviour [192], and to induce its redistribution into punctate, juxtanuclear aggregates [193]. In addition, the binding to F-actin seems to be involved in transforming ability of BCR-ABL.

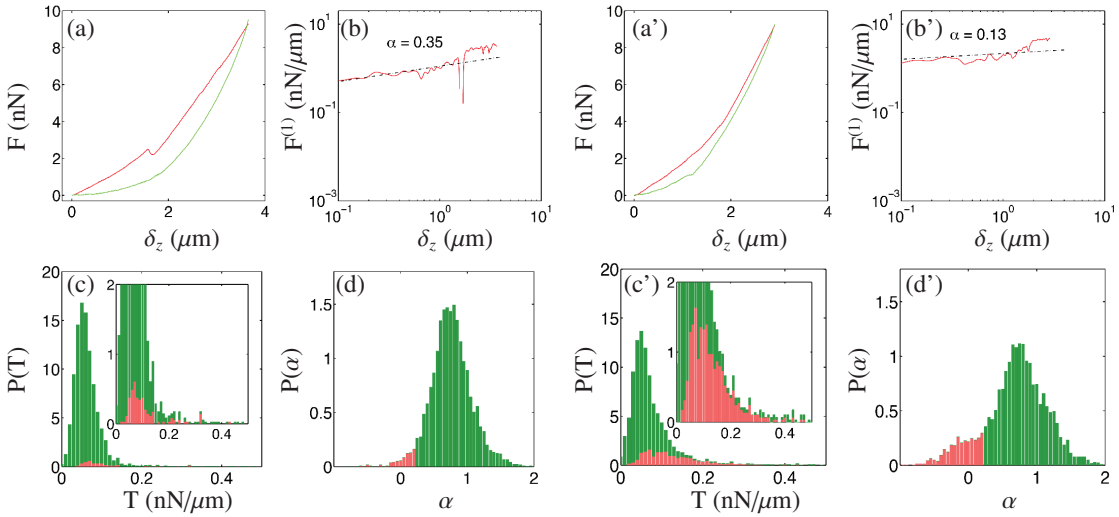

Figure 2.8 – **Force indentation curve analysis of control and cancer TF1 cell lines, in adherent conditions**. (a) Force indentation curves $F(\delta_z)$ on a TF1-GFP adherent cell: approach curve (red), retract curve (green). (b) Logarithmic representation of the first derivative $F^{(1)}$ of the force curve. The black dashed line corresponds to a linear regression fit estimate of the exponent α. (c) Histogram of T values computed from 240 TF1-GFP adherent cells (4367 force curves). (d) Corresponding histogram of α-values; red: $\alpha < 0.25$.(a'-d') same as (a-d) for TF1-BCR-ABL adherent cells. The T and α histograms where computed from 240 TF1-BCR-ABL adherent cells (4058 force curves). (adapted from Laperrousaz *et al.* [160])

Unlike adherent cells, non adherent hematopoietic cells raise a challenge for AFM studies because they tend to slip from the cantilever tip when performing the nano-indentation. We have let the cells to adhere on a fibronectin-coated coverslip before AFM probing [194, 195] . Interaction of the integrins at the membrane of cells with fibronectin-coated surface not only confines cell movements on the glass surface but likely changes its cytoskeleton architecture, inducing a cascade of molecular events leading to cell spreading phenomenon. In Fig. 2.8 are reported the results of a comparative analysis on adherent transduced TF1 cells, respectively the TF1-GFP cell line transduced with a MSCV-based retroviral vector encoding the enhanced green fluorescent protein cDNA alone used as a control, and the TF1-BCR-ABL cell line transduced by the same vector containing BCR-ABL cDNA upstream from an IRES-eGFP sequence [160].

We observe on the sampled force curves in Fig.2.8a, a' that $F(\delta_z)$ is much flatter in the first micrometer indentation range, which is confirmed by the computation of the scaling exponent $\alpha = 0.35$ for the TF1-GFP cell (Fig. 2.8b) and $\alpha = 0.13$ for the TF1-BCR-ABL cell (Fig. 2.8b'). These two cells have a cortex that is definitely stiffer than their internal cytoskeleton. We have colour-coded in red the force curves with $\alpha < 0.25$ as an indication that the cortical actin shell behaves much stiffer than the underlying cytoskeleton. Note that we do not get the exponent $\alpha = 1$ predicted by the Sneddon's model [184]. The fact that $0 < \alpha < 1$ means that if we compare the forces required at large and small indentations, their ratio is smaller than expected from the Sneddon's model. Another interesting observation is the difference between the retract and approach curves which is much smaller for the TF1-BCR-ABL cell, suggesting

that the deformation of this cell involves less dissipative loss. The comparison of the histograms of T and α values obtained from the analysis of 240 adherent cells of both kinds is even more instructive, since it reveals that whereas the percentage of TF1-GFP cells with a cortical shell signature ($\alpha < 0.25$) is less than 3.5% of total cell responses, it reaches 14.6 % with the TF1-BCR-ABL cells, which represents a 4-fold increase of these responses for the cancer cells. This difference is not so much marked on the T histograms. However, if we select the force curves with $\alpha < 0.25$ (red), we observe a drastic change in the T histograms, with a significant increase of the median T value from 0.087 ± 0.006 nN/μm to 0.120 ± 0.004 nN/μm respectively. When approximating T by $E\delta_{z_0}/(1-\nu^2)$, where ν is the Poisson ratio (which is incorrect since the exponent α is not strictly equal to zero), we get a median Young's modulus at 150 nm indentation depth which confirms some increase from $E = 435$ Pa for the control cells to $E = 600$ Pa for the cancer cells. We did this approximation to show that we recover the same order of magnitude for these HSCs as previously reported in the literature [177]. We must insist on the fact that the pre-factor T (as the Young modulus) only informs on the strength of the cell, but does not precisely quantify its strain-to-stress dynamical response as given by the power-law exponent α. The footprint of the cellular modifications produced by the transduction of these cells by the BCR-ABL oncogene is thus clearly revealed by their strain-to-stress response (decrease of α and increase of T) when they are confined to adherence. These transformed cells have a stiffer shell cortex that protects them from deformation. In consequence, these cells are also less motile because they loose their contractility and spreading ability.

When investigating mechanical responses of immature normal and cancer cells in adherent and non-adherent conditions, we observe that when BCR-ABL interacts with actin cytoskeleton, the AFM force-indentation scaling-laws are impacted [190]. Tracking the scaling-law exponent α of these force curves with a wavelet-based computation of their local slopes, we reconstruct histograms of α values that reveal for the first time that BCR-ABL expression in immature cells modifies their mechanical responsiveness to stress through a decrease of α towards zero. This is an indication that the first stages of TF1 transformation upon BCR-ABL could likely involve a stiffening of the outer cortex of these immature cells relative to their cytoskeleton.

2.5 Temporal survey of the cell mechanical fluctuations

We want to address here the question of contact of soft materials at the nanoscale, and more precisely the contact of materials with ill-defined surfaces, or fluctuating surfaces. Indeed, at the submicron-scale thermal fluctuations are no longer negligible and they may even drive the mechanical response of a mechanical system. This situation is very common in biology and sub micrometer soft matter structures since these systems are very sensible to external fluctuations.

The impact of thermal fluctuations is decisive in intracellular dynamics as well as cell-to-cell interaction mechanisms, from nuclear transcription, replication, repair and recombination machineries to acto-myosin molecular motors, mitochondrial fission-fusion processes, transmembrane transport and sensing complexes, a very large set of macromolecular com-

plexes are working stochastically while maintaining a global shape and biological function of the cell. In particular if thermal fluctuations are diminished, the conformational change of molecular motors by ATP to ADP that drives cell motility become inefficient and most cellular mechanotransduction functions are cancelled.

In some situations the cooperative interplay of molecular machines can lead to the rising of periodic or quasiperiodic dynamics from the background noise [196–198]. In other situations, the local cell dynamics remains apparently stochastic and scale invariant be highlighted by magnetic twisting cytometry [50, 142, 144, 146] or atomic force microscopy [112, 147].

2.5.1 Cantilever dynamics and thermal noise

Let us consider the AFM cantilever as a damped spring-mass system with N degrees of freedom (fig. 2.9), where N is given by the number of symmetric modes of vibration that can be measured. The equation of motion in its matricial form is:

$$\mathbf{M}\ddot{\mathbf{x}}(t) + \mathbf{C}\dot{\mathbf{x}}(t) + \mathbf{K}\mathbf{x}(t) = \mathbf{p}(t) \tag{2.36}$$

where $\mathbf{M}$, $\mathbf{K}$, and $\mathbf{C}$, are respectively the mass matrix, stiffness matrix, and damping matrix. All of them are square matrices of NxN, and $\mathbf{M}$ is a diagonal matrix. The position vector is given by $\mathbf{x}(t) = x_1(t), ..., x_N(t)$, and $\mathbf{p}(t) = p_1(t), ..., p_N(t)$ is the external force or excitation.

Assuming the vibration is simply harmonic, the resonance frequencies ω_n for mode n are obtained from the eigenvalue problem:

$$||\mathbf{K} - \omega^2\mathbf{M}|| = \mathbf{0} \tag{2.37}$$

This equation is called the *frequency equation* of the system. Expanding the determinant will give an algebraic equation of the Nth degree on the frequency parameter ω^2 for a system having N degrees of freedom. The N roots of this equation $(\omega_1^2, \omega_2^2, ..., \omega_N^2)$ represent the frequencies of the N modes of vibration which are possible in the system. It can be shown that for real, symmetric, positive mass and stiffness matrices, that is, for a stable structure system, all roots of the frequency equation will be real and positive.

According to the orthogonality properties, which can be demonstrated by applying Betti's law, there is a coordinate system Y_n (normal-coordinates) where the system can be written as N *uncoupled* equations. Then, using the eigenvectors $\Phi_\mathbf{n}$, we can define the generalised mass $M_n = \Phi_\mathbf{n}^\mathbf{T}\mathbf{M}\Phi_\mathbf{n}$, the general stiffness $K_n = \Phi_\mathbf{n}^\mathbf{T}\mathbf{K}\Phi_\mathbf{n}$, and assuming that the orthogonality conditions also apply to the damping matrix, the generalised damping $C_n = \Phi_\mathbf{n}^\mathbf{T}\mathbf{C}\Phi_\mathbf{n}$. In a similar way we define the excitation for each mode n as $p_n(t) = \Phi_\mathbf{n}^\mathbf{T}\mathbf{p}(t)$.

The total response of the system now can be obtained by solving the N uncoupled modal equations:

$$\ddot{Y}_n(t) + 2\xi_n\omega_n\dot{Y}_n(t) + \omega_n^2 Y_n(t) = \frac{p_n(t)}{M_n} \tag{2.38}$$

where $\xi_n = \frac{C_n}{2\omega_n M_n}$.

Assuming that Y_n is of the form $Y_n = y_n e^{i\omega t}$, Eq.(2.38) becomes:

$$Y_n(-\omega^2 - 2i\omega\xi_n\omega_n + \omega_n^2) = \frac{p_n(t)}{M_n} \tag{2.39}$$

Solving Eq.(2.38), the amplitude response function of mode n is given by:

$$y_n^2 = \frac{A_n^2}{(\omega_n^2 - \omega^2)^2 + \omega^2 {\Delta\omega_n}^2} \tag{2.40}$$

with $A_n := |p_n|/M_n$, and $\Delta\omega_n$ is the difference between ω_n and the frequency at $y_n^2 = (y_n^2)_{max}/\sqrt{2}$. Additionally, a practical parameter to characterise the nth mode is the quality factor Q, defined as $Q = \omega_n/\Delta\omega_n$.

Note that experimentally we measure the frequency of resonance of the **damped** system, ω_{Dn}, and is given by $\omega_{Dn} = \omega_n\sqrt{1-2\xi_n^2}$.

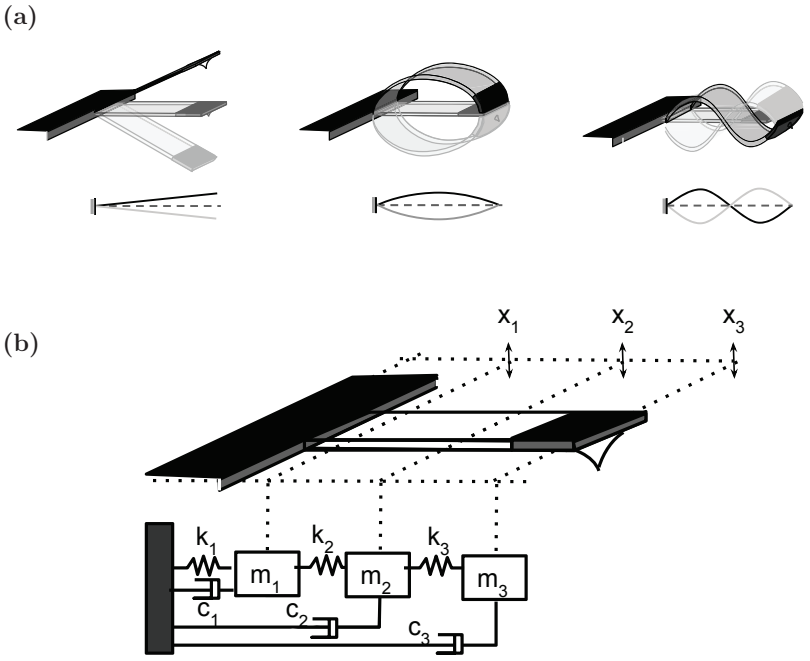

Figure 2.9 – **AFM cantilever as a damped spring-mass system.** (a) Scheme of the first three symmetric modes for a rectangular cantilever. (b) Scheme for a damped spring-mass system with 3 degrees of freedom, where the mass is coupled in series

.

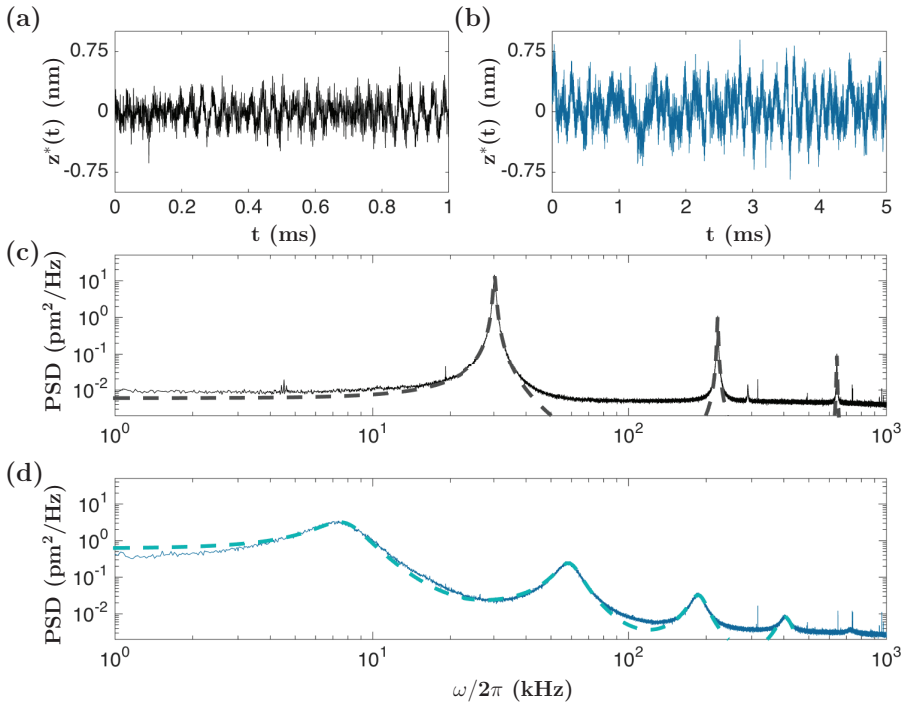

Figure 2.10 – **Oscillations from a clamped-free rectangular cantilever**. (a) Thermal excitation of the cantilever in air. A fraction of the recorded deflection signal was selected to show the oscillations corresponding to the first vibration mode. (c) Power Spectral Density (PSD) of the cantilever deflection $z^*(t)$. The experimental data is plotted in solid line, and the fit using eq.(2.40) in dashed. (b) and (d) same as (a) and (c) for the same cantilever oscillating in water.

2.5.1.a Parametrisation of experimental curves

The effective deflection signal was recorded for a rectangular cantilever (qp-CONT Nanosensors, with nominative stiffness k_c=0.08-0.15 N/m), oscillating freely in air (Fig.2.10a) or in water (Fig.2.10b) far from the surface. The Power Spectral Density (PSD) was computed and the data was fitted using eq.2.40, for each mode (see Table 2). The complete curve is the result of the sum of all the modes (Fig.2.10c-d)

We can easily appreciate the damping effect on the resonant modes due to the liquid chamber, as all the peaks become wider. The damping ratio is estimated by the curve parametrisation as at least one order of magnitude larger in the free oscillations in liquid (table 2.2). Note that although we observe more resonant peaks in the PSD of the oscillations in water than for the spectrum in air (Fig.2.10c-d), the ratio between the frequencies ω_n/ω_1 remains quite the same (table 2.2), indicating that the cantilever still behaves as a campled-free beam.

The characteristic spectrum of the cantilever fluctuations is very informative about its potential utility to capture the dynamics of living cells. On one side we have to consider a cantilever soft enough to be flexible and able to deform upon the cell movement, and on the other side

	n	$\omega_{Dn}/2\pi$ (kHz)	$\omega_n/2\pi$ (kHz)	Q_n	ξ_n	K_n (N/m)	M_n (ng)	C_n (ng/ms)	ω_n/ω_1
Air	1	30.19	30.19	47.94	0.0104	0.15	4.174	16.5	1
	2	221.38	221.39	117.88	0.0042	0.67	0.347	4.0	7.32
	3	641.9	641.9	183.88	0.0027	4.05	0.249	5.4	21.26
Liquid	1	7.41	7.81	2.25	0.22	0.12	50.700	1100	1
	2	58.3	59.0	4.55	0.10	0.41	3.043	247.5	7.55
	3	186.0	187.2	6.21	0.805	1.33	0.966	183.1	23.96
	4	404.1	406.33	6.77	0.073	2.68	0.412	155.53	52.02

Table 2.2 – Values of the parameters obtained using eq. 2.40 to fit the experimental data recorded from a rectangular cantilever oscillating free far from the surface (~500μm).

we need to be careful about the background noise that the cantilever could capture. If the cantilever is too soft, it will be oversensitive to the noise due to the liquid chamber and/or AFM instrument, leading to a 'contamination' of the fluctuation signals. For this reason we have made a comparison of different cantilevers normally used in experiments with soft cells. Figure 2.11 shows the spectrum obtained from different triangular cantilevers (MLCT series, from Bruker) oscillating in air (black curves) or in liquid (blue curves). From the resulting PSD curves, we can see that a cantilever with a spring constant $k_c \geq 0.2$ will not be appropriate for these type of dynamic experiments. Additionally, the problem that arises when considering a triangular geometry is the importance of the torsion signal, requiring a very precise alignment

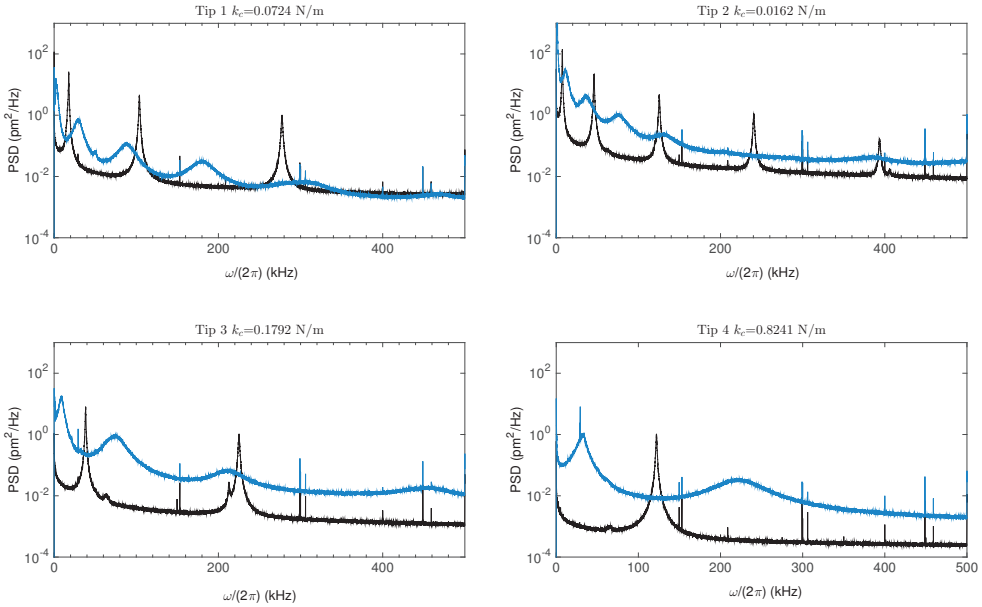

Figure 2.11 – **PSD comparison of v-shaped cantilevers oscillating free in air or in water**. We recorded the fluctuation signals of four different v-shaped cantilevers oscillating free in air (black curves) or in water (blue curves). The data set was obtained on the same working conditions (instrument, support, liquid chamber, temperature, etc..). The cantilevers used are Bruker's MLCT probe, cantilever type A (tip 1), B (tip 2), E (Tip 3), and F (tip 4).

of the laser spot on the cantilever tip to avoid an undesired mixing of torsion and deflection, as it can be seen on the side small peaks appearing notably on the spectrum in air of Tip 3, and the spectrum in water of Tip 1. Although it has been widely accepted that triangular or v-shaped cantilevers are more stable to lateral forces, our results are in agreement with the work of Sader [199, 200], where he states via modelling and its experimental validation that in fact, v-shaped cantilevers are more unstable to lateral forces than cantilevers with a rectangular geometry.

We have chosen to work with a rectangular cantilever with a nominative spring constant k_c=0.08-0.15 N/m. Besides the advantages offered by its geometry, this cantilever has a thin reflective gold coating only at the free end of the cantilever, where the tip is localised (sketched in Fig.2.9). This type of coating has been designed to optimise the measurements in liquid environments, and mainly, it allow us to have a clearer optical image of the cantilever and to check if we have a proper beam (without any material stuck to its surface) during the full test. This is particularly important when capturing the fluctuations of living cells, as there could be floating cells that may stick to the cantilever surface, changing the way it deforms.

2.5.2 Dynamics of healthy and leukaemic HSCs

We have recorded the temporal fluctuations of two adherent healthy TF1 cells and two adherent leukaemic cells (TF1-BCR-ABL). As it can be seen from the topography image shown in Fig.2.12, and as it will be shown later on section 3.7.3 with experiments performed with DPM, in forced-adhesion conditions the leukaemic cells are quite easy to distinguish from healthy ones due to their more rounded shape.

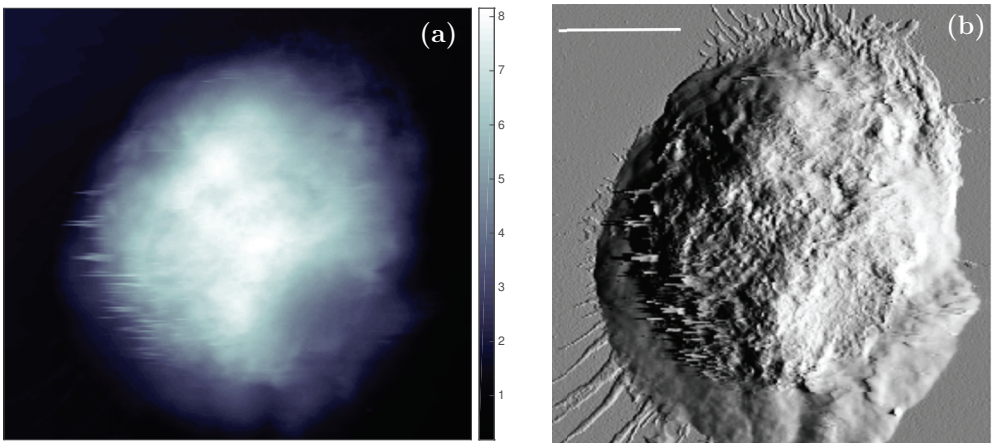

Figure 2.12 – **AFM topography image of an adherent TF1-BCR-ABL cell.** (a) Height image (colour coded in μm). (b) Deflection error image, colour coded in grey scale from -30 nm (black) to 30 nm (white). Scale bar is 10μm.

For each cell, we have established a contact between the AFM cantilever and the surface of the cell, maintaining the force constant at $F \sim$2 nN. The temporal evolution of the cantilever vertical and lateral deflection were recorded using two data acquisition systems coupled to the

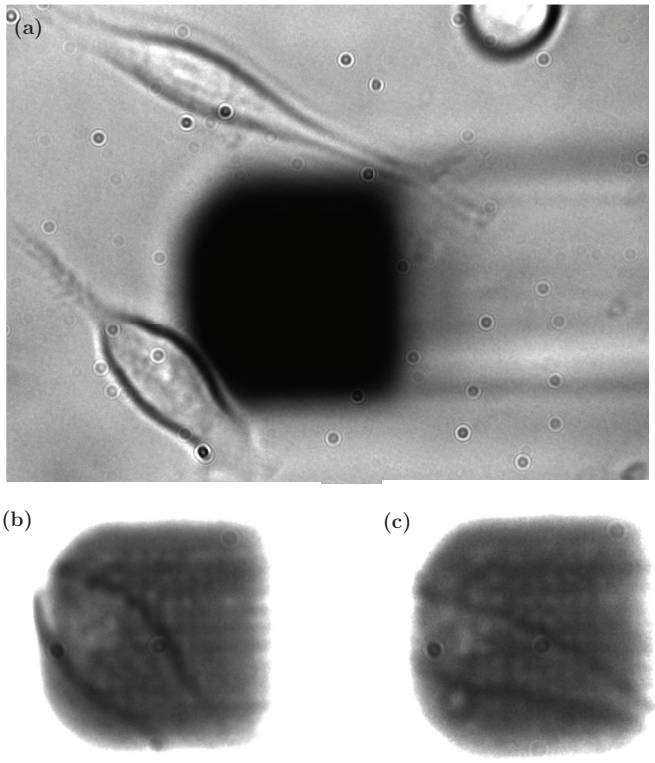

Figure 2.13 – **Positioning of the AFM cantilever tip on TF1-GFP cells.** . Transmission images of the AFM cantilever and the TF1-GFP cells (a), and the positioning of the tip over the cell 1 (b) and 2 (c). In (b) and (c) the exposure time of the camera has been adjusted to be allow visibility on the coated portion of the cantilever.

AFM instrument. This allows us to measure simultaneously the fluctuations at two different frequency ranges. The low-frequency range refers to data recorded at 100 kHz during ~300 seconds. The higher frequency range on the other hand, corresponds to data acquisition at a rate of 2.5 MHz during 2 seconds.

We start by looking at the data obtained from a TF1-GFP cell. We have selected cells with an elongated shape (Fig.2.13a), and we have tried to position the cantilever tip above the nuclear area of the cell (Fig.2.13b,c). The tip positioning is performed using only the optical transmission microscope. The AFM setup that we use to measure the dynamics of single-cells (CellHesion from JPK instruments) does not perform topography images, allowing a more stable system. Even if we would like to perform a topographic image of the cell, this would certainly change dramatically the shape and the state of the cell. Since we want to capture the local cell fluctuations, we do not need this information presently.

Figure 2.14 shows the vertical deflection signal at low frequencies from the cantilever in contact with cell 1 (Fig.2.13b). This cell presents a very interesting effect, as it amplifies the move-

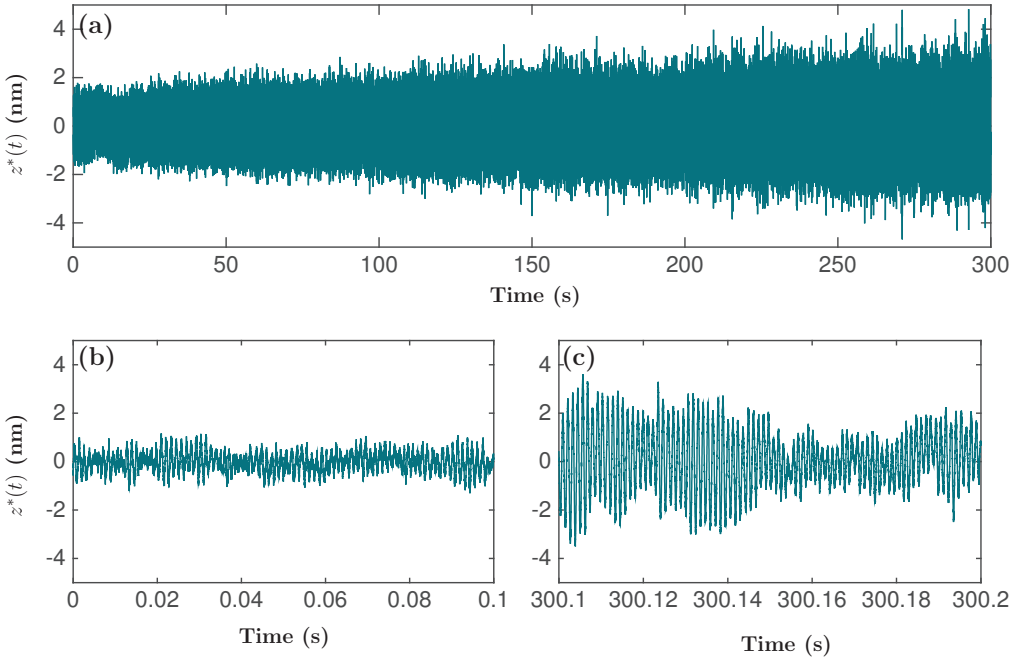

Figure 2.14 – **AFM vertical deflection from a cantilever in contact with an TF1-GFP cell.** (a) Total recording signal fro the cell shown in Fig.2.13(b). (b) and (c) Zoom of (a) at the beginning of contact or at the end, respectively.

ment of the cantilever towards the end of the signal. This amplification occurs in a gradual manner, as seen in Fig.2.14(a). At the end of the signal (Fig.2.14c) we can encounter fluctuations that double the amplitude of the deflection at the beginning of the signal (Fig.2.14b). This effect does not occur at the other cells that we have tested so far, and it could account for an active response of the cell to the mechanical stimuli applied with the cantilever. Further experiments are required to test whether this effect of amplification is recurrent or it was a single-event. We emphasise here the importance of long-temporal recordings. If we would have recorded just a part of the signal, in this case we would not have observed the amplification effect. Nevertheless, as we are applying a constant load on the cell, and we do not establish any control of the environmental conditions (temperature, humidity, etc...), there is a limitation on the maximum time that we can record the temporal signals. The chosen time of 300 s is a compromise between relative high-frequencies, and a data size suited for an efficient computation.

We present in Fig.2.15(a,c) the lateral deflection signal for the TF1-GFP cell 1 or 2, respectively. We can easily observe the appearance of peaks at different positions in time, as indicated by the arrows. These peaks could be the result of an instability of the cantilever, however, they are rather too slow and appear in a quite regular manner to be the case. We have plotted in Fig.2.15(b) the position in time where the peaks occur. We see that they follow almost a straight line, with the cell 1 presenting a shorter time difference (Δt) between peaks (shown in royal blue) than for cell 2, with an average $\Delta t \sim 45$ s, for cell 1, and $\Delta t \sim 22$ s for cell 2. We observe also that for cell 2, the peaks seem to have segregated in three different groups, of ~

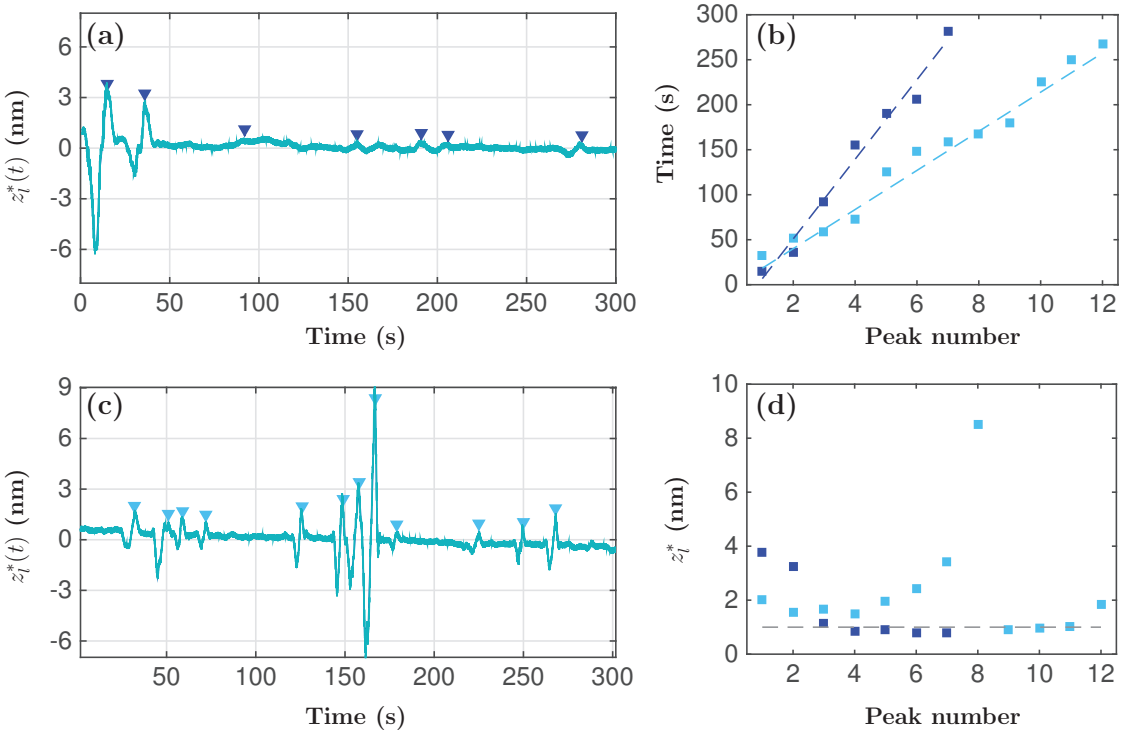

Figure 2.15 – **TF1-GFP cell dynamics extracted from the cantilever torsion signal.** (a) and (c) Lateral deflection signal z_l^* recorded from a cantilever in contact with the TF1-GFP cell 1(a) or cell 2 (c)(Fig.2.13b,c). The arrows indicate the detected peaks. (b) Temporal position of the detected peaks detected in (a,c) The lines show the linear fit of the data. (d) Value of the torsion signal (lat. deflection) of the detected peaks in (a,c). The dashed line corresponds to a value of 1 nm.

4 peaks each, occurring each ~100 s. Given the temporal scales that we are dealing with, the peaks could be reflecting a structural change of the cytoskeleton, and/or an active mechanical response by the cell. As we do not know the spring constant for the torsional movement of the cantilever, we cannot estimate properly the measured force at these events. However, most of these peaks have a torsion value of ~ 1 nm (Fig.2.15d). Note that in the case of cell 2, the amplitude of the peaks seem to increase with time, reaching a maximum value at peak number 8, where it breaks and continues with a peak of minimum amplitude, to start increasing again by peak 12. Another interesting thing to notice about these peaks is that they are preceded by an almost symmetric peak in the opposite direction. This implies that the cell experiences first a process of relaxation followed by a mechanical response that causes the deformation of the cantilever.

Although these events are not that clear on the deflection signal (Fig.2.14a), we should observe a change in the dynamics of the cantilever deflection. To detect the cell response on the deflection signal, we have applied the Continuous Wavelet Transform, using the first derivative of a gaussian as mother wavelet. Figure 2.16(c-d) shows the scale-time representation of the CWT, where the CWT modulus in log scale has been colour coded. Hence, the change in the dynamics of the cantilever will be identified by the CWT modulus maxima (brightest regions on the figure). We can see that the CWT modulus maxima regions occur all along the

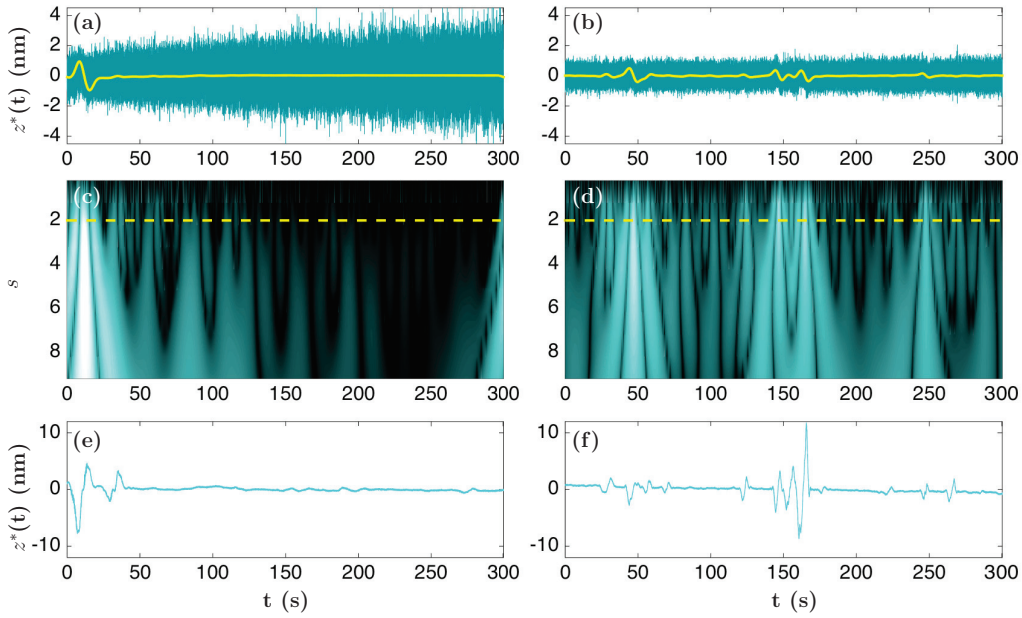

Figure 2.16 – **Wavelet transform for the detection of the cell response in the deflection signal of TF1-GFP cells.** (a) Vertical deflection signal from the TF1-GFP cell 1. The yellow curve shows the filtered signal using a gaussian window, taken at the scale shown in dashed in (c). (c) CWT of the deflection signal, using the first derivative of a gaussian as mother wavelet. The yellow dashed line shows the scale where the signal has been filtered. The modulus of the CWT has been colour coded in log scale, from black to white (in a.u.). (e) Torsion signal from the TF1-GFP cell 1. (b,d,f) Same as (a,c,e) for the TF1-GFP cell 2.

length of the signal, and they are enhanced at the same time points where we observe the torsion peaks (Fig.2.16e-f). To get an estimated of the measured force, we have filtered the deflection signal using a gaussian window with a width of 2 seconds. The resulting filtered signal is shown in yellow in Fig.2.16(a-b). The detected peaks for cell 1 have an amplitude of 1 nm, whereas the cell 2 presents peaks with an average amplitude of nearly 0.5 nm, corresponding to roughly 1.3 nN and 0.65 nN respectively.

When we measure the fluctuations of the cantilever in contact with leukaemic TF1-BCR-ABL

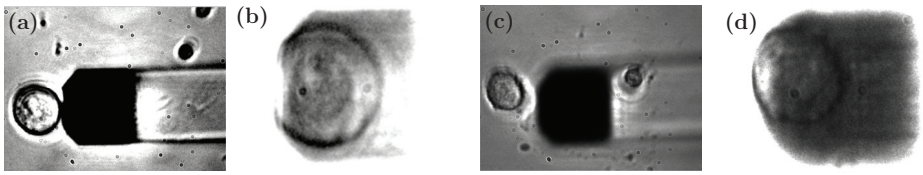

Figure 2.17 – **Positioning of the AFM cantilever tip on TF1-BCR-ABL cells.** . Transmission images of the AFM cantilever and the TF1-BCR-ABL cells (a,c), and the positioning of the tip over the cell 1 (b) and 2 (d).

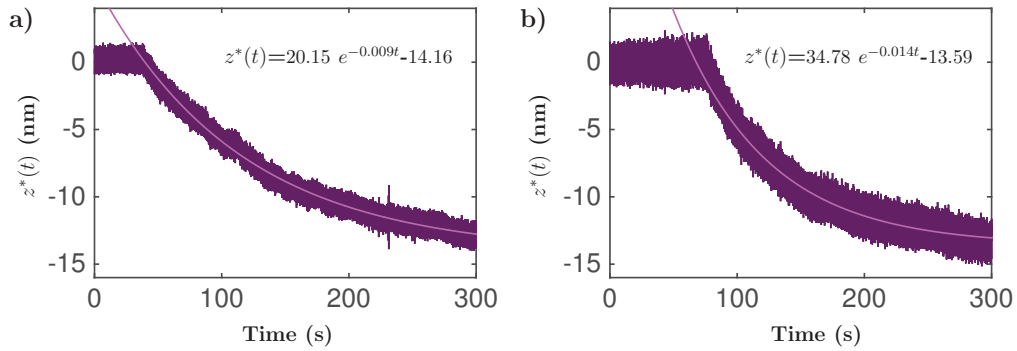

Figure 2.18 – **TF1-BCR-ABL cell dynamics extracted from the cantilever deflection signal.** (a) and (b) show respectively the data obtained from cell 1 (Fig.2.17a,b) and cell 2 (Fig.2.17c,d). The pink line shows the exponential fit.

cells (Fig.2.17) we do not observe the same type of signals as the ones for TF1-GFP cells. In fact, in Fig.2.18 we recognise a typical viscoelastic creep response curves with relaxation times of 110 s (for cell 1) and 70 s (for cell 2).

If we follow our hypothesis that the oncogene *BCR-ABL* causes a transformation in the cell cytoskeleton that results in less motility, as we saw in the quasi-static strain-stress response in section 2.5.2, then it is possible that TF1-BCR-ABL cells loose their ability to respond immediately to the mechanical stimuli, because their cytoskeleton has lost it correct anchoring to the external cortex (these transformed cells again have more difficulty to spread on fibronectin coated surfaces [160]). It takes between 50 s - 100 s for the cell to respond and adapt to the applied load, and once it starts relaxing, it is not able to respond immediately, as we saw for TF1-GFP cells in Fig.2.15. We have parametrised the curves obtained for TF1-BCR-ABL cells with an exponential fit, estimating the relaxation time as $\tau \sim 110$ s for cell 1, and $\tau \sim 70$ s for cell 2 (Fig.2.18).

2.5.2.a From fluctuation signals to cell mechanics

Prior to spectral decomposition of the cantilever fluctuations in contact of TF1 cells, we have computed their static shear modulus G_0 of these cells from large scale force-indentation curves (5 μm scan at 1μ/s velocity) for the 4 cells: TF1-GFP cell 1, G=144 ± 31 Pa; TF1-GFP cell 2, G= 410 ± 77 Pa; TF1-BCR-ABL cell 1 G= 160 ± 42 Pa; TF1-BCR-ABL cell 2, G= 295 ± 40 Pa.

Extraction of complex shear modulus by spectral analysis of cantilever fluctuations.
The complex shear modulus of the viscoelastic media surrounding the tip of an AFM cantilever can be retrieved from its thermal fluctuations given that this media [201, 202] behaves as a causal memory function $\zeta = 0$ for $t < 0$. This means that the energy stored in the media due to random fluctuations can return to the tip dynamics in a later time. If $z(t)$ denotes the vertical position of the cantilever tip, this temporal variable has a zero mean (in stationary conditions), and is defined for positive values of t.

In AFM experiments, the cantilever tip is not completely immersed in the viscoelastic medium,

so the continuum approach of Stokes equations must be modified to take into account different boundary conditions. When the motion of the probe is perpendicular to the surface as in AFM or indentation experiments, the Hertz (resp. the generalised Sneddon) law applies to a spherical (resp. conical or pyramidal) probe indenting a viscoelastic medium. This relation describes the force required to move the tip by an infinitesimal quantity δ_z inside a viscoelastic media with shear modulus G, it takes the following for for a conical tip:

$$F(\omega) = \frac{4\,\tan\theta\,h_0}{\pi(1-\nu)} G(\omega)\delta_z(\omega) \tag{2.41}$$

$2*\theta$ is the angle of the conical tip, h_0 is the depth of indentation of the tip (given that this quantity, which depends on the load does not change during the experiment), ν the Poisson ratio. $G(\omega) = G'(\omega) + iG''(\omega)$.
The spectral density of z fluctuations $\mathscr{E}_z(\omega)$ which can be computed by Fourier transforming its auto-covariance function $C_z(\tau)$ is therefore related to the loss modulus $G''(\omega)$ of the media surrounding the tip[201]:

$$\mathscr{E}_z(\omega) = \int_{-\infty}^{\infty} C_z(\tau) e^{-i\omega\tau} d\tau = \frac{b k_B T\, G''(\omega)}{h_0\,|G(\omega)|^2}\,,$$

$C_z(\tau) = \mathbb{E}\{\delta_z(t)\delta_z(t+\tau)\}$ with $\mathbb{E}\{u\}$ the expectation of u. h_0 is a characteristic length, it is proportional to the depth of penetration of the cantilever tip inside the material, k_B is the Boltzmann constant, b is a constant which depends on the property of the tip and the Poisson ratio: $b = \pi(1-\nu)/(2\tan\theta)$.

If we take $\Xi(\omega) = 1/G(\omega)$, $\Xi'' = G''/|G(\omega)|^2$, Eq. (2.42) reads:

$$\mathscr{E}_z(\omega) = \frac{b k_B T\, \Xi''(\omega)}{h_0}\,, \tag{2.42}$$

From the spectral density of the tip fluctuations we can therefore retrieve the behaviour of $\Xi''(\omega)$ and by a Kramers-Kronig transformation, compute the real part of Ξ':

$$\Xi'(\omega) = \frac{2}{\pi} P \int_0^{\infty} \frac{\zeta\ \Xi''(\zeta)}{\zeta^2 - \omega^2} d\zeta\,, \tag{2.43}$$

where P denotes the principal-value of the integral.

The observation of power-law regimes in the frequency range [100 Hz, 10 kHz] of the spectral density of cantilever fluctuations when indented inside the TF1 cells suggests therefore that their rheology can be described by a structural damping or hysteric model (see also Chapter 1), of which we give here the full model:

$$G(\omega) = G_0\left(\frac{\omega}{\omega_0}\right)^{x-1}(1+i\overline{\eta})\cos(\frac{\pi(x-1)}{2}) + i\omega\mu\,, \tag{2.44}$$

where $\overline{\eta} = \tan(x-1)\pi/2$ has been called the structural damping coefficient [203], $\omega = 2\pi f$ is the radian frequency, x is a scaling exponent, $x = 1$ for an ideal elastic material and $x = 2$ for a Newtonian viscous fluid, G_0 and ω_0 are material dependent scaling factors for stiffness

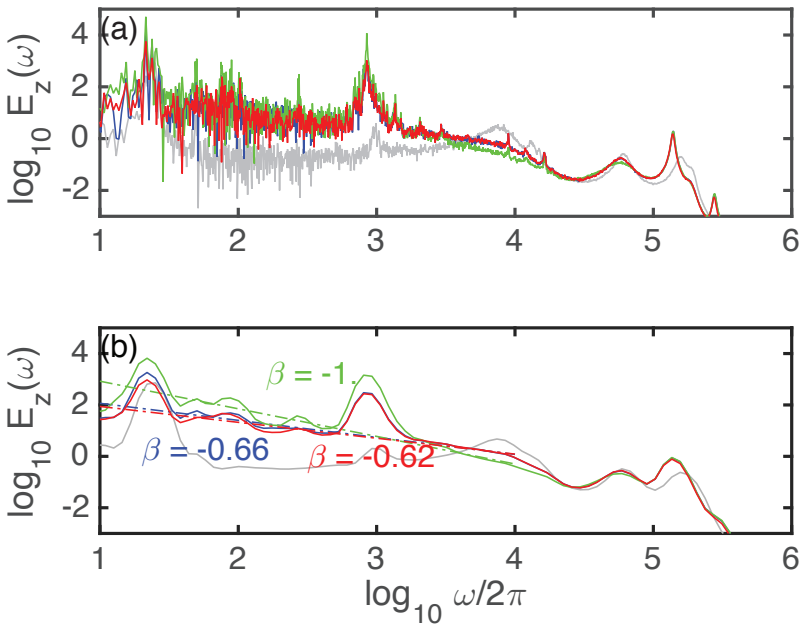

Figure 2.19 – **Comparison of periodograms $v_z(\omega)$ and wavelet spectrums $V(\omega)$ of cantilever fluctuations when placed in contact with a TF1-GFP cell.** (a) Periodograms. (b) Wavelet spectral densities. Correspondance of the curves color coding. Grey: free cantilever in liquid, blue, (resp. green and red): cantilever in contact with a TF1-GFP for a 2 nN loading force.

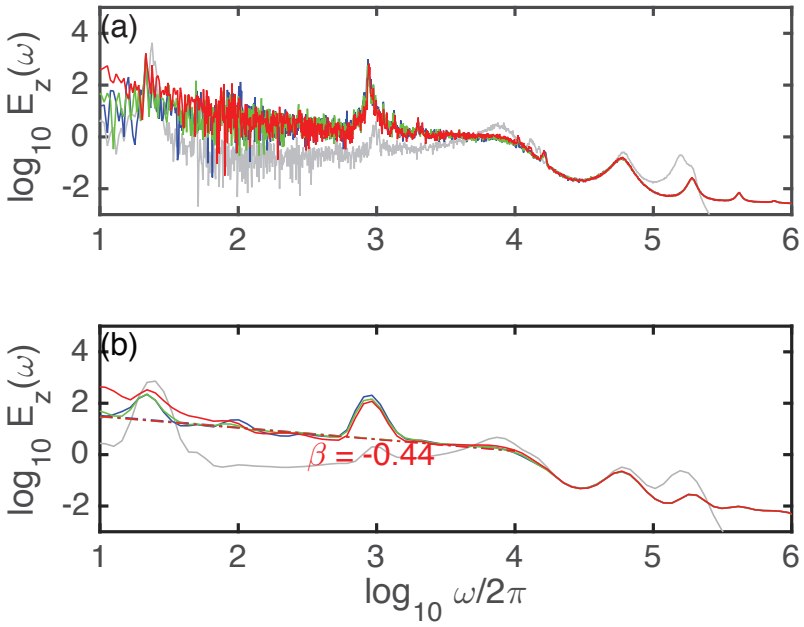

Figure 2.20 – **Comparison of periodograms and wavelet spectra $E_z(\omega)$ of cantilever fluctuations when placed in contact with a TF1-BCR-ABL cell.** (a) Periodograms. (b) Wavelet spectral densities. Correspondance of the curves color coding. Grey: free cantilever in liquid, blue, (resp. green and red): cantilever in contact with a TF1-BCR-ABL for a 2 nN loading force.

and frequency, $G(\omega) = G'(\omega) + iG''(\omega)$, μ is an additive Newtonian viscous term, $i^2 = -1$. If the spectral density $\mathscr{E}_z(\omega)$ behaves as $\omega^{-\beta}$, Eq. (2.42) tells us that we have a simple relation in between β and x: $\beta = 1 - x$. The spectral analysis (periodograms) of cantilever fluctuations, when indented inside TF1 cells are reported in Fig. 2.19(a) for a TF1-GFP cell and Fig. 2.20(b) for a TF1-BCR-ABL cell. We computed the power spectra from the square modulus of the FFT of the AFM cantilever fluctuation signals (periodograms) with a total duration of 2 s to discard transitory effects discussed in the previous section and we realised that it was very difficult to extract correct exponents in the low frequency range (<10 kHz), very recently we again choose a time frequency decomposition of these signals using Cauchy wavelet transforms from which we computed wavelet spectra which are shown in Figs 2.19(b) and 2.20(b). This work has been written in a publication this summer, and we have added this preprint at the end of this manuscript (Appendix B) for those interested in the rigorous equations for wavelet spectral decompositions.

The power law behaviours shown in Figs 2.19(b) and 2.20(b) suggest that in the frequency range from 10 to 10 kHz these cells actually behave as structural damping systems with an exponent x that varies in the range $[1.45 : 1.7]$. This dispersion of x values and the fact that they can get closer to the limit $x = 2$ is rather different from what has been observed on strongly adherent cells [144] ($x \sim 1.26$ for myoblasts, $x \sim 1.22$ for macrophages, $x \sim 1.2$ for fibroblasts), for these later cases this exponent x seems to be an invariant, independently of their static shear modulus G_0. The TF1 cell line mimics hematopoietic stem cells, it is very immature, and it is much softer than myoblasts or fibroblasts which have a important mechanical function in migration and tissular cohesion. Besides being softer, hematopoietic stem cells look more like viscous balls than elastic balls when $x > 1.5$. It comes clearly from this preliminary study that the exponent x is smaller for the few tested TF1-BCR-ABL cells than the few tested TF1-GFP cells, suggesting that the TF1-BCR-ABL cells may have restored some elasticity after their transformation by the oncogene. One may wonder if the static G_0 extracted from large scale indentation force curves is correlated to the exponent x or if, as observed for muscular cells x may vary independently of G_0. This would require a further study that we did not have time to perform, since we preferred first to check the accuracy of this method on standard polymer layers (PDMS, agar) and other cells (myoblasts) (see Appendix B).

Summary

We have studied the strain-stress response of healthy and leukaemic TF1 cells over different temporal scales. The quasi-static measurement of force-indentation curves confirms that the cell response is not linear, contrarily to what is traditionally assumed using the Sneddon's or Hertz models. In fact, the cell behaves as a multi-layer viscoelastic object, where the actin cortex plays the role of a mechanical barrier. By tracking the scaling law of force-indentation curves, we showed that the introduction of the chronic myelogenous leukemia oncogene *BCR-ABL* induces a stiffening of the cortex of TF1 cells when they are forced to adhere on fibronectin, resulting in a stress-strain response typical of shell-like structures. This loss of motility and contractility of TF1-BCR-ABL cells is also reflected on the temporal recordings of the cell mechanical fluctuations. While TF1-GFP cells are able to respond to the mechanical stimuli in real time, likely involving cytoskeletal structural changes, the oncogene transformed cells are incapable of respond rapidly to the applied load. The temporal signals show that healthy cells present creep relaxation time ~30 seconds, while TF1-BCR-ABL cells present creep relaxation times $\tau \sim 85$ seconds. The slower response found on leukaemic cells suggests that their mechanotransduction pathway may have been transformed, besides the previously reported actin redistribution in the litterature. Finally, the characterization of the rheology of these cells in the frequency range [100 Hz : 10 kHz] showed that these cells locally respond with a structural damping law, with a scaling exponent x in the [1.4 : 1.7] interval, and that they are closer to viscous balls than muscle cells such as myoblasts. This study on a few TF1 cells lead us to the preliminary conclusion that x would be smaller the transformed TF1-BCR-ABL cells ($x \sim 1.4$) than the normal TF1-GFP cells ($x \sim 1.6$) , suggesting that the TF1-BCR-ABL cells may have restored some elasticity after their transformation by the oncogene, that could be produced by a reinforcement (stiffening) of their actin cortex.

Chapter 3

Diffraction Phase Microscopy

In the past two decades Quantitative Phase Imaging (QPI) has become a rapidly emerging field. QPI encloses a large set of interferometric and non-interferometric methods employed to measure the optical phase of an object [204**?** –217]. The interest in measuring the phase relies on the fact that the phase of light is much more sensitive to the specimen structure and is less prone to artefacts than the amplitude. As electromagnetic fields emerging from the illumination source interact with the specimen, it leads to a phase shift containing information about the material topography and the morphology of the sample under investigation [218, 219]. Then, the main difficulty when measuring the phase of an object with high sensitivity is posed by the noise due to mechanical vibrations and air fluctuations that affect any interferometric system.

Diffraction Phase Microscopy (DPM), introduced by Popescu *et. al* in 2006 [209], is a common-path QPI method that significantly reduces the noise problem and it combines the main advantages of other current QPI techniques: it has a stable compact configuration with an acquisition speed limited only by the speed of the camera, as it requires a single-shot for the measurement [215, 220]. As DPM is a fast non-intrusive optical technique, it is particularly suited to study the morphology and the dynamics of living biological specimens [221–223].

3.1 Principles of DPM

3.1.1 Phase objects

Very thin and transparent objects like cells or biological tissues, present a low light-absorption resulting in small changes on the amplitude of the transmitted light and thus lack contrast to recognise and distinguish image details such as intracellular structures. However, the object interior may present small differences on its composition or density, leading to slightly variations of the refractive index. If lightwaves go through these variations, they will experience a certain phase shift that is proportional to the optical path length, deforming the light wavefront (Fig.3.1).

The optical phase of the object (ϕ) at a given position x, y is given by

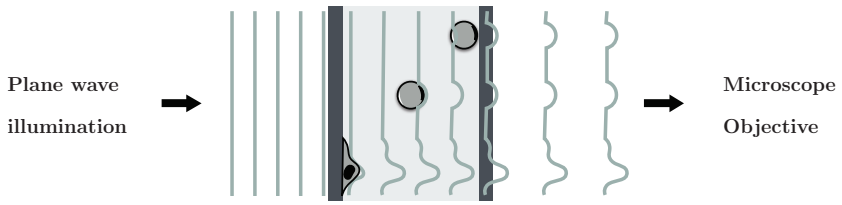

Figure 3.1 – **Wavefront deformation induced by a phase object.** Scheme of the deformation encountered by the illumination wavefront when light passes through a transparent object.

$$\phi(x,y) = \frac{2\pi}{\lambda}\int_{z_m(x,y)}^{z_M(x,y)} \Delta n(x,y,z)\,dz \tag{3.1}$$

where λ is the illumination wavelength, $\Delta n = n - n_0$ is the difference between the refractive indices of the object (n) and the external medium (n_0). z_m and z_M are respectively the lower and the upper bound of the object at position (x,y), with the total thickness of the object at point (x,y) being $h(x,y) = z_M(x,y) - z_m(x,y)$. Given that the optical phase (ϕ) depends on the illumination wavelength, in practice it is more convenient to work with the Optical Path Difference (OPD), defined as $\Phi = \phi\lambda/2\pi$. As the OPD has an unit of length, it can be easily compared and related to spatial characteristics of the object.

There are two important things to notice about the phase of the object measured by DPM: (i) it is an integration across the object thickness, and as such, the direct measurement of $\phi(x,y)$ will lose information on the z axis, (ii) the thickness and the refractive index of the object are coupled, implying that if both quantities vary at the same time, $\phi(x,y)$ cannot distinguish between the variations of one or the other.

The uncoupling of refractive indices and thickness has been tackled by other experimental techniques, usually at the expense of diminishing the acquisition speed. Among the proposed methods we can find imaging from different points of view [224], spectroscopic phase microscopy [225, 226] and changing the refractive index of the medium [227].

3.1.2 Theoretical background

The DPM interferometer designed by Popescu *et al.* [222] is composed basically of a diffraction grating coupled to a $4f$ lens system. By placing the diffraction grating at the image plane of an inverted microscope, multiple diffraction orders are generated containing the full spatial information about the transparent object crossed by the light beam. We have recently assembled a DPM setup based on this principle (Fig.3.2) [228]. After the transmission grating G, the zeroth and first order components of the diffracted beams are separated in the conjugated Fourier plane of the image plane of the microscope. Then, the zeroth order is low-pass filtered with a spatial filter and recombined with the first order, thanks to a second Fourier lens L_2 to give a spatially modulated interference image $I(x,y)$.

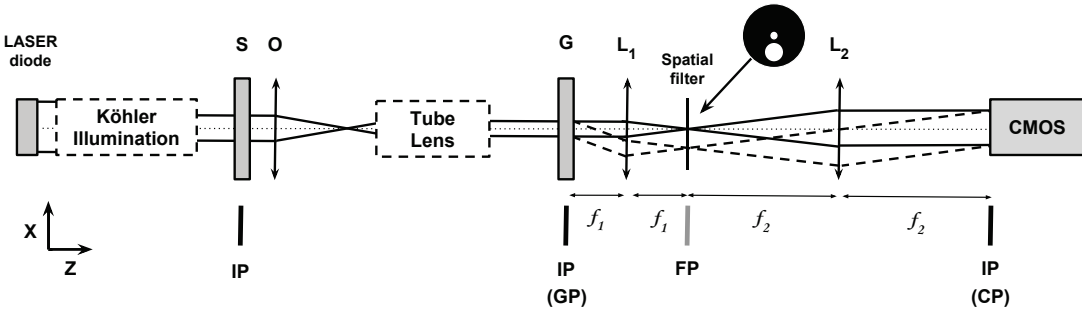

Figure 3.2 – **Diffraction Phase Microscopy (DPM) setup**. A transmission grating (G) is placed at the image plane (IP) of the microscope objective lens (O). The zeroth-order beam (reference field) is low-pass filtered and the first-order beam (imaging field) is selected by using a spatial filter at the Fourier plane (FP) of lens L_1. The two beams are recombined at the camera plane (CP) through a second lens L_2.

Starting at the grating plane (GP), we have

$$U_{GP}(x,y) = U_0(x,y) + U_1(x,y)e^{i\beta x} \tag{3.2}$$

where U_0 and U_1 are respectively, the zeroth and first order fields [1]. Here, $\beta = 2\pi/\Lambda$, where Λ is the grating period [220]. The first $2f$ lens system takes a Fourier transform of this field such that before the filter in the Fourier plane (FP-) we have

$$\hat{U}_{FP-}(k_x,k_y) = \hat{U}_0(k_x,k_y) + \hat{U}_1(k_x-\beta,k_y) \tag{3.3}$$

with

$$k_x = \frac{2\pi}{\lambda f_1}x_1 = \alpha x_1; \qquad k_y = \frac{2\pi}{\lambda f_1}y_1 = \alpha y_1 \tag{3.4}$$

$$\beta = 2\pi/\Lambda = \frac{2\pi}{\lambda f_1}\Delta x = \alpha \Delta x \tag{3.5}$$

and

$$\Delta x = \lambda f_1/\Lambda \tag{3.6}$$

where (x_1, y_1) are the coordinates at the FP, and the quantity Δx represents the physical spacing between the two diffraction orders in the FP. As the zeroth order is filtered, immediately after the spatial filter (FP+) we have

$$\hat{U}_{FP+}(\alpha x_1,\alpha y_1) = \underbrace{\hat{U}_0(0,0)\delta(\alpha x_1,\alpha y_1)}_{\substack{\text{Spatial frequency domain}\\ \text{representation of the DC signal}}} + \underbrace{\hat{U}_1(\alpha x_1-\beta,\alpha y_1)}_{\substack{\text{Unfiltered signal}\\ \text{with image information}}} \tag{3.7}$$

The second $2f$ system takes another forward Fourier transform, so the resulting field at the camera plane (CP) is

[1] We consider here only the 0th and +1st orders, as the other ones either do not pass through the first lens, or they are filtered out at the Fourier plane.

$$U_{CP}(x,y) = \frac{1}{|\alpha|}\left[U_0 + U_1(-x/M_{4f}, -y/M_{4f})e^{i\beta x/M_{4f}}\right] \tag{3.8}$$

where the magnification of the $4f$ system, $M_{4f} = -f_2/f_1$ has been substituted in the equation. In deriving the irradiance on the camera, we can write

$$U_0(x,y) = A_0(x,y)e^{i\phi_0(x,y)}\,; \qquad U_1(x,y) = A_1(x,y)e^{i\phi_1(x,y)} \tag{3.9}$$

If we define

$$x' = -x/M_{4f}\,; \qquad y' = -y/M_{4f} \tag{3.10}$$

and

$$A_0' = A_0/|\alpha|\,; \qquad A_1' = A_1/|\alpha| \tag{3.11}$$

eq.(3.8) becomes

$$U_{CP} = A_0'e^{i\phi_0} + A_1'(x',y')e^{i\phi_1(x',y')}e^{i\beta x'} \tag{3.12}$$

Thus, at the camera plane we have the interference of two magnified copies of the image, where one is filtered to DC, and both are inverted in x and y. The inversion results because two forward transforms are taken by the lenses rather than a transform pair (forward and backward).

Finally, the resulting intensity measured at the camera is

$$\begin{aligned} I_{CP}(x',y') &= U_{CP}(x,y)U_{CP}^*(x,y) \\ &= |A_0'|^2 + |A_1'(x',y')|^2 + 2|A_0'||A_1'(x',y')|\cos(\beta x' + \Delta\phi) \end{aligned} \tag{3.13}$$

where

$$\Delta\phi = \phi_1(x',y') - \phi_0 \tag{3.14}$$

The phase information from the sample can be extracted from the modulation term (cosine) which is a result of the interference between the image and the reference field.

3.1.3 Design considerations

The crucial components on the design of the DPM setup are the diffraction grating and the spatial filter. Therefore, for a given microscope objective and taking into account the pixel size of the camera, a correct combination of diffraction grating, $4f$ lenses and spatial filter must be chosen. The general guidelines for the design of the DPM system are the following [220]:

- First, the grating modulation period is chosen based on the objective lens magnification M_{obj} and numerical aperture NA_{obj}. In order to perform at optimal resolution, the

grating period Λ must be

$$\Lambda_T \leq \frac{\lambda M_{obj}}{3NA_{obj}} \tag{3.15}$$

- Second, the magnification of the $4f$ lenses can be tuned according to the pixel size of the camera to obtain a good sampling of the grating fringes.
- Third, the size of the spatial filter is chosen such that the reference beam contains only the DC component, and that the interference pattern produces a uniform reference image at the camera plane. The fringe contrast can be optimised by adjusting the intensity of the diffraction orders.
- Finally, the numerical aperture of the second lens L_2, needs to be large enough for the lens to capture both beams and make them interfere at the camera plane.

3.2 DPM setup characterisation and phase extraction method

We use a low-coherence laser diode (Thorlabs, GmbH, Germany, λ=532nm) as a light source. In order to have a spatially coherent field at the image plane (IP), the laser is directed to the sample using Köhler illumination. A transmission grating (110 grooves/mm) is localised at the IP of the microscope equipped with an objective (O) 40x (Olympus, France SPlan40, N.A.=0.7). The first-order beam (imaging field) created by the grating is selected without any filtering, while the zeroth-order beam (reference field) low-pass filtered, letting pass only the DC component. This filtering is made through a custom made spatial filter (Thorlabs) placed at the Fourier plane of lens L_1. The design of the spatial filter consists of two circular apertures with diameters of 1 mm and 15 μm. Our spatial filter has been made by making circular apertures on a plastic-like material, which filters the reference field with a window of sharp edges. The size of the small aperture has been chosen trying different pre-fabricated filters or pinholes, and a careful inspection of the Fourier transform of the intensity image obtained with the same setup, where the diffraction grating was removed (see next section for details). The two beams are recombined using a second Fourier lens L_2, and the resulting interferogram is recorded as an image of 2048x2048 or 1024x1024 pixels with a CMOS camera (Hamamatsu, Japan, ORCA-Flash 4.0) with an acquisition speed of 10 kHz. The $4f$ lens system adds a 5.9x magnification (f_1=25.4 mm, f_2=150 mm)(Fig.3.2).[2]

3.2.1 Spatial filter

We have used a set of four pinholes with different aperture sizes to determine empirically the adequate spatial filter design for the reference beam. The reference beam is obtained by filtering the 0th diffracted order at the Fourier plane of lens L_1. To evaluate the quality of the filtered image, we have imaged a fixed adherent cell while placing the different pinholes at the Fourier plane of lens L_1, in the same position as the final spatial filter.

[2]The data recorded on myoblasts was performed with an alternative setup consisting of a diffraction grating of 70 grooves /mm, a spatial filter with circular apertures of 2 mm and 15 μm in diameter, and a $4f$ lens system (f_1=50 mm, f_2=250 mm) adding a 5x magnification.

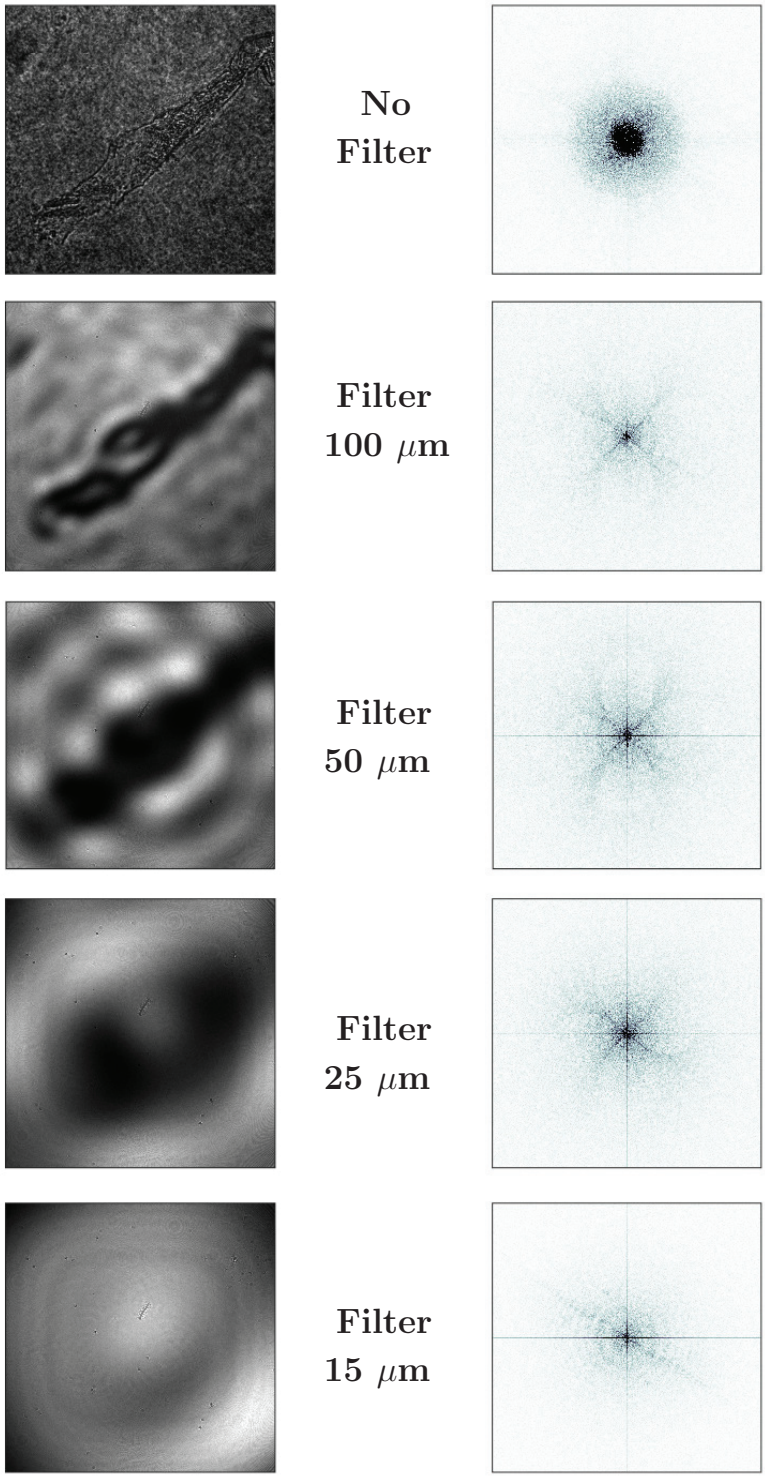

Figure 3.3 – **Evaluation of the filtered image with different pinholes.** Intensity images (left column) and their corresponding 2D Fourier transform (right column, where the modulus has been colour coded from white to black) for different pinholes of variable sizes placed at the Fourier plane of lens L_1, and where the grating has been taken-off. A fixed adherent cell has been captured in a 2048x2048 pixels image. The scale in real space corresponds to an image of 75 x75 μm.

By evaluating both the intensity images and their corresponding 2D Fourier Transform (Fig.3.3) we have chosen a filter with a circular aperture of 15 μm. This aperture size filters most of the low-frequencies and it still allows to cover almost all of the field of view. As it can be seen at the bottom row in Fig. 3.3, the intensity is not homogeneous over the full field of view, with a noticeable decrease at the corners of the image. As it will be seen on the untreated DPM images shown later on this chapter, even with this inhomogeneous intensity, we can still have an interference pattern over the full field of view, although perhaps in some cases, the fringe contrast is slightly diminished at the corners of the image.

3.2.2 DPM setup resolution

For a transmission microscope, the transverse resolution is given by Abbe's formula:

$$\Delta p = \frac{1.22\lambda}{NA_{obj}} \tag{3.16}$$

where plane wave illumination is assumed and Δp represents the diffraction spot radius or the distance from the peak to the first zero of the Airy pattern. It follows that, in order to get better resolution a higher NA is required, usually implying a higher magnification and a smaller field of view.

Besides the transverse resolution of the transmission microscope, we need to take into account the fringe sampling, the magnification due to the $4f$ lens system (M_{4f}) and, as we use the wavelet transform to retrieve the optical phase, we should also consider the width of the analysing wavelet to have a full description of the resolution obtained with our DPM system. Table 3.1 summarises the main characteristics of the optical setup and the phase extraction method that determine the resolution of the system.

As seen in table 3.1, the resolution of our system is limited by the transmission microscope. We can expect to resolve objects down to a size of ~1 μm, without any additional information loss introduced by the image processing method. In the context of living cells, this means

Parameter	Variable	Value
Transverse resolution of the transmission microscope	Δp	927.2 nm
Magnification $4f$ lens system	M_{4f}	5.9x
Field of view	-	75.68 μm
Required grating modulation period	Λ_T	10.13 μm
DPM setup grating modulation period	Λ_S	9.1 μm
Fringe sampling	-	~ 12 pixels/fringe
Fringe width	-	~ 440 nm
Morlet wavelet half width	$\Delta x_{\frac{1}{2}\lvert\Psi_M\rvert_{max}}$	700 nm (in x)

Table 3.1 – **DPM setup parameters determining the spatial resolution of the system.** The reported values are for a DPM setup using a 40x objective with NA_{obj}= 0.7. The Morlet wavelet width has been taken at the mid height of the gaussian envelope, $\frac{1}{2}|\Psi_M|_{\max}$.

that we are concerned by the observations at a single-cell level, including the large intracellular structures, such as the nucleus. In adherent cells, it could be also possible to observe the perinuclear structures like the Golgi apparatus and the endoplasmic reticulum, as well as large and complex mitochondrial networks. However, the capacity of resolving these structures will depend greatly on the distance between them. For example, we can be unable to distinguish the nucleus from the cytoplasmic area if the distance between the nuclear and the intracellular side of the cell membrane is too small. We have then chosen a compromise between a field of view large enough to visualise large adherent cells, and a micrometric resolution that allows us to observe cells of a few micrometers in size, such as erythrocytes. If on the contrary, the interest will be mainly on studying only small cells, and/or to resolve the intracellular structure, an objective with a higher magnification should be used. In this way, the resolution will be increased, having more fringes per micrometer, while keeping the fringes pixel sampling.

Nevertheless, as it has been mentioned previously, diffraction phase microscopy measures the optical path depth of an object, which is an integration of its internal structures along the object thickness. Hence, given the complexity of a living cell, it is not straightforward to identify individually the intracellular components. Having this difficulty in mind, it is more useful to avoid interpreting the phase image of a cell based on the identification of cellular organelles, and instead focus on the composition and/or density of the underlying structure. Section 3.5 includes a more detailed discussion about the information obtained by the phase measured with DPM and its interpretation in the context of living cells.

3.2.3 Revisiting the phase extraction method with the 2D wavelet transform

To retrieve the phase image associated with the sample object, different methods have been proposed, including Hilbert transform followed by phase unwrapping, [206], derivative methods [223], and Fourier filtering to avoid unwrapping problems [229]. All these phase retrieval algorithms rely on the assumption that the object phase does not alter the fringe carrier patter, allowing a quasi one-dimensional analysis of interference patterns. To improve this approach and delineate more precisely the validity of this assumption, we propose here to generalise the Fourier filtering methods using a two-dimensional space-scale analysis based on Morlet wavelet transform [228, 230].

The two-dimensional (2D) continuous wavelet transform (CWT) of an interferogram $I(\vec{x})$ with $\vec{x} = (x, y)$ is defined as [231]:

$$W_\Psi(\mathbf{b}, a, \theta) = a^{-\eta} \int_{\Re}^{2} I(\mathbf{x}) \Psi^*[a^{-1} r_\theta(\mathbf{x} - \mathbf{b})] \mathrm{d}^2\mathbf{x} \tag{3.17}$$

$W_\Psi(\mathbf{b}, a, \theta)$ is the wavelet transform coefficient at position $\mathbf{b}$, scale parameter a and rotation angle θ. $\mathbf{b} = (b_x, b_y)$ is a 2D translation parameter describing the position of the wavelet, $a > 0$ is the scale dilation parameter (nondimensioned), θ is a rotation parameter, $\mathbf{r}_\theta$ is the 2x2 rotation operator matrix, Ψ^* is the complex conjugate of the mother wavelet Ψ, and η is a normalisation exponent.

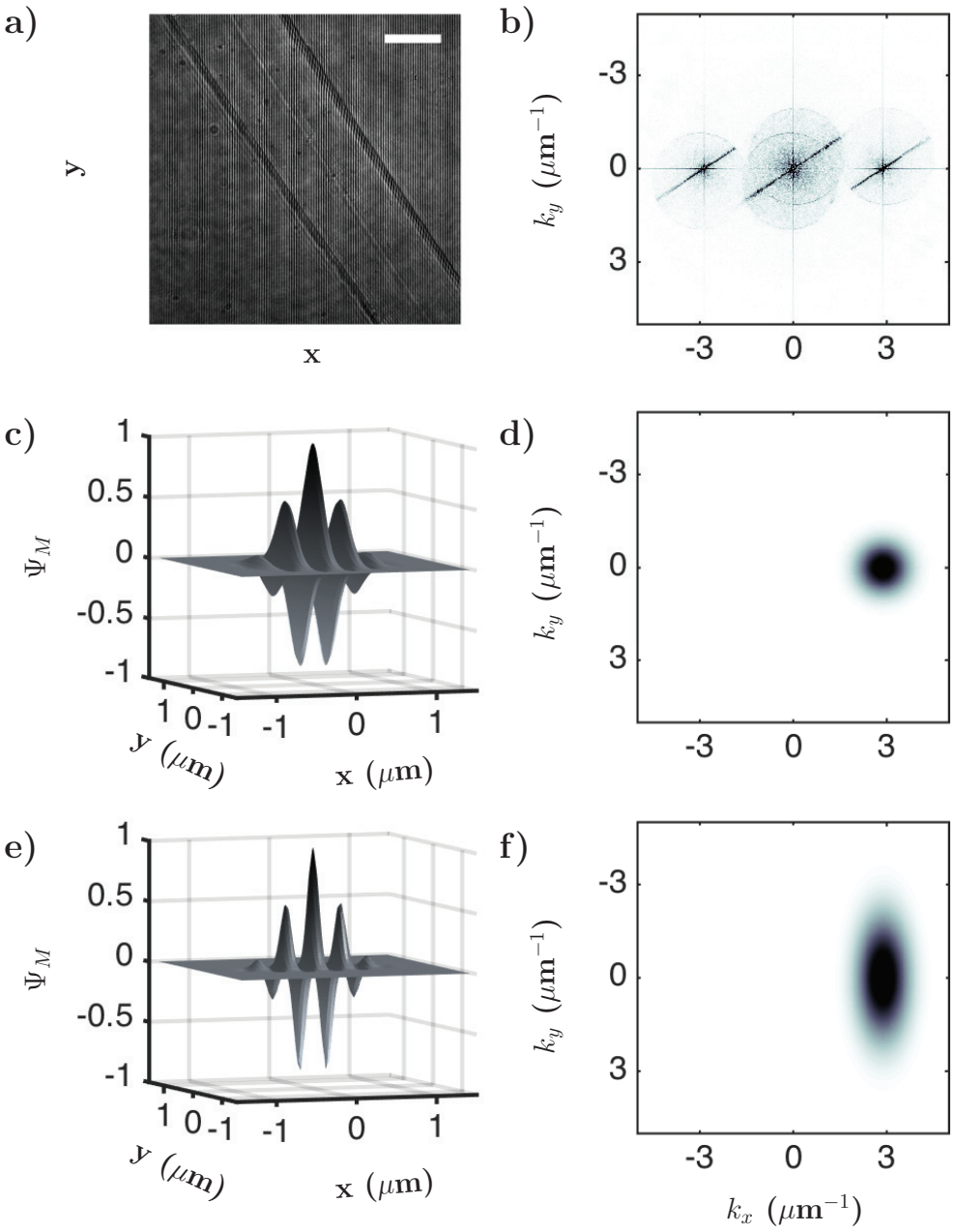

Figure 3.4 – **2D anisotropic Morlet wavelet.** (a) Untreated DPM image of a glass coverslip coated with polymer layer including a scratch in the diagonal direction. The scale bar is 10 μm. (c) Real part of the symmetric two-dimensional Morlet wavelet Ψ_M with $\epsilon = 1$. (e) Real part of the anisotropic two-dimensional Morlet wavelet Ψ_M with $\epsilon = 10$). (b,d,f) Modulus of the 2-D Fourier transforms of (a), (c), and (e), respectively.

A typical mother wavelet commonly used to detect localised and oriented features is the 2D Morlet wavelet:

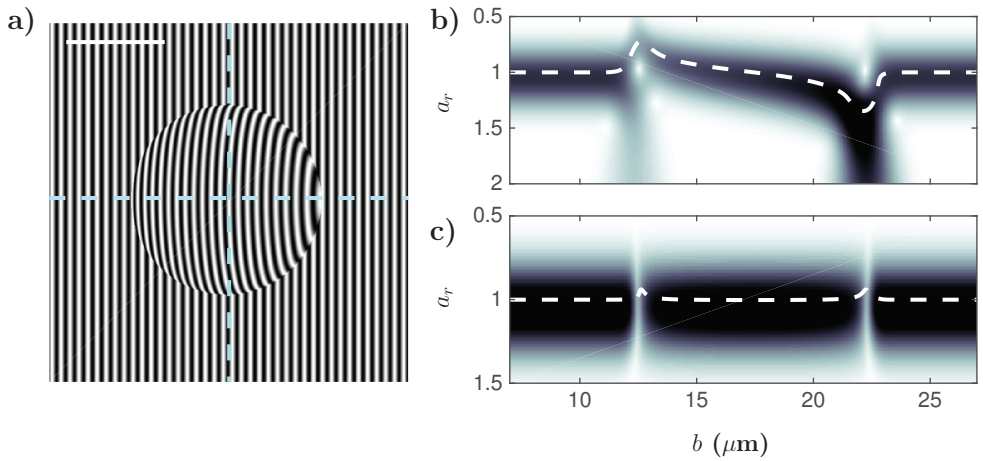

Figure 3.5 – **Wavelet transform modulus maxima.** (a) Theoretical DPM intensity image of a transparent microbead simulating a polystyrene bead immersed in glass matching oil. The scale bar is 5μm. (b) and (c) Modulus of the 2D continuous wavelet transform using the anisotropic Morlet wavelet ($\epsilon = 10$) on the horizontal (b) or vertical (c) section shown in (a) by a dashed blue line. a=1 corresponds to the fringe frequency f_g. The dashed white lines outline the WTMM. the colour coding goes from zero (white) to 0.8 (black).

$$\Psi_M(\mathbf{x}) = e^{i\mathbf{k}_0\cdot\vec{x}} e^{-\frac{1}{2}|A\mathbf{x}|^2} - e^{-\frac{1}{2}|A^{-1}\mathbf{k}_0|^2 - \frac{1}{2}|A^{-1}\mathbf{k}|^2} \tag{3.18}$$

The parameter k_0 is the wave vector and $A = diag[1, \epsilon^{1/2}]$ is a 2x2 anisotropic matrix ($\epsilon \geq 1$). We use here the anisotropic 2D continuous Morlet wavelet transform with anisotropy factor $\epsilon > 1$ to extract the phase of the fringe patterns obtained with the DPM[3], such as the one shown in Fig.3.4(a). The Morlet wavelet is a complex function; the modulus of the Morlet wavelet is a Gaussian, elongated in the x direction if $\epsilon < 1$, and its phase is constant along the direction orthogonal to $\mathbf{k}_o$, and linear in $\mathbf{x}$,mod$(2\pi/|k_0|)$, along the direction of $\mathbf{k}_0$. In Fourier space, the effective support of the function $\hat{\Psi}_M$ is an ellipse centered at $\mathbf{k}_0$ and elongated in the k_y direction (Fig.3.4). Since the ratio of the axes is equal to $\sqrt{\epsilon}$, the cone of the wavelet in Fourier space elongates along k_y direction as ϵ increases. This wavelet preferentially detects edges perpendicular to the y-direction.

The advantage of taking a smooth wavelet and not a simply circular window in Fourier space is not only to avoid the introduction of artificial oscillations produced by the sharp boundary of such a window, but also to have the ability to use the mathematical formalism of wavelet analysis, for instance the wavelet transform modulus maxima (WTMM). The WTMM can be computed at each spatial point $\mathbf{x}$ (Fig.3.5); it corresponds to the wavelet ridge skeleton [**?**] where the optical phase ϕ produced by the object fulfils the equation

$$\mathbf{k}_0 / a_r(\mathbf{b}) = f_g + \nabla\phi(\mathbf{b}) \tag{3.19}$$

[3]We have fixed the rotation angle $\theta = 0$ and chosen $\eta = 2$

where $a_r(\mathbf{b})$ is the scale at the wavelet ridge. It can be demonstrated analytically that the WTMM detection method is independent of the modulation intensity of the original fringe pattern. As a general remark, this wavelet-based method intrinsically eliminates background intensity variations that do not affect the fringe pattern modulations.

We discuss the efficiency of the 2D WTMM method on a model system made of a microbead particle (Fig.3.5a). Figure 3.5(b,c) shows a colour-coded representation of the modulus of the 2D CWT on the horizontal and vertical section shown in Fig.3.5(a). The horizontal section shows a strong deformation on the fringe pattern that is reflected on the detected scale a_r of the WTMM: on the left side of the bead the fringes are compressed (smaller scale a_r), whereas on the right side they are dilated(larger scale a_r). Close to the border of the bead, the CWT modulus shows two maxima, corresponding to the existence of two local frequencies slightly splitted apart from the carrier fringe frequency f_g, corresponding to $a = 1$ here. From this 2D CWT analysis, we can propose three methods for phase retrieval [228]:

- **Fourier filtering method (I).** It uses the 2D Morlet wavelet only as a Fourier filter, with a fixed scale $a = 1$ corresponding to the fringe pattern modulation f_g.
- **WTMM integral method (II).** It uses the WTMM method to compute the phase derivative of the fringe pattern (eq.3.19) and it makes an integration of this derivative along x.
- **WTMM argument method (III).** It uses the WTMM method to compute the new complex quantity $W_\Psi[b, a_r(\vec{b})]$ on the WTMM and takes its argument to compute the phase.

The three methods are compared on Fig. 3.6, for two values of the anisotropy factor ϵ. The Fourier filtering method does not succeed to recover the theoretical phase whatever ϵ (Fig.3.6a,b) because on the border of the bead the local frequency of the fringes is too far from the fringe carrier f_g. The WTMM integral method (Fig.3.6c,d) can estimate correctly the phase of the bead when ϵ is high enough (Fig.3.6d), but presents an accumulation of the computation errors on $\phi(\mathbf{x})$ when integrating along $\mathbf{x}$. When using an anisotropic morlet wavelet, the WTMM argument method succeeds to reproduce the theoretical phase of the bead with a 10^{-3} relative error on the phase (Fig.3.6e,f). The possibility to adjust the anisotropy of the wavelet is, therefore, important for analysing phase discontinuities. For more details on the phase extraction with the wavelet transform, please refer to the Appendix C.

3.2.4 Homogeneity in the field of view

As we are interested in the study of living cells, the typical imaging conditions consist of a thin closed chamber filled with liquid. The chamber is composed by two glass coverslips hold together by a spacer of a specific thickness. To test the typical intensity and phase variations that we may encounter on this conditions, we have imaged a chamber filled with only deionised water.

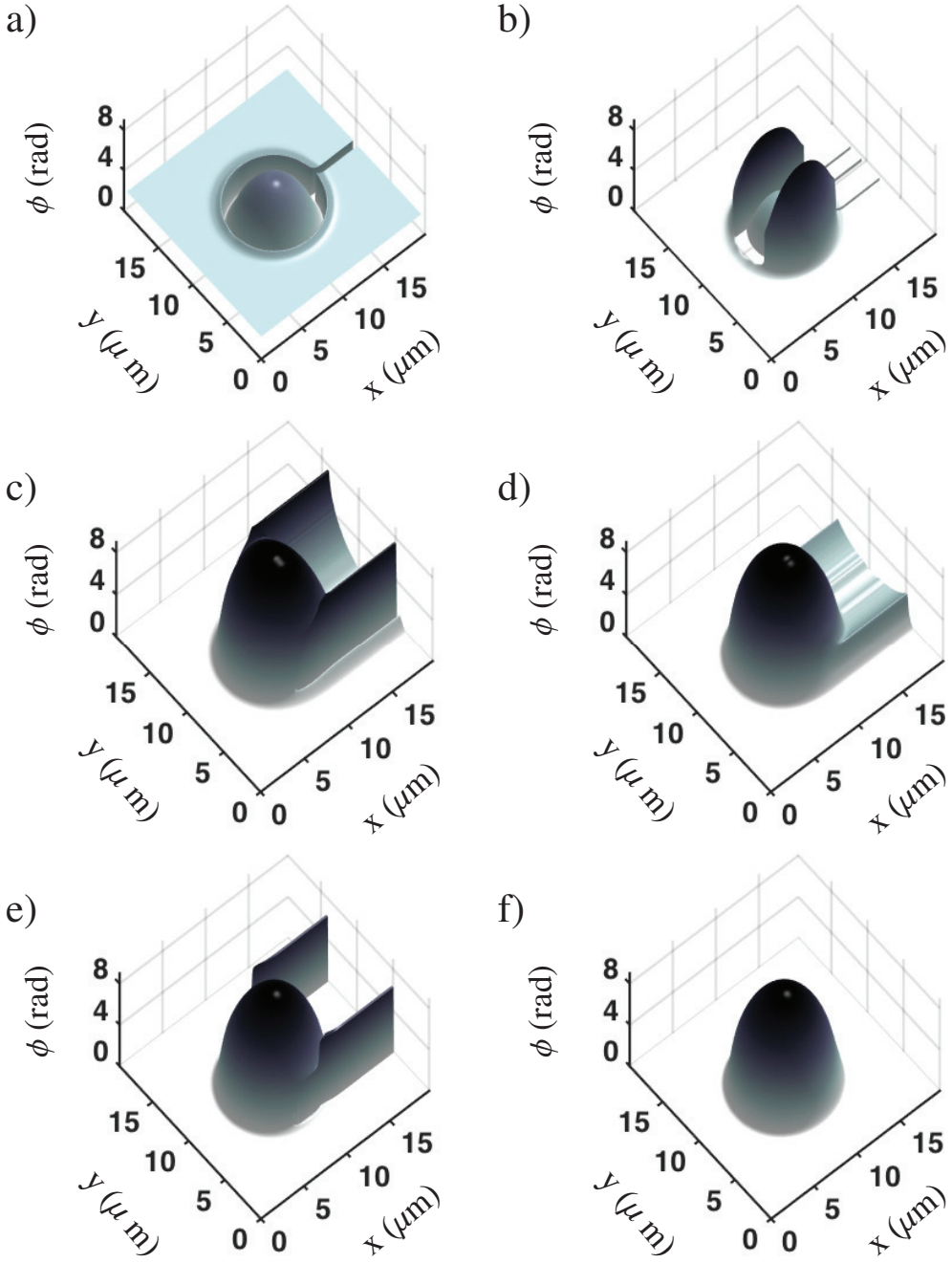

Figure 3.6 – **Phase extraction methods comparison.** Three-dimensional representation of the reconstructed phases from the fringe pattern of Fig.3.5(a), with methods **I** (a,b), **II** (c,d) and **III** (e,f). The left column (a,c,e) shows the phase profiles computed with the isotropic Morlet wavelet (ϵ=1), and the right column (b,d,f) with the anisotropic Morlet wavelet (ϵ=10).

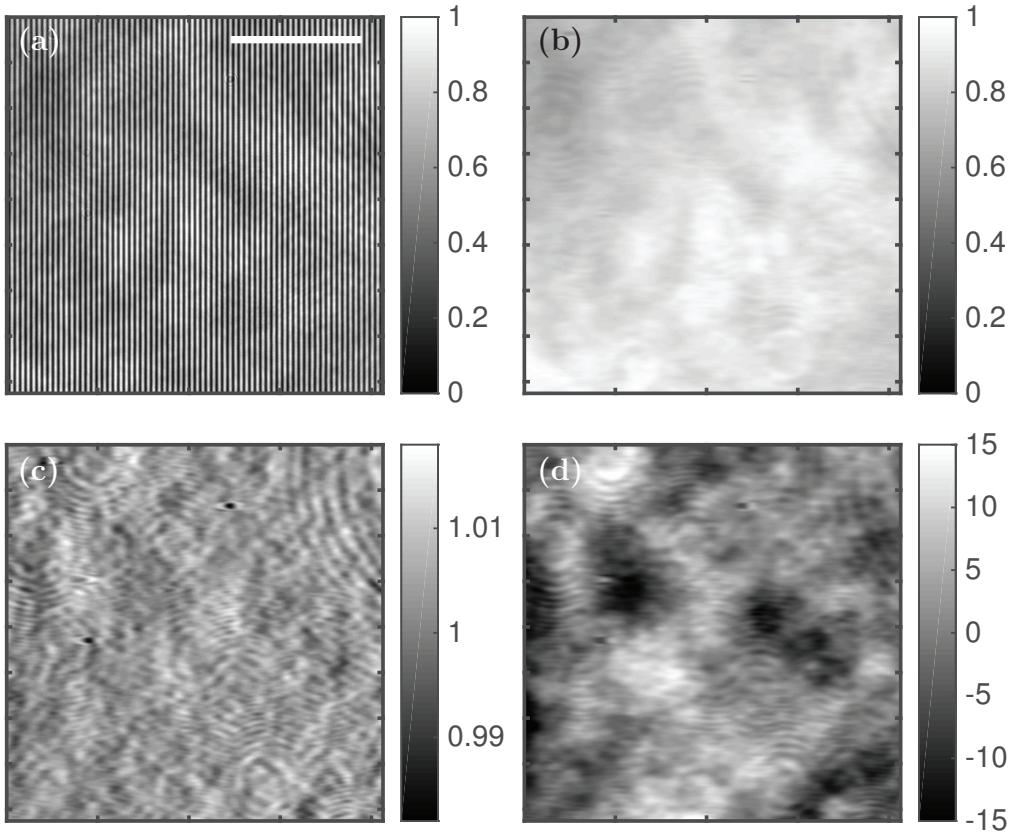

Figure 3.7 – **Homogeneity in a liquid chamber.** (a) DPM image of a chamber filled with deionised water. Scale bar is 10μm. (b) Filtered intensity image where the modulus of the wavelet transform maxima, WTMM, has been normalised and coded in grey scale. (c) WT scale image (a_r), where 1 corresponds to the fringe modulation. (d) OPD image Φ (in nm) .

Figure 3.7(a) shows a typical DPM image of a liquid chamber. We can note slight intensity variations that are independent of the fringe modulations, but no appreciable fringe deformation, consistent with the absence of any object. After applying the wavelet transform modulus maxima (WTMM) method for phase recovery (section 3.2.3), the resulting filtered intensity image (Fig.3.7b) seems to have damped the intensity variations. The distribution of the filtered intensity values (Fig.3.8b) shows a rather narrow range, with most of the values localised at the upper 20%. To compare with the intensity distribution of the original image (Fig.3.8a), we have fitted a gaussian curve (shown in blue in Fig.3.8a-b), and taken the width of the gaussian for each observed peak: $\delta_1 = 0.085, \delta_2 = 0.152, \delta_3 = 0.088$. We would have expected to find two well separated peaks for the intensity distribution of the original image, as we get from the fitted curves, however the intensity variations enlarge the second peak and provoke a slight asymmetry. The WTMM method manages to filter most of the intensity variations, with a small tail on the distribution seen on Fig.3.8(b), likely due to intensity variations close to those coming from the fringe modulation.

The fringe modulation, although perceived as constant on the DPM image (Fig.3.7a), shows

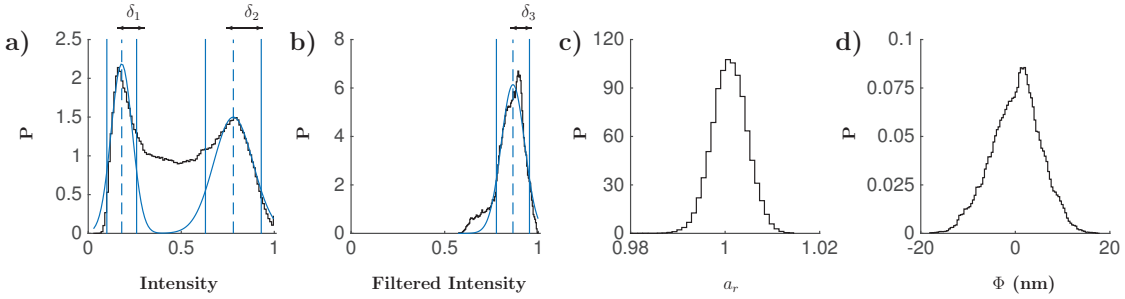

Figure 3.8 – **Values distribution for a liquid chamber.** Normalised distributions for the data shown in Fig.3.7: (a) normalised image intensity, (b) normalised filtered intensity (WTMM), (c) WT scale (a_r) and (d) OPD (Φ). The blue curves on (a) and (b) show the gaussian fitted curve, with the vertical dashed lines indicating the centre of the gaussian and the solid lines showing the gaussian widths, $\delta_1, \delta_2, \delta_3$.

small variations as shown by the WTMM scale image (Fig.3.7c). The scale of the WTMM (a_r) quantifies the relative frequency with respect to the carrier frequency f_g given by the grating ($a_r = 1$ for f_g). To capture as much of the image details as possible, we have used a scale step of $\Delta a = 0.001$ in the computation of the Wavelet Transform (WT). As expected, the scale values follow a normal distribution centred at $a_r = 1$ (Fig.3.8b), with a standard deviation of $3.9 \cdot 10^{-3}$. Such width distribution is given by the experimental phase fluctuations (sample and optical element defaults) as it is almost four times the fixed resolution step for the WT.

Finally, we evaluate the phase variations induced by the liquid chamber (Fig.3.7d) using the WTMM argument method (see section 3.2.3). The optical path difference (OPD) distribution (Fig.3.8c) is sligthly asymmetric with a standard deviation of 5.21 nm. If we assume that such variations of the OPD image are due to inhomogeneities on the liquid contained in the chamber (the thickness h is fixed by the spacer), that is, variations in the refractive index (Δn) of the medium inside the chamber, taking h=270.8 μm, we can estimate differences in Δn of $\sim 1.5 \cdot 10^{-4}$ for the total variation in Φ, roughly 40 nm, and of $\sim 1.9 \cdot 10^{-5}$ for the standard deviation.

We can conclude from the data shown in Fig.3.7 and Fig.3.8 that the liquid chamber that is normally used for imaging living cells is quite homogeneous within the field of view of our microscope, even if there is no special cleaning or treatment of the glass coverslips. Moreover, the use of the WTMM method to retrieve the optical phase decouples the impact of the intensity modulation on its computation [228]. Therefore, considering objects with an optical path depth ≥100 nm, the influence of the liquid chamber may be considered as a minor influence when measuring the OPD of the object of interest. Nevertheless, the recording of a reference image, although not necessary, can be particularly useful for removing different artefacts, for example, imperfections of the optical components and dust particles on their surfaces, as well as constant phase shifts in the image caused by a global tilt of the sample on the x-y plane.

3.3 Materials and methods: cell culture and sample preparation

3.3.1 Cell culture

TF1 cell line
The TF1 cell line (ATCC CRL-2003) was maintained at 1x10^5 cells/mL in RPMI-1640 medium, 10 % FCS and granulocyte macrophage colony-stimulating factor (GM-CSF, 10 ng/mL) (Sandoz Pharmaceuticals). Engineered TF1-GFP and TF1-BCR-ABL-GFP cell lines were obtained by transduction with an MSCV-based retroviral vector encoding either the enhanced green fluorescent protein cDNA alone (EGFP) as a control or the BCR/ABL-cDNA upstream from an IRES-eGFP sequence. EGFP+ TF1 cells were sorted using a Becton Dickinson FACSAria. For imaging, 65 μL of the solution were contained between two glass-coverslips glued by a GeneFrame (ThermoScientific). The data was taken within the next 15 minutes of preparation at room temperature $T \sim 22°$C, and taking a reference image of the background next to the area containing the cell. We thank Bastien Laperrousaz and Véronique Maguer-Satta (Centre de Recherche en Cancerologie de Lyon) for providing the cell samples.

C2C12 cell line
C2C12 mouse cells (ATCC CRL-1772TM) were grown in high glucose (4.5 g/L) Dulbecco's modified Eagle medium (DMEM), (GE Healthcare Life Science, Dominique Dutscher, France) supplemented with 20% fetal bovine serum (GE Healthcare Life Science) and 1% antibiotics (penicillin/streptamicine). Adherent myoblasts on 50 mm petri dishes with a glass bottom of 0.17 mm thickness were maintained at 37°C and 5% CO2 up to 60% confluence until they were used. The glass surface was not treated to avoid a too strong cell adhesion. We thank Laura Streppa (Physics lab, ENS Lyon) and Laurent Schaeffer (LBMC, ENS Lyon) for providing the cell samples.

HepG2 cell line
HepG2 cells (ATCC HB-8065) were grown in high glucose (4.5 g/L), with glutamine (GlutaMax, 0.862 g/L) and sodium pyruvate (0.11 g/L) Dulbecco's modified Eagle medium (DMEM), (GE Healthcare Life Science, Dominique Dutscher, France) supplemented with 20% fetal bovine serum (GE Healthcare Life Science) and 1% antibiotics (penicillin/streptamicine). Adherent hepatocytes on 50 mm petri dishes with a glass bottom of 0.17 mm thickness coated with collagen were maintained at 37°C and 5% CO2 up to 60% confluence until they were used.

Human primary cells
After informed consent in accordance with the Declaration of Helsinki and local ethics committee bylaws (from the Délégation à la recherche clinique des Hospices Civils de Lyon, Lyon, France), peripheral blood and bone marrow samples were obtained from chronic myelogeneous leukaemia patients. Mononuclear cells were separated using a Ficoll gradient (Bio-Whittaker) and were then subjected to CD34 immunomagnetic separation (Stemcell Technologies). The purity of the CD34$^+$ enriched fraction was checked by flow cytometry and was over 95% on average. Selected bulk CD34$^+$ cells were seeded at 6x10^5 cells/mL and cultured in serum-free Iscove's Modified Dulbecco's Medium (IMDM) (Invitrogen) in the presence of

15% BSA, Insulin and Transferrin (BIT) (Stemcell Technologies) supplemented with 10 ng/mL interleukin-6 (IL-6), 50 ng/mL stem cell factor (SCF), 10 ng/mL IL-11 and 10 ng/mL IL-3 (Peprotech). For imaging, 65 μL of the solution were poured between two glass-coverslips glued by a GeneFrame (ThermoScientific). The data was taken within the next 15 minutes of preparation at room temperature $T \sim 22^{\circ}$C, and taking a reference image of the background next to the area containing the cell. We thank Bastien Laperrousaz and Véronique Maguer-Satta (Centre de Recherche en Cancerologie de Lyon) for providing the cell samples.

Red Blood Cells
Red Blood Cells (RBCs) were extracted from blood samples of healthy donors or from patients with CML. The blood sample was centrifuged for 30 min at 900g at room temperature, and the pellet was recovered. The cells were sorted using the CD45 - marker. We thank Eve Mattei, Adriana Plesa, and Charles Dumontet (Centre d'hematologie des hôpitaux Lyon sud) for providing the cell samples.

3.3.2 Microbeads and polymer layers

Polystyrene beads preparation
1 μL of an aqueous solution containing polystyrene beads (FLUKA 72986, average size: 10μm, refractive index: 1.59) was diluted in 10 mL of deionised water. 250 μL of the dilution were deposited on a small petri dish with a glass bottom and let overnight in an oven at 70°sC to dry. Before imaging, 500 μL of glass index matching oil were added.

Low-refractive beads preparation
0.1 g of a powder containing polymethylsilsesquioxane microbeads (KOBO Diasphere KS1000, average size: 10μm, refractive index: 1.41) was added in 25 mL of ethanol. For imaging, 65 μm of the solution were contained between two glass-coverslips spaced by a GeneFrame (ThermoScientific).

PMMA layer preparation
A solution of 10% poly(methyl methacrylate) (PMMA, Sigma- Aldrich, France) in toluene was spin coated over a glass coverslip at a speed of 1000 rpm during 50 s. A time of 10 s was fixed to reach the nominal speed. After coating, the film was annealed for 1 h at 140°C. Prior to imaging, a portion of the PMMA layer was removed with a scalpel.

3.4 Imaging of model systems

In order to illustrate the performance of our DPM setup we will start by imaging two model examples: PMMA layers and polystyrene microbeads. In the case of PMMA layers, a coverslip has been coated with PMMA, and stripes of this layer have been scratched off using a scalpel. We get a structure that is almost unidimensional on the x-y plane, and with the thickness of the polymer layer imitating a step-like function. The polystyrene beads, on the contrary,

present a true three-dimensional structure. Their spherical shape is of particular importance as they will serve as a base model for comparing with cells in suspension.

3.4.1 PMMA layers

We imaged a sample of a PMMA layer covering a glass coverslip. The PMMA solution was spin coated on the coverslip to obtain a homogeneous thin layer. After annealing, a scalpel was used to remove the PMMA, resulting in thin stripes where the coverslip is no longer coated with the polymer (Fig.3.9a-c). As it can be seen on the WTMM images (Fig.3.9d-f), the intensity is quite inhomogeneous over the full image, very likely due to the beam shape. Therefore, we also take a reference image, recorded in the absence of any object at the image plane of the transmission microscope. The reference image is processed in the same manner as the sample image by the WTMM method. Hence, we retrieve the wavelet transform at the WTMM scale ($W_\Psi(\mathbf{b}, a_r)$) from the sample ($W_{\Psi,obj}$) , and from the background ($W_{\Psi,ref}$). To remove any effect due to the background, we normalise $W_{\Psi,obj}$ on its complex form by $W_{\Psi,ref}$,

$$W_{\Psi,r^-} = \frac{W_{\Psi,obj}(\mathbf{b}, a_r)}{W_{\Psi,ref}(\mathbf{b}, a_r)} \tag{3.20}$$

where the subscript r^- indicates that the wavelet transform has been normalised. From now on we will adopt this notation, such that the subscript r^- will mean that a reference image has been used to remove effects from the background, and that the WTMM method has been employed. Figure 3.9(g-i) shows the modulus of the normalised wavelet transform ($|W_{\Psi,r^-}|$) where the inhomogeneities on the intensity values have been drastically reduced, producing a highly uniform image of the sample.

Next, we look at the WT scale image (Fig.3.10a-c), and the OPD image (Fig.3.10d-f) obtained from the three different regions of the PMMA sample (Fig.3.9a-c). In general, the WTMM scale a_r is properly detected, with the exception of very irregular areas on the border of the second sample (Fig.3.10b). However, since we are retrieving the OPD by the WTMM argument method, that is, by taking the phase directly from W_{Ψ,r^-}, the difficulties on the detection of the scale a_r at the indicated points have a small effect on the OPD profile, affecting only a couple of pixels (Fig.3.10e), and thus they can be neglected.

Once we have retrieved the OPD map of the samples, we can estimate the thickness of the PMMA layer, assuming the refractive index is known. We have used a scanning surface plasmon microscope to measure the refractive index of a PMMA layer prepared from the same solution, but spin coated on a gold coated coverslip [232]. The measured value, $n = 1.488$ is in good agreement with the literature [233], resulting in a relative refractive index $\Delta n \sim 0.08$ for the DPM imaging, given that we are working in air.

Figure 3.11(a,c,e) shows the estimated thickness h for an horizontal cross section taken at the centre of the image of each of the three imaged areas of the PMMA layer (Fig.3.10d-e, respectively). We can easily see in these thickness profiles the step-like function we were expecting to obtain by 'cutting' the layer with a scalpel. We have also computed the thickness profile

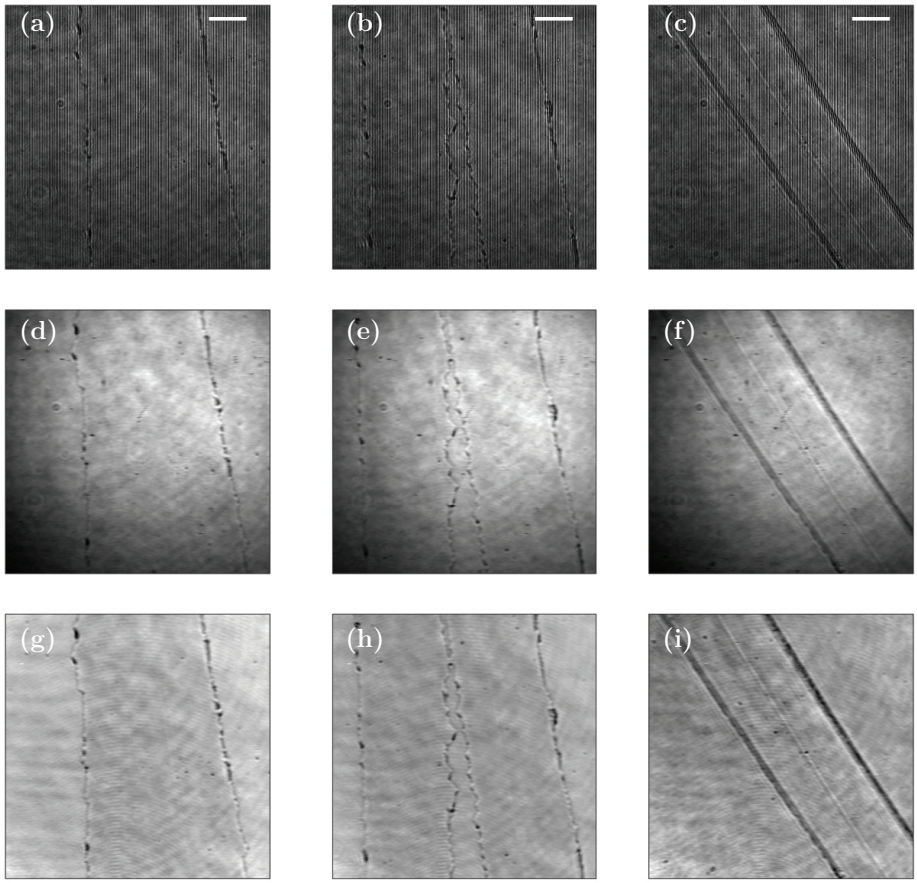

Figure 3.9 – **Imaging of PMMA layers.** (a-c) Untreated DPM image of three different regions from the same sample of a PMMA layer. Scale bar is 10 μm. (d-f) Equivalent intensity image where the WTMM ($|W_{\Psi,\mathrm{obj}}|$) has been colour coded in grey scale. (g-i) Normalised intensity image where the $|W_{\Psi,r^-}|$ has been colour coded in grey scale.

from the OPD retrieved with the Hilbert transform method (Fig.3.11a,c,e, dashed grey lines). In general we obtain almost the same thickness profile regardless of the method, as this sample fulfills the requirements for a good performance of the Hilbert transform method, i.e., low intensity variations and slow changes on the phase modulation.

To estimate the average thickness of the PMMA layer, we compute the distribution of the thickness values ($P(h)$). As it can be seen on figure 3.11(b,d,f), the distributions present two peaks, the first one corresponding to the part where the polymer has been scratched off, while the right peak corresponds to the thickness on the part of the image where we find the PMMA layer. The fact that the measured thickness on the stripped coverslip does not correspond to 0 nm, is because the measure done with the DPM system is relative, that is, the optical phase that we extract is in fact a difference in the optical path of the wavefront, and as such is not an absolute value. Thus, to get the actual thickness of the layer, we take the difference between the values $h(x, y)$ where the distribution is maxima for each peak, leading to an average layer

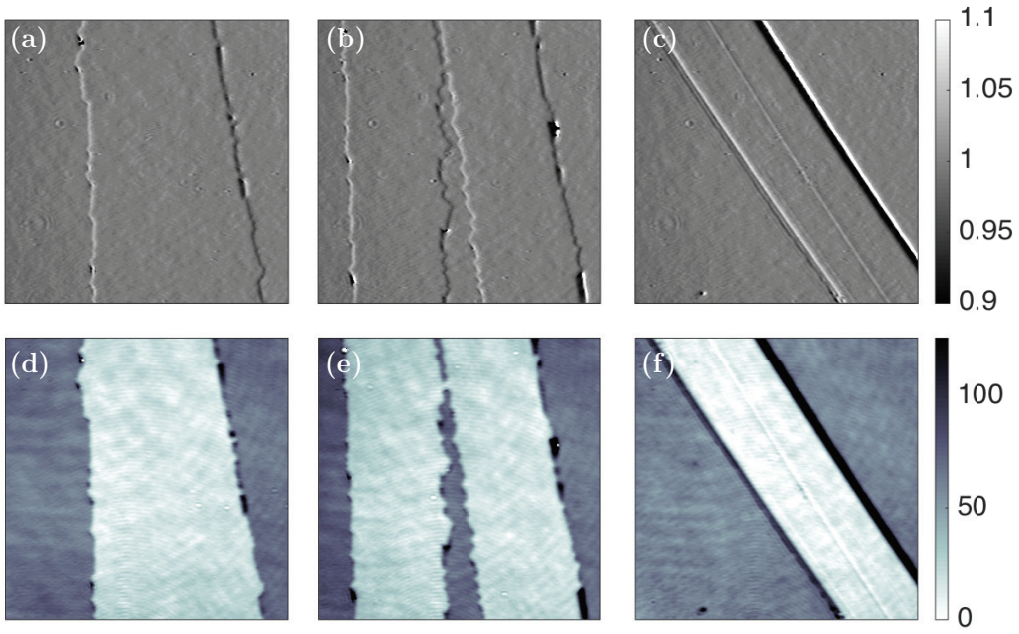

Figure 3.10 – **OPD maps of PMMA layers.** (a-c) WT scale image for the DPM images shown in Fig.3.9(a-c), where a_r has been colour coded in the same grey scale for the three images. (d-f) OPD images, where the background has been subtracted from the sample image, and $\Phi(x,y)$ (in nm) has been colour coded in the same range for the three images.

thickness of $< h >= 97$ nm ± 4 nm.

To verify if the thickness has been correctly estimated, we have used an Atomic Force Microscope to check the height of the same polymer layer sample that we have imaged with DPM. The height of the polymer has been measured on a region of 20x15 μm where the PMMA layer has been scratched off using a scalpel as before (Fig.3.12a). However, note that this region does not correspond strictly to those imaged with DPM, and thus can present some differences. Figure 3.12(b) shows the distribution of the height values $P(h)$, where we can identify the two peaks corresponding to the stripped coverslip and to the polymer, as in figure 3.11(b,d,f). Taking the difference on the positions of the maxima from both peaks, we get an average polymer layer of $< h >= 115$ nm ± 3 nm. Even if the averaged height value might seem far from the thickness estimated with DPM, the distribution of height is to some extend close to the ones obtained for the three regions imaged with DPM (Fig.3.11b,d,f), resulting in a overall good estimation of thickness for the polymer layer by DPM.

This simple example serves to illustrate how the OPD of the sample is measured with our DPM system and the necessity of image correction by the background, which can be easily done by taking a reference image. Moreover, it emphasises the advantages of looking at the changes in the phase rather than the intensity variations induced by the object (Fig.3.9). Beyond the information that we can obtain about the thickness and/or composition of the sample, the improved contrast on the x-y plane of the phase related images (Fig.3.10) can also improve

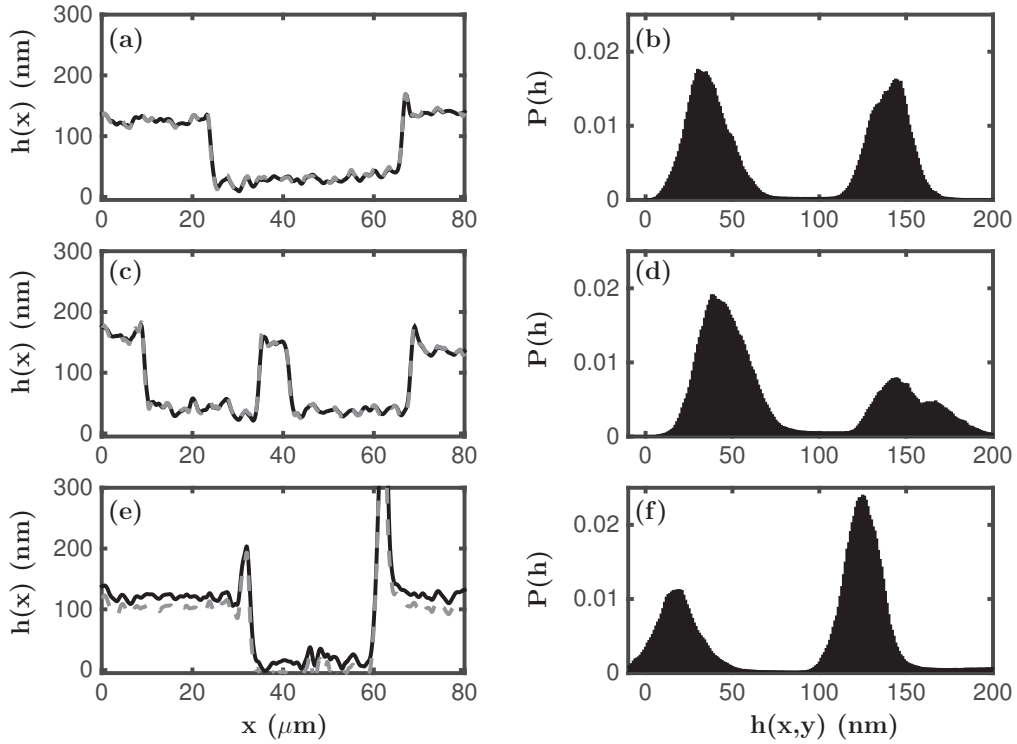

Figure 3.11 – **Thickness distribution from a PMMA layer.** (a,c,e) Thickness profile from horizontal sections taken at the middle of the image of the PMMA layers shown in Fig.3.10(d-f), respectively. Solid black line: WTMM method, dashed grey line: Hilbert transform method. The thickness has been computed from the OPD maps assuming a relative refractive index $\Delta n = 0.48$. (b,d,f) Normalised distribution of the thickness values for the PMMA layers shown in Fig.3.10(d-f), respectively.

the data treatment and analysis of the object at the image plane.

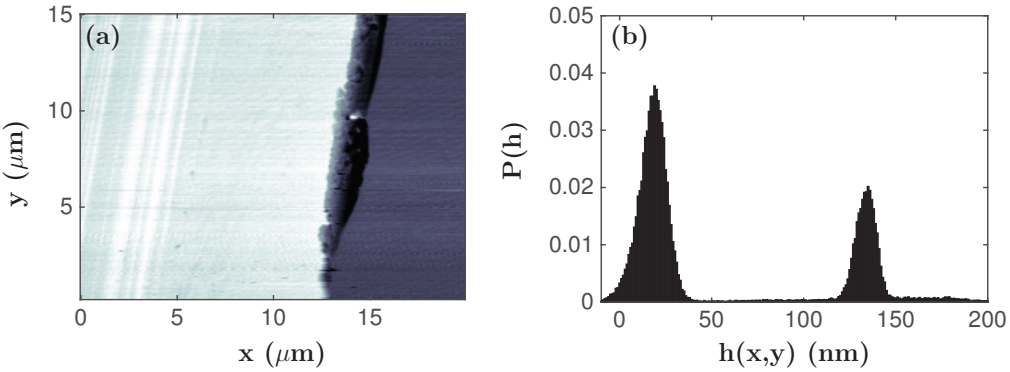

Figure 3.12 – **PMMA layer thickness measured by AFM.** (a) Height image measured by AFM, where the height $h(x, y)$ has been colour coded from 0 to 200 nm. (b) Normalised distribution of the height values for the PMMA layer showed in (a).

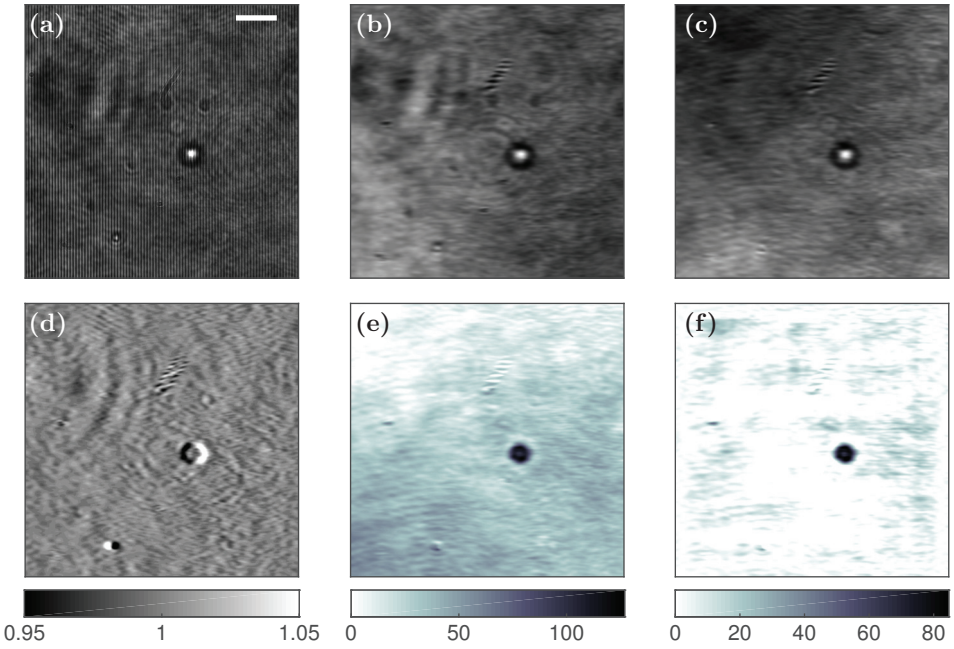

Figure 3.13 – **Imaging of small polystyrene beads.**(a) Untreated DPM image of a single polystyrene bead with a diameter of 1 μm. Scale bar is 5 μm. (b) WTMM image without removing the background. (c) WTMM normalised by the background, $|W_{\Psi,r^-}|$. (d) WT scale image. (e) OPD_{r^-} image, where $\Phi(x,y)$ (in nm) has been colour coded. (f) Corrected OPD_{r^-} image.

3.4.2 Polystyrene beads

The importance of studying micro-spheres relies on the similar geometry found on a large number of living cells, as is the case for several types of blood cells and living cells in suspension, who present a nearly spherical structure. The particular advantage of polymer beads is their homogeneous structure and rigidity. Additionally, the relative easy access to synthetic beads with controlled size and/or refractive index makes polymer beads a suitable model system to test the performance of our DPM setup under very similar conditions to those encountered on the study of living single cells.

We start by imaging small polystyrene beads. Notice that we use the term of 'small' relative to the expected average size of single cells ($\sim 5-10$ μm). Figure 3.13 shows a representative example of a small bead, with a nominative size of 1μm and refractive index $n = 1.59$. The high refractive index requires to immerse the bead in a medium with a close RI. We have chosen an oil with a refractive index $n_0 = 1.5167$ as the immersion medium, resulting in a relative RI of $\Delta n = 0.0733$ for the beads.

The bead DPM untreated image presents defects linked to particles deposed on the optical components and the camera window (Fig.3.13a-b). Such defects are successfully removed by taking a reference image, as it can be seen on Fig.3.13c, proving the utility of the WT normalisation step. Nevertheless, the reconstructed OPD image presents variations likely due to a global tilt in the sample (Fig.3.13e), leading to an overestimation of the bead OPD. To correct

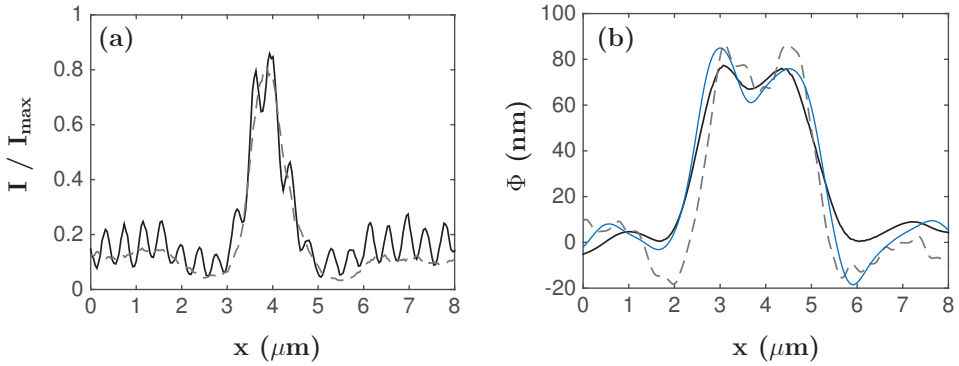

Figure 3.14 – **Intensity and phase profiles of a cross section from a small bead.** (a) Intensity profile for the horizontal (solid line) and vertical (dashed line) sections taken at the centre of the bead shown in Fig.3.13(a), where the intensity has been normalised by the maximum intensity of the image. (b) OPD profiles from the same sections as in (a), for the data shown in Fig.3.13(f). The blue line shows the horizontal OPD profile obtained with the Hilbert transform method.

this tilt, we perform a linear fit of the OPD profile. The data used for this purpose is the first and the last 50 pixels of each line, and we substract the fitted line from all the section. To take into account the tilt in both directions, we first perform the correction along the x direction for the full image, then for the y direction, and we repeat once more for the x direction, as we have noticed that in our data this direction always presents a bigger tilt. Figure 3.13(f) shows the corrected OPD image, where the bead OPD seems to be correctly estimated, giving a value of $\Phi \sim 80$ nm at the centre of the bead, which is in good agreement with the expected $\Phi = 73.33$ nm based on the nominative RI values of the bead and the immersion oil.

Note, however, that the bead appears slightly bigger than 1μm from the x-y plane. If we recall the spatial resolution of our system (Table 3.1), in the best case scenario, we can resolve objects down to a size of about 1 μm, so we are working at the limit of our microscope resolution. By looking at the untreated data from the vertical and horizontal cross sections that pass by the middle of the bead (Fig.3.14a), we can observe that the bead has a great effect on the intensity profile and, if we consider that the edge of the observed intensity peak corresponds to the border of the bead, it presents a diameter larger than 1 μm. The bead profile is further widened by the phase recovery process, as it can be seen from the OPD profile on Fig. 3.14(b). This widening is not linked to the width of the analysing wavelet, as we observe the same effect when using the Hilbert transform method (Fig. 3.14b, blue line). Besides the wider OPD profile (particularly on the x direction), we also note a local minima at the middle of the bead, reflecting either a defect on the bead, or more likely, a consequence of the limited amount of fringes used to detect the phase of the bead. Therefore, we confirm that, even if our DPM has a great resolution on the z axis and we can easily recover the OPD from small objects, the transverse resolution of our microscope with this magnification does not allow us to study objects on the order of 1 μm size.

We proceed now to image 'normal' sized polystyrene beads with the same RI as the small beads and with a nominative size of 10 μm. Figure 3.15 shows the WT scale image and the OPD image for a single bead in the same immersion oil. In this case we don't encounter prob-

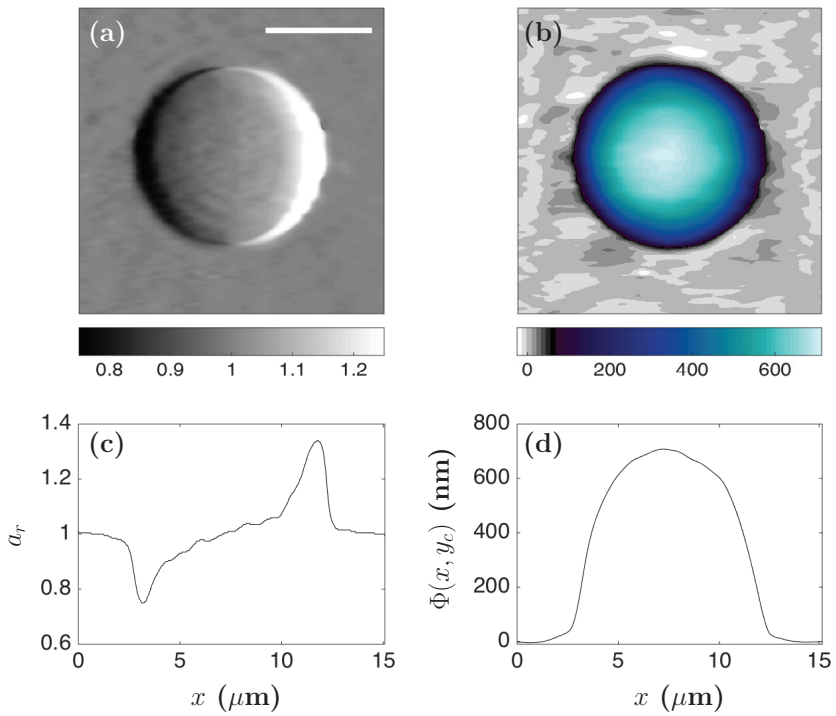

Figure 3.15 – **OPD image of a 10 μm polystyrene bead.** (a) WT scale image, where a_r has been colour coded in grey scale. Scale bar is 5 μm. (b) Corrected OPD$_{r^-}$ image, where $\Phi(x, y)$ (in nm) has been colour coded . (c-d) Horizontal sections taken at the middle of the bead in (a) and (b) respectively.

lems caused by the transverse resolution of the microscope, with a good agreement between the estimated size from the x-y plane and the z axis. On the x-y plane we take the points where the WT scale changes drastically with respect to 1, that is, the absolute minima and maxima , corresponding to ~ 9.4 μm for the section shown in Fig.3.15(c). On the z axis we estimate the bead thickness from the OPD profile, taking the nominative RI difference, at the centre of the bead we have then $\Phi \sim 700$ nm, which corresponds to $h = 9.55\mu$m, that is, an overestimation of 1.5% in the bead thickness. We can observe on Fig. 3.15 the homogeneity that we can typically find on these kind of polystyrene beads, showing a highly controlled size with very small defects on its spherical structure.

Finally, to test our DPM setup and phase recovery method on a more complex structure we look at aggregates of polystyrene beads. The difficulty on these type of images comes from the fringe deformation at the regions where the edges of the beads are in contact or very close to each other (Fig.3.16a). This is perhaps one of the most remarkable situations where we can observe the potential and the advantages of the WTMM method with the choice of an anisotropic wavelet. First of all, the anisotropy of the chosen mother wavelet allows a good detection of the fringe deformation even at the points of contact between beads (Fig.3.16b). Next, by taking a reference image we obtain a highly homogeneous intensity image $|W_{\Psi,r^-}|$ (Fig.3.16c), as well as an outstanding recovery of the OPD map (Fig.3.16d) , especially when we compare it to the OPD image obtained with the Hilbert transform method (Fig.3.16e). In

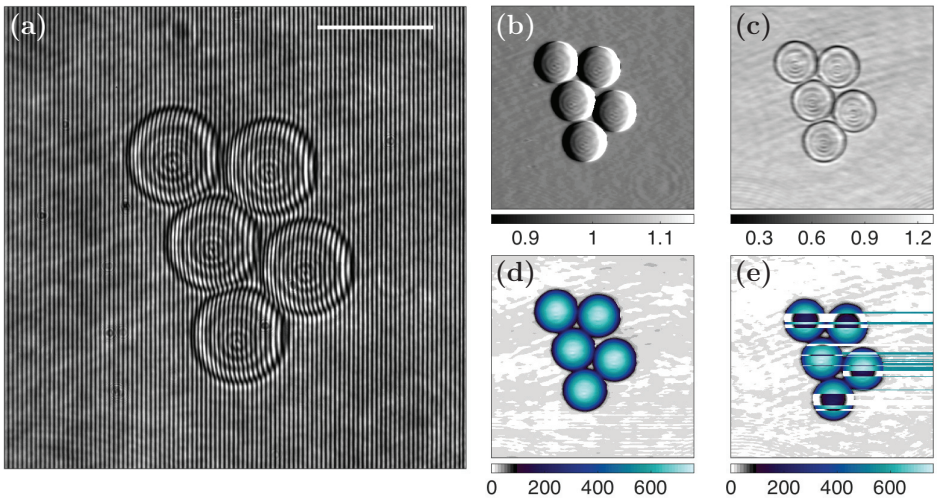

Figure 3.16 – **Imaging of 10 μm polystyrene beads aggregates.** (a) Untreated DPM image of an aggregate of polystyrene beads of 10 μm diameter. Scale bar is 10 μm. (b) WT scale image. (c) $|W_{\Psi,r^-}|$ (d) Corrected OPD_{r^-} image, where $\Phi(x,y)$ (in nm) has been colour coded. (e) Hilbert transform OPD image.

this case, the Hilbert method fails to properly recover the phase due to the intensity modulation produced by the light scattering by the bead. As established by Bedrosian [234], when the intensity modulation contains frequencies that overlap with the fringe carrier frequency f_g, the extraction of the phase with the Hilbert method is biased and leads to a false estimation. Indeed, from the Hilbert transform of a function $I(\vec{x}) = Q(\vec{x})\cos[f_g x + \phi(\vec{x})]$, we would like to recover a function like $Q(\vec{x})\sin[f_g x + \phi(\vec{x})]$ from which the phase could be computed straightforwardly. Bedrosian's theorem shows that this is workable only if the amplitude modulation $Q(\vec{x})$ does not contain frequencies that mix with the carrier frequency f_g. This condition is not experimentally satisfied as illustrated in Fig.3.16(a). In that case, when using the WTMM method, the WT offers the advantage of leading to a measure of the frequency from the WTMM that considerably reduces the effects of fringe modulation amplitude on phase retrieval [228].

3.5 Characterisation of living cells

Quantitative Phase Microscopy (QPM) has been proposed as a non-intrusive alternative to fluorescence microscopies to characterise the internal complexity of living cells. The distribution of refractive index of a living cell contributes in a non intuitive manner to its optical phase image and quite rarely can be inverted to recover its internal structure. The interpretation of the optical phase image of a living cell remains a difficult task because (i) we still have very little knowledge of the impact of its internal macromolecular complexes on the local refractive index and (ii) phase changes produced by light propagation through the sample are mixed with diffraction effects by the internal cell bodies. With the exception of red blood cells,

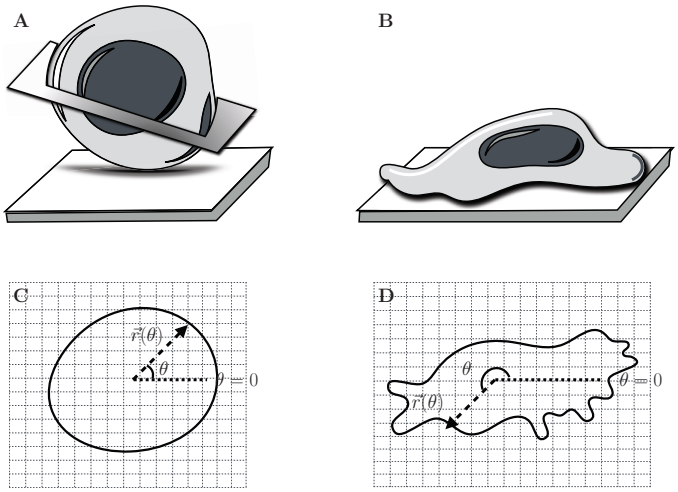

Figure 3.17 – **Geometrical description of living cells.** 3D sketch of suspended (A) or adherent (B) cells. Their geometrical characterisation is based on the 2D detected boundaries (C-D) from the OPD images obtained with the DPM. The plane in (A) shows the cross-section corresponding to the 2D projected contour shown in (C). The detected contours $\vec{r}(x, y)$ have been mapped to polar coordinates $\vec{r}(\theta)$, with θ increasing counterclockwise from 0° to 360°, and interpolated to increase the spatial resolution in r (dr=1.8 nm) and θ (dθ=4.4 $\cdot 10^{-3}$).

whose refractive index can be presupposed as homogeneous, the extraction of RIs from phase images often requires the use of rather complex algorithms. However, when the 3D shape of the cell can be established *a priori*, the computation of RIs from phase images is then possible. For instance, non adherent cells in liquid generally adopt a spherical shape, which facilitates the inversion problem. Because living cells are made of crowded macromolecules which may condensate or dilute at some stages of their fate to assist global processes as growth, cell division, invasion, apoptosis and migration, their internal structure bears a rather high level of complexity.

3.5.1 Geometrical parameters

Let's consider a living cell as a three-dimensional object. When they are imaged with DPM, what we observe is a two-dimensional projection on the x-y plane (Fig.3.17). We will focus mainly on the boundary that separates the cell from its surrounding medium, whom we will refer to as the cell outer boundary, as it contains all the information necessary to characterise the type of cells that we study. However, under certain circumstances, the cell interior may present other well defined structures, for example the nuclei, to whom we can also associate additional boundaries. The cell outer boundary represents a cross section of the cell which does not necessarily corresponds to an horizontal plane (Fig.3.17A), except in the rare case where the cell geometry is invariant by rotation around its vertical axis. Since the DPM image is an integration along the z axis of the whole cell body, we get an apparent 2D outer contour of the cell projection on the x-y plane that may differ from the real cell boundary. This means that, even tough the properties of the 2D outer contour are quite informative and useful for the cell characterisation, they do not provide a direct measure of the whole cell morphology.

Once the outer contour ($\vec{r}_0$) has been identified, we proceed to change the coordinate system from cartesian coordinates $\vec{r}(x,y)$, to polar coordinates $\vec{r}(\theta)$, and interpolating the data to avoid any bias from the xy grid (see section 3.6.3.a for details). We choose as origin the centre of mass of the cell with θ increasing counterclockwise from 0° to 360° (Fig.3.17C-D). Having $\vec{r}_i(\theta)$ for the detected contour, we can compute the following geometrical characteristics of the boundary:

- Perimeter (P_i) of the detected contour $\vec{r}_i$

$$P_i = \int_0^{2\pi} r_i(\theta) d\theta \tag{3.21}$$

- Area (A_i) of the surface enclosed by the detected contour $\vec{r}_i$, which in the case of the outer contour $\vec{r}_0$ is equivalent to the surface of the object's cross section

$$A_i = \frac{1}{2}\int_0^{2\pi} r_i^2(\theta) d\theta \tag{3.22}$$

- The aspect ratio (D_i) is a function of the largest diameter (d_{max}) and the smallest diameter orthogonal to it (d_{min})

$$D_i = \frac{d_{min}}{d_{max}} \tag{3.23}$$

  The normalised aspect ratio varies from approaching zero for a very elongated object, to one for a circle.

- The circularity index C_i computes the perimeter ratio of the detected contour $\vec{r}_i$ to the equivalent circle that covers the same surface

$$C_i = \frac{P_i}{P_{eq}} = \frac{\int_0^{2\pi} r_i(\theta)\, d\theta}{\left(2\pi \int_0^{2\pi} r_i^2(\theta)\, d\theta\right)^{1/2}} \tag{3.24}$$

  where P_{eq} is the perimeter of the equivalent circle. It is used only to characterise round-shaped cells.

- The signed curvature $\kappa_i(\theta)$ at each point $p(r,\theta)$ on the curve

$$\vec{\kappa}_i(\theta) = -\frac{1}{R_{oc}(\theta)}\, \hat{\mathbf{r}}_\mathbf{i}(\theta) \tag{3.25}$$

  where R_{oc} is the radius of the osculating circle at $p(r,\theta)$, and $\hat{\mathbf{r}}_\mathbf{i}(\theta)$ is the unit vector pointing from the origin towards $p(r,\theta)$. It is used to characterise only anisotropic cells, such as adherent cells.

3.5.2 Composition and refractive index

There are a few subtleties on the interpretation of the phase image of a living cell that are linked to its structure. As discussed on section 1.2 of the introductory chapter, a living cell

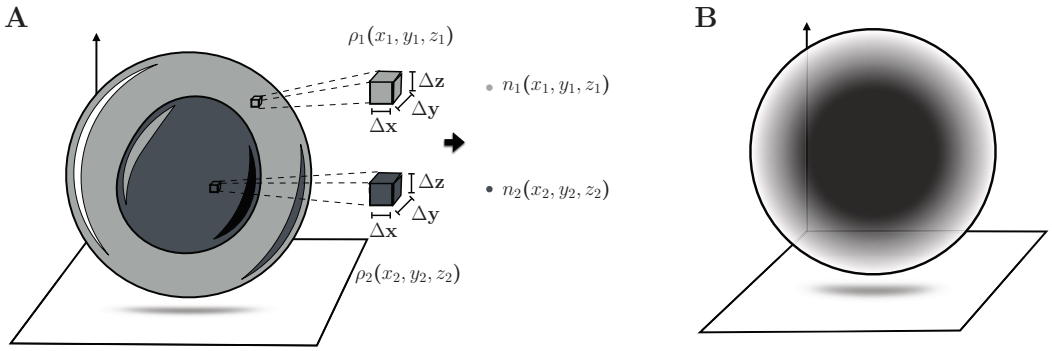

Figure 3.18 – **Cell composition and refractivity.** (A) Representation of the cell as a three-dimensional object. By taking small boxes of volume $\Delta V = \Delta x \Delta y \Delta z$ and density ρ_i, we can discretise the cell as N points of different refractive indices (n_i). (B) Scheme of a cell as an optical object, defined only by point-like particles of refractive index n_i, and taking as a physical barrier the plasma membrane.

has a highly complex and dynamical structure. Therefore, when integrating along the cell thickness (z-axis), it is quite unlikely that we can observe any structure delimited by smooth physical boundaries except, perhaps, for the nucleus. To have a more adequate interpretation of the cell OPD, it is important to relate the cell RI values based to its composition, i.e., its density (Fig.3.18). We represent the cell as a three-dimensional object, assuming that it has at least one physical barrier, which is the plasma membrane. This is the only component of the cell that we consider *a priori* to form a closed boundary (Fig.3.18B). For the cell interior we proceed as follows: we take a small volume ΔV_i at position (x_i, y_i, z_i) with $\Delta V_i = \Delta x_i \Delta y_i \Delta z_i$ and density ρ_i (Fig.3.18A); if we take N boxes of volume ΔV to cover the full range on the spatial coordinates (x, y, z), we can associate to each box i a point-like particle of refractive index n_i and position (x_i, y_i, z_i). The boundary of the object is precisely defined by an abrupt change in the RI slope at the interface between the interior and the exterior media. Because domain interfaces in biological matter will not be very sharp, we will rather consider them as transitory zones.

It has been shown that the refractive properties of the cell exhibit a strong dependence on the total cell protein concentration [235]

$$n_c(x, y) = n_w + \alpha_p \mathrm{C_p}(x, y) + \alpha_l \mathrm{C_l}(x, y) \tag{3.26}$$

where n_w is the RI of water, α is a constant know as the refractive index increment (in ml/g) that depends on the RI of the protein (p) or the lipidic (l) component, and C is the number of grams of dry protein (p) or lipids (l) per ml of solution. There is some uncertainty on the value of α, particularly when dealing with complex mixtures of proteins. It normally takes values between 0.18 ml/g and 0.21 ml/g, with $\alpha_p = 0.193$ ml/g for haemoglobin. However, even if the absolute value cannot be measured precisely, it is possible to use relative values for cell characterisation, taking an average value $\overline{\alpha}$ that takes into account the contribution from the protein and lipid components of the cell. For instance, by integrating the OPD over the projected cell area A_c,

$$M = \frac{1}{\overline{\alpha}} \int_{A_c} \Phi(x,y)\, dA \tag{3.27}$$

the total cell dry mass (M) of the the cell material can be used to quantify cell growth using the OPD images [222, 235].

3.5.3 Optical path depth

It has been shown that parameters based on the OPD profile of the cell are biologically relevant, serving for example, to characterise the cell cycle and as a marker for pathologies [236–238]. Even in the case of cells with an heterogeneous refractive index, it is possible to characterise them using OPD parameters without the need of uncoupling the cell thickness and refractive index, leading to the survey of the global cell morphology, its temporal evolution, and its alteration in pathologies. Note that in the case of round-shaped cells, such as cells in suspension, an isotropic OPD profile (Fig.3.19) may allow to define additional parameters accounting for the cell roundness and moreover, to uncouple the cell refractive index from the thickness, as we can assume a spherical shape and estimate the three-dimensional geometrical parameters. Next, we will introduce the parameters that we will employ for the characterisation of the morphology of single cells.

- Optical volume (V_Φ) of the cell . It is computed based on the OPD directly and does not require uncoupling of the cell thickness from the refractive index.

$$V_\Phi = \int_{A_c} \Phi(x,y)\, dA \tag{3.28}$$

  The optical volume is proportional to the dry mass by a factor $\overline{\alpha}$. While both quantities are equivalent, we will report both values as the optical volume has a more physical notion whereas the dry mass can be more intuitive.

- In the case of rounded shape cells, it is possible to estimate the average cell refractive index ($\langle \Delta n_c \rangle$), approximating the actual cell volume as the one of a sphere:

$$\langle \Delta n_c \rangle = \frac{V_\Phi}{V_c} \tag{3.29}$$

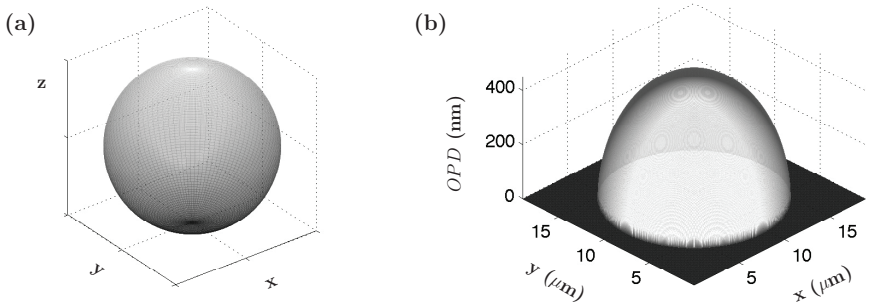

Figure 3.19 – **Characterisation based on the Optical Path Depth.** (a) 3D representation of a solid sphere. (b) OPD map from a solid sphere of radius $R = 5\mu$m and relative refractive index $\Delta n = 0.03$.

where V_c is the physical cell volume.

- The projected area to optical volume ratio (AV) describes the flatness of the cell

$$AV = \frac{A_0}{V_\Phi} \tag{3.30}$$

- Optical sphericity index (S_p), defined as the ratio of the projected area of the cell and the equivalent sphere with the same optical volume as the cell

$$S_p = \frac{A_0}{A_{eq}} = A_0 \left(\frac{3\sqrt{\pi}}{4} \frac{V_\Phi}{\Delta n_c} \right)^{-2/3} \tag{3.31}$$

where A_{eq} is the area of the equivalent sphere.

Additionally we can compute the OPD statistical parameters, such as the OPD kurtosis, skewness and variance. As these parameters are based on changes in the OPD values, they reflect structural changes.

- OPD variance (σ^2_Φ)

$$\sigma^2_\Phi = \frac{1}{n-1} \sum_{i=1}^{n} \left(\Phi_c(n) - \mu_{\Phi_c} \right)^2 \tag{3.32}$$

where $\Phi_c(n)$ is the cell OPD values with mean value μ_{Φ_c}.

- The OPD skewness (Sk_Φ) is a measurement of the lack of symmetry of the cell OPD values from their mean

$$Sk_\Phi = \sum_{i=1}^{n} \frac{\left(\Phi_c(n) - \mu_{\Phi_c} \right)^3}{\sigma^3_\Phi} \tag{3.33}$$

- The OPD kurtosis (Kr_Φ) measures whether the cell OPD distribution is more peaked or flatter

$$Kr_\Phi = \sum_{i=1}^{n} \frac{\left(\Phi_c(n) - \mu_{\Phi_c} \right)^4}{\sigma^4_\Phi} \tag{3.34}$$

3.6 Methods for the characterisation of the cell structure

3.6.1 Image segmentation for object identification

Almost all of the analysis done on the DPM images requires a first step of image segmentation or object identification, which consists in separating the object from the background in order to avoid the noise introduced by the surrounding medium that can lead to computation errors. Additionally, by identifying the object on the initial steps, we can significantly reduce the size of the area of the image analysed, which means less amount of stored data and faster computation times. An important remark is that we base the object segmentation algorithm on the phase data. As we have discussed before, the phase information is much more sensitive and offers a more precise identification of the object contour. This implies, however, that

	Parameter	Type of cells	Formula	Units
Geometry of the cross section	Perimeter	All	$P_i = \int_0^{2\pi} r(\theta) d\theta$	μm
	Area	All	$A_i = \frac{1}{2}\int_0^{2\pi} r_i^2(\theta) d\theta$	μm^2
	Aspect ratio	All	$D_i = \frac{d_{min}}{d_{max}}$	no units
	Circularity index	Round (suspended)	$C_i = \frac{\int_0^{2\pi} r_i(\theta)\, d\theta}{\left(2\pi \int_0^{2\pi} r_i^2(\theta)\, d\theta\right)^{1/2}}$	no units
	Curvature	Adherent	$\vec{\kappa}_i(\theta) = -\frac{1}{R_{oc}(\theta)}\, \hat{\mathbf{r}}_\mathbf{i}(\theta)$	μm^{-1}
Optical Path Difference	Optical Volume	All	$V_\Phi = \int_{A_c} \Phi(x,y)\, dA$	μm^3
	Area to Volume ratio	All	$AV = \frac{A_0}{V_\Phi}$	no units
	Sphericity	Round (suspended)	$S_p = A_0 \left(\frac{3\sqrt{\pi}}{4}\frac{V_\Phi}{\Delta n_c}\right)^{-2/3}$	no units
	OPD variance	All	$\sigma_\Phi^2 = \frac{1}{n-1}\sum_{i=1}^{n} \left(\Phi_c(n) - \mu_{\Phi_c}\right)^2$	μm^2
	OPD skewness	All	$Sk_\Phi = \sum_{i=1}^{n} \frac{\left(\Phi_c(n) - \mu_{\Phi_c}\right)^3}{\sigma_\Phi^3}$	no units
	OPD kurtosis	All	$Kr_\Phi = \sum_{i=1}^{n} \frac{\left(\Phi_c(n) - \mu_{\Phi_c}\right)^4}{\sigma_\Phi^4}$	no units
Composition	Cell dry mass	All	$M = \overline{\alpha}^{-1} V_\Phi$	pg
	Cell refractive index	Round (suspended)	$\langle \Delta n_c \rangle = \frac{V_\Phi}{V_c}$	no units

Table 3.2 – **Parameters used for the characterisation of living cells.**

the phase recovery algorithm is implemented on the whole image, limiting the optimisation of the computation time.

The segmentation method starts by taking the WT scale image (Fig.3.20a). Recall that the

WT scale is the scale a_r corresponding to the WTMM, and is directly related to the phase derivative. The advantage of taking the WT scale image and not the phase derivative relies on working with a less noisy data (although significantly discretised), and it avoids an extra step on the computation time, as we already obtain the WT scale image from the phase recovery with the WTMM method. We compute the histogram of the WT scale image (Fig.3.20b) where we find a prominent peak at $a_r \sim 1$, the highest the ratio between the background area and the object of our interest, the highest the peak. As the object contour will produce a modification on the fringe modulation, the value of a_r will be deviated from $a_r = 1$, so we search for the lowest and highest values of a_r in the histogram. We determine these values by dividing the histogram in two approximately equal parts, each one goes from one extreme towards the centre of the distribution, that is, the peak around a_r. For each half, we extract the part of the curve that covers only 10% of the area under the curve (Fig.3.20b, area in black). Then, we localise the pixels on the image that correspond to the selected values of a_r and we obtain a first coarse identification of the border of the object (Fig.3.20c).

We now consider the OPD image (Fig.3.20d), and to separate the object from the background, we take as a threshold value the minimum Φ value localised on the object border detected by the previous step (black contour in Fig.3.20d). Figure 3.20(e) shows the distribution of OPD values found on the border of the object, where we observe a rather inhomogeneous distribution, as compared to a single peak or hump that we will expect from a fine border. Indeed, if we use look at the part of the image identified as the object shown in Fig.3.20(f), we can see a very irregular contour that does not seem to correspond to the shape of our object (Fig.3.20a) and that includes some parts of the background. Therefore, we proceed to refine the border detection by using only the data contained in the identified are of the image by the previous step (Fig.3.20g,j), extending it by 5 pixels in each direction, and we repeat the proceeding by taking this time only 2.5% of the area under the curve of the WT scale histogram (Fig.3.20h). As seen in Fig.3.20(i), this time we do obtain a quite narrow border, with a single hump in the distribution of OPD values (Fig.3.20k). By taking the minimum OPD value found at the detected border, we do recover the expected object (Fig.3.20l).

3.6.2 Multi-sphere boundary model: phase isocontours

Spherical objects are one of the simplest cases of study because they are described by rather simple geometrical relations. In the following, three model examples will de discussed namely, a solid sphere, an empty cortex and a cortex filled with a denser medium (Fig.3.21a,b). We will also extend the model to a multi-layered spherical object (Fig.3.21c) to mimic spherical mono-nucleated cells. Later on, we will present the algorithm that we will employ to detect the contours of the internal structures on living hematopoietic stem cells, based on the distribution of their OPD values.

3.6.2.a One-dimensional case: Isotropic structures

In addition to the OPD profiles reconstructed from sections of the object, it is useful to describe the phase object from the distribution of the OPD values. As we are dealing with

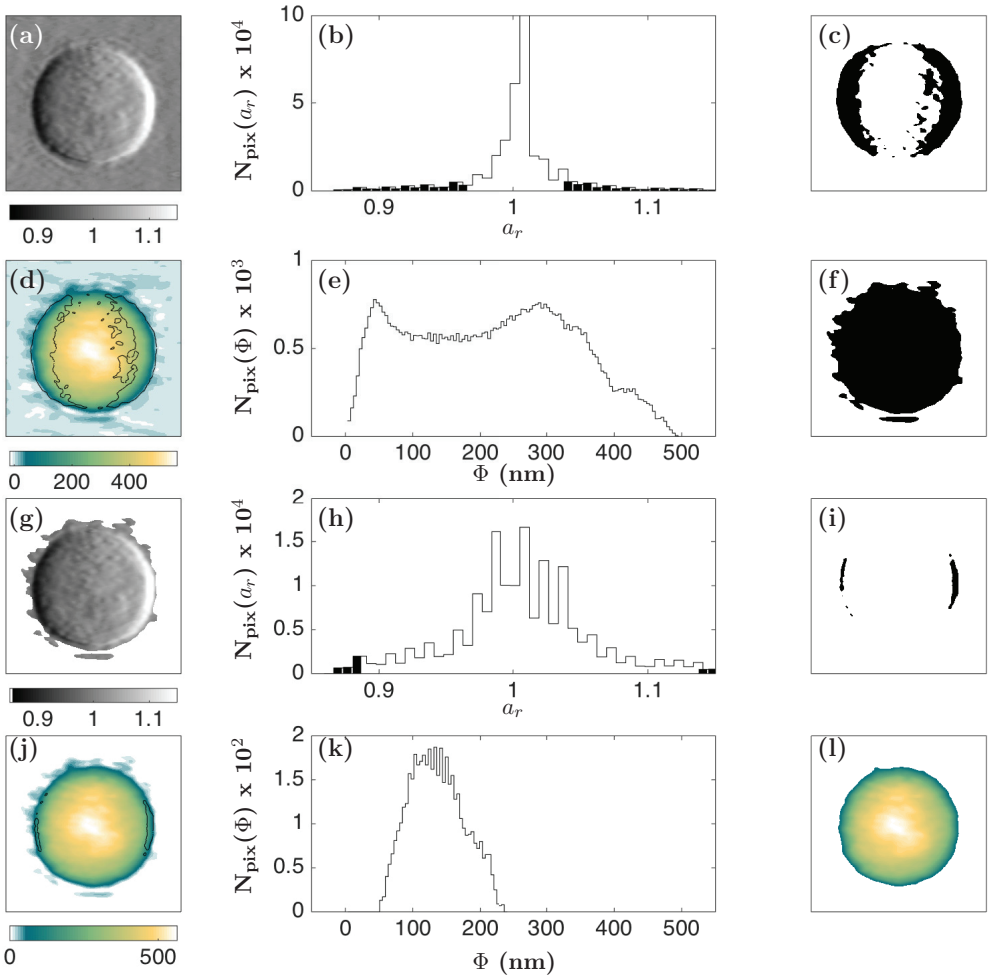

Figure 3.20 – **Image segmentation method for object identification.** (a) WT scale image of a living cell in suspension (TF1-GFP cell line). (b) Distribution of the WT scale values a_r, where N_{pix} is the number of pixels. The black line shows the full distribution, whereas the part of the curvedarkened, represents the values taken for the border detection. (c) Binary mask of the detected border. (d) OPD image of the same cell as in (a), where the black contour indicates the detected border. (e) Distribution of the OPD values corresponding to the detected border shown in (c). (f) Binary mask identifying the detected object. (g-j) Same as (a-d) for the refined step of the algorithm, where the input data has been chosen with the binary mask shown in (f). (l) Final OPD image containing only the object of interest.

isotropic spherical structures, it is convenient to use a polar coordinate system and take advantage of the symmetry of the object. due to the rotational symmetry, we can simply take a section at a certain angle θ. The OPD function $\Phi(x,y)$ then reduces to a one-dimensional function: $\Phi(\vec{r})$, where $\vec{r}$ is the radial vector taken at a given θ. The distribution of Φ, $P(\Phi)$, is given by:

$$P(\Phi) = \left| \frac{\mathrm{d}r(\Phi)}{\mathrm{d}\Phi} \right| \tag{3.35}$$

When a function f is monotonous (monotonously increasing or decreasing), the inverse of

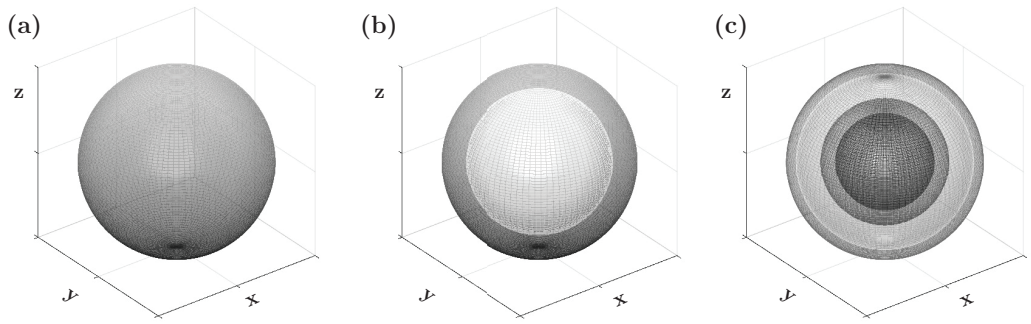

Figure 3.21 – **3D representation of the isotropic multilayer model structures:** a solid sphere (a), a cortex filled with an homogeneous medium (b), and a multi-sphere structure (c).

the derivative of f is actually the derivative of its reciprocal, so we can write $P(\Phi)$ as

$$P(\Phi) = \left| \left(\frac{\mathrm{d}\Phi}{\mathrm{d}r} \right)^{-1} \right| \tag{3.36}$$

Solid sphere

Consider a solid sphere centred at the origin, with a radius R and a relative refractive index (RI) Δn. The optical path depth (Φ) of the sphere at a given distance r to its centre is given by

$$\Phi(r) = \Delta n \left(2\sqrt{R^2 - r^2} \right), \quad r \geq 0 \tag{3.37}$$

where the term inside brackets corresponds to the total thickness of the sphere at the point r (Fig.3.22a). It follows that the derivative with respect of r (Fig.3.22b), is given by:

$$\frac{\mathrm{d}\Phi}{\mathrm{d}r} = -2\Delta n \frac{r}{\sqrt{R^2 - r^2}} \tag{3.38}$$

Substituting eq.(3.38) into eq.(3.36):

$$P(\Phi) = \left| \left(\frac{\mathrm{d}\Phi}{\mathrm{d}r_\Phi} \right)^{-1} \right| = \frac{1}{2\Delta n} \frac{\sqrt{R^2 - r_\Phi^2}}{r_\Phi} \tag{3.39}$$

with $r_\Phi = r(\Phi)$, (Fig.3.22c).

Cortex filled with a denser medium

Following the same computation method we obtain the distribution of OPD values for a structure composed of a cortex where the interior is filled with an homogeneous medium (homogeneous RI). The OPD function is given by:

$$\Phi(r) = \begin{cases} 2\Delta n_1 \sqrt{R_1^2 - r^2} & \text{for} \quad r > R_2 \\ 2\left[\Delta n_1 \sqrt{R_1^2 - r^2} + (\Delta n_2 - \Delta n_1) \sqrt{R_2^2 - r^2} \right] & \text{for} \quad r \leq R_2 \end{cases} \tag{3.40}$$

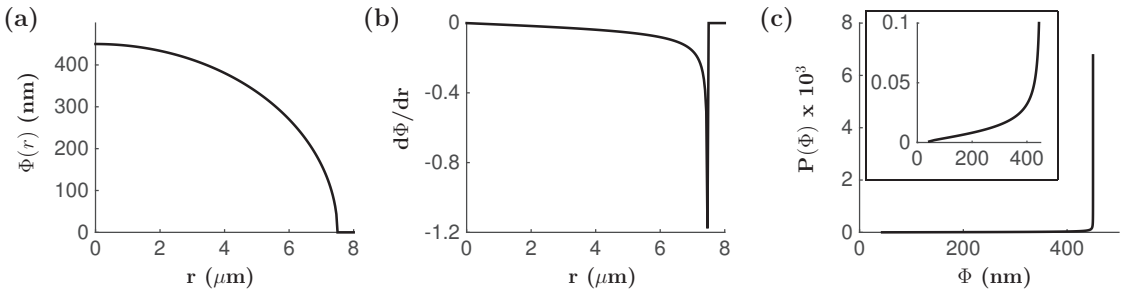

Figure 3.22 – **OPD profile and OPD distribution for the radial section of a solid sphere.** OPD section for a solid sphere (a), its derivative (b) and the inverse of the derivative (c), which is equivalent to the OPD distribution (eq.3.36). To appreciate how the distribution behaves, a zoom is shown on the inset. $R = 7.5\mu$m and $\Delta n = 0.03$.

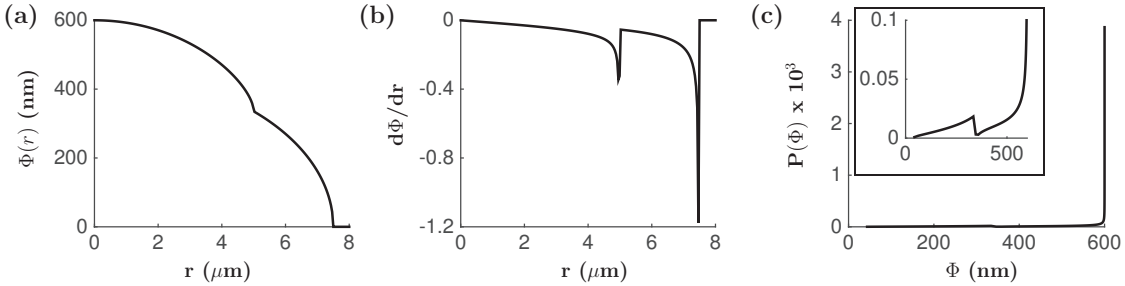

Figure 3.23 – **OPD profile and OPD distribution for the radial section of a cortex filled with a denser medium.** (a) OPD section for a cortex enclosing a denser material. $R_1 = 7.5\mu$m, $R_2 = 5\mu$m, $\Delta n_1 = 0.03$, and $\Delta n_2 = 0.045$. (b) OPD derivative from the section shown in (a). (d) Distribution of the OPD values.

where R_1 and R_2 are respectively the outer and inner boundaries of the cortex, with Δn_1 the relative RI of the cortex and Δn_2 of the interior, both with respect to the outer medium (Fig.3.23a). By inverting the the derivative of eq.(3.40) with respect to r (Fig.3.23b), we get the OPD distribution as

$$P(\Phi) = \begin{cases} \frac{1}{2\Delta n_1} \frac{\sqrt{R_1^2 - r^2}}{\Phi} & \text{for} \quad r > R_2 \\ \left| \frac{1}{2r_\Phi} \frac{\sqrt{R_1^2 - r_\Phi^2}\sqrt{R_2^2 - r_\Phi^2}}{(\Delta n_1 - \Delta n_2)\sqrt{R_1^2 - r_\Phi^2} - \Delta n_1 \sqrt{R_2^2 - r_\Phi^2}} \right| & \text{for} \quad r \leq R_2 \end{cases} \tag{3.41}$$

It is interesting to know how $P(\Phi)$ behaves at the centre of the sphere ($r_{b_0} = 0$) and at the boundaries, namely, $r_{b_1} = R_1$ and $r_{b_2} = R_2$, where the subscript b_i denotes the ith boundary. For this, we can estimate the limit when r_Φ tends to r_{b_i}:

$$\lim_{r_\Phi \to R_1} P(\Phi) = \lim_{r_\Phi \to R_2} P(\Phi) = 0 \tag{3.42}$$

and

$$\lim_{r_\Phi \to 0} P(\Phi) = +\infty \tag{3.43}$$

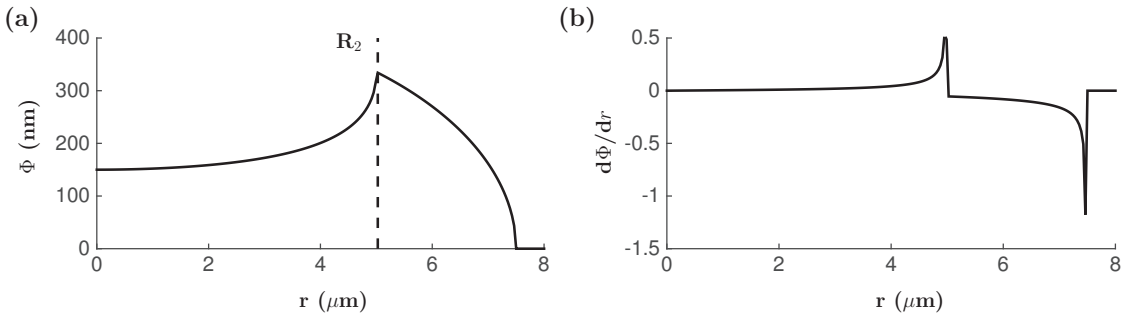

Figure 3.24 – **OPD profile for the radial section of an empty cortex.** (a) OPD section of an empty cortex, where the dashed line shows the inner boundary (R_2) of the cortex. (b) Derivative of the OPD section shown in (a)

Note that $\mathrm{d}\Phi/\mathrm{d}r$ presents a singularity that corresponds to the inner boundary of the cortex, R_2, that is, when $\Phi = \Phi(R_2)$ (Fig.3.23b), while the curve $P(\Phi)$ diverges toward the maximum value of Φ, as expected for a 'solid' sphere (Fig.3.23c and Fig.3.22c).

Empty cortex

As stated before, eq.(3.36) is only valid when the OPD function is monotonous, otherwise to perform the inversion, the OPD function must be partitioned into regions that are monotonous increasing or decreasing. This is the case when we want to compute the OPD distribution for an empty cortex. In fact, when we talk here about an empty cortex, we are truly referring to a cortex whose interior medium has the same refractive index as the outer medium. Since the OPD depends on the relative RI (Δn_i), then the cortex can be considered of as an empty structure. With $\Delta n_2 = 0$, eq.(3.40) reduces to

$$\Phi(r) = \begin{cases} 2\Delta n_1 \sqrt{R_1^2 - r_\Phi^2} & \text{for} \quad r > R_2 \\ 2\Delta n_1 \left[\sqrt{R_1^2 - r_\Phi^2} - \sqrt{R_2^2 - r_\Phi^2} \right] & \text{for} \quad r \leq R_2 \end{cases} \tag{3.44}$$

Then, the total distribution of OPD values will be simply the summation of the distributions computed for each sub-interval (Fig.3.25). From eq.(3.41) we have for $\Delta n_2 = 0$:

$$P(\Phi) = \begin{cases} \left| \frac{1}{2\Delta n_1} \frac{\sqrt{R_1^2 - r_\Phi^2}}{r_\Phi} \right| & \text{for} \quad r > R_2 \\ \left| \frac{1}{2\Delta n_1 r_\Phi} \frac{\sqrt{R_1^2 - r_\Phi^2}\sqrt{R_2^2 - r_\Phi^2}}{\sqrt{R_1^2 - r_\Phi^2} - \sqrt{R_2^2 - r_\Phi^2}} \right| & \text{for} \quad r \leq R_2 \end{cases} \tag{3.45}$$

As before, we compute the limit as r tends to R_2 since it is the boundary that interests us the most:

$$\lim_{r_\Phi \to R_2^+} P(\Phi) = \frac{\sqrt{R_1^2 - R_2^2}}{2\Delta n_1 R_2} \tag{3.46}$$

In comparison to a cortex filled with a denser medium, we can associate a different feature of the distribution to the inner boundary of the cortex by noting that $\Phi(R_2) = \Phi_{max}$ (Fig.3.25a), and knowing from eq.(3.46) that $P(\Phi)$ tends to a constant value when $r \to R_2$.

3.6.2.b Phase profiles on 2D

Isotropic structures

We will now extend the discussion made above for OPD radial sections to two-dimensional OPD maps. The distribution of OPD values is given by the product of the probability $P(\Phi)$ with the projected area of the surface which has this OPD ($\S_\Phi$)

$$P_{2D}(\Phi) = P(\Phi) \int_{S_\Phi} r \, d\theta \, dr \tag{3.47}$$

As the OPD functions described above remain valid, the missing element is now the determination of the projected area. It is necessary then to define an angular variable θ in addition to the already existent radial variable r. In the case of isotropic structures, $\Delta\theta = 2\pi$, and recalling eq.(3.36), eq.(3.47) becomes for a band of radius r and width dr

$$P_{(r,dr)}(\Phi) = 2\pi r \left| \left(\frac{\mathrm{d}\Phi}{\mathrm{d}r} \right)^{-1} \right| \tag{3.48}$$

From eq.(3.48) we can see that in order to obtain the OPD distributions in the two-dimensional case, we use $P(\Phi)$ for the 1D sections discussed above, and multiply it by a factor of $2\pi r$, which eliminates the $1/r$ trend found in all the distributions (Fig.3.26d-f). This will, in general, remove the divergence of $P(\Phi)$ at Φ close to Φ_{max}, the effect being more notorious for the OPD distribution of a solid sphere. Substituting the OPD function, $\Phi(r)$ for a solid sphere (eq.3.37) in eq.(3.48), we obtain:

$$P(\Phi) = \frac{\pi}{\Delta n} \sqrt{R^2 - r^2} \tag{3.49}$$

Since $\sqrt{R^2 - r^2} = \frac{\Phi}{2\Delta n}$,

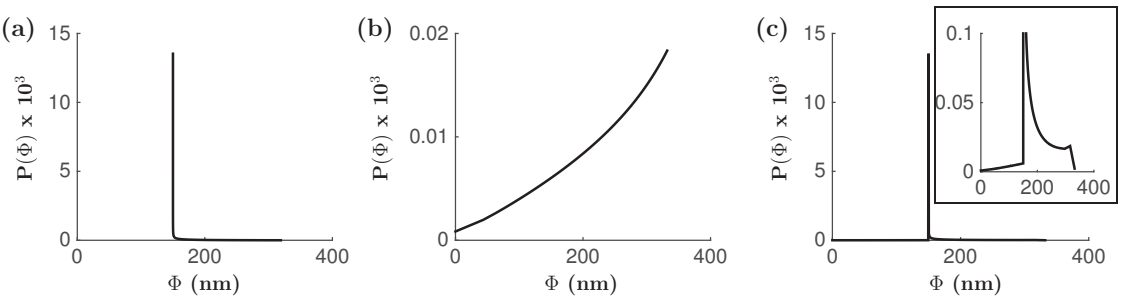

Figure 3.25 – **OPD distribution for the radial section of an empty cortex.**. OPD distribution of an empty cortex for the range $r \leq R_2$ (a) and $r > R_2$ (b). (c) Sum of the two distributions shown in (a) and (b). The inset shows a zoom on the curve.

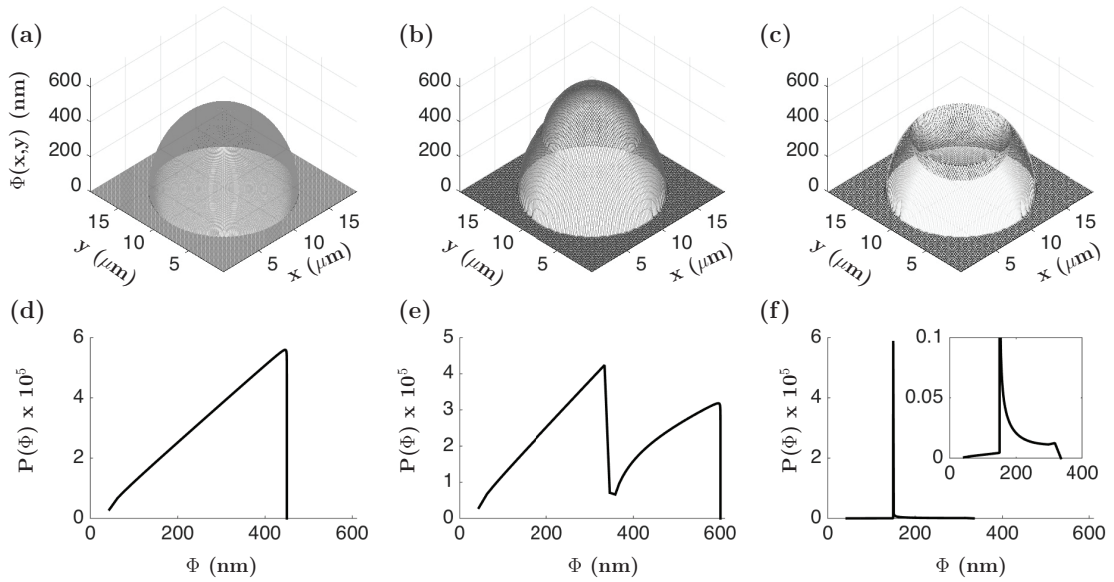

Figure 3.26 – **OPD distributions from two-dimensional OPD maps.** OPD distribution (d-f) of the complete OPD map (a-c) from a solid sphere (a,d), a cortex filled with a denser medium (b,e), and an empty cortex (c,f).

$$P(\Phi) = \frac{\pi}{2\Delta n^2}\Phi \tag{3.50}$$

showing that the 2D distribution behaves as a linear function of Φ (Fig.3.26d).

It is now straightforward to compute the distribution of the OPD values for a multi-sphere structure. The importance of such structure relies on the possibility of modelling a living spherical cell as a multi-layered object, the layers being defined by regions with the same average refractive index. The considerations and implications of this model will be discussed in detail on section 3.6.2.c. Therefore, in the following we will only describe the OPD function and the distribution of its values, and more importantly, we will explain how is it possible to detect the inner boundaries of the object by looking at the $P(\Phi)$ probability distribution.

We build our object by including four concentrical layers as follows: an outer cortex (Δn_1) filled with a slightly less dense medium (Δn_2), and immersed on the inside another cortex (Δn_3) filled with a denser medium (Δn_4)(Fig.3.27a), such that

$$\begin{aligned} R_1 \geq r > R_2, &\quad \Delta n = \Delta n_1 \\ R_2 \geq r > R_3, &\quad \Delta n = \Delta n_2 \\ R_3 \geq r > R_4, &\quad \Delta n = \Delta n_3 \\ R_4 \geq r \geq 0, &\quad \Delta n = \Delta n_4 \end{aligned}$$

with

$$0 \leq \Delta n_2 < \Delta n_1 \leq \Delta n_3 < \Delta n_4$$

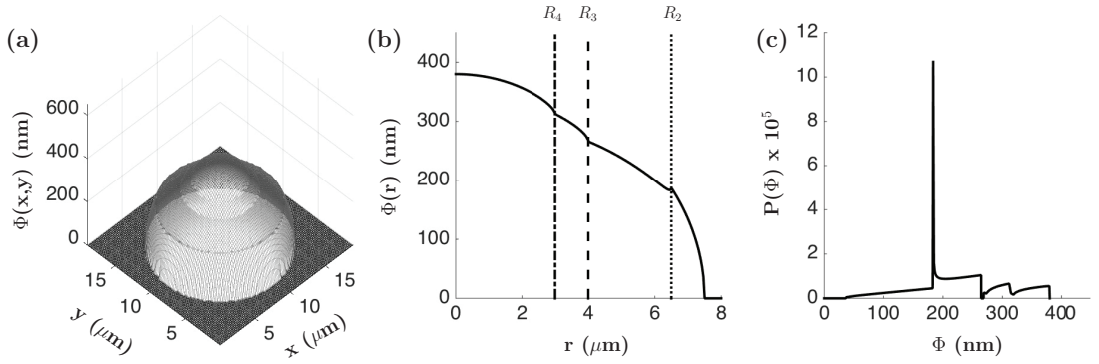

Figure 3.27 – **OPD map and OPD distribution of a multi-sphere structure.**(a) OPD map of a multi-sphere structure as the one represented in Fig.3.21c. With $R_1 = 7.5\mu m, R_2 = 6.5\mu m, R_3 = 4\mu m, R_4 = 3\mu m$; $\Delta n_0 = 0.025, \Delta n_1 = 0.02, \Delta n_2 = 0.025, \Delta n_3 = 0.03$. (b) Radial OPD section, where the vertical lines separate the subintervals required to invert the function and compute the OPD distribution. (c) OPD distribution for the complete 2D OPD profile, where $P(\Phi)$ has been computed as the sum of the distributions of each subinterval separated on (b).

The OPD function $\Phi(r)$ can be written as:

$$\Phi(r) = 2\sum_{i=1}^{3} \Delta n_i \left(\sqrt{R_i^2 - r^2} - \sqrt{R_{i+1}^2 - r^2} \right) + 2\Delta n_4 \sqrt{R_4^2 - r^2} \tag{3.51}$$

Following the same method used to compute the distribution of an empty cortex, we can obtain the total probability function $P(\Phi)$ as the sum of the distributions for each interval (Fig.3.27c). Note that, as before, each of the inner boundaries (R_2, R_3, R_4) will be linked to a feature characteristic on the OPD distribution curve: $P(\Phi)$ diverges when the boundary delimitates a region of lower refractive index, and $P(\Phi) \to 0$ at each of the other boundaries. Thus, we can expect that, if we have enough resolution, we can identify such boundaries by looking for these features of the OPD distribution.

Asymmetric structures

One important remark about the detection of isophase contours based on the OPD distribution is its validity for asymmetric structures. So far, we have shown that it is possible to identify the inner borders of a multi-shell structure based solely on the features of its OPD distribution. This requires for the multiple spheres to be concentrical, such that there is an isophase contour that can be associated to each of the spheres boundaries. However, as soon as there is a displacement on the positioning of one of the inner spheres, the above description is no longer true: there will be no isophase contour that can be associated directly to the border of the inner sphere. Figure 3.28(a) and (b) shows respectively, the OPD profiles along the x and y direction for a structure composed of two non-concentrical spheres. The solid black lines in Fig.3.28 correspond to a structure whose inner sphere has been displaced a distance of 1μm along the y direction ($\theta = \pi/2$) (Fig.3.28b). As expected, this shift causes a change on the value of Φ corresponding to the border of the sphere, which is more noticeable on the y direction than on the x direction (Fig.3.28a). When the displacement of the sphere is more important (2.75μm), it can cause a shift on the OPD values along both directions, even if the

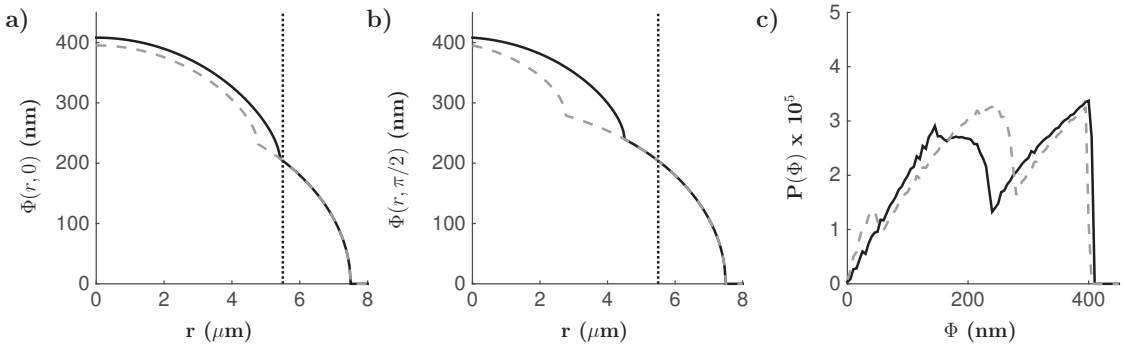

Figure 3.28 – **OPD distribution of an asymmetric multi-shell structure.** (a) OPD radial profile along the x direction ($\theta = 0$) for a bi-sphere structure, where the centre of the inner sphere is displaced with $r_{c_2} = 1\mu$m (black solid line) or $r_{c_2} = 2.75\mu$m (dashed grey line). The vertical dotted line indicates the position of the border of the inner sphere for the concentrical case (isotropic structure). (b) Same as (a) for a section along the y direction ($\theta = \pi/2$). (c) OPD distribution for the complete 2D OPD profile, where $P(\Phi)$ has been computed using the function `histc` of MATLAB. $R_1 = 7.5\mu$m, $R_2 = 5.5\mu$m, $\Delta n_1 = 0.02$, $\Delta n_2 = 0.03$.

position changed only in one (Fig.3.28a-b, dashed grey lines). This effect propagates to the OPD distribution (Fig.3.28c), shifting the local minima and even causing the appearance of an additional local minima (Fig.3.28c, dashed grey line), leading to a biased or false detection of the inner boundaries of the multi-sphere structure.

Nevertheless, if we detect a pronounced local minima on the OPD distribution of the 2D OPD profile, we will relate it to the boundary of a structural domain with a similar relative refractive index and, if this contour on the x-y plane possesses a high degree of circularity, and is centred at less than 1μm away from the cell centre, we will make the assumption that it is a nearly concentrical sphere, and thus, the multi-sphere model presented above can be applied.

3.6.2.c Application of the multi-shell model to single cells.

The detection of intracellular boundaries based on the multi-shell model proposed above is relatively fast and easy to implement, as it requires only the detection of local minima present on the curve of the distribution of OPD values. The difficulty comes, as in all the minima/-maxima detection of experimental curves, on the correct data sampling and denoising. The data sampling in our case, refers to the bin width to compute the histogram from the OPD image. We choose the bin width to sample the full range of the data with 400 bins, on a typical spherical cell, Φ has a range between [0,400 nm], leading to bin width of 1 nm. Figure 3.29(b) shows the histogram curve for the OPD image of a TF1-GFP cell (see section 2.5.2 for the description of these cells), shown in Fig.3.29(a).

We smooth the data with a gaussian window with a 8 nm width, and we detect the local minima simply by inverting the smoothed curve, and using the function `findpeaks` of MATLAB. The position of the detected minima determines the threshold value of Φ (Fig.3.29b, vertical lines) to segment the cell interior and detect the isocontours of the domain boundaries.

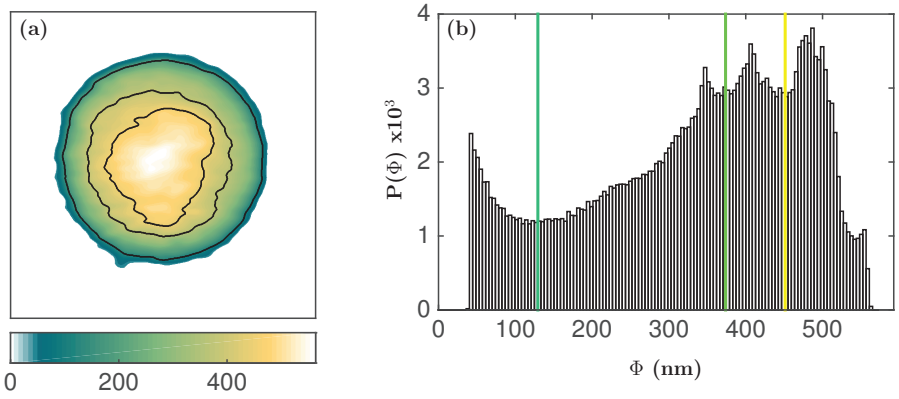

Figure 3.29 – **Phase isocontours of a living cell.** (a) OPD_r- image after image segmentation of a TF1-GFP living cell, where $\Phi(x,y)$ (in nm) has been colour coded. The black contours indicate the detected boundaries. (b) Distribution of OPD values for the cell shown in (a). The vertical coloured lines indicate the detected local minima that determine the threshold values for the boundary detection.

The multi-shell model requires for the boundaries to be highly circular and concentrical. Hence, we must evaluate if the detected contours fulfil these conditions if we want to apply the multi-shell model to extract some information about the refractive index of the domain. Although, we can still perform a geometrical characterisation of the detected contours since it could provide interesting results when comparing different cell types if we are rather interested on the relative information than in absolute values.

For the cell shown in Fig.3.29, we detect three contours that we label going from the cell borders towards the centre $i = 1,2,3$. We start computing the circularity index C for each contour: $C_1 = 0.997, C_2 = 0.995, C_3 = 0.988$. Even if all the contours seem to have high circularity, if we look at the third contour, it does not appear to be that circular, so we will choose as a criteria for consider high circularity, that $C \geq 0.99$. This discards contour 3 for the multi-shell model. The other two contours are circular and concentrical with $|r_{c_i} - r_{c_0}| \leq 0.74\mu$m, where r_{c_i} and r_{c_0} are respectively the barycentre of the contour i and of the cell. We can, therefore, estimate the refractive index of each domain, considering the cell as a structure composed of 3 concentrical spheres (cell border + two internal domains).

For a structure of N concentrical spheres with $\Delta n_{i,i-1}$ the relative RI of sphere i of radius R_{i-1}, we have:

$$\Delta n_{1,0} = \frac{\Phi(R_1)}{2\sqrt{R_0^2 - R_1^2}} \tag{3.52}$$

$$\Delta n_{i,i-1} = \frac{1}{\sqrt{R_{i-1}^2 - R_i^2}} \left(\frac{1}{2}\Phi(R_i) - \sum_{j=1}^{i-1} \Delta n_{j,j-1} \sqrt{R_{j-1}^2 - R_i^2} \right) \tag{3.53}$$

$$\Delta n_{N,N-1} = \frac{1}{R_{N-1}} \left(\frac{1}{2} \Phi_{\max} - \sum_{j=1}^{N-1} \Delta n_{j,j-1} R_{j-1} \right) \tag{3.54}$$

Then, for the example shown in Fig.3.29, $N = 3$, counting the cell border ($i = 0$), we have:

$$\Delta n_{1,0} = \frac{87.067\text{nm}}{2\sqrt{7.79^2 \mu m - 7.30^2 \mu m}} = 0.0160 \tag{3.55}$$

$$\Delta n_{2,1} = \frac{1}{\sqrt{7.3^2 \mu m - 5.29^2 \mu m}} \left(\frac{1}{2} 331.43\text{nm} - \Delta n_{1,0} \sqrt{7.79^2 \mu m - 5.29^2 \mu m} \right) = 0.0148 \tag{3.56}$$

$$\Delta n_{3,2} = \frac{1}{5.29 \mu m} \left(\frac{1}{2} 521.3\text{nm} - 7.79 \mu m \Delta n_{1,0} - 7.30 \mu m \Delta n_{2,1} \right) = 0.005 \tag{3.57}$$

giving a total $\Delta n_c \sim 0.0361$ compared to the RI obtained using the optical path volume, $\Delta n_c \sim 0.0337$, which makes a difference of 3.7% between both methods.

3.6.3 Wavelet transform maxima chains

We develop here a method for the detection of optical path depth contours from single cells based on local maxima chains of the OPD derivative in two dimensions. These maxima define interface chains where the RI and/or the cell shape vary and can be considered as domain boundaries. Even if we do not know *a priori* which is the prominent variation (RI or thickness) at each maxima, their connectivity, or maxima chains, gives us direct access to the complexity of the cell interior.

The OPD function is an integral on the RI change through the cell, whose integration limits depend on the point **x**=(x,y) :

$$\Phi(\mathbf{x}) = \int_{z_m(\mathbf{x})}^{z_M(\mathbf{x})} \Delta n(\mathbf{x}, z) dz = \Delta N(\mathbf{x}, z) \Big|_{z_m(\mathbf{x})}^{z_M(\mathbf{x})} \tag{3.58}$$

$\Delta N(\mathbf{x}, z)$ is therefore the integral function of $\Delta n(\mathbf{x}, z)$. For example, if $\Delta n(\mathbf{x}, z) = \Delta n_c$, with Δn_c a constant,

$$\Delta N(\mathbf{x}, z) = \Delta n_c z + B \tag{3.59}$$

is a linear function of the variable z, and

$$\Phi(\mathbf{x}) = \Delta n_c (z_M - z_m)(\mathbf{x}) = \Delta n_c h(\mathbf{x}) \tag{3.60}$$

The OPD function follows precisely the shape of the object and its derivative is proportional to the derivative of its thickness h at each point (x,y). In general, the derivative of Φ along a

radial coordinate on the x-y plane results from both RI and the topography variations

$$\frac{\partial\Phi(\mathbf{x})}{\partial r} = \frac{\partial\Delta N(\mathbf{x}, z_M)}{\partial r} - \frac{\partial\Delta N(\mathbf{x}, z_m)}{\partial r} \tag{3.61}$$

If Δn is an integrable function, the two integral values $\Delta N(\mathbf{x}, z_M)$ and $\Delta N(\mathbf{x}, z_m)$ exist and can be derived again along r. The boundary of the object is precisely the domain in space where the RI slope changes at the interface of the interior and the exterior media, if this interface is fuzzy, the slope will not be sharp. Because domain interfaces in biological matter will not be very sharp, we will rather consider them as transitory zones with a sharpness described by the OPD gradient. The local maxima of this OPD spatial gradient will follow the boundary zones wherever they can be detected, whether they correspond to the object boundary or its internal structure. If we consider that the object is made of the assembly of different internal structures with RI variations, we will apply the same assumption as above for the internal boundaries detection. The main difficulty will therefore be to compute correctly these spatial gradients and extract local maxima lines. If the maxima lines are closed we will conclude to the existence of well defined internal structures with a quite homogeneous composition. On the contrary, if the maxima lines are not closed and rather randomly distributed, we will rather conclude to a more complex organisation of the internal structure of the considered object.

Let us take a theoretical example of a spherical object of radius R, with a radial RI function varying from n_0 (the outer medium) to n_c (at the centre of the sphere):

$$\Delta n_{t1}(\mathbf{x}, z) = \begin{cases} \Delta n_c |(R-r)/R|^{\alpha} & \text{for } r \le R \\ 0 & \text{for } r > R \end{cases} \tag{3.62}$$

with $r = \sqrt{x^2+y^2+z^2}$ the radial distance, and $\Delta n_c = n_c - n_0$. The height of the sphere at position $\mathbf{x}$ with $x^2+y^2 < R^2$ is given by

$$h(x,y) = 2\sqrt{R^2-(x^2+y^2)} \tag{3.63}$$

Centring the middle of the sphere at the origin ($x_c = 0, y_c = 0, z_c = 0$), we plot in Fig.3.30(a) the RI profiles along the x axis, for α= 0, 0.25, and 0.5 (black solid, dashed, and dotted lines respectively), superimposed to the sphere thickness profile (dashed blue line).

The OPD of this spherical object at position $\mathbf{x}$ with $x^2+y^2 < R^2$ is given by

$$\Phi(\mathbf{x}) = \Delta n_c \int_0^{h(x,y)} |1 - r/R|^{\alpha} \, \mathrm{d}z \tag{3.64}$$

The three OPD functions corresponding to α=0, 0.25, and 0.5 are plotted in green in Fig.3.30(b), with the same line style as in (a). When the RI is increasing monotonously from the border to the centre of the sphere, the OPD keeps a global single humped shape, with a nonlinearity that depends on the exponent α. The local maxima of the first derivative of the OPD functions point to the sphere border (Fig.3.30b). Note also that the OPD functions are symmetric with respect to the centre of the sphere, so they keep the object symmetry. In this example, we

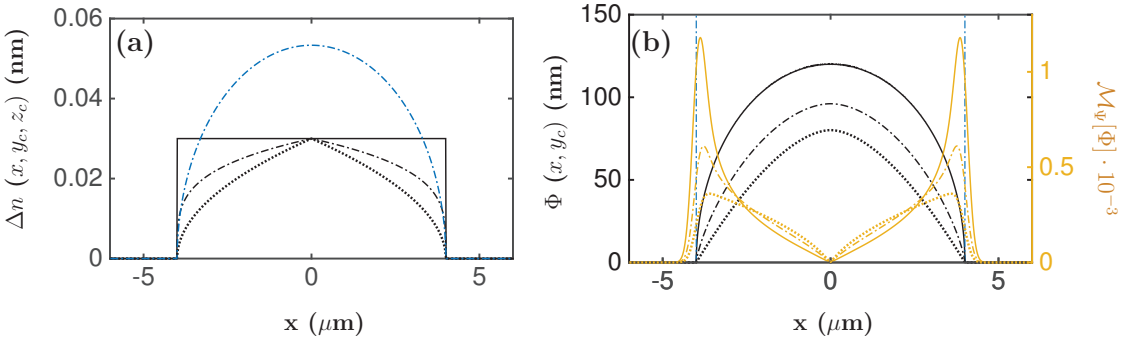

Figure 3.30 – **OPD profiles from model spheres with radial RI profiles.** (a) Horizontal section of the monotonously increasing RI radial profiles, $\Delta n(x, y_c, z_c)$, described by Eq.3.62, for different values of α: 0 (solid line), 0.25 (dashed line) and 0.5 (dotted line). (b) $\Phi(x)$ (black lines) and $\partial\Phi/\partial x$ (yellow lines) computed from the profiles shown in (a).

have computed the first derivative of the OPD with a smoothing first derivative of a gaussian (see section 3.6.3.a for details) in a similar way as it will be done in the experimental situations. The slight shift of the maxima of the $\partial\Phi/\partial x$ compared to the sphere borders (dashed blue line) is due to the gaussian filtering.

To introduce an internal variation of the RI we construct another structure with the same outer spherical shape, containing an internal concentric spherical shell with higher RI, the boundary of this internal shell is also varying smoothly with the radius r:

$$\Delta n_{t2}(\mathbf{x}, z) = \begin{cases} \Delta n_{t1} + \Delta n_c \left[cos\left(2\pi(1 - r/R)\right) - 1\right]^2/6 & \text{for } r \leq R \\ 0 & \text{for } r > R \end{cases} \tag{3.65}$$

The corresponding RI profiles for α=0, 0.25, and 0.5 are shown in Fig.3.31(a). Note the two supplementary local maxima at $x = \pm 2\,\mu$m, which are superimposed to the smoothly increasing profiles, similar to those of Fig.3.30(a). The corresponding Φ and $\partial\Phi/\partial x$ profiles plotted in black in Fig.3.31(b) are very instructive since they show that the combination of both the spherical shape and non monotnous RI profile may lead to an unexpected behaviour. In this situation, not only the underlying spherical shape of the object is smeared out but the local maxima of the index profiles are also strongly damped, giving the place to a quasi OPD plateau in the middle interval [-2μm,2μm]: the higher α, the flatter the plateau.

From this model, we conclude that trusting the OPD isocontours to delineate regions of different RIs from a reconstructed phase image may be completely misleading but that we can still recover some information of the boundary (internal and external) properties with the computation of the local derivative of the OPD function.

3.6.3.a 2D Gaussian derivative WT and local maxima detection

Given that the OPD images are two-dimensional, these derivative computations must be performed along both directions x and y, and we must also include in the computation the pos-

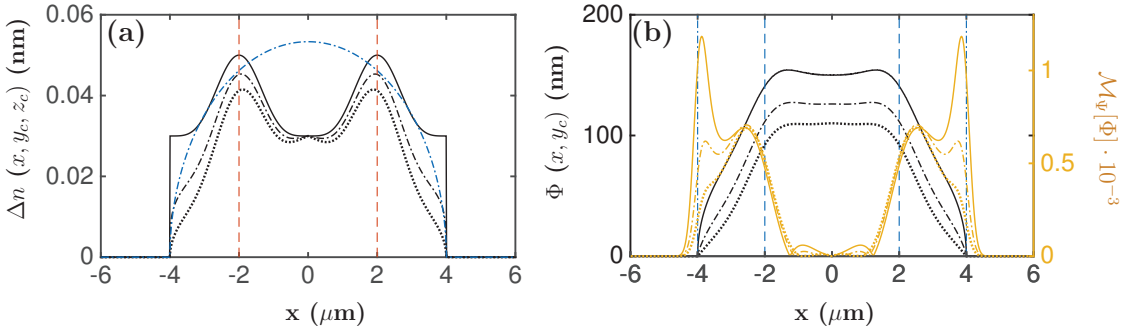

Figure 3.31 – **OPD profiles from model spheres with non-monotonous radial RI profiles.** (a) Horizontal section of the non monotonously increasing RI radial profiles, $\Delta n(x, y_c, z_c)$, described by Eq.3.65. α: 0 (solid line), 0.25 (dashed line) and 0.5 (dotted line). (b) $\Phi(x)$ (black lines) and $\partial\Phi/\partial x$ (yellow lines) computed from the profiles shown in (a).

sibility to smooth out the enhanced noise that could come from the derivative procedure. We use a 2D Gaussian derivative wavelet to simultaneously compute the gradient and smooth the signal.

As originally noticed by Mallat and collaborators [163, 239] the 2D wavelet transform [240, 241] can be used to revisit the Canny's multi-scale edge detector [242]. The principle of this analysis is to smooth the image by convolving it with a filter and then to compute the gradient of the smoothed signal. Let us consider the two wavelet defined respectively as the partial derivatives with respect to x and y of a 2D smoothing function $\psi(\mathbf{x})$:

$$\Psi_1 = \frac{\partial\psi(\mathbf{x})}{\partial x} \text{ and } \Psi_2 = \frac{\partial\psi(\mathbf{x})}{\partial y} \tag{3.66}$$

The smoothing function ψ must be well localised (around $x = y = 0$), isotropic and dependent on the modulus of ($\mathbf{x}$) only. The Gaussian function is the mostly used function that fulfils these conditions:

$$\psi_g(x, y) = e^{-(x^2+y^2)/2} \tag{3.67}$$

For any function $f(x, y) \in L^2(\mathbf{R})$, where $L^2(\mathbf{R})$ consists of all square integrable functions, the

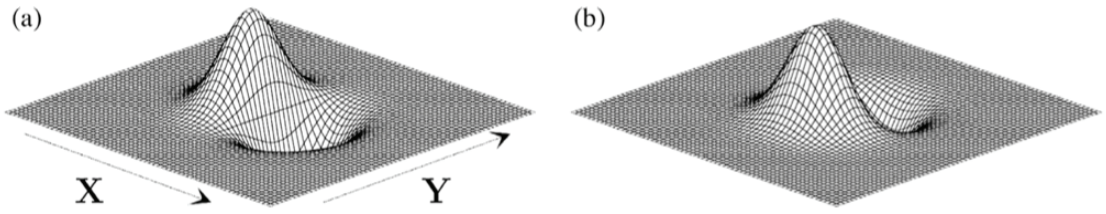

Figure 3.32 – **2D Gaussian derivative wavelet.** 3D plot of the partial derivatives of the 2D Gaussian wavelet function: (a) $\Psi_{G_1}(x, y)$; (b) $\Psi_{G_2}(x, y)$.

continuous wavelet transform of f with respect to Ψ_{G_1} and Ψ_{G_2} is expressed as a vector [243, 244]:

$$\mathbf{T}_\Psi(\mathbf{b},a) = \begin{pmatrix} T_{\Psi_{G_1}}[f] = a^{-2}\int \mathrm{d}^2\mathbf{x}\Psi_{G_1}(a^{-1}(\mathbf{x}-\mathbf{b}))f(\mathbf{x}) \\ T_{\Psi_{G_2}}[f] = a^{-2}\int \mathrm{d}^2\mathbf{x}\Psi_{G_2}(a^{-1}(\mathbf{x}-\mathbf{b}))f(\mathbf{x}) \end{pmatrix} \tag{3.68}$$

By a straightforward integration by parts [241], this 2D wavelet transform can be rewritten as:

$$\mathbf{T}_\Psi(\mathbf{b},a) = \nabla\{T_{\psi_g}[f](\mathbf{b},a)\} = \nabla\{\psi_{g,\mathbf{b},a} * f\} \tag{3.69}$$

If $\psi(\mathbf{x})$ is a smoothing filter like the Gaussian function (Eq.3.67), then Eq.(3.69) amounts to define the 2D wavelet transform as the gradient vector of $f(\mathbf{x})$ smoothed by dilated versions of $\psi_g(a^{-1}\mathbf{x})$ of the gaussian filter. If $\psi(\mathbf{x})$ has some vanishing moments, then $T_\psi[f](\mathbf{b},a)$ in Eq.(3.69) is the continuous 2D wavelet (C2DWT) of $f(\mathbf{x})$)[231], provided that $\psi(\mathbf{x})$ is an isotropic analysing wavelet. Further on, we compute its modulus and argument

$$\mathbf{T}_\Psi(\mathbf{b},a) = (\mathscr{M}_\Psi[f](\mathbf{b},a), \mathscr{A}_\Psi[f](\mathbf{b},a)) \tag{3.70}$$

where

$$\mathscr{M}_\Psi[f](\mathbf{b},a) = \sqrt{(T_{\Psi_{G_1}}[f](\mathbf{b},a))^2 + (T_{\Psi_{G_2}}[f](\mathbf{b},a))^2} \tag{3.71}$$

and

$$\mathscr{A}_\Psi[f](\mathbf{b},a) = \mathbf{Arg}(T_{\Psi_{G_1}}[f](\mathbf{b},a) + i\,T_{\Psi_{G_2}}[f](\mathbf{b},a)) \tag{3.72}$$

In practice, at a given scale a, we first compute the 2D Fast Fourier Transform (FFT) of Ψ_{G_1} and Ψ_{G_2} and we multiply these images by the FFT of f: $\tilde{\Psi_{G_1}}\cdot\tilde{f}$ and $\tilde{\Psi_{G_2}}\cdot\tilde{f}$, and from the inverse FFT of these products we get the wavelet transforms $T_{\Psi_{G_1}}[f]$ and $T_{\Psi_{G_2}}[f]$t We then identify the so-called wavelet transform modulus maxima (WTMM) as the points where the modulus of the WT, $\mathscr{M}_\Psi[f](\mathbf{b},a)$ is locally maximum.

To increase the resolution of the local maxima detection when applying the method to the images obtained with DPM, we transform the pixelated images into radial representations. To switch from cartesian to cylindrical geometry, we interpolate the WT argument and the modulus on 1440 radial axes crossing the centre of the cell with angular shift of $\delta\theta = 4.4\ 10^{-3}$ radian. On each of these rotating axes with θ varying from 0 to 2π, we interpolate each pixelated image along the radial variable r with a spatial resolution $dr = 1.8$ nm. This allows a very acute determination of the local angle θ and of the argument of the wavelet transform vector. From the radial coordinates of the WTMMs, we reconstruct the maxima chains as 2D curves made of sequences of neighbouring points (distant of less than $2r\delta\theta$).

When the maxima chain is circular (Fig.3.33a), and the wavelet transform vector $\mathbf{T}_\Psi[\Phi](\mathbf{b},a)$ is

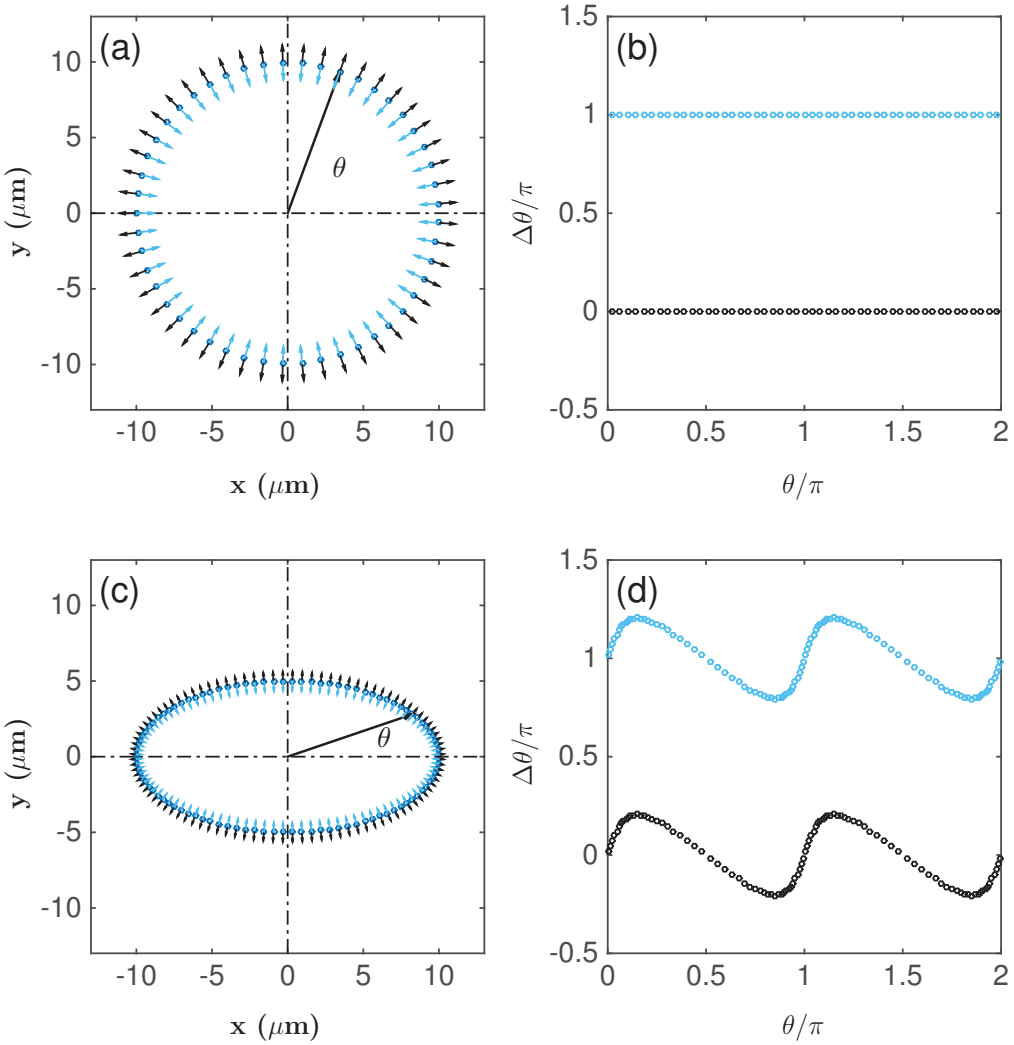

Figure 3.33 – **Wavelet transform argument for a spheroid and an ellipsoid contour.** (a) Circular chain model with outward (resp. inward) wavelet transform vectors $\mathbf{T}_\Psi[\Psi](\mathbf{r},a)$.(b) $\Delta\theta = \mathscr{A}_\Psi[\Phi]_{WTMM} - \theta$ on the WTMM chain line of (a). The outward (resp. inward) correspond to black (resp. blue) dots. (c-d) Same as (a-b) for an ellipsoidal chain model.

oriented outward (black arrows in Fig.3.33a), the argument of the wavelet transform is equal to the radial angle θ, $\Delta\theta = \mathscr{A}_\Psi[\Phi]_{WTMM} - \theta = 0$ (Fig.3.33b, black dots). If the wavelet transform vector is oriented inward (blue arrows in Fig.3.33a), the argument is equal to π (Fig.3.33b, blue points). If we take an ellipsoidal shaped maxima chain (Fig.3.33c), the argument of the wavelet transform is no longer a constant function versus the angle θ. Again we consider the two cases of outward wavelet transform vector (black arrows in Fig.3.33c, and black dots in Fig.3.33d) and inward wavelet transform vector (blue arrows in Fig.3.33c, and magenta dots in Fig.3.33d). It is important to note that when the WTMM chain deviates from a circular contour, the angle difference $\Delta\theta$ may oscillate versus the radial angle θ, with alternating increasing ($\theta < 0.15\pi$) and decreasing ($0.15\pi < \theta < 0.85\pi$) intervals in Fig.3.33(d). The flatter the shape of the chain the larger the slope of these curves (in absolute values). The positive slopes of $\Delta\theta$ vs. θ curves (which may reach vertical lines) correspond to highly curved chains

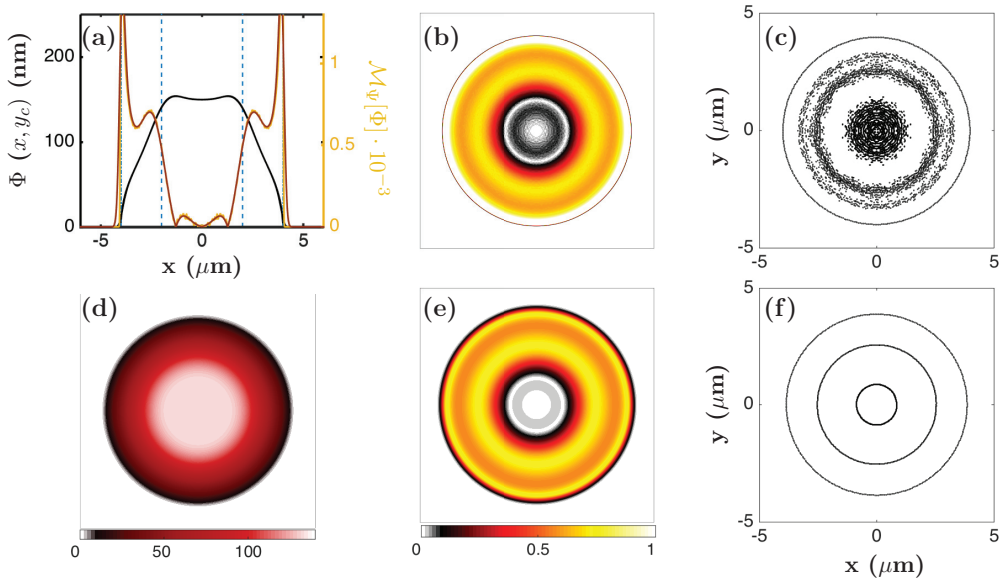

Figure 3.34 – **WTMM chain detection from the OPD profile of a noisy RI spherical model.** (a) OPD (black line) computed from Eq.(3.73) for α=0.25 and its WTM modulus $\mathscr{M}_\Psi[\Phi](b,a)$ estimated for two scales $a=2$ (yellow line), and $a=10$ (brown line). (b) 2D colour coded image of $\mathscr{M}_\Psi[\Phi]\cdot 10^{-3}$ for $a=2$. (c) Local maxima of $\mathscr{M}_\Psi[\Phi]$ for $a=2$. (d) OPD image computed from the model on Eq.3.73, where Φ has been colour coded. (e) and (f) same as (b,c) respectively, for a=10.

(compared to a circle), whereas the negative slopes correspond to flatter chains (compared to a circle).

We illustrate the WTMM method for detecting the local maxima chains from the OPD gradient from noisy data, taking again the previous model of a spherical object with an internal spherical shell of higher RI with an additive noise term to the RI function before computing the OPD image:

$$\Delta n(\mathbf{x},z)=\begin{cases}\Delta n_{t2}+\zeta\Delta n_c & \text{for } r\le R\\ \zeta & \text{for } r>R\end{cases} \tag{3.73}$$

with ζ being a uniformly distributed random variable in the [-1/10,1/10] interval, giving a standard deviation of ζ equal to 2.8%. We report in Fig.3.34 the wavelet transform modulus and the local maxima for two scales a of the analysing wavelet computed on the noisy shell model (Eq.3.73).

From the OPD image (3.34d) and its x-section through the middle of the sphere (Fig.3.34a, black line) we do not see much difference with the noise-free profile (Fig.3.31a). However, when computing the derivative with a small value of the scale parameter a (yellow curve in Fig.3.34a and 2D image of Fig.3.34b), we notice that the background white noise that we have added to the RI introduces fluctuations that perturb dramatically the detection of the local maxima of the wavelet transform modulus (Fig.3.34c). To circumvent this problem, we increase the scale parameter a in such a way that the number of local maxima chains and their

structure no longer change. In this simple theoretical example, we simply increased the scale a by a factor of five to get the three expected maxima chain lines corresponding respectively to the outer boundary and the two (inner and external) boundaries on the internal concentric shell of higher RI. Once the scale a is chosen correctly to smooth down the background noise, the maxima lines predicted by the model are recovered.

3.6.3.b Application of the WTMM method to single cells

We choose first red blood cells (RBCs) to test the WTMM detection of phase boundary contours because these anucleated cells have an almost homogeneous cytoplasm with a high concentration of haemoglobin and a refractive index $n_c \sim 1.4010 \pm 0.006$ [245–247]. Their shape has also been fully described in the literature [225, 247–250], with a biconcave equation in cylindrical coordinates (r, θ, z), derived from experimental observations in isotonic buffers:

$$h(r) = \sqrt{1 - r^2/R^2} \left(0.72 + 4.512 \frac{r^2}{R^2} - 3.426 \frac{r^4}{R^4} \right) \tag{3.74}$$

We recognise in Fig.3.35(a) the characteristic OPD 'donut' shape of a red blood cell [225, 250], with a central hole, and cylindrical symmetry. This example is particularly interesting to test the performance of the local maxima detection with the wavelet transform method, as shown in Fig.3.35(b-f). Fig.3.35(c) shows the corresponding sections of Φ (black line) and $\mathscr{M}_\Psi[\Phi]$ (yellow line) along the x direction, taken at the centre of the cell. The blue line in Fig.3.35(c) gives the biconcave shape predicted by Eq.(3.74). This method detects two WTMM chains, one exterior and one interior (Fig.3.35d). The detected chains are clearly separated, and as seen in Fig.3.35(e), they conserve a radial geometry with a high circularity.

The plot of the evolution of $\Delta\theta = \mathscr{A}_\Psi[\Phi] - \theta$ in Fig.3.35(f) for each WTMM chain shows a shift of the internal chain from the external one. This shift corresponds to the direction of the wavelet vector, who gives the direction of the steepest descent of the wavelet transform modulus: the internal chain will present an inward direction, contrary to the external chain.

Notice that in this case all the detected WTMM chains form a closed contour, and thus, we can characterise them in the more 'traditional' manner, using the geometrical and OPD-related parameters reported on Table 3.2. However in general, for other types of cells the detected inner boundaries will rarely delimit a closed domain, requiring additional parameters to characterise the complex internal structure of a living cell. To illustrate this point and to show how we can use the detected WTMM to study single cells exhibiting inhomogeneous structures, we will present one more example of living cells with an increased level of complexity on its internal structure.

We consider now spherical mono-nucleated immature blood cells unforced to adherence (we do not treat the glass coverslips after cleaning with ethanol). These CD34+ cells are sorted from the bone marrow by the CD34 antigen, resulting in a mixture of hematopoietic stem and progenitor cells with various degrees of maturity. In healthy conditions, these cells remain

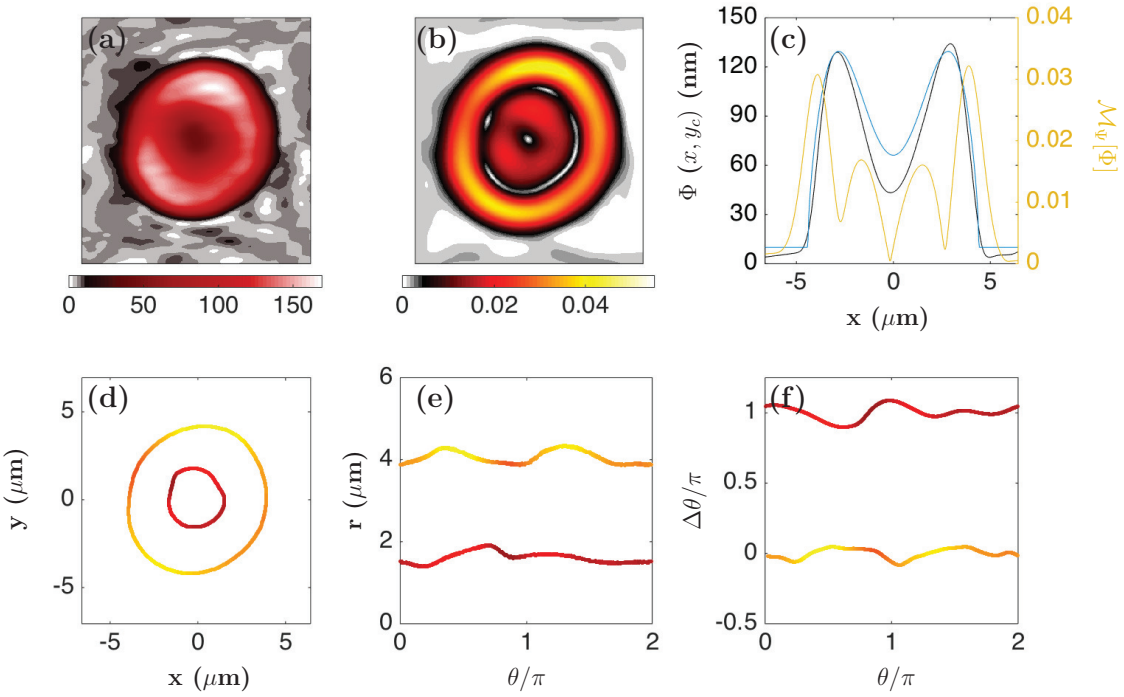

Figure 3.35 – **WTMM chain detection on a living red blood cell.** (a) Corrected OPD_r- image, where Φ (in nm) has been colour coded. (b) $\mathscr{M}_\Psi[\Phi](\mathbf{b}, a)$ for a=15. (c) Horizontal sections through the cell centre. Black line: OPD profile, yellow line: $\mathscr{M}_\Psi[\Phi]$, and blue line: biconcave shape predicted by Eq.(3.74), with R=4.4 μm, and a relative RI $\Delta n = 0.078$. (d) WTMM chains for the RBC shown in (a), where $\mathscr{M}_\Psi[\Phi]$ has been colour coded with the same colour scale as in (b), on the range [0.0,0.055]. (e) Radial position of the detected WTMM chains shown in (d). (f) Plot of $\Delta\theta = \mathscr{A}[\Phi] - \theta$ as a function of θ.

in the bone marrow, whereas in chronic myeloid leukaemia they may also be found in the blood. These mono-nucleated cells have a rather high nuclear to cytoplasm ratio (N:C) in the interphase, which indicates the maturity of the cell. For example for immature leukocytes it may reach 4:1. If we assume that the nucleus is a concentric sphere of radius R_n inside the cell of radius R_C, a 4:1 N:C would give $R_N = (4/5)^{1/3} \cdot R_C \sim 0/93 R_C$. If we take $R_c = 4\mu$m, $R_n = 3.7\mu$m,leaving only 300 nm distance in between the outer cytoplasmic and the inner nuclear membrane. Such large nuclei should not be distinguishable from the outer membrane shell in our DPM setup (Table 3.1). If the N:C drops to 3:1, the radius of the nucleus decreases only by 70 nm, which should remain undetectable with our optical setup. The impact of the nucleus should therefore only be visible on the amplitude of the OPD or its derivative. However, we should be able to detect internal structures of the nuclei on this type of cells.

Figure 3.36 illustrates the WTMM method on a living CD34+ cell. The outer boundary of this spherical cell is detected straightforwardly by the chain with the maximum OPD gradient, or $\mathscr{M}_\Psi[\Phi]$. From Fig.3.36(a) and (b) we can already observe the inhomogeneous structure of the cell. This is clearer when we look at the horizontal section of Fig.3.36(c), where the OPD profile is no longer a single dome corresponding to an homogeneous sphere, but it appears to

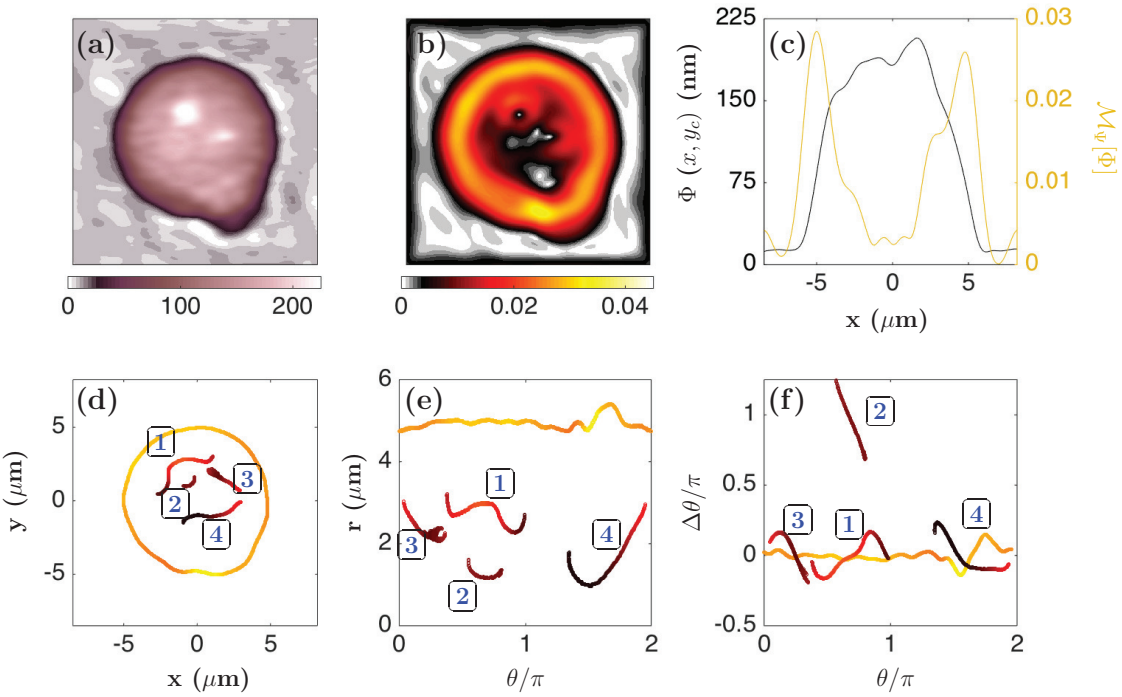

Figure 3.36 – **WTMM chain detection on a living CD34+ primary cell.** (a) Corrected OPD_r- image, where Φ (in nm) has been colour coded. (b) $\mathcal{M}_\Psi[\Phi](\mathbf{b}, a)$ for a=15. (c) Horizontal sections through the cell centre. Black line: OPD profile, yellow line: $\mathcal{M}_\Psi[\Phi]$. (d) WTMM chains for the cell shown in (a), where $\mathcal{M}_\Psi[\Phi]$ has been colour coded as in (b). (e) Radial position of the detected WTMM chains shown in (d). (f) Plot of $\Delta\theta = \mathcal{A}[\Phi] - \theta$ as a function of θ. In (e) and (f) the labelling of the chains correspond to the nu,bering in (d),

have small 'bumps' added to the top, which are very likely zones with a higher density. Nevertheless, these zones do not form a closed domain, as the detected WTMM chains do not form a closed contour (Fig.3.36d). Given the spatial distribution of the chains, its characterisation becomes slightly more complicated. We have chosen the following parameters for the study of the cell structure based on the WTMM chains, (who for simplification we will note $\mathcal{M}_{c_i}$) :

- Radial position of a given chain $r_{\mathcal{M}_{c_i}}$, taking $r = 0$, as the centre of the cell.
- Orientation of a given chain $\Delta\theta_{\mathcal{M}_{c_i}}$, where $\Delta\theta_{\mathcal{M}_{c_i}} = 0$, corresponds to a chain whose normal vector is the same as the normal vector pointing from the origin (0,0) towards (r, θ).
- Length of a given chain $L_{\mathcal{M}_{c_i}}$.
- Number of chains per cell $N_{\mathcal{M}_{c_i}}$.

We have labelled on Fig.3.36(d) the detected chains from the example of a CD34+ primary cell. By imposing a lower limit to the chain length of $L_{\mathcal{M}_c} = 100$ nm, we can account for 4 chains detected on this cell of similar length, except for chain number 2, which is relatively

smaller. Although they are not equidistant from the cell centre, they do seem to be restrained to a distance range between [1 μm,3μm], as seen in Fig.3.36(e), and again with the exception of the chain number 2, presenting an orientation not so far from the one of a circle-like contour (Fig.3.36f), probably indicating a domain who is not concentrical with the cell at the x-y plane, and with some fuzzy boundaries that avoid the detection of a closed contour.

We have shown here that when the phase profiles are not monotonous nor smooth functions, the OPD gradient may display local maxima that reflect a local change of RI or of the topography of the cells. The introduction of the WTMM method to detect these maxima allows a robust and automatised reconstruction of their outer and inner boundary chains, from which morphological and global RI characterisation can be performed. Fore more illustrations on this method, please refer to the Appendix D.

3.7 Cell morphology characterisation

In this section we employ the methods described above to characterise the morphology of different types of cells. We start with blood cells including erythrocytes, primary CD34+ cells, and a model for hematopoietic stem cells (TF1 cell line) for whom we discuss the cell transformation in leukaemia by studying their morphology after transduction with an oncogene, serving as a model for Chronic Myelogeneous Leukaemia (CML). We continue with the characterisation of two adherent cell lines with very different properties: C2C12 mouse embryonic myoblasts, and hepatocytes from the carcinoma cell line HepG2.

By covering a broad range of cell types we show the possibilities offered by DPM combined with the analysis tools that we have described in the previous section. Furthermore, a better understanding of the cell morphology and DPM imaging of some of these cell types will prove to be very useful in the study of single cell dynamics.

We begin by looking at the morphology at the whole-cell level, since it provides a first survey on the cell characteristics that can indicate already the cell state (healthy, stressed, adherent, etc.) and hopefully highlight in a quantitative manner the differences between cell types. Moreover, the detection of the cell contour is probably the part of our analysis that is less prone to computation errors, and as it is the common point for the two presented methods for boundary detection, the wavelet transform maxima chains and the phase isocontours, we can make a direct comparison of both methods.

3.7.1 Red Blood Cells

The shape of red blood cells (RBCs) is very sensitive to the environment [252, 253]. Under physiological conditions, a normal human RBC assumes a biconcave discoid shape with a $\sim 8\mu$m diameter. This shape is modified systematically by several conditions of the medium [251], such as the salt content, pH level, ATP or even cholesterol, producing either concave shapes called stomatocytes, or cells called echinocytes, which present convex rounded protrusions or spicules, called crenated shapes [254](Fig.3.37).

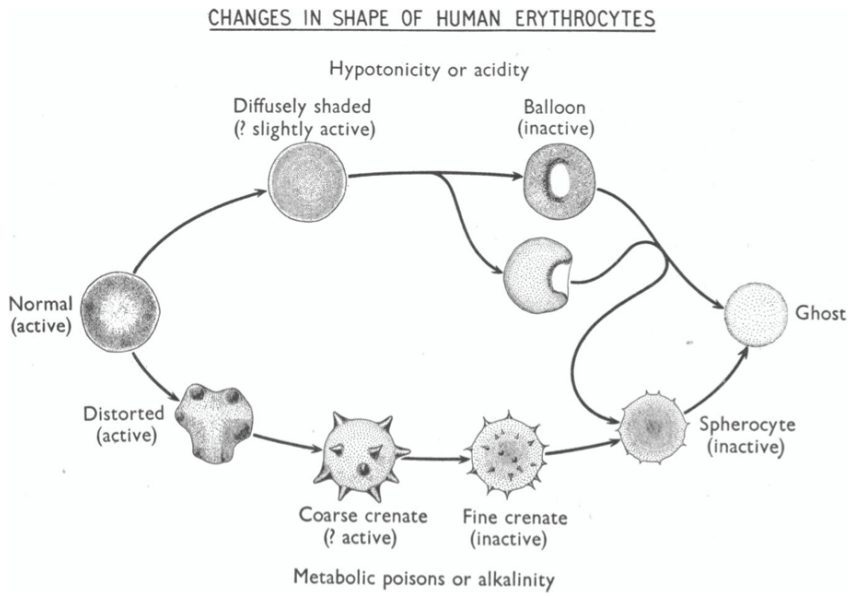

Figure 3.37 – **Changes in shape of a human erythrocyte and flicker activity** (Blowers et al.) [251]

We have imaged erythrocytes obtained from a single human blood sample, using Phosphate Bovine Serum (PBS) 1x for dilution prior to imaging. It has been observed that on these slight hypertonic conditions, the RBCs adopt different shapes, resulting in a mixture of biconcave and crenate morphology [255]. Figure 3.38 shows some examples of OPD images for the cells that we have imaged with DPM, where we can observe the different shapes that a living erythrocyte can adopt. We find that in general, both methods used to detect the border of the cell are congruent with each other (Fig.3.39), displaying noticeable differences on the geometrical parameters such as the mean radius, perimeter and area, as shown in Fig.3.39(a-c), with the method of WT maxima chains tending to lower values than those obtained with the isocontours. Probably for RBCs the most reliable method is the one of WT maxima chains, as it shows a good agreement with the values found in the literature, i.e., $< R >= 3.84 \pm 0.25 \mu$m, and the distributions look overall more homogeneous than those obtained with the phase isocontours (Fig.3.39, WT maxima chains in dashed-dotted line, phase isocontours shown with bars).Given that RBCs have been widely studied, there is not much that we can say about their global morphology that hasn't been reported yet in literature, so we will just make a few remarks on our results.

Perhaps one of the most informative quantities to look at is the optical volume V_Φ (Fig.3.39e), mainly because it can be used to estimate an averaged refractive index of the cell. Note that as we are not dealing with spherical cells, we can not simply divide the optical volume with the volume of a sphere with the equivalent mean radius, as it will be a complete erroneous estimation of RI. However, we can use the average physical volume known for human RBCs, namely, $V_c \sim 90 \mu m^3$ to make a very coarse estimation of the global RI of the RBC. With this assumption and using the WT maximas chain method, we obtain an average relative RI of

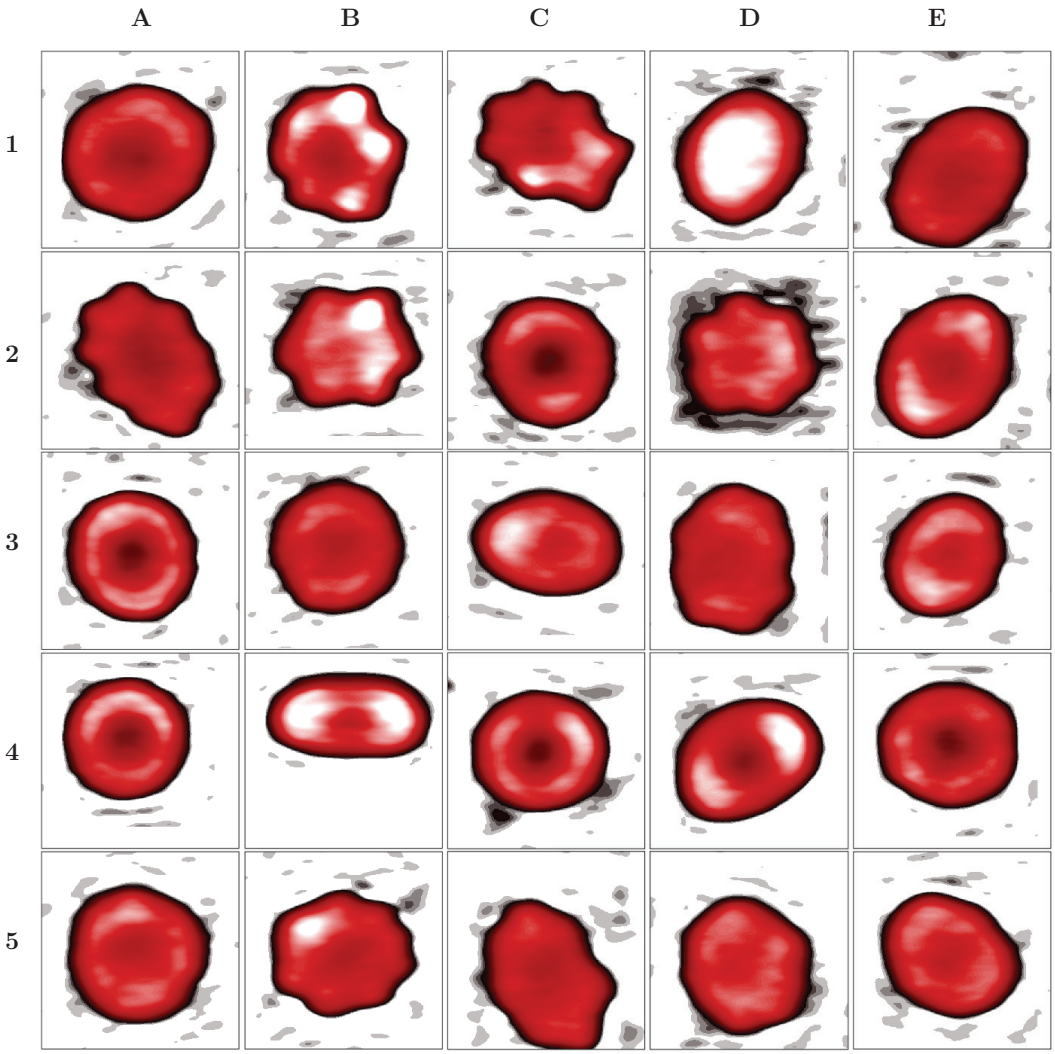

Figure 3.38 – **OPD images of living red blood cells.** Some representative examples of the type of cells imaged with DPM. The grid is composed of squares of 13μm, and $\Phi(x, y)$ has been colour coded as in Fig.3.35(a), from 0 (black) to 180 nm (light red-white).

0.0611±0.008, that if consider the refractive index of the medium as 1.33, it leads to a RI of 1.391±0.008, in good agreement with literature [221, 225]. We can also use the optical volume to estimate the cell dry mass M, considering that α=1.93x10^{-3} for haemoglobin [235], we get $M = 28.48 \pm 0.39$ pg, finding again the expected value for healthy RBCs [221].

It is quite interesting that our results fall exactly within the values expected for healthy human RBCs, specially considering the poor-controlled conditions in which we have performed the experiment: slightly hypertonic solution by using PBS 1x instead of other more physiological serum, no temperature control hence, imaging at room temperature T~ 22°C, and without any rigorous cleaning of the coverslips used for imaging beyond cleaning the surface with ethanol. Perhaps this is due to the high number of cells imaged, $N_{\text{cells}} = 326$ cells, or maybe it is a reflect of the resistance of erythrocytes to non-optimal conditions. In any case, our results

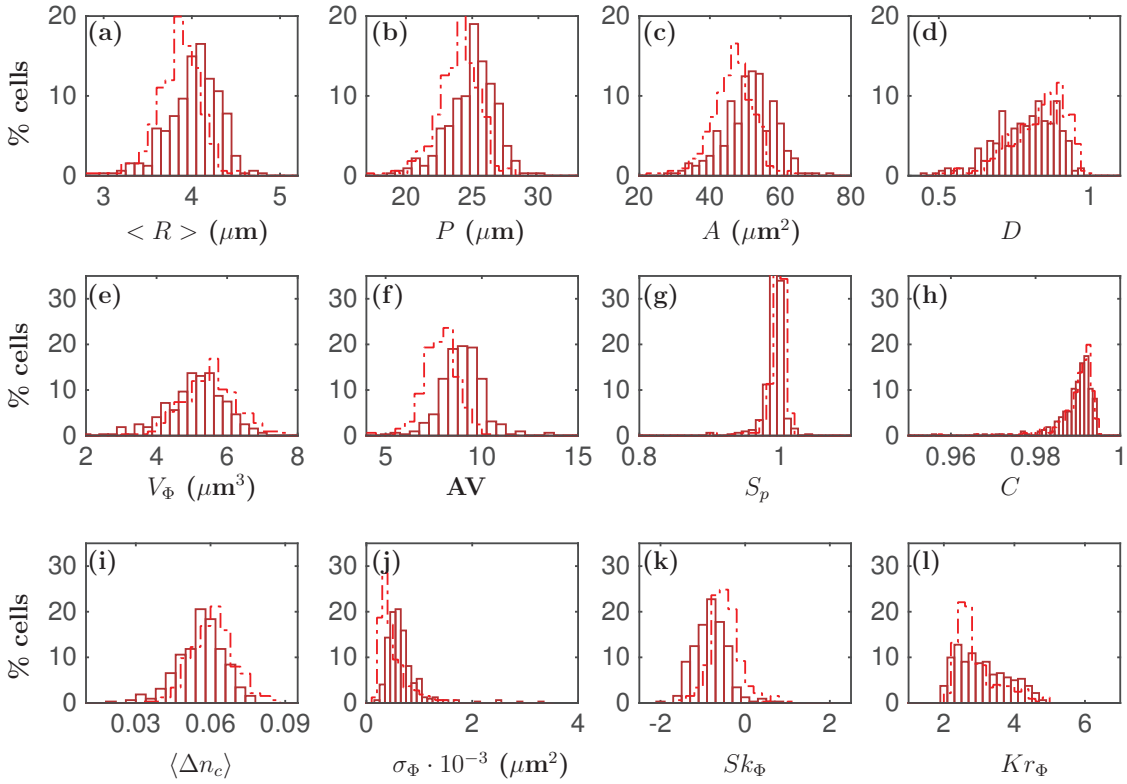

Figure 3.39 – **Morphological parameters of RBCs.** Distribution of the geometrical values for (a) mean cell radius $< R >$, (b) perimeter P, (c) projected area A, (d) aspect ratio D, (e) optical volume V_Φ, (f) projected area to optical volume ratio AV, (g) sphericity index S_p, (h) circularity index C, (i) average cell relative refractive index $\langle \Delta n_c \rangle$, (j) OPD variance σ_Φ, (k) OPD skewness Sk_Φ, and (l) OPD kurtosis Kr_Φ. The bars show the distribution obtained using the detection of phase isocontour, and the dashed-dotted line the distribution obtained with the WT maxima chain detection. Total number of cells: $N_{\text{cells}} = 326$.

suggest that the conditions in which we perform the DPM experiment are good enough to maintain human RBCs in a healthy state. This is particularly important at the moment of using our DPM setup to study the dynamics of single-cells, so we can be confident that if we observe a single cell with a global shape not so far to those observed so far (Fig.3.38), it will be a healthy cell.

3.7.2 Primary CD34+ cells

Now we pass to slightly more complicated cells, where we no longer encounter a quasi- homogeneous cytoplasm so we cannot assume a constant refractive index. As it has been said before, the primary cells CD34+ are cells sorted with the CD34 antigen from the bone marrow, resulting in a mixture of spherical mononucleated immature blood cells, with a high ratio between the nucleus and the cytoplasm. We show in Fig.3.40 some examples of CD34+ cells that we have imaged with DPM. We can easily see their spherical shape with the exception of some cases, like the cells on position E1 and E4, who seem to have lost their sphericity, maybe due to a stressed and non-optimal state of the cell. We start by looking at the geometrical pa-

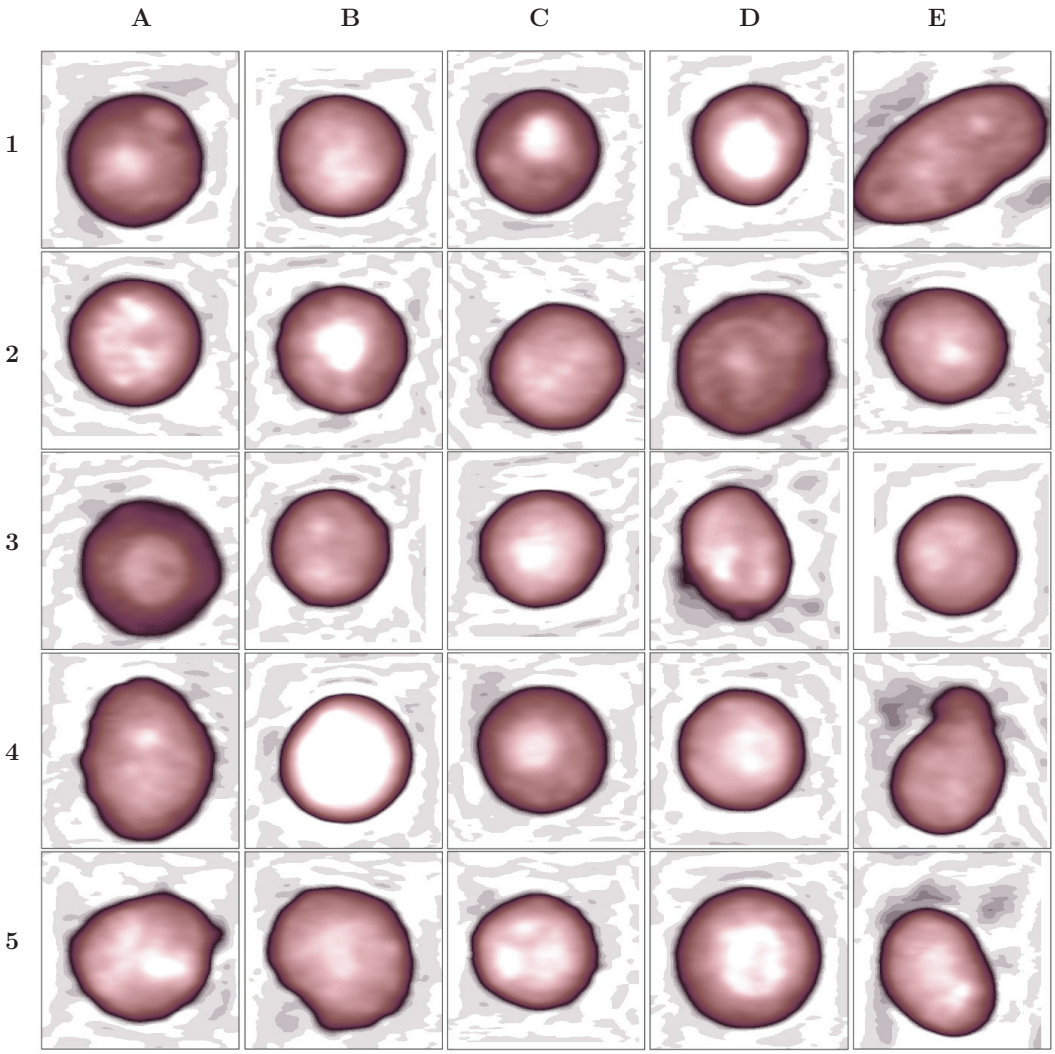

Figure 3.40 – **OPD images of living CD34+ primary cells.** Some representative examples of the type of cells imaged with DPM. The grid is composed of squares of 14.75μm, and $\Phi(x,y)$ has been colour coded as in Fig.3.36(a), from -5 nm (black) to 325 nm (light pink-white).

rameters computed from the detected cell boundary with both methods (Fig.3.41a-d). We see again the systematical shift to lower values and the narrowing of the distributions obtained with the WT maxima method. The CD34+ cells are slightly bigger than RBCs and they also show a higher dispersion in size (Fig.3.41a-c). They are in general more symmetric, as seen in their aspect ratio and circularity values (Fig.3.41d,h), but they seem to be separated into two groups, according to the two peaks observed on Fig.3.41(d), probably indicating two prominent shapes: highly circular cells and in less proportion, the elongated shaped cells, as it can be seen in the OPD images from Fig.3.40.

The division of cells into two subpopulations is observed again for the distribution of optical volume (Fig.3.41e). However, the two groups are not necessarily the same as the ones obtained when looking at the cells aspect ratio (Fig.3.41d). The low values of optical vol-

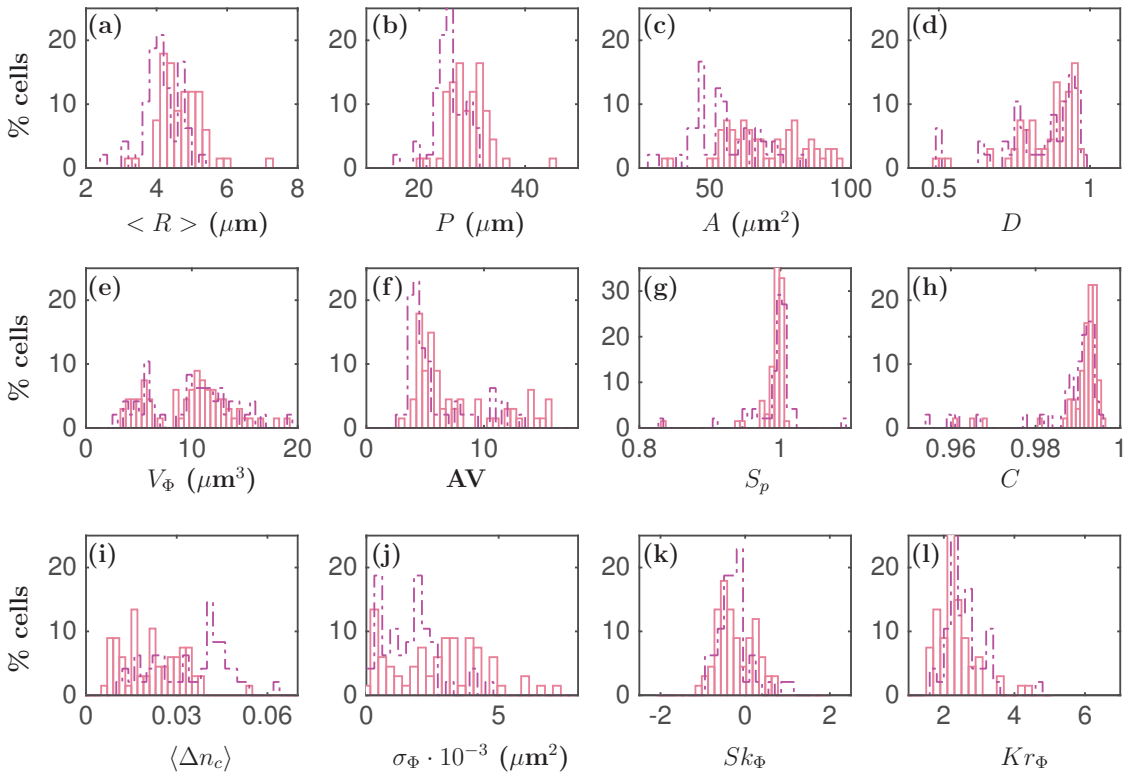

Figure 3.41 – **Morphological parameters of CD34+ cells.** Distribution of the geometrical values for (a) mean cell radius $< R >$, (b) perimeter P, (c) projected area A, (d) aspect ratio D, (e) optical volume V_Φ, (f) projected area to optical volume ratio AV, (g) sphericity index S_p, (h) circularity index C, (i) average cell relative refractive index $\langle \Delta n_c \rangle$, (j) OPD variance σ_Φ, (k) OPD skewness Sk_Φ, and (l) OPD kurtosis Kr_Φ. The bars shown the distribution obtained using the detection of phase isocontour, and the dashed-dotted line the distribution obtained with the WT maxima chain detection. Total number of cells: $N_{\text{cells}} = 70$.

ume, $V_\Phi < 10\mu m^3$, suggest that the cells falling in this group are not in good shape or even dead. Let's take as an example a cell with a mean radius $< R >= 4\mu m$ (Fig.3.41a), for it to produce an optical volume $V_\Phi = 5\mu m^3$, which is the centre of the first peak at the distribution in Fig.3.41(e), the cell needs to have a relative RI $\Delta n \sim 0.018$, leading to the cell RI of ~1.348, which is very low for a living mono-nucleated cell, who usually present a relative RI of ~0.03.

Note the quite big difference between the estimated relative RI from both methods (Fig.3.41i). The WT maxima method easily doubles the values obtained by the phase isocontours. This difference is a direct consequence of the detection of the border, and the tendency for the WT maxima method to retrieve smaller values for the mean radius (Fig.3.41a). In this case, we have a difference of at least 1μm for the mean radius computed from both methods, if we take for example a cell with an optical volume $V_\Phi = 10\mu m$, and a radius of either 4 or 5 μm, the estimated RI changes from $\langle \Delta n \rangle = 0.0373$ to $\langle \Delta n \rangle = 0.0191$. Based on the criteria of the estimated RI, it would seem that once again the WT maxima method surpasses the phase isocontour detection.

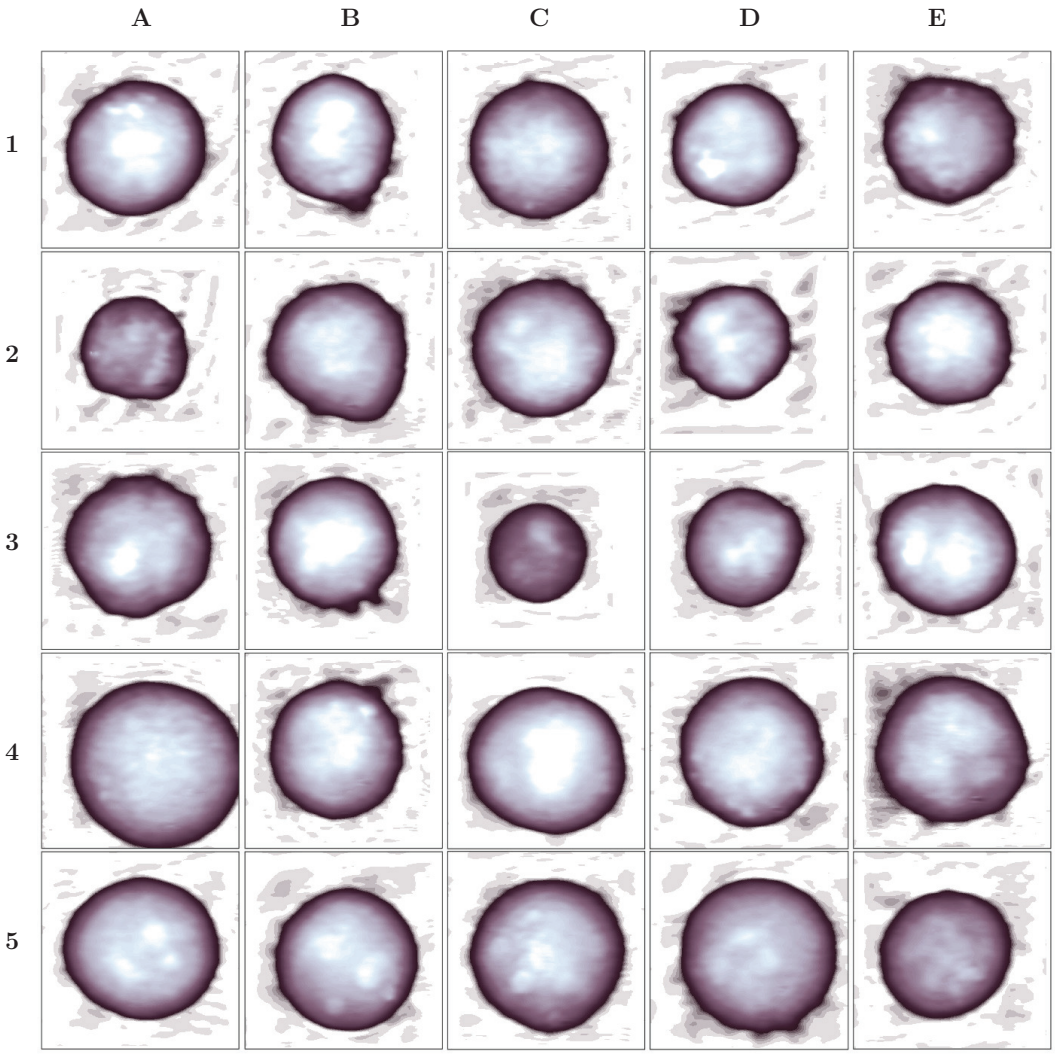

Figure 3.42 – **OPD images of living TF1-GFP cells.** Some representative examples of the type of cells imaged with DPM. The grid is composed of squares of 22 μm, and $\Phi(x, y)$ has been colour coded from -5 nm (dark purple -black) to 475 nm (light blue-white).

3.7.3 TF1 cell line: transformation induced by an oncogene and adherence

Primary CD34+ cells are much more difficult to maintain alive than laboratory cell lines. We used the TF1 cell line as model of immature CD34+ cells because it displays clongenic ability similar to human bone marrow CD34+ cells and is able to differentiate into myeloid lineages [256]. As compared to wild-type or transduced with an empty vector cells, BCR-ABL-transduced (CML oncogene) TF1 cells (TF1-BCR-ABL, short name: TF1-BA) increase their transcriptional levels of BCR-ABL and ABL [160]. These CML cell models were easier to maintain in culture and we have been able to increase therefore the statistics for comparing healthy (TF1-GFP) and transduced (TF1-BA) cells.

Figure 3.42 shows some representative examples of healthy TF1 cells. Although they are sig-

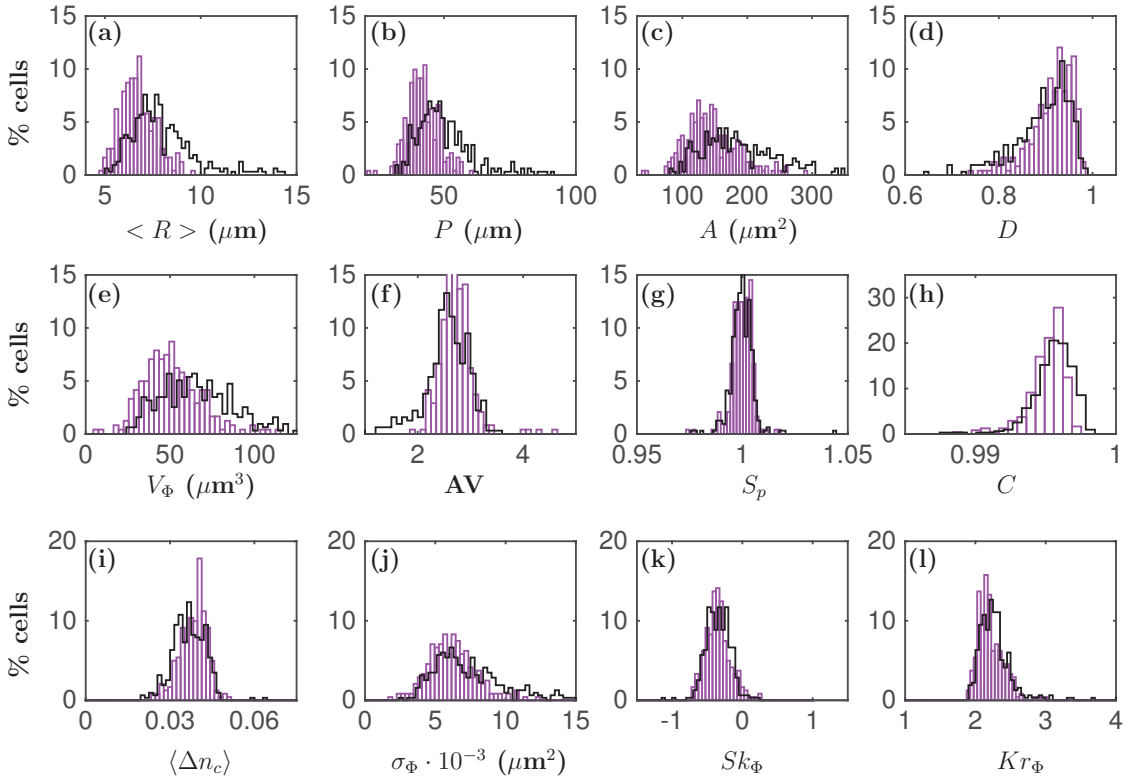

Figure 3.43 – **Morphological parameters of TF1-GFP vs. TF1-BA cells** Distribution of the geometrical values for (a) mean cell radius $< R >$, (b) perimeter P, (c) projected area A, (d) aspect ratio D, (e) optical volume V_Φ, (f) projected area to optical volume ratio AV, (g) sphericity index S_p, (h) circularity index C, (i) average cell relative refractive index $\langle \Delta n_c \rangle$, (j) OPD variance σ_Φ, (k) OPD skewness Sk_Φ, and (l) OPD kurtosis Kr_Φ. Bars: TF1-GFP cells, solid black line: TF1-BA cells. Total number of cells: $N_{\text{cells}} = 244$ for TF1-GFP and $N_{\text{cells}} = 327$ for TF1-BA.

nificantly bigger than the CD34+ cells (Fig.3.43a-c), we find now a more uniform cell shape with a high circularity and sphericity (Fig.3.43d,g,h). We show in Fig.3.43 the results obtained using the WT maxima method for healthy cells (TF1-GFP, shown in purple bars) and for cells transduced with an oncogene (TF1-BA, shown with a black solid line). The TF1-BA cells have increased in size, with $< R >= 8.027 \pm 1.79 \mu$m, with respect to $< R >= 6.808 \pm 0.94 \mu$m for TF1-GFP, which translates to an increase of nearly 18%.

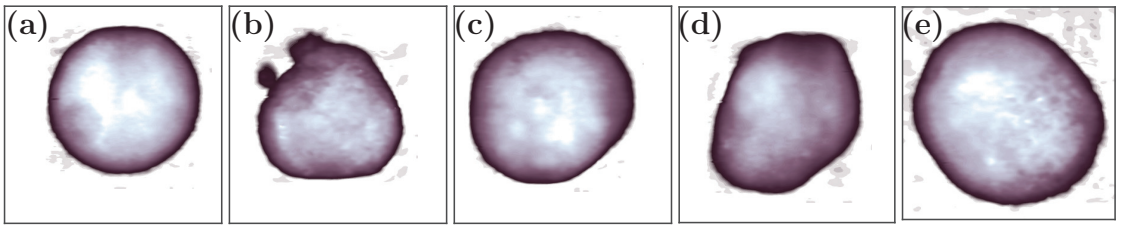

Figure 3.44 – **OPD images of TF1-BA cells clearly transformed by the oncogene.** The grid is composed of squares of 40 μm, and $\Phi(x, y)$ has been colour coded from -5 nm (dark purple -black) to 800 nm (light blue-white).

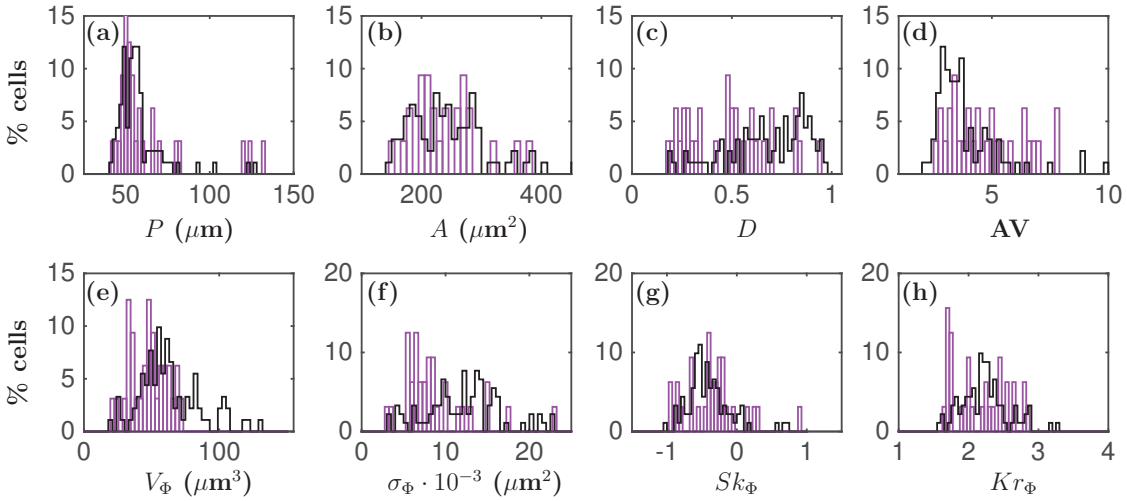

Figure 3.45 – **Morphological parameters of adherent TF1-GFP vs. TF1-BA cells** Distribution of the geometrical values for (a)perimeter P, (b) projected area A, (c) aspect ratio D, (d) projected area to optical volume ratio AV, (e) optical volume V_Φ, (f) OPD variance σ_Φ, (g) OPD skewness Sk_Φ, and (h) OPD kurtosis Kr_Φ. Bars: TF1-GFP cells, solid black line: TF1-BA cells. Total number of cells: $N_{\text{cells}} = 32$ for TF1-GFP, $N_{\text{cells}} = 91$ for TF1-BA.

Surprisingly, even if the optical volume tends also to increase (Fig.3.43e), we see a slight decrease on the mean RI of TF1-BA cells (Fig.3.43i), with $\langle \Delta n \rangle = 0.0367 \pm 0.005$, who compared to the relative RI of TF1-GFP cells $\langle \Delta n \rangle = 0.0391 \pm 0.005$ represents a difference of roughly -3%. However, this difference takes into account all the population of cells, and it is very likely that not all the cells have been transformed by the oncogene. If we base our first criteria on the cell mean radius to distinguish between transformed and healthy cells, by choosing only those cells with a mean radius bigger than 9 μm (Fig.3.43a, and Fig.3.44), the selected TF1-BA (20% of the total cell population), present a mean relative RI of $\langle \Delta n \rangle = 0.0326 \pm 0.004$, being a difference of almost 9% with the RI of TF1-GFP cells.

It has been observed that some of the most noticeable differences between TF1-GFP and TF1-BA cells occurs when they are cultured on a fibronectin-coated surface, as adhesion reveals strong alterations of their cytoskeleton contractility, where the transformed cells loose their ability to mature adhesion by the formation of actin stress fibres, empeded by the formation of small actin aggregates [189], in agreement with the reported ability of BCR-ABL to decrease progenitor cell adhesion to the BM stroma [257]. Therefore, we have imaged TF1-GFP and TF1-BA cells that have been cultured on a fibronectin-coated glass surface. Indeed, we observe notable differences on the quantities that reflect the level of adhesion, that is, the aspect ratio D, and the area to optical volume ratio AV (Fig.3.45c-d). It appears that TF1-BA cells maintain a more rounded shape, meaning that they have lost their ability to spread, whereas TF1-GFP cells do show a more flattened profile, as indicated by their high area to optical volume ratio (Fig.3.45d).

Figure 3.46 shows some examples of clearly transformed TF1-BA cells and adherent TF1-GFP

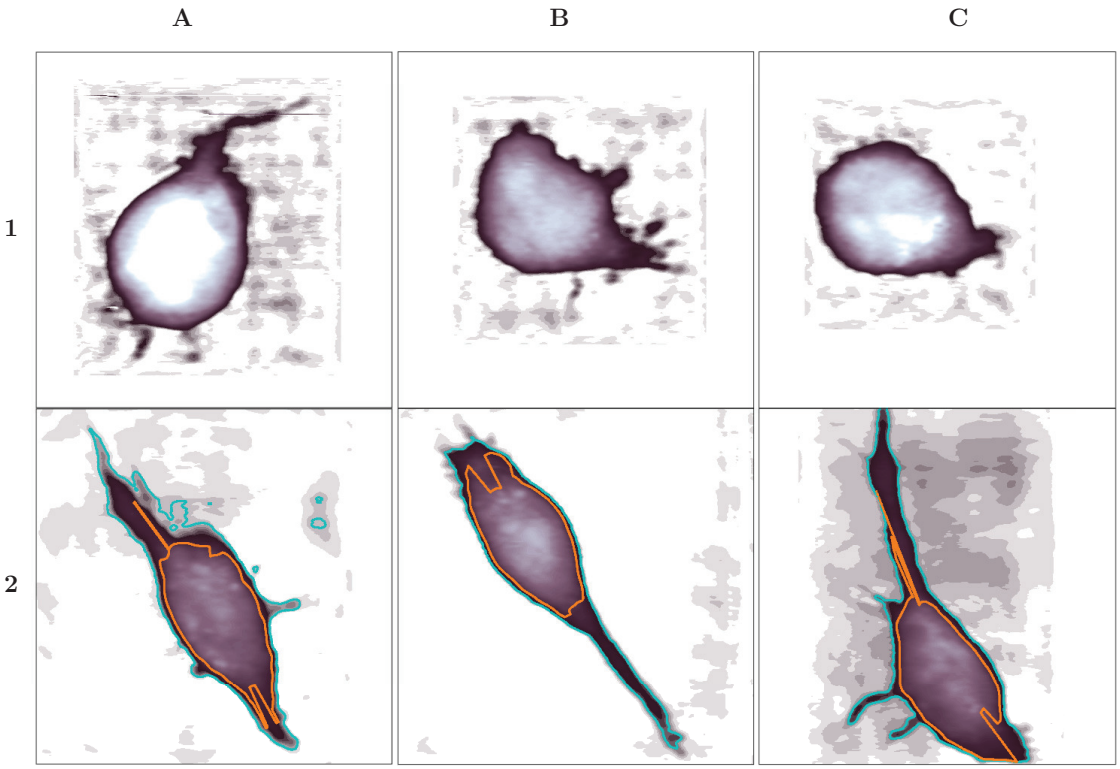

Figure 3.46 – **OPD images of adherent TF1-GFP vs. TF1-BA cells clearly transformed by the oncogene.** The grid is composed of squares of 45 μm, and $\Phi(x, y)$ has been colour coded from -5 nm (dark purple -black) to 450 nm (light blue-white). In the second row, the teal line indicates the contour detected with the phase isocontour method, and the orange line shows the contour detected with the WT maxima method.

cells. While the healthy cells (2nd line in Fig.3.46) present a very elongated form as a result of mature adhesion and spreading, the transformed cells remain in a quite regular rounded shape with small protrusions on the side, indicating that they may be adherent, but incapable of spreading as their healthy counterparts.

When extracting the morphological parameter of adherent cells we have used the border detection based on phase isocontours. As it can be seen on the second row of Fig.3.46, the detection with the WT maxima method (orange contour lines) often detects incorrectly the cell border, neglecting the thinner parts of the cell, such as the protrusions characteristic of adherent cells, as they present a low OPD gradient, particularly compared to the nuclear part of the cell. The phase isocontours, on the contrary (blue contour lines on Fig.3.46), appear to have a much better performance on this kind of cells, as it is shown with the cell on position C2.

It is important to say that the WT maxima method can be improved and adapted to correctly detect the contours on adherent cells by, for example, applying a multi-scale approach, or by imposing robust rules in a more complicated algorithm to enchain the WT maxima lines that correspond to the outer contour. However, most of the solutions proposed will certainly in-

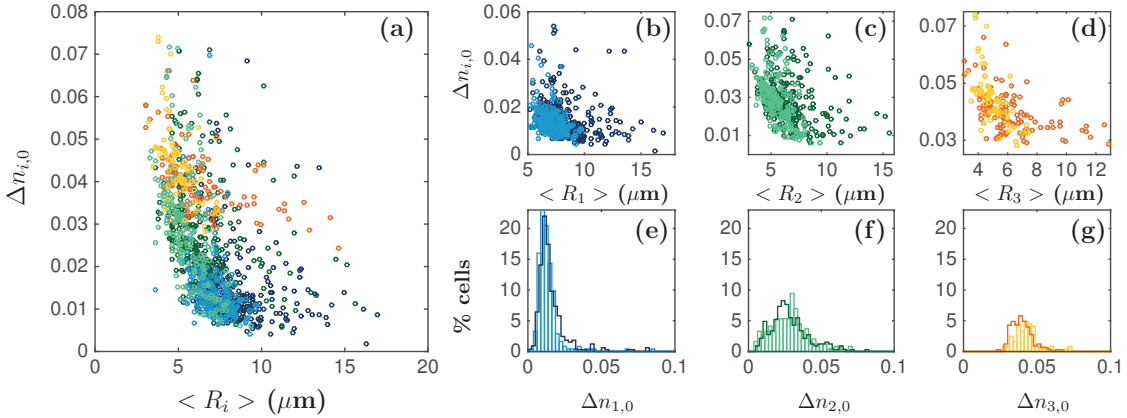

Figure 3.47 – **Cell segmentation of healthy and cancer TF1 cells based on isophase contours.** (a) Dispersion plot of the relative RI $\Delta n_{i,0}$ versus the mean radius $< R_i >$, for the first three intracellular regions: blue - C_1, green - C_2, and orange C_3. The darker colours show the data from TF1-BA cells, and the light colours represent the TF1-GFP cells. (b-d) Same as (a) showing each region separately. (e-g) Distribution of relative RI of each intracellular region.

crease significantly the computation time. Given that our main goal is the study of single-cell dynamics, we will choose the detection of phase isocontours as a good compromise between the quality of the border detection and the computation time.

3.7.3.a Intracellular structure characterisation

We start by detecting the phase isocontours to delineate the intracellular regions with a similar RI, according to the method explained in section 3.6.2. To being able to apply the multi-sphere model to estimate the RI of each region, we have chosen a circularity index $C \geq 0.99$ as a validity criteria of the detected contour. Figure 3.47 shows the results obtained from 244 TF1-GFP cells and 327 TF1-BA cells. We have limited our analysis to the first three segmented intracellular regions, and we report the total relative RI of each region, that is, the RI relative to the extracellular medium n_0, and not to the medium of the precedent layer.

As expected based on the previous results, we encounter a more spread distribution of values for TF1-BA cells, when compared to TF1-GFP cells. However, we see almost no difference between both cell types on the estimated RI of the first two layers (Fig.3.47b,c,e,f). The third layer on the contrary, shows a slight decrease on the estimated RI for TF1-BA cells, in agreement with our previous observation on the smaller RI at the whole cell level (Fig.3.43i). Unfortunately, it is not possible for us to conclude any transformation induced by the oncogene on TF1-BA cells with this method, confirming that the heterogeneity of the intracellular structure on this type of cells (TF1 cell line) is poorly adapted for a proper characterisation with a multi-sphere model.

We have performed the WTMM chain detection analysis on two large sets of TF1-GFP (294) and TF1-BA (216) cells and we computed the statistical distributions of the angle difference $\Delta\theta$, the number of chains per cells $\overline{N_{\mathcal{M}}}$, and the chain length $L_{\mathcal{M}}$ (Fig.3.48). The oncogene

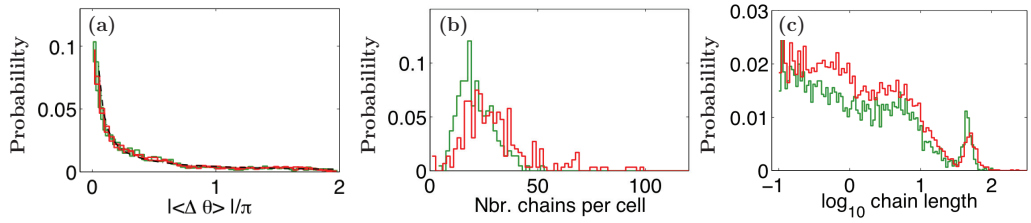

Figure 3.48 – **Statistical analysis of cell structural parameters from the WTMM analysis of control and cancer TF1 cells.** (a) Distribution of $\Delta\theta$ values. (b) Distribution of the numbers of chains per cell $\overline{N_{\mathscr{M}}}$=21±7 for TF1-GFP cells and $\overline{N_{\mathscr{M}}}$=30±9 for TF1-BA cells. (c) Distribution of chain lengths, $\log_{10}(L_{\mathscr{M}})$ of the length in μm. The green lines are obtained from a set of 294 TF1-GFP cells, and the red lines show the results from a set of 216 TF1-BA cells.

transduction seems to increase the variability of the cell structural properties.

The distribution of angle differences $\Delta\theta$ follows a power law distribution $P(\Delta\theta) \propto |\Delta\theta|^{-\alpha}$, with $\alpha = 1$. The fact that the shape of this distribution does not change when switching from control to oncogene-transduced TF1 cells means that the statistics of angular orientation of the maxima chains are not immediately impacted by the cell transformation. In contrast, the number of chains per cell is affected by oncogene transduction. The median value of the two distributions in Fig.3.48(b) increases from 21 to 30 chains per cell (considering only the chains of length larger than 100 nm). Again we observe that the distribution of these chain numbers of TF1-BA cells is more spread than for control TF1-GFP cells. The distribution of length of these chains (above 100 nm) follows a smoothly decreasing (logarithmic decrease) function for chains smaller than 5 μm, which drops rapidly to zero for larger chains. The peak popping up around 45 μm corresponds to the outer chain length, the slight flattening and shifting to higher values of this peak for transduced TF1-BA cells means that the circumference of these cells increases (as their radius) and is more variable than for non transformed cells. This observation corroborates our previous remarks on the cell radius distribution (Fig.3.43a).

3.7.4 Adherent cells: Myoblasts C2C12 and hepatocytes HepG2

Myoblasts are precursors of muscle cells, upon differentiation they elongate and fuse to form myotubes. C2C12 is a laboratory cell line of mouse myoblasts. These cells are naturally adherent, they do not require a special treatment of the surface to be able to adhere and spread, although as most of the adherent cells, a substrate closer to physiological conditions, such as collagen, will promote adhesion maturation.

We have imaged a sample of myoblasts cultured on a glass-bottom petri dish, without any treatment of the surface. Figure 3.49 shows some representative examples of C2C12 cells. Notice that we have inverted the colour coding, such that the darkest colours correspond to the highest OPD. This choice of colour scale enhances our contrast perception and allows to observe with more detail the intracellular structures. Most of these cells show a very elongated and almost uniaxial shape, with a clear distinction of their nuclear part, and in some cases we can even appreciate the distribution of the intranuclear material.

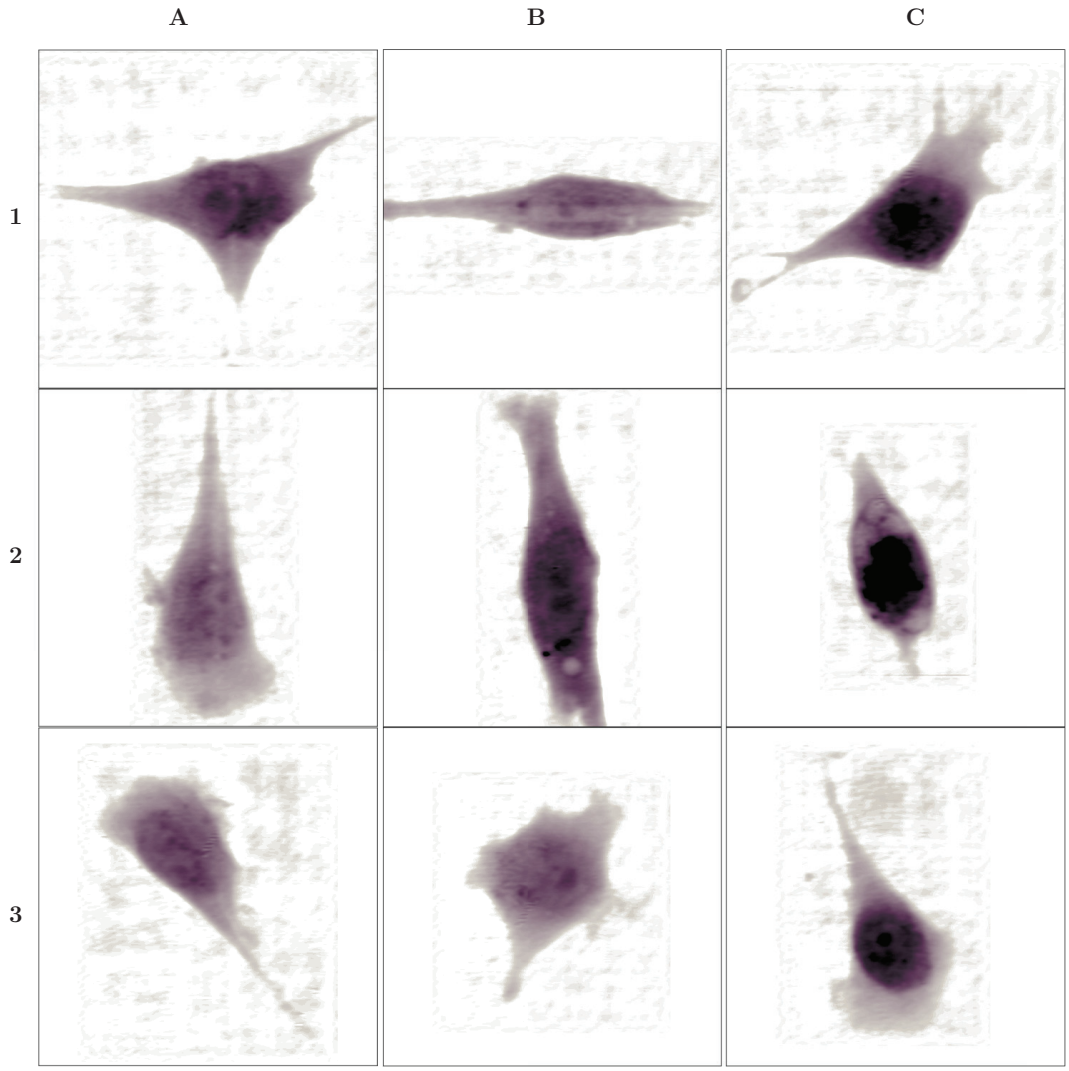

Figure 3.49 – **OPD images of living myoblasts.** Some representative examples of the type of cells imaged with DPM. The grid is composed of squares of 68 μm, and $\Phi(x, y)$ has been colour coded from -5 nm (light-grey) to 400 nm (dark purple-black).

As for the adherent TF1 cells, we use the border detection based on phase isocontours to characterise the cell morphology (Fig.3.50). Unfortunately we did not imaged a high number of cells ($N_{\text{cells}} = 29$) so we cannot conclude much about the results. We observe a wide dispersion on the distributions of the geometrical values of the projected cell area (Fig.3.50a-d), but the optical volume shows a quite narrow range of values with the exception of some cases (Fig.3.50e), resulting in $< V_\Phi >= 68.85 \pm 18.6 \mu\text{m}^3$, which is not that different from the TF1 cell line. Probably the variability encountered on the morphological parameters is caused by an asynchronous state on the cell cycle, as cells preparing to divide will start to loose adherence and to adopt a more rounded shape.

Myoblasts present what is probably the most intuitive OPD image for an adherent cell, with

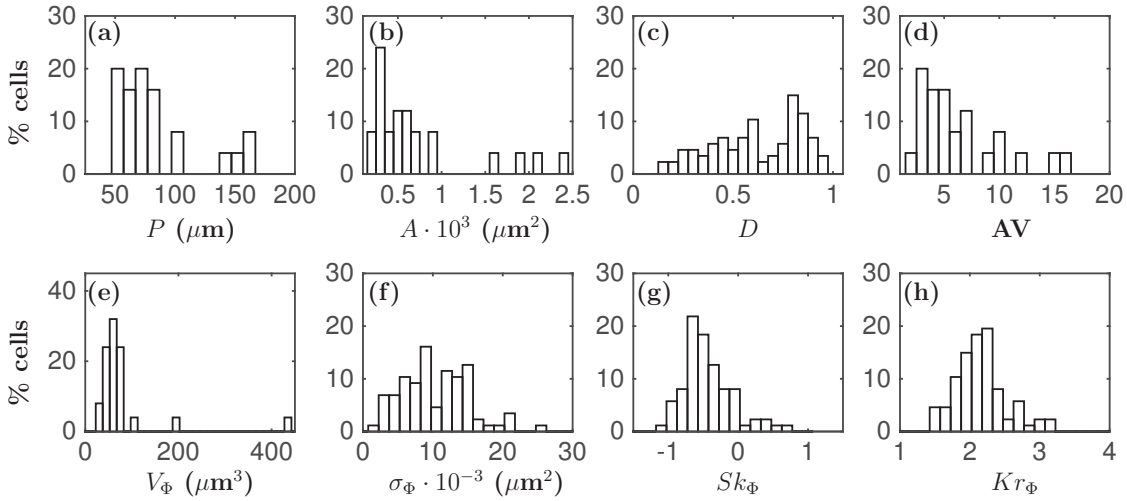

Figure 3.50 – **Morphological parameters of adherent C2C12 myoblasts.** Distribution of the geometrical values for (a) perimeter P, (b) projected area A, (c) aspect ratio D, (d) projected area to optical volume ratio AV, (e) optical volume V_Φ, (f) OPD variance σ_Φ, (g) OPD skewness Sk_Φ, and (h) OPD kurtosis Kr_Φ. Total number of cells: $N_{\text{cells}} = 29$.

the OPD practically following the cell shape, in other words, the changes in the cell thickness are far more important than the variations on the cell composition, or refractive index, with the exception of the nuclear part. It is interesting to compare myoblasts to another type of adherent cells that show a very different morphology.

To show in a qualitatively manner another type of cell morphology, we have imaged living HepG2 hepatocytes cultured on a glass-bottom petri dish treated with collagen to enhance adhesion. HepG2 is a human carcinoma cell line that presents a high concentration of lipidic structures around the nuclear area. As it can be seen in Fig.3.51, these structures cause a strong variation on the OPD image, and they can lead to an OPD higher than the one of the nuclear part. This effect is quite interesting as we are faced with variations on the intracellular material that might be as important as the variations of the cell thickness, challenging the interpretation of the OPD image. Cells with this type of morphology are particularly difficult to image with DPM. The small lipidic structures will produce a high and fast variation on the optical phase that the phase recovery method might fail to follow, as it is the case for the cell 2A on Fig.3.51. One possible solution is to increase the magnification of the microscope in such a way that we have more fringes per μm and the changes on the phase will be slower. However, this magnification implies reducing the field of view, and as hepatocytes are spreading on the surface, this will likely imply to be able to image only a part of the cell. Thus, although hepatocytes are a really intriguing type of cells, they require to revisit the design of our setup to optimise the imaging conditions, and therefore, we are unable to present a proper statistical study with our current setup.

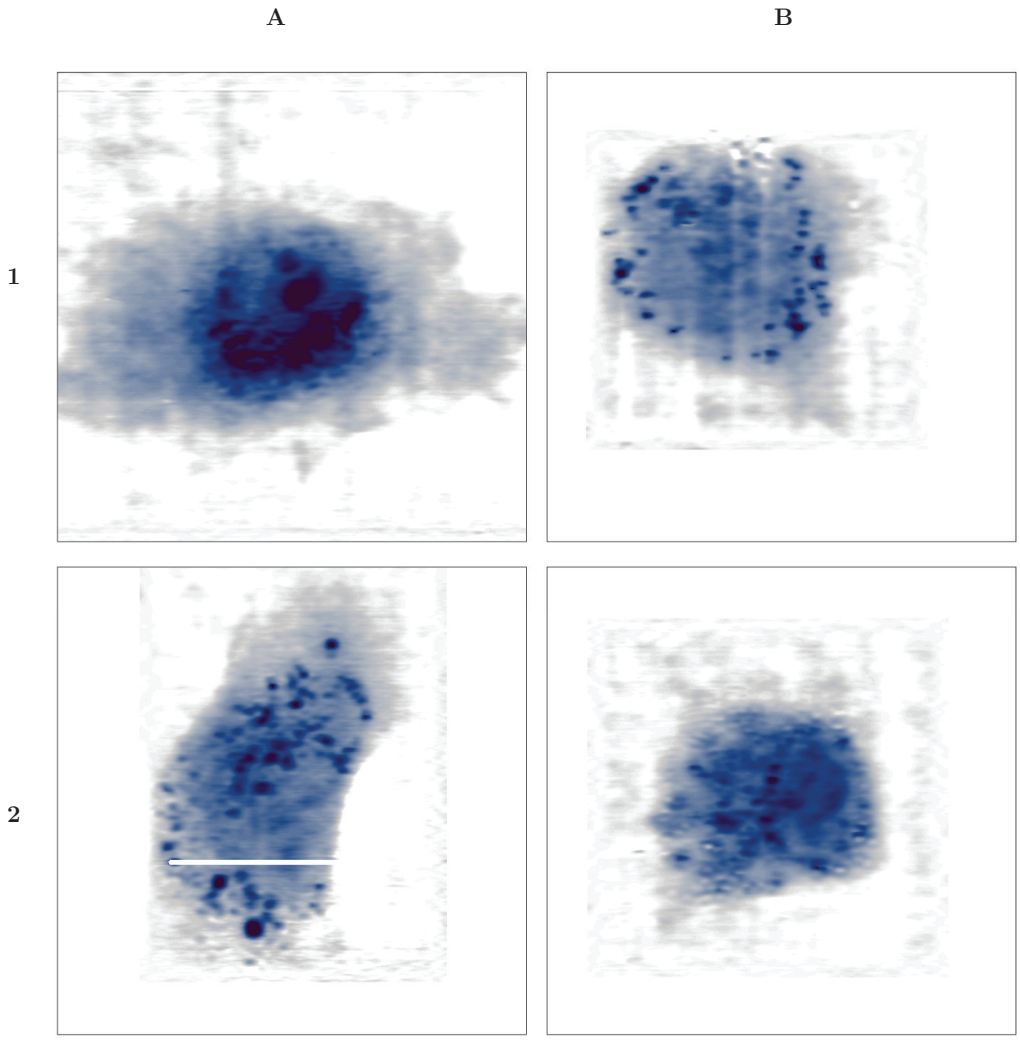

Figure 3.51 – **OPD images of living hepatocytes.** Some representative examples of the type of cells imaged with DPM. The grid is composed of squares of 54 μm, and $\Phi(x, y)$ has been colour coded from -5 nm (light-grey) to 300 nm (dark blue).

3.8 Living cell dynamics

3.8.1 Healthy and leukaemic Red Blood Cells

We recorded a temporal data series for a single healthy RBC and a RBC from a sample obtained from a patient with CML. The DPM images were recorded in FBS serum, with an acquisition rate of one image every 3 ms, with a total number of images of 8192. This implies that we are looking at a frequency range of 10 Hz$<f<$300 Hz. All the images have been processed using the WTMM method for phase extraction, corrected for a tilt on the xy plane, and the cell contour has been detected using the WTMM chain method. Then, we can track the cell movement on the xy plane by extracting the position of the cell centre of mass. Figure 3.52 shows the temporal evolution of the cell position in the x (black curve) and y direction

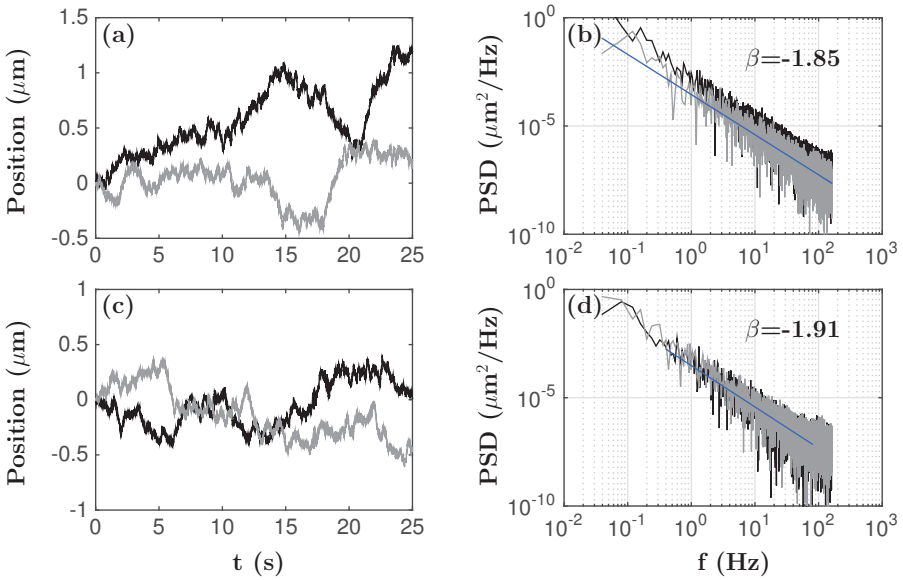

Figure 3.52 – **Temporal evolution of the cell position of healthy and leukaemic RBCs.**(a) The cell position from a healthy RBC in x (black curve) and in y (grey curve) is shown as a function of time. (b) PSD of x(t) (in black), and y(t) (in grey). The blue line shows the linear fit. (c-d) Same as (a-b) for a CML RBC.

(grey curve) separately, as well as the PSD curve of each trajectory. We perform a linear fit of the $\log_{10}$(PSD) vs. $\log_{10}(f)$, in the form:

$$\log_{10}(PSD) = \beta \log_{10}(f) + A \tag{3.75}$$

therefore, β is a scaling exponent such that

$$PSD \propto f^{\beta} \tag{3.76}$$

The scaling exponent β can be used to described the type of motion of our object. Let's take as an example three types of signals: white noise, $1/f$ noise also called pink noise or flickering, and a brownian signal. White noise ($\beta = 0$) is a completely uncorrelated signal produced by a random superposition of uncorrelated jumps (steps). Brownian motion ($\beta = -2$), on the other extreme, is the integral of a white noise, it is obtained by a 'random walk' process: the position of the particle at some time $t+1$ is the result of adding a random step to its previous position, similar to the thermal effect of a fluid on a particle. In between we encounter pink noise or flickering. $\beta = -1$ separates two different types of behaviours. When $-2 < \beta < -1$, we have a trajectory, like a brownian walk, called fractional brownian motion, where the steps of the walk are persistent. If $-1 < \beta < 0$ the signal is discontinuous, made of antipersistent jumps.

We do not observe any major difference between the cell displacements. Both of them present β ~-2, typical of brownian motion. Although, the leukaemic RBC has a reduced frequency range with this scaling exponent (Fig.3.52d).

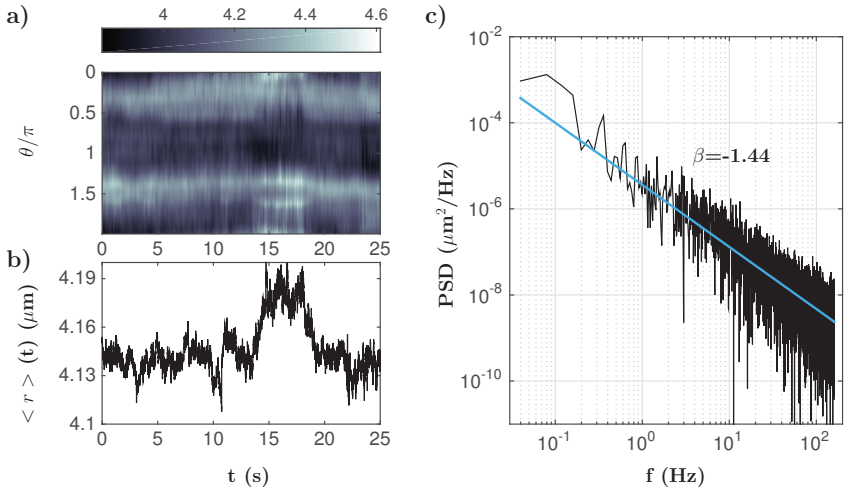

Figure 3.53 – **Deformation of a healthy RBC.** (a) Temporal map of the cell contour, where $r(\theta)$ has been colour coded. (b) Mean radius $< r(\theta) > (t)$. (c) PSD of the mean radius shown in (b). The blue line shows the linear fit.

Next, we look at the deformation of the cell on the xy plane by measuring its mean radius $< r(\theta) > (t)$. We show in Fig.3.53(a) the complete detected cell contour, where the $r(\theta)$ has been colour coded. We can notice a slight asymmetry of the cell, producing the two light/-dark bands on the image. We see no noticeable cell rotation, and only a sudden increase in size at t=15-20 s. As it can be seen in Fig.3.53(b), this sudden increase is inherent to the cell and not a result of the contour detection method, as it occurs in a gradual manner, and not as a single jump. For the leukaemic RBC we do not encounter this sudden increase in the cell size, presenting a slightly more uniform mean radius along time. However, we find again that both cells behave in a very similar way, with a scaling exponent $\beta \sim -1.5$, indicating the

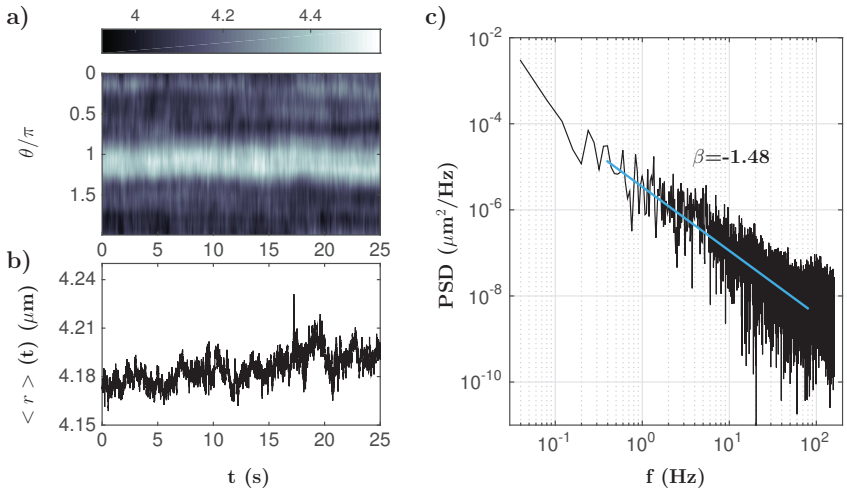

Figure 3.54 – **Deformation of a CML RBC.** (a) Temporal map of the cell contour, where $r(\theta)$ has been colour coded. (b) Mean radius $< r(\theta) > (t)$. (c) PSD of the mean radius shown in (b). The blue line shows the linear fit.

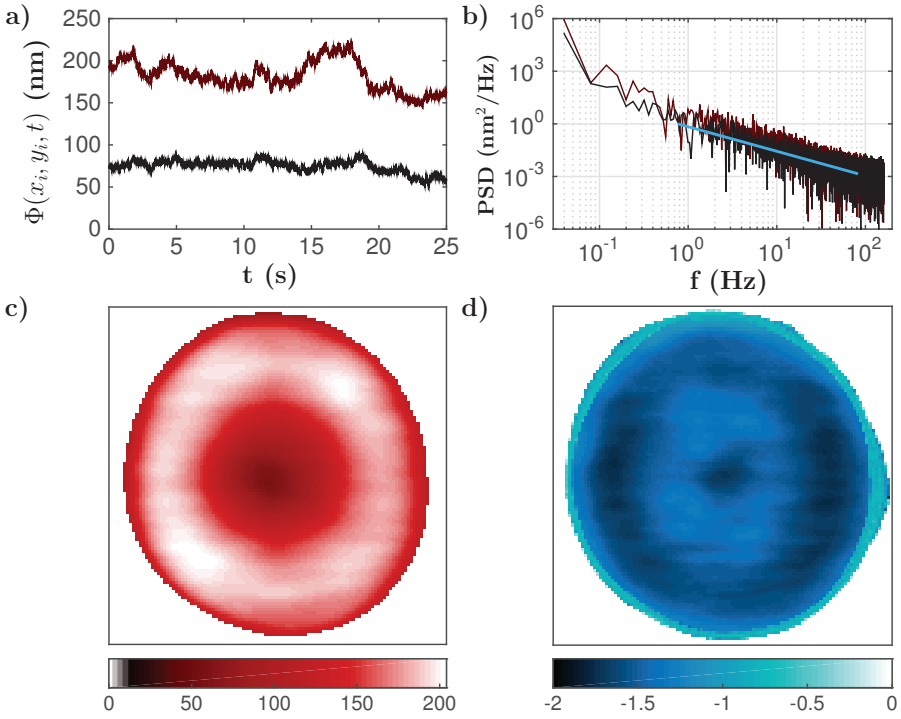

Figure 3.55 – **Spatial distribution of the OPD scaling exponent for a healthy RBC.** (a) $\Phi(t)$ for two positions inside the cell: black line - cell centre, red line - left side on the maximum of the phase profile shown in (c). (b) PSD(Φ) of the signals shown in (a). (c) RBC OPD image at the initial time $t = 0$, where Φ (nm) has been colour coded. (d) Spatial distribution of the scaling exponent β.

presence of flicker noise, which is a characteristic behaviour of RBCs.

The deformation of the cell on the xy plane could also be analysed regarding the spatial frequency, similar to the method developed by Evans *et al* [258]. They used a bright-field microscope to image the membrane fluctuations of RBCs, and they extracted the excursion of the cell edge from the mean position, $U_{\theta,t}$. Then, the Fourier transform of U in space gives the mean-square amplitude as a function of the wave number mode q, following the general form of $\langle U_q^2 \rangle \propto q^{-\mu}$. The exponent μ indicates whether the fluctuations are dominated by the bending modulus ($\mu \sim 3$), or by the membrane tension ($\mu \sim 1$). Using theoretical models, the membrane fluctuations can be used to compute the bending modulus or membrane tension. Unfortunately, we did not have time to complete this analysis, although preliminary results show a power-law $\mu \sim 2.7$ for 3<q<8, suggesting that the bending modulus is predominant, in good agreement with the work of Evans *et al* [258].

The following step focus on the phase fluctuations. Figure 3.55(a) shows $\Phi(t)$ for the position at the centre of the cell (black curve), and at the left side (red curve), taken at the maximum of the 'donut' shape. It is important to mention that we have chosen both cells with a discocyte shape (Fig.3.55c), which is the most natural RBC shape, avoiding strange effects induced by the morphological state of the cell.

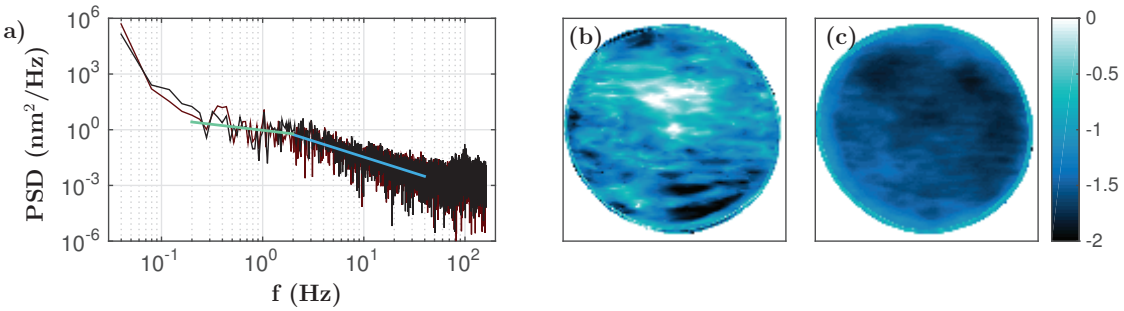

Figure 3.56 – **Spatial distribution of the scaling exponents of a CML RBC.** (a) PSD(Φ), where the green line indicates the first fitted interval to extract β_1, and the blue line indicates the second fit interval (β_2). (b) Spatial distribution of β_1. (c) Spatial distribution of β_2. In (b,c) β has been colour coded with the same colour scale.

Recall that for each pixel we have an OPD(t) signal, we then compute the PSD of Φ(Fig.3.55) at each pixel in the image, Hence, we can reconstruct an image showing the scaling exponent found for that position, as shown in Fig.3.55(d). Notice that β seems to follow somehow the cell morphology, as it is easy to recognise the 'donut' shape of the cell. The band around the cell with $\beta \sim -1$ reflects the fact that we are particularly sensible at this region of the cell, as it has a strong OPD gradient. Inside the cell we encounter an exponent -1.5≤ β ≤-2, consistent with values reported in the literature [253, 259–261].

Interestingly, when we look at the leukaemic RBC, we find that the PSD of Φ is quite different (Fig.3.56a). In this case we do not encounter only one scaling exponent, but two, with a clear cutoff at $f \sim 2$Hz. Moreover, there seems to be no morphology follow-up by the scaling exponent, at any of the frequency intervals (Fig.3.56b-c). Additionally, we see the appearance of a weak resonant peak at $f \sim 100$Hz. Based on the results obtained from the OPD data, we find three possible markers of CML RBCs: (i) a cross-over on the PSD curve, happening at $f \sim 2$Hz, with β going from -0.5 to -1.5, (ii) the loss of a morphological signature of the scaling exponent β, and (iii) the appearance of a resonant peak at $f \sim 100$Hz. It has been proposed that the cut-off on the frequency dependence is related to thermodynamical equilibrium [262]. At high frequencies ($f > 10$Hz), the equilibrium thermodynamics is dominant, whereas at lower frequencies, the nonequilibrium effects become apparent, and there is a bigger effect coming from the composition of the membrane and its elasticity. This could implicate that LMC RBCs have a different membrane elastic behaviour and/or composition. Further experiments are required to conclude about the occurrence of any of these events.

3.8.2 TF1 cell line: round-shaped cells with a complex internal structure

A data set of DPM images for 4 different TF1-GFP cells was recorded at different acquisition rates. For the first two cells (cell 1 and cell 2), the total time series is composed of 8100 images, plus a reference image taken in a zone where there is no cell to subtract the effects of the background. The acquisition rate was set to either 50 images/second (cell 1) or 10 images/second (cell 2).

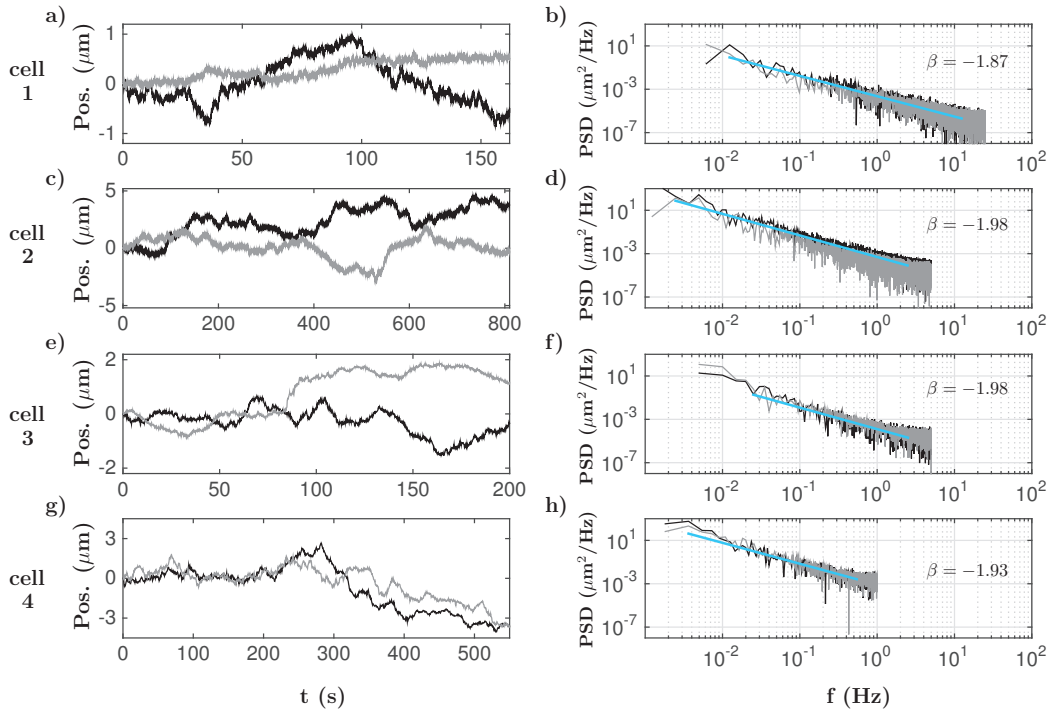

Figure 3.57 – **Temporal evolution of the cell position of TF1-GFP cells.** (a,c,e,g) The cell position in x (black curve) and in y (grey curve) from different TF1-GFP cells is shown as a function of time. (b,d,f,h) PSD of x(t) (in black), and y(t) (in grey) of the signals shown in (a,c,e,g). The blue line shows the linear fit. Each line represents the data for one different cell.

To improve the detection of intracellular structures, we have increased the spatial transverse resolution of our DPM setup by changing the microscope objective, from 40x to 100x. Using this configuration, we have recorded a time series for two other TF1-GFP cells (cells 3 and 4) with an acquisition rate of 10 images/second or 2 images/s, respectively. We reduced the acquisition rate to have an efficient data processing, as the region of the image treated is now at least twice as large, requiring more computation time. Also for this reason, we have reduced the total number of images to 2000 (cell 3) and 1100 (cell 4). We employ the contour detection using the WTMM method, and we correct the phase tilt for each image.

Figure 3.57 shows the temporal tracking of the cell position as well as its power spectrum, where again we find a scaling exponent $\beta \sim -2$ indicating brownian noise. Note that the cell position in X shows in some cases a modulation at low frequencies (black curve in Fig.3.57c,e), with the signal oscillating with a period $\sim$ 200-300 s for cell 2 (Fig.3.57c), and $\sim 30s$ for cell 3 (Fig.3.57e). For cell 4 we see an initial 'steady' state followed by a continuos drift (Fig.3.57g). Perhaps this drift is compensated at longer times, resulting on the slow motion that we saw before for the other TF1-GFP cells. However, when we look at the cell contour tracking in Fig.3.58(b,d), we can recognise a rotation motion that seems consistent with the motion seen for the cell displacement on the x direction. Unlike the scaling exponent, this low-frequency motion is not robust enough to be present in the data collected from all the cells, perhaps for

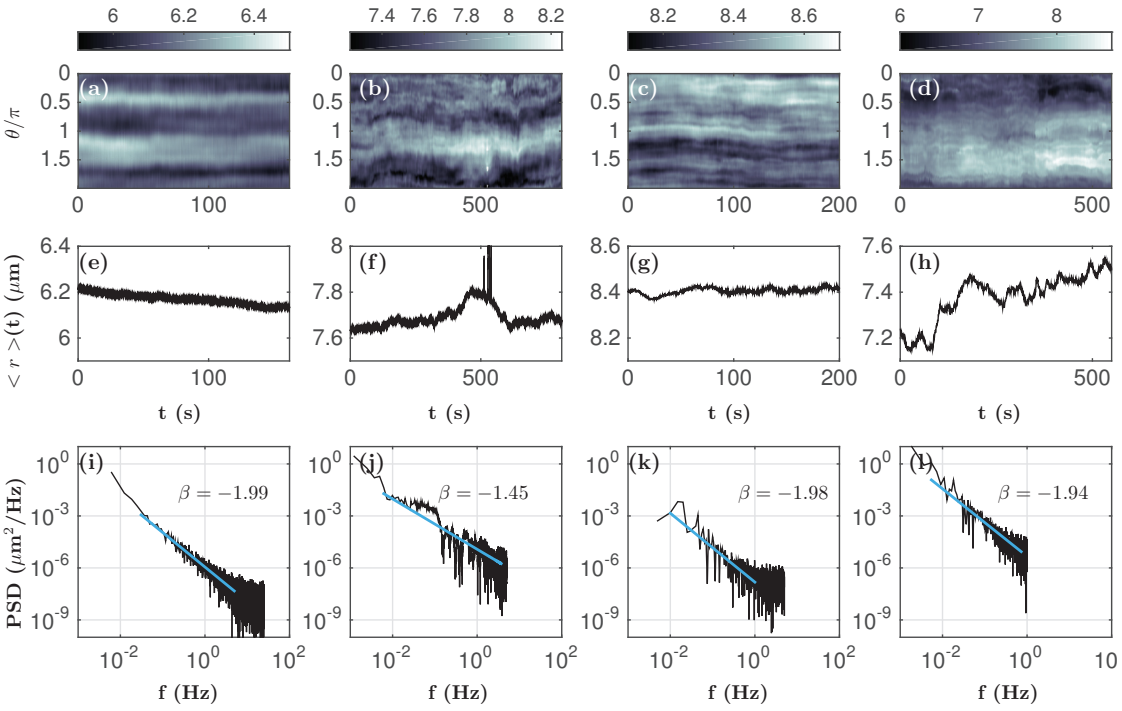

Figure 3.58 – **Deformation of TF1-GFP cells.** (a-d) Temporal map of the cell contour, where $r(\theta)$ has been colour coded. (e-h) Mean radius $< r(\theta) > (t)$ of the maps shown in (a-d). (i-l) PSD of the mean radius shown in (e-h). The blue line shows the linear fit. Each column presents the data of one different cell.

the limited duration of the recording. If other cells also show this slow displacement/rotation motion, they could do so at even lower frequencies and thus it will be not measured with the chosen recording time.

The fluctuations of the cell mean radius (3.58e-h) are significantly larger than those encountered for a RBC. It is not clear at this point if this fluctuations are truly the cell membrane fluctuations, or they have been amplified by the contour detection method. Again we encounter a value $\beta \sim -2$, with the exception of cell 2 (Fig.3.58j), which is closer to -1.5. This scaling behaviour is limited to the frequency interval [0.01Hz,2Hz]. However, there seems to be a difficulty to correctly detect the contour of this particular cell, as shown by the sudden jumps in the mean radius signal of Fig.3.58(f).

In an unexpected result, the cell 4 which is less asymmetric (Fig.3.58d), appears to increase continuously in size, as shown in Fig.3.58(h). In spite of that, we still recover a scaling exponent consistent with the data from other cells. Interestingly, we see a clear frequency cut-off at $f \sim 1$ Hz for cell 3 (Fig. 3.59k). This cell also presents a quite homogeneous shape along the whole time series (Fig. 3.59c,g), showing a slight different behaviour from the other cells, likely related to a difference in their mechanical properties.

Figure 3.59 shows $\Phi(t)$ for a point at the cell center. Notice that this time, the value of the exponent β and the range of frequencies where it occurs is far more variable between the cells.

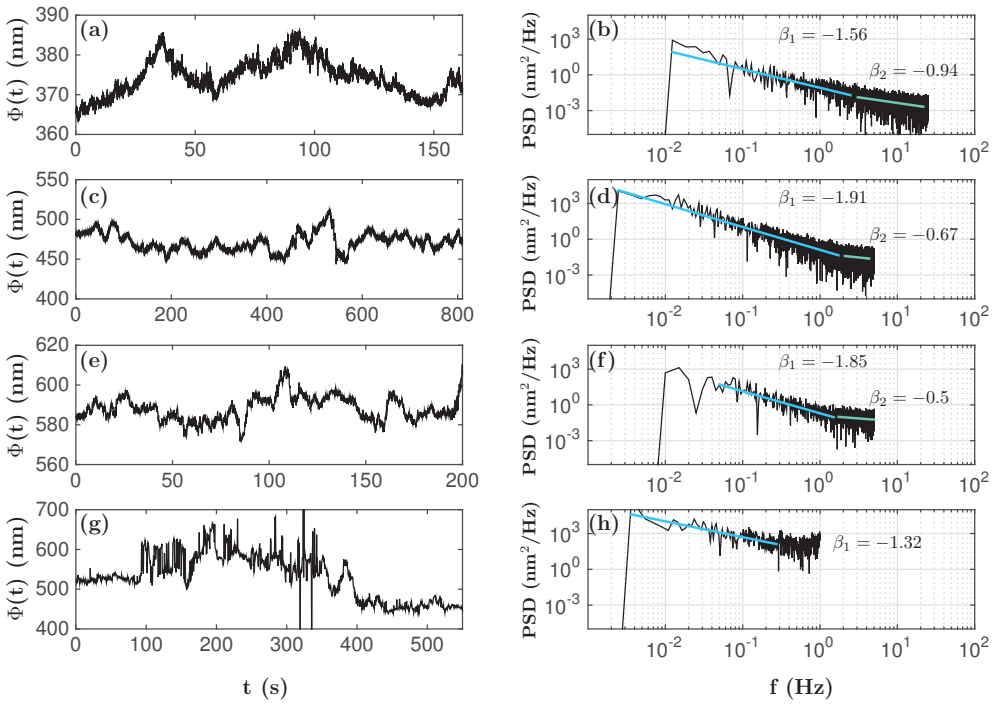

Figure 3.59 – **OPD scaling exponent for a TF1-GFP cells.** (a,c,e,g) $\Phi(t)$ for a point corresponding to the cell centre. (b,d,f,h) PSD(Φ) of the signals shown in (a). Each line corresponds to a different cell.

Nevertheless, we find a quite robust frequency cut-off at $f \sim 1-3$ Hz, which is more evident for cell 3 (Fig.3.59f). We also note that the scaling exponent β has significantly increased, approaching more to a value -2, and less to a flicker noise, as it was the case for RBC cells. In a surprising result, we observe a very noisy OPD signal for cell 4 (Fig.3.59g). This could be a consequence of the improved resolution, such that we are more sensitive to small movements of the intracellular structure. However, this is very unlikely, as fluctuations are too large too be just the result of the intracellular movement. It is more probable that is an unwanted effect of the cell re-positioning and/or the correction of the phase tilt. The scaling exponent of the PSD, $\beta \sim$-1.3 (Fig.3.59h) is smaller (in absolute value) than those estimated for the three other cells. Although we cannot be confident about this estimation, given the noisy OPD signal.

The spatial distribution of the exponent β_1 and the factor A present to some extend a structural organisation. This spatial distribution is not as clear as for RBCs probably due to the complex internal structure of TF1 cells. As it was shown in section 3.7.3.a, the intracellular cell structure presents in some cases clearly organised domains, but in general, these domains and/or inner boundaries are randomly distributed.

We have imaged two other TF1-GFP cells with the same parameters as the cell 1 presented above. However, the data was processed differently. There was no correction of the phase tilt, and the cell contour was detected using the image segmentation method described in section 3.6.1, repositioning the cell at each frame. We did not employ the WTMM detection method

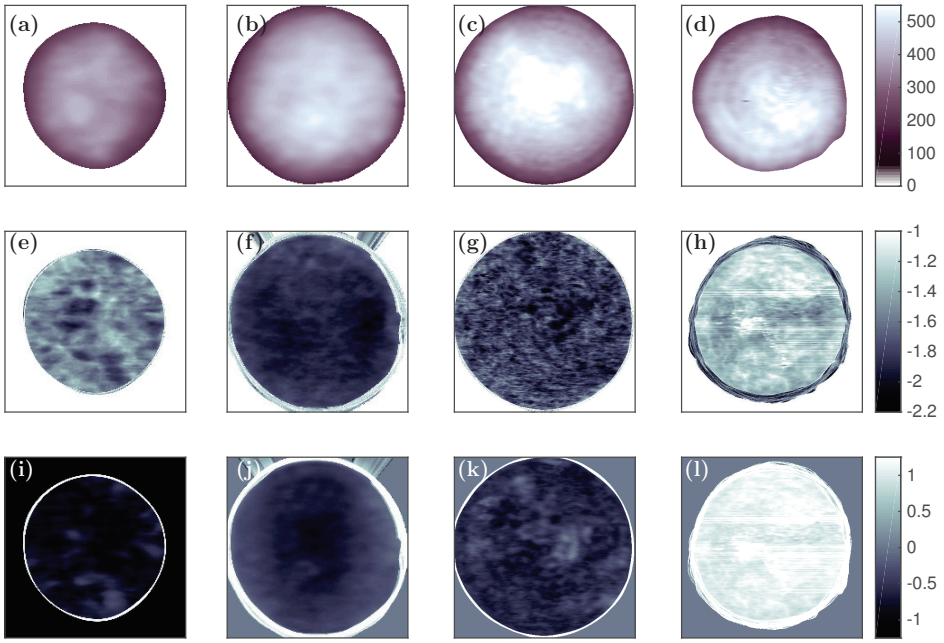

Figure 3.60 – **Spatial distribution of the scaling exponents of TF1-GFP cells at different frequency ranges.** (a-d) OPD images of the 4 different cells observed, where $\Phi(t = 0)$ (in nm) has been colour coded. (e-h) Spatial distribution of the scaling exponent β_1 (i-l) Spatial distribution of the factor A_1 obtained from the linear fit, and indicating the intensity of the noise.

since it was not yet developed at the time the data was analysed, and due to the long computation time, we have not re-processed the data yet.

The shape of the power spectrum is very similar for all the three TF1-GFP cells observed at this spatial and temporal resolution. We present in Fig.3.61 the spatial distribution of the scaling exponent β_1 (a,c) and the factor A (b,d) obtained from the linear fit for the two other TF1-GFP cells. We can see in these examples a marked structural organisation of the scaling exponent, very likely associated to the cell structure. It is difficult to conclude whether this

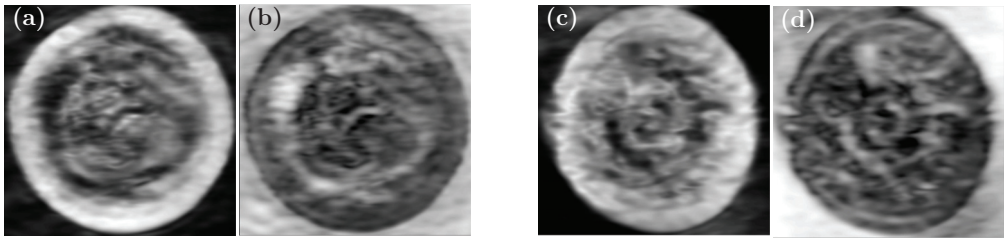

Figure 3.61 – **Spatial distribution of the scaling exponents of TF1-GFP cells.** Spatial distribution of the scaling exponent β (a,c) and the factor A (b,d) obtained from the linear fit. β has been colour coded in grey scale from -2 (black) to -0.5 (white), and A from -1.5 (black) to 4 (white).

spatial distribution is a robust feature of this type of cells. We have to keep in consideration that it depends greatly on the temporal scale of observation. The longer the time of observation, the more likely this organisation will be lost, as the cell will be constantly re-structuring its internal material. On the other extreme, if we focus at very high frequencies, it is probable that we will observe only the background noise of the liquid and/or setup, rather that the fluctuations of the cell structure. Thus, it is important to determine the range of frequencies where this effect may occur. Moreover, the detection of the WTMM chains on the time series could be really helpful in understanding the dynamics of the cell internal structure.

We have recorded a time series of a TF1-BA cell for comparison. The cell was chosen using a size criteria, as it has been shown that transformed cells tend to increase in size. The data consists of 900 images taken each 0.5 s. We corrected the phase tilt and detected the cell contour with the WTMM method. We have assembled the results obtained for this cell in Fig.3.62. We find no big differences between this cell and TF1-GFP cells. In general we observe an uncorrelated brownian motion for the cell displacement (Fig.3.62a-b) and contour tracking (Fig.3.62c-e), and a lower scaling exponent for the OPD signals, with a very weak structural organisation.

It is not surprising to obtain very similar results between TF1-GFP and TF1-BA cells, as it has been shown that the main differences arise when the cells are forced to adhere. Nevertheless, it is important to fully explore the frequency range accessible with this technique, as there might be interesting mechanical behaviour of these cells at a different scales of time. By increasing the range of temporal scales, the number of cells observed, and complementing the global cell dynamics analysis that we have performed with the study of their internal structure with the WTMM chain method, we should be able to conclude on the impact of the oncogene BCR-ABL on the dynamical properties of suspended cells.

In fact, the temporal evolution of the cell WTMM chains could lead to a passive study of the cell rheology. The chains would act as intracellular markers, offering the possibility to track the cell rotation, and to apply the concepts used in other passive rheological techniques such as magneto twisting cytometry or even thermally excited AFM, discussed on chapter 2. Therefore, this chain tracking can be the direct link between a non-intrusive measurement of the cell viscoelasticy and the mechanical properties measured with AFM on the previous chapter.

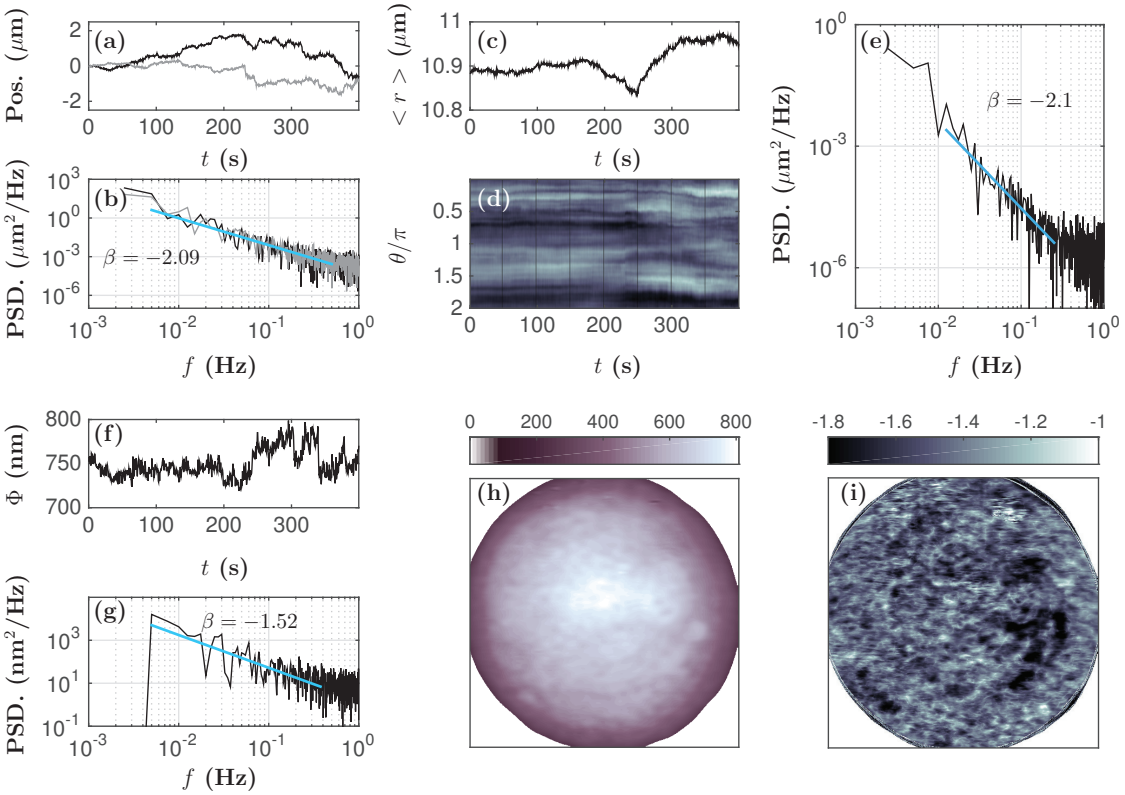

Figure 3.62 – **TF1-BA cell dynamics measured by DPM.** (a) The cell position in x (black curve) and in y (grey curve) from a TF1-BA cell is shown as a function of time. (c) Mean radius $< r(\theta) > (t)$ of the map shown in (d). (d) Temporal map of the cell contour, where $r(\theta)$ has been colour coded, from 10.5 μm to 11.5 μm. (f) $\Phi(t)$ for a point corresponding to the cell centre. (b,e,g) PSD of the signals shown in (a,c,f), respectively. The blue line shows the linear fit. (h) OPD image of the cell, where $\Phi(t = 0)$ (in nm) has been colour coded. (i) Spatial distribution of the scaling exponent β.

Summary

Diffraction phase microscopy is a powerful non-intrusive technique to study living cells. A fast and stable common-path interferometer was constructed to measure the optical phase of the micrometric objects in a single-shot. The optical phase has a high sensitivity to the object structure, as it is given by the product of its thickness and refractive index.

We have revisited the method to extract the phase from the DPM interferograms. We propose a 2D anisotropic Morlet wavelet transform that is capable of recovering the phase in extreme cases. For instance, when the object is thick or dense enough to produce rapid phase variations. Additionally, the WT modulus maxima method can filter intensity variations that are external to the object of interest.

We have employed DPM and this WTMM method to characterise the morphology of different types of cells, both adherent and non-adherent. The results obtained on RBCs are consistent with those reported in the literature, validating our methodology. In particular we have focused our attention on the hematopoietic cell line TF1, transduced either with GFP or the oncogene *BCR-ABL*. We have shown that their morphology is drastically altered when they are forced to adhere on a fibronectin-coated surface. To characterise their internal structure, we proposed a novel method based on the WTMM chain detection of the OPD gradient, using the derivative of a gaussian as a mother wavelet. This WTMM chain method is capable of distinguishing leukaemic TF1 cells from their healthy counterparts when they are in suspension and they adopt a spherical form.

Finally, we showed preliminary results about the dynamic of RBCs and TF1 cells. Once more, our results on RBCs agree with the literature. Moreover, we have encountered possible differences between a leukaemic RBC and a healthy one, consisting on the frequency dependence of their membrane fluctuations. The scaling exponent found on the power spectrum of the OPD from these cells reveals a different behaviour for the LMC RBC. In an interesting result, this scaling exponent seems to follow some structural organisation for TF1 cells, very likely associated to the cell internal structure.

Chapter 4

Conclusions and prospects

Experimental aspects and methodologies implemented in this work

One of the fundamental steps for characterizing cell mechanical properties is to capture their ability to deform under a given load. Experiments performed with atomic force microscope (AFM) usually address the cell deformation with the so-called force-indentation curves, where the AFM cantilever moves at a fixed velocity and indents the cell until a given load is reached. In the quasi-static approach, the velocity is constant and its value is empirically optimised to minimise the hydrodynamic effects and viscosity of the sample[1]. At very small indentations, that is, in the low deformation regime, the cell can be considered as a linear elastic system, and either the Hertz or the Sneddon's model can be used to compute the cell elastic modulus. In the present work we were rather interested in the large deformation regime, as we wanted to observe also the response of the underlying cell structure, and not only the cortex. Therefore, we could no longer assume the linearity of the system, and we considered instead a more general form of the strain-to-stress response:

$$F(\delta_z) \propto T_0 z_0 \left(\frac{\delta_z}{z_0}\right)^h \tag{4.1}$$

We emphasise here that the cell mechanical response is characterised by two quantities: the power-law h that describes the type of behaviour or structure, and the prefactor T_0 that quantifies the stiffness of the cortex [2]. We implemented a wavelet-based method to overcome the practical difficulties of the treatment of the force-indentation curves: determination of the contact point, filtering the data, and extraction of the scaling exponents.

The second type of experiments that we performed with AFM, focused on the spectral characterisation of cantilever fluctuations when it is excited by thermal noise, with and without interaction with a soft sample. To our knowledge, there are only a few reported works where AFM thermal noise spectra are analysed with the aim to extract the mechanical properties of biological systems. In material and engineering sciences, this approach is more common, although they are usually based on the parametrisation of the resonant peaks (change of reso-

[1] In animal cells, the cantilever tip velocity is typically set to values lower than 1μm s^{-1}, with a single force-indentation curve being recorded on the order of 5-30 seconds.

[2] We have chosen the actin cortex as a reference layer, with typical thickness $z_0 \sim 150$ nm.

nant frequency, width, ...), as they are related to the viscoelastic properties of the sample and the medium. To perform the spectral analysis, the cell body has to be stationary, and if the cell moves or remodels its internal structures during the experiment, the lower frequency part of the spectrum will be biased. Under steady conditions, the autocorrelation function of the thermal fluctuations of the cantilever pressed on a living cell is related to the local shear modulus $G(\omega)$ of the material, as can be shown using the fluctuation dissipation theorem (FDT) and a generalised Stokes equation for sharp tip cantilevers. The main constraints to use this approach are experimental and mainly due to limitation of the data recording and data processing of commercial AFM systems. The data are frequently filtered by the manufacturer in a frequency band that is sometimes difficult to know precisely from him, and whenever raw data can be collected, the acquisition frequency and/or buffer memory sizes are not suited for a correct spectral analysis of experiments with living cells. Therefore, it was necessary to add to the AFM another board for collecting the signals with an external A/D converter board. We believe that this approach has a great potential to study cells in real-time, as the data required for the spectral analysis can be recorded in less than 1 second, opening the possibility to perform spatial maps of the cell mechanical properties in a very short time, compared to traditional force-indentation curves. This method is also attractive because it gives access to the ratio of storage to loss moduli and therefore on the percentage of viscous and elastic components of the cell mechanics.

One may wonder, however, until what point does the cell get perturbed by the indentation process. As it has been pointed out all along this document, a living cell will react to the measurement tools, causing structural rearrangements. A remaining open question is if this restructuration of its interior will affect the cell behaviour. It is easy to imagine, for example, that under a big perturbation, the cell structure will be reinforced to prevent any further damage, specially if this perturbation is repetitive, such as in force-indentation curves. Although such modification in the cell structure will require at least a couple of minutes to occur, it is not clear yet if it can take place on a typical indentation experiment. With this question in mind, we wanted to complement the AFM indentation experiments, with a non-intrusive study of the cell structure. We chose a diffraction phase microscopy method fast enough to follow in real-time the cell deformation and intracellular rearrangements. The advantage of DPM over other quantitative phase microscopies, is precisely its high-acquisition speed limited only by the camera (in our case up to 10kHz), and the high stability due to its common-path interferometer design. Although it is relatively easy and fast to build a home-made DPM setup, compared to other optical set-ups, it takes a fair amount of time to optimise the design so it can be suited for the desired application. Additionally, the typical methods used to retrieve the phase of phase objects from the recorded interferograms are not necessarily adapted to several types of cells, particularly for non-adherent cells. In our case, we wanted to apply DPM to cells in suspension which keep a spherical geometry. When the phase gradient is too high due to a high relative refractive index or a sudden increase in thickness, methods like the Hilbert transform or Fourier filtering fail to correctly retrieve the phase of the object. We developed a phase recovery method based on an anisotropic wavelet transform (Morlet) whose performance surpasses the methods previously mentioned. Nevertheless, it does require more computing time, making the treatment of long video recordings quite challenging.

To study internal cell structures, we implemented a wavelet based contour detection method that, besides an easy identification of the cell contour, is also suited to detect intra-cellular phase boundaries. The method is based on the OPD gradient, we showed that, when the OPD gradient is locally maximum, there is a change in the composition of the structure (either its refractive index or thickness). Hence, the identification of such points, which have been shown in this work to organized into finite length and unclosed chains, were used to characterise the homogeneity of the intra-cellular structure. Furthermore, these OPD chains could serve as intracellular markers, opening the possibility to study the cell rheology, in a similar way to what is done with literature, with microparticles, magnetic/optical tweezers or intracellular fluorescence markers, in a non-intrusive manner. Beyond this aspect, the spatial complexity of these chains, their statistics of lengths, their spatial arrangements and how they reorganize dynamically could become a dynamical marker to compare healthy from pathologic cells.

Transformation of HSCs by the oncogene of chronic myelogeneous leukaemia

We have found clear differences between TF1-GFP and TF1-BCR-ABL cells that are enhanced when the cells are forced to adhere. The confinement of cells on fibronectin coated surface compels them to adhere and to spread. The cytoskeletal reorganisation of F-actin microfilaments was observed by fluorescence staining (Fig. 4.1). Whereas actin is mainly localised in the cortical cytoskeleton in non adherent normal cells, in transformed cells, BCR-ABL binds actin filaments (F-actin) [191], a major determinant of cell mechanical behaviour [192], and induces its redistribution into punctate, juxtanuclear aggregates [193]. In BCR-ABL-transduced TF1 cells, juxtanuclear actin aggregates were found in almost 30% of the cells in addition to the cortical F-actin staining (Fig. 4.1a,b). Very likely these structures were induced by BCR-ABL since they were rarely observed in the parental or GFP-transduced cell lines [189]. Consistently BCR-ABL-transduced cells show fewer actin stress fibres, as compared to parental or GFP-transduced TF1 cells in adhesion. As expected, GFP proteins do not co-localise with F-actin in TF1 cells. They exhibit a diffuse localisation in both the nucleus and the cytoplasm. In contrast, GFP-BCR-ABL proteins are localised in both the nucleus and the cytoplasm and a small fraction of the total proteins co-localises with actin stress fibres as well as with juxtanuclear F-actin aggregates.

The re-distribution of actin in TF1-BCR-ABL cells results in strong alterations of their cytoskeleton contractility. The transformed cells loose their ability to mature adhesion by actin stress fibres assembly. TF1-BCR-ABL cells maintain a more rounded shape when they are cultured on a fibronectin-coated surface, whereas TF1-GFP cells do show a more elongated form and a flattened profile as confirmed by DPM (section 3.7.3). It is important to point out that the transformed cells do adhere to the surface, as shown by the small protrusions seen in DPM images and AFM topography images (section 2.5.2). Thus, the rounded morphology is a consequence of the altered or inhibited mature adhesion, which in normal conditions would result in the cell elongation or spreading.

When the oncogene BCR-ABL interacts with the actin cytoskeleton, the mechanical response of the cell is impacted particularly in the low frequency range. The expression of BCR-ABL in

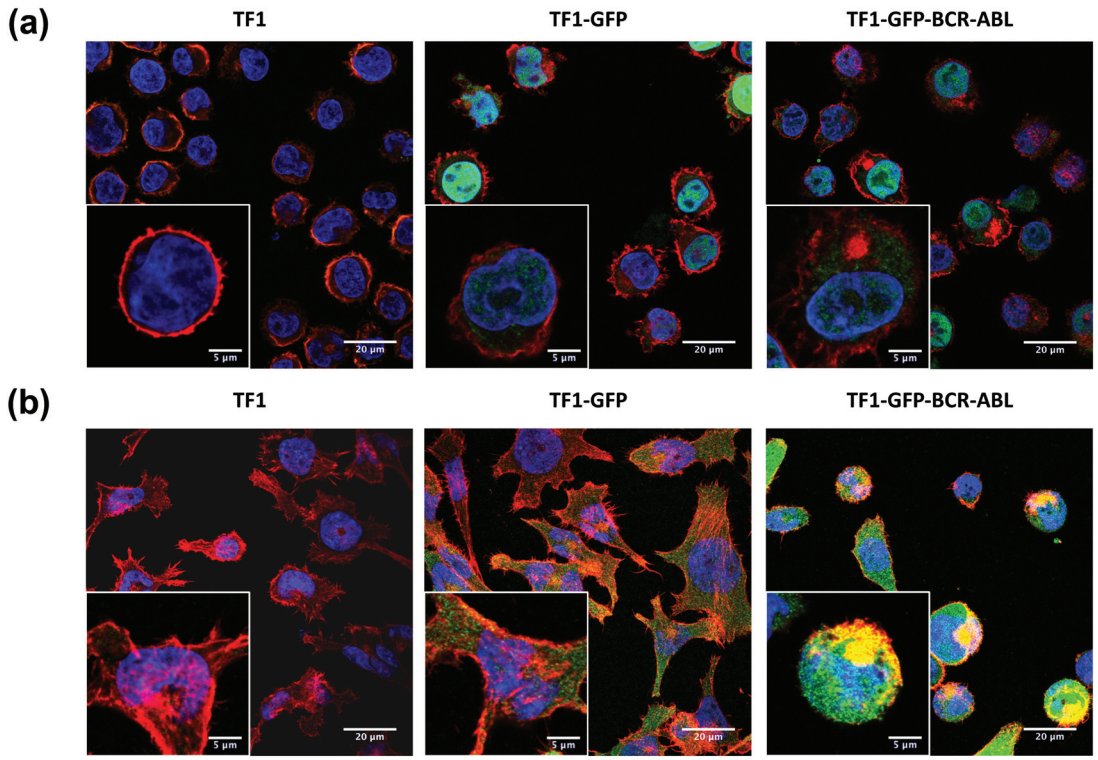

Figure 4.1 – **BCR-ABL induces an alteration of F-actin distribution in TF1 cells**. Filamentous actin (F-actin) was labeled with phalloidin-rhodamin (red), GFP signal was amplified using a rabbit polyclonal anti-GFP antibody-Alexa Fluor 488 conjugate (green) and the nuclei were labeled with DAPI (blue). Immunofluorescence images representative of 6 different experiments were taken using a confocal microscope on TF1, TF1-GFP and TF1-BCR-ABL cells either in a non adherent state **a** or in adhesion to fibronectin **b**. Scale bar 20 μm. Magnification examples are presented in lower left panels for each condition. Scale bar 5 μm. Figure courtesy of Bastien Laperrousaz.

immature cells modifies their strain-to-stress response when they are confined in adherence (chapter 2). The quasi-static measurement of force-indentation curves confirmed that the cell behaves as a multi-layer viscoelastic object, where the actin cortex plays a main role. By tracking the scaling laws on AFM force-indentation curves (section 2.4.2.a) we have observed that transformed cells present a marked shell-like response ($\alpha < 0.25$). The stiffening of the actin cortex could protect TF1-BCR-ABL cells from deformation, and is therefore a footprint of the cellular modifications induced by this oncogene.

There seems to be a slower response to a constant stress of TF1-BCR-ABL cells. While TF1-GFP cells are able to respond to a mechanical load in real time, the transformed cells require a longer adaptation time (~ 100 s) before creeping. The expected creeping relaxation of TF1-GFP cells occurs very differently, with a progressive increase of the cantilever fluctuations after ~ 35 s, likely involving a whole cytoskeleton structural change (section 2.5.2). TF1-BCR-ABL cells on the contrary, experience a single relaxation process with a relaxation time of 70 s - 110 s. The slower response found on transformed cells suggests that the mechanotrans-

duction pathway has also been altered. Perhaps, as actin filaments are disrupted, there may occur a modification of the mechanical coupling of the cell membrane, cytoskeleton, and/or the nucleus. It would be interesting to see if these differences on time response are only revealed by the applied stress, or if they also occur without mechanical perturbation. For instance, the supervision of the intracellular OPD chains obtained with DPM could indeed give further informations. Preliminary results have shown that at least, the number of chains TF1-GFP cells changes with time, indicating an active intracellular structure. Further analysis has to be done to conclude about the type of dynamics and mechanical properties that can be obtained from this data, and to confirm if there is an alteration of TF1-BCR-ABL cells.

The power-law regimes revealed in the low frequency range of the spectral densities of the cantilever fluctuations when loaded on TF1 cells pointed out their ressemblance to a structural damping model. Once again, the mechanical response of the transformed TF1-BCR-ABL cells was different from their healthy counterparts, suggesting a more elastic behaviour. A more complete statistical analysis of such power-laws is necessary to conclude about the variability of these values, as well as the degree of correlation between the static shear modulus obtained from the force-indentation curves and the exponent x characterising their structural damping. We could also think about performing such rheology experiments during a slow indentation and generalize the wavelet averaged spectra to a wavelet time-frequency spectral decomposition to follow the modification of the power-law exponent x when the tip encounter different structures. Again the wavelet method is a very powerful mathematical tool, suited to tackle this multi-scale problems, furthermore it could help us to define dynamical extension of the fluctuation dissipation theorem.

The transformation induced by the BCR-ABL oncogene is less evident when the cells are in suspension. Their morphology is slightly altered, with an increase in size of roughly 18% of transformed cells in comparison with TF1-GFP cells (section 3.7.3). The lower refractive index of TF1-BCR-ABL cells suggests that this change in size is due to the cell swelling. The modifications on the internal structure of these cells is also revealed by DPM in combination with a WTMM chain detection method of the OPD gradient (section 3.7.3.a). Even if we do not encounter any closed domains on neither TF1-GFP or TF1-BCR-ABL cells, the later present a larger number of WTMM chains, reflecting a more complex intracellular structure.

The dynamics of spontaneous phase fluctuations captured from DPM of suspended TF1-BCR-ABL cells are not that different from their healthy counterparts. Globally, we encounter that both cell types present an uncorrelated brownian motion ($\beta \sim -2$) of planar (x, y) movement of their center of mass, with some cells exhibiting low-frequency oscillations of their position around 100 s (section 3.8.2). The deformation of the cell contour also behaves as a brownian motion, although the amplitude of the fluctuations is quite variable between cells. Finally, the scaling exponent of the OPD signals is not as robust as for the cell displacement or contour deformation. We find values between [-2,-1], without any distinction between transformed and TF1-GFP cells. However, we observe a clear cut-off in frequencies around $f \sim 1$Hz that could be a characteristic feature of TF1 cells. This frequency value may be related to distinct intracellular viscoelastic properties, or it could account for some active behaviour of the cell (molecular motors) at higher frequency. The dependence of such behaviour with temper-

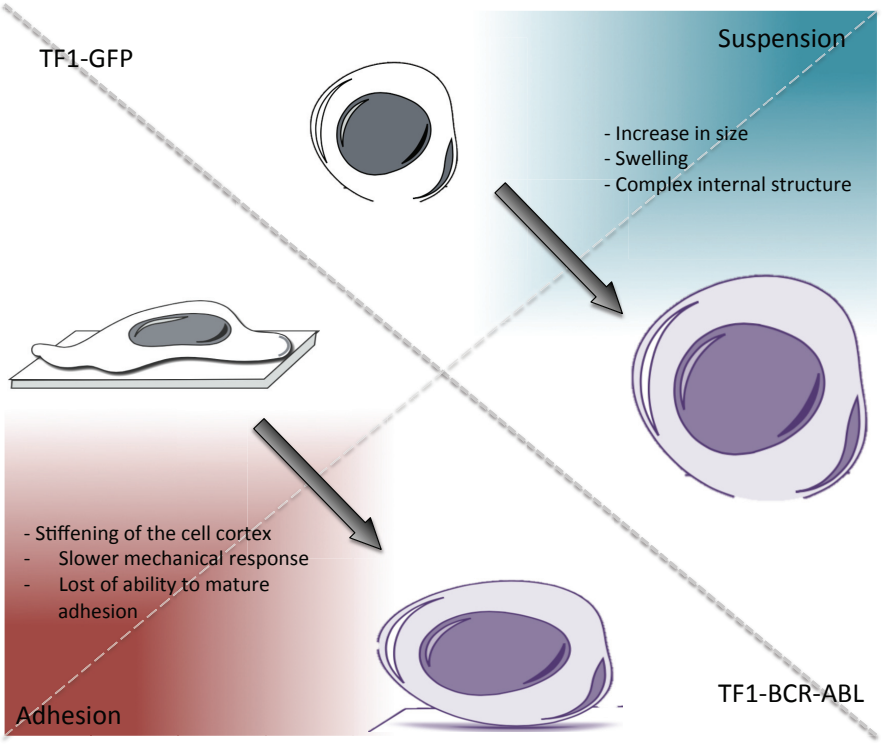

Figure 4.2 – **TF1 cell transformation by the oncogene BCR-ABL.**

ature, tonicity, or ATP levels can be really informative about the type of fluctuations which are observed (passive or active).

Finally, one of the most interesting perspectives for the methodology reported in this work, is the possibility to combine both types of microscopy on the same setup. This would allow the simultaneous observation of the cell structure and its response to indentation, providing strong evidence to tackle questions that have remained unanswered on the present document.

Bibliography

[1] C. Auffray and L. Nottale, "Scale relativity theory and integrative systems biology: 1: founding principles and scale laws," *Progress in Biophysics and Molecular Biology* **97**(1), 79–114 (2008).

[2] N. Kenkel and D. Walker, "Fractals in the biological sciences," *Coenoses* **11**, 77–100 (1996).

[3] O. Kučera and D. Havelka, "Mechano-electrical vibrations of microtubulesólink to subcellular morphology," *Biosystems* **109**(3), 346–355 (2012).

[4] R. Phillips, J. Kondev, J. Theriot, and H. Garcia, *Physical biology of the cell*, Garland Science (2012).

[5] Z. Qu, A. Garfinkel, J. N. Weiss, and M. Nivala, "Multi-scale modeling in biology: how to bridge the gaps between scales?," *Progress in Biophysics and Molecular Biology* **107**(1), 21–31 (2011).

[6] Y. Yaniv, E. Lakatta, and V. A. Maltsev, "From two competing oscillators to one coupled-clock pacemaker cell system," *Frontiers in Physiology* **6**, 28 (2015).

[7] D. DeWoskin, W. Geng, A. R. Stinchcombe, and D. B. Forger, "It is not the parts, but how they interact that determines the behaviour of circadian rhythms across scales and organisms," *Interface Focus* **4**(3), 20130076 (2014).

[8] M. A. Henson, "Multicellular models of intercellular synchronization in circadian neural networks," *Chaos, Solitons & Fractals* **50**, 48–64 (2013).

[9] J. Miro-Bueno and P. Sosík, "Brain clock driven by neuropeptides and second messengers," *Physical Review E* **90**(3), 032705 (2014).

[10] S. Schnell, R. Grima, and P. Maini, "Multiscale modeling in biology new insights into cancer illustrate how mathematical tools are enhancing the understanding of life from the smallest scale to the grandest," *American Scientist* **95**(2), 134–142 (2007).

[11] J. Ricard, *Biological complexity and the dynamics of life processes*, Elsevier (1999).

[12] S. Dinicola, F. D'Anselmi, A. Pasqualato, S. Proietti, E. Lisi, A. Cucina, and M. Bizzarri, "A systems biology approach to cancer: fractals, attractors, and nonlinear dynamics," *Omics: a journal of integrative biology* **15**(3), 93–104 (2011).

[13] F. Castiglione, F. Pappalardo, C. Bianca, G. Russo, and S. Motta, "Modeling biology spanning different scales: An open challenge," *BioMed Research International* **2014** (2014).

[14] P. V. Coveney and P. W. Fowler, "Modelling biological complexity: a physical scientist's perspective," *Journal of The Royal Society Interface* **2**(4), 267–280 (2005).

[15] I. R. Cohen and D. Harel, "Explaining a complex living system: dynamics, multi-scaling and emergence," *Journal of the Royal Society Interface* **4**(13), 175–182 (2007).

[16] S. Dumont and M. Prakash, "Emergent mechanics of biological structures," *Molecular Biology of the Cell* **25**(22), 3461–3465 (2014).

[17] G. Nicolis, I. Prigogine, and P. Carruthers, "Exploring complexity: an introduction," *Physics Today* **43**, 96 (1990).

[18] A. MYa, "Universal biological scaling and mortality," *Proceedings of the National Academy of Sciences* **91**(26), 12453–12457 (1994).

[19] T. McMahon and J. Bonner, "On size and life, scientific american library," *New York* (1983).

[20] D. West and B. J. West, "Physiologic time: a hypothesis," *Physics of Life Reviews* **10**(2), 210–224 (2013).

[21] B. B. Mandelbrot, "The fractal geometry of nature/revised and enlarged edition," *New York, WH Freeman and Co., 1983, 495 p.* **1** (1983).

[22] K. Klein, T. Maier, V. C. Hirschfeld-Warneken, and J. P. Spatz, "Marker-free phenotyping of tumor cells by fractal analysis of reflection interference contrast microscopy images," *Nano Letters* **13**(11), 5474–5479 (2013).

[23] A. L. Goldberger, L. A. Amaral, J. M. Hausdorff, P. C. Ivanov, C.-K. Peng, and H. E. Stanley, "Fractal dynamics in physiology: alterations with disease and aging," *Proceedings of the National Academy of Sciences* **99**(suppl 1), 2466–2472 (2002).

[24] P. C. Ivanov, M. G. Rosenblum, C. Peng, J. Mietus, S. Havlin, H. Stanley, and A. L. Goldberger, "Scaling behaviour of heartbeat intervals obtained by wavelet-based time-series analysis," *Nature* **383**(6598), 323–327 (1996).

[25] B. Pilgram and D. T. Kaplan, "Nonstationarity and 1/f noise characteristics in heart rate," *American Journal of Physiology-Regulatory, Integrative and Comparative Physiology* **276**(1), R1–R9 (1999).

[26] J. Van den Berg, *Wavelets in physics*, Cambridge University Press (2004).

[27] N. Scafetta, D. Marchi, and B. J. West, "Understanding the complexity of human gait dynamics," *Chaos: An Interdisciplinary Journal of Nonlinear Science* **19**(2), 026108 (2009).

[28] C.-Y. Lee, "Self-similarity of rrna secondary structures: A clue to rna folding," *Physica A: Statistical Mechanics and its Applications* **392**(20), 4937–4945 (2013).

[29] A. Bancaud, C. Lavelle, S. Huet, and J. Ellenberg, "A fractal model for nuclear organization: current evidence and biological implications," *Nucleic Acids Research* , gks586 (2012).

[30] A. Arneodo, C. Vaillant, B. Audit, F. Argoul, Y. díAubenton Carafa, and C. Thermes, "Multi-scale coding of genomic information: From dna sequence to genome structure and function," *Physics Reports* **498**(2), 45–188 (2011).

[31] S. Havlin, S. Buldyrev, A. Bunde, A. Goldberger, P. C. Ivanov, C.-K. Peng, and H. E. Stanley, "Scaling in nature: from dna through heartbeats to weather," *Physica A: Statistical Mechanics and its Applications* **273**(1), 46–69 (1999).

[32] M. Costa, I. Ghiran, C.-K. Peng, A. Nicholson-Weller, and A. L. Goldberger, "Complex dynamics of human red blood cell flickering: alterations with in vivo aging," *Physical Review E* **78**(2), 020901 (2008).

[33] S. Lee, J. Y. Lee, C.-S. Park, and D. Y. Kim, "Detrended fluctuation analysis of membrane flickering in discocyte and spherocyte red blood cells using quantitative phase microscopy," *Journal of Biomedical Optics* **16**(7), 076009–076009 (2011).

[34] D. Szekely, T. W. Yau, and P. W. Kuchel, "Human erythrocyte flickering: temperature, atp concentration, water transport, and cell aging, plus a computer simulation," *European Biophysics Journal* **38**(7), 923–939 (2009).

[35] S. Bilokapic and T. U. Schwartz, "3d ultrastructure of the nuclear pore complex," *Current Opinion in Cell Biology* **24**(1), 86–91 (2012).

[36] U. Aebi, J. Cohn, L. Buhle, and L. Gerace, "The nuclear lamina is a meshwork of intermediate-type filaments," *Nature* (1986).

[37] F. Guilak, J. R. Tedrow, and R. Burgkart, "Viscoelastic properties of the cell nucleus," *Biochemical and Biophysical Research Communications* **269**(3), 781–786 (2000).

[38] G. Cao, J. Sui, and S. Sun, "Evaluating the nucleus effect on the dynamic indentation behavior of cells," *Biomechanics and Modeling in Mechanobiology* **12**(1), 55–66 (2013).

[39] K. N. Dahl, A. J. Engler, J. D. Pajerowski, and D. E. Discher, "Power-law rheology of isolated nuclei with deformation mapping of nuclear substructures," *Biophysical Journal* **89**(4), 2855–2864 (2005).

[40] M. Amendola and B. van Steensel, "Mechanisms and dynamics of nuclear lamina–genome interactions," *Current Opinion in Cell Biology* **28**, 61–68 (2014).

[41] P. M. Davidson and J. Lammerding, "Broken nuclei–lamins, nuclear mechanics, and disease," *Trends in Cell Biology* **24**(4), 247–256 (2014).

[42] M. Crisp, Q. Liu, K. Roux, J. Rattner, C. Shanahan, B. Burke, P. D. Stahl, and D. Hodzic, "Coupling of the nucleus and cytoplasm role of the linc complex," *The Journal of Cell Biology* **172**(1), 41–53 (2006).

[43] M. Brosig, J. Ferralli, L. Gelman, M. Chiquet, and R. Chiquet-Ehrismann, "Interfering with the connection between the nucleus and the cytoskeleton affects nuclear rotation, mechanotransduction and myogenesis," *The International Journal of Cell Biology and Biochemistry* **42**(10), 1717–1728 (2010).

[44] K. N. Dahl and A. Kalinowski, "Nucleoskeleton mechanics at a glance," *Journal of Cell Science* **124**(5), 675–678 (2011).

[45] E. A. Booth-Gauthier, T. A. Alcoser, G. Yang, and K. N. Dahl, "Force-induced changes in subnuclear movement and rheology," *Biophysical journal* **103**(12), 2423–2431 (2012).

[46] M. Versaevel, J.-B. Braquenier, M. Riaz, T. Grevesse, J. Lantoine, and S. Gabriele, "Super-resolution microscopy reveals linc complex recruitment at nuclear indentation sites," *Scientific Reports* **4** (2014).

[47] F. Huber, J. Schnauss, S. Rönicke, P. Rauch, K. Müller, C. Fütterer, and J. Käs, "Emergent complexity of the cytoskeleton: from single filaments to tissue," *Advances in Physics* **62**(1), 1–112 (2013).

[48] D. Das, D. Das, and R. Padinhateeri, "Force-induced dynamical properties of multiple cytoskeletal filaments are distinct from that of single filaments," *PLoS One* **9**(12), e114014 (2014).

[49] D. Mizuno, C. Tardin, C. Schmidt, and F. MacKintosh, "Nonequilibrium mechanics of active cytoskeletal networks," *Science* **315**(5810), 370–373 (2007).

[50] P. Bursac, G. Lenormand, B. Fabry, M. Oliver, D. A. Weitz, V. Viasnoff, J. P. Butler, and J. J. Fredberg, "Cytoskeletal remodelling and slow dynamics in the living cell," *Nature Materials* **4**(7), 557–561 (2005).

[51] P. Bursac, B. Fabry, X. Trepat, G. Lenormand, J. P. Butler, N. Wang, J. J. Fredberg, and S. S. An, "Cytoskeleton dynamics: fluctuations within the network," *Biochemical and Biophysical Research Communications* **355**(2), 324–330 (2007).

[52] M. Gardel, J. Shin, F. MacKintosh, L. Mahadevan, P. Matsudaira, and D. Weitz, "Elastic behavior of cross-linked and bundled actin networks," *Science* **304**(5675), 1301–1305 (2004).

[53] E. Fuchs and K. Weber, "Intermediate filaments: structure, dynamics, function and disease," *Annual Review of Biochemistry* **63**(1), 345–382 (1994).

[54] H. Herrmann, H. Bär, L. Kreplak, S. V. Strelkov, and U. Aebi, "Intermediate filaments: from cell architecture to nanomechanics," *Nature Reviews Molecular Cell Biology* **8**(7), 562–573 (2007).

[55] M. B. Omary, P. A. Coulombe, and W. I. McLean, "Intermediate filament proteins and their associated diseases," *New England Journal of Medicine* **351**(20), 2087–2100 (2004).

[56] H. Herrmann, M. Häner, M. Brettel, N.-O. Ku, and U. Aebi, "Characterization of distinct early assembly units of different intermediate filament proteins," *Journal of Molecular Biology* **286**(5), 1403–1420 (1999).

[57] L. Kreplak, H. Bär, J. Leterrier, H. Herrmann, and U. Aebi, "Exploring the mechanical behavior of single intermediate filaments," *Journal of Molecular Biology* **354**(3), 569–577 (2005).

[58] C. P. Brangwynne, F. C. MacKintosh, S. Kumar, N. A. Geisse, J. Talbot, L. Mahadevan, K. K. Parker, D. E. Ingber, and D. A. Weitz, "Microtubules can bear enhanced compressive loads in living cells because of lateral reinforcement," *The Journal of Cell Biology* **173**(5), 733–741 (2006).

[59] O. Esue, A. A. Carson, Y. Tseng, and D. Wirtz, "A direct interaction between actin and vimentin filaments mediated by the tail domain of vimentin," *Journal of Biological Chemistry* **281**(41), 30393–30399 (2006).

[60] A. Desai and T. J. Mitchison, "Microtubule polymerization dynamics," *Annual Review of Cell and Developmental Biology* **13**(1), 83–117 (1997).

[61] D. Havelka, O. Kučera, M. A. Deriu, and M. Cifra, "Electro-acoustic behavior of the mitotic spindle: A semi-classical coarse-grained model," *PLoS One* **9**(1), e86501 (2014).

[62] C. P. Brangwynne, F. MacKintosh, and D. A. Weitz, "Force fluctuations and polymerization dynamics of intracellular microtubules," *Proceedings of the National Academy of Sciences* **104**(41), 16128–16133 (2007).

[63] A. D. Bicek, E. Tüzel, D. M. Kroll, and D. J. Odde, "Analysis of microtubule curvature," *Methods in Cell Biology* **83**, 237–268 (2007).

[64] M. E. Janson, E. Mathilde, and M. Dogterom, "Dynamic instability of microtubules is regulated by force," *The Journal of Cell Biology* **161**(6), 1029–1034 (2003).

[65] G. J. Brouhard and L. M. Rice, "The contribution of $\alpha\beta$-tubulin curvature to microtubule dynamics," *The Journal of Cell Biology* **207**(3), 323–334 (2014).

[66] L. Laan, J. Husson, E. L. Munteanu, J. W. Kerssemakers, and M. Dogterom, "Force-generation and dynamic instability of microtubule bundles," *Proceedings of the National Academy of Sciences* **105**(26), 8920–8925 (2008).

[67] L. Blanchoin, R. Boujemaa-Paterski, C. Sykes, and J. Plastino, "Actin dynamics, architecture, and mechanics in cell motility," *Physiological Reviews* **94**(1), 235–263 (2014).

[68] S. Köhler, V. Schaller, and A. R. Bausch, "Structure formation in active networks," *Nature Materials* **10**(6), 462–468 (2011).

[69] P. M. Bendix, G. H. Koenderink, D. Cuvelier, Z. Dogic, B. N. Koeleman, W. M. Brieher, C. M. Field, L. Mahadevan, and D. A. Weitz, "A quantitative analysis of contractility in active cytoskeletal protein networks," *Biophysical Journal* **94**(8), 3126–3136 (2008).

[70] K. Carvalho, F.-C. Tsai, E. Lees, R. Voituriez, G. H. Koenderink, and C. Sykes, "Cell-sized liposomes reveal how actomyosin cortical tension drives shape change," *Proceedings of the National Academy of Sciences* **110**(41), 16456–16461 (2013).

[71] Y.-W. Heng and C.-G. Koh, "Actin cytoskeleton dynamics and the cell division cycle," *The International Journal of Biochemistry and Cell Biology* **42**(10), 1622–1633 (2010).

[72] M. Mavrakis, Y. Azou-Gros, F.-C. Tsai, J. Alvarado, A. Bertin, F. Iv, A. Kress, S. Brasselet, G. H. Koenderink, and T. Lecuit, "Septins promote f-actin ring formation by crosslinking actin filaments into curved bundles," *Nature Cell Biology* **16**(4), 322–334 (2014).

[73] K. Hu, L. Ji, K. T. Applegate, G. Danuser, and C. M. Waterman-Storer, "Differential transmission of actin motion within focal adhesions," *Science* **315**(5808), 111–115 (2007).

[74] J. Allard and A. Mogilner, "Traveling waves in actin dynamics and cell motility," *Current Opinion in Cell Biology* **25**(1), 107–115 (2013).

[75] T. Bretschneider, K. Anderson, M. Ecke, A. Müller-Taubenberger, B. Schroth-Diez, H. C. Ishikawa-Ankerhold, and G. Gerisch, "The three-dimensional dynamics of actin waves, a model of cytoskeletal self-organization," *Biophysical Journal* **96**(7), 2888–2900 (2009).

[76] E. Bernitt, C. G. Koh, N. Gov, and H.-G. Döbereiner, "Dynamics of actin waves on patterned substrates: A quantitative analysis of circular dorsal ruffles," *PLoS Biology* **10**(1), e0115857 (2015).

[77] M. J. Footer, J. W. Kerssemakers, J. A. Theriot, and M. Dogterom, "Direct measurement of force generation by actin filament polymerization using an optical trap," *Proceedings of the National Academy of Sciences* **104**(7), 2181–2186 (2007).

[78] M. P. López, F. Huber, I. Grigoriev, M. O. Steinmetz, A. Akhmanova, G. H. Koenderink, and M. Dogterom, "Actin–microtubule coordination at growing microtubule ends," *Nature Communications* **5** (2014).

[79] S. Singer and G. L. Nicolson, "The fluid mosaic model of the structure of cell membranes," *Science* , 7–47 (1972).

[80] E. Evans and S. Simon, "Mechanics of bilayer membranes," *Journal of Colloid and Interface Science* **51**(2), 266–271 (1975).

[81] L. Deseri and G. Zurlo, "The stretching elasticity of biomembranes determines their line tension and bending rigidity," *Biomechanics and modeling in mechanobiology* **12**(6), 1233–1242 (2013).

[82] R. Parthasarathy and J. T. Groves, "Curvature and spatial organization in biological membranes," *Soft Matter* **3**(1), 24–33 (2006).

[83] S. Semrau and T. Schmidt, "Membrane heterogeneity–from lipid domains to curvature effects," *Soft Matter* **5**(17), 3174–3186 (2009).

[84] A. Pietuch, B. R. Brückner, and A. Janshoff, "Membrane tension homeostasis of epithelial cells through surface area regulation in response to osmotic stress," *Biochimica et Biophysica Acta (BBA)-Molecular Cell Research* **1833**(3), 712–722 (2013).

[85] D. Raucher and M. P. Sheetz, "Characteristics of a membrane reservoir buffering membrane tension," *Biophysical Journal* **77**(4), 1992–2002 (1999).

[86] G. T. Charras, J. C. Yarrow, M. A. Horton, L. Mahadevan, and T. Mitchison, "Non-equilibration of hydrostatic pressure in blebbing cells," *Nature* **435**(7040), 365–369 (2005).

[87] G. T. Charras, M. Coughlin, T. J. Mitchison, and L. Mahadevan, "Life and times of a cellular bleb," *Biophysical Journal* **94**(5), 1836–1853 (2008).

[88] J.-Y. Tinevez, U. Schulze, G. Salbreux, J. Roensch, J.-F. Joanny, and E. Paluch, "Role of cortical tension in bleb growth," *Proceedings of the National Academy of Sciences* **106**(44), 18581–18586 (2009).

[89] S. Ramaswamy, J. Toner, and J. Prost, "Nonequilibrium fluctuations, traveling waves, and instabilities in active membranes," *Physical Review Letters* **84**(15), 3494 (2000).

[90] A. Maitra, P. Srivastava, M. Rao, and S. Ramaswamy, "Activating membranes," *Physical Review Letters* **112**(25), 258101 (2014).

[91] A. Pierres, V. Monnet-Corti, A.-M. Benoliel, and P. Bongrand, "Do membrane undulations help cells probe the world?," *Trends in Cell Biology* **19**(9), 428–433 (2009).

[92] H.-G. Döbereiner, B. J. Dubin-Thaler, J. M. Hofman, H. S. Xenias, T. N. Sims, G. Giannone, M. L. Dustin, C. H. Wiggins, and M. P. Sheetz, "Lateral membrane waves constitute a universal dynamic pattern of motile cells," *Physical Review Letters* **97**(3), 038102 (2006).

[93] E. A. Evans and D. A. Calderwood, "Forces and bond dynamics in cell adhesion," *Science* **316**(5828), 1148–1153 (2007).

[94] K. L. Hui, C. Wang, B. Grooman, J. Wayt, and A. Upadhyaya, "Membrane dynamics correlate with formation of signaling clusters during cell spreading," *Biophysical Journal* **102**(7), 1524–1533 (2012).

[95] O. F. Zouani, V. Gocheva, and M.-C. Durrieu, "Membrane nanowaves in single and collective cell migration," *PLoS One* **9**(5), e97855 (2014).

[96] P. D. Antonio, M. Lasalvia, G. Perna, and V. Capozzi, "Scale-independent roughness value of cell membranes studied by means of afm technique," *Biochimica et Biophysica Acta (BBA)-Biomembranes* **1818**(12), 3141–3148 (2012).

[97] A. Bitler, R. Dover, and Y. Shai, "Fractal properties of macrophage membrane studied by afm," *Micron* **43**(12), 1239–1245 (2012).

[98] B. Loubet, P. L. Hansen, and M. A. Lomholt, "Electromechanics of a membrane with spatially distributed fixed charges: Flexoelectricity and elastic parameters," *Physical Review E* **88**(6), 062715 (2013).

[99] M. Tajparast and M. Glavinović, "Elastic, electrostatic and electrokinetic forces influencing membrane curvature," *Biochimica et Biophysica Acta (BBA)-Biomembranes* **1818**(3), 411–424 (2012).

[100] G. Bao and S. Suresh, "Cell and molecular mechanics of biological materials," *Nature Materials* **2**(11), 715–725 (2003).

[101] K. E. Kasza, A. C. Rowat, J. Liu, T. E. Angelini, C. P. Brangwynne, G. H. Koenderink, and D. A. Weitz, "The cell as a material," *Current Opinion in Cell Biology* **19**(1), 101–107 (2007).

[102] Y.-Q. Chen, C.-Y. Kuo, M.-T. Wei, K. Wu, P.-T. Su, C.-S. Huang, and A. Chiou, "Intracellular viscoelasticity of hela cells during cell division studied by video particle-tracking microrheology," *Journal of Biomedical Optics* **19**(1), 011008–011008 (2014).

[103] A. J. Engler, S. Sen, H. L. Sweeney, and D. E. Discher, "Matrix elasticity directs stem cell lineage specification," *Cell* **126**(4), 677–689 (2006).

[104] E. M. Darling, M. Topel, S. Zauscher, T. P. Vail, and F. Guilak, "Viscoelastic properties of human mesenchymally-derived stem cells and primary osteoblasts, chondrocytes, and adipocytes," *Journal of Biomechanics* **41**(2), 454–464 (2008).

[105] K. Bhadriraju and L. K. Hansen, "Extracellular matrix-and cytoskeleton-dependent changes in cell shape and stiffness," *Experimental Cell Research* **278**(1), 92–100 (2002).

[106] A. Asnacios and O. Hamant, "The mechanics behind cell polarity," *Trends in Cell Biology* **22**(11), 584–591 (2012).

[107] U. S. Schwarz, T. Erdmann, and I. B. Bischofs, "Focal adhesions as mechanosensors: the two-spring model.," *Biosystems* **83**(2-3), 225–232 (2006).

[108] P. Moreo, J. M. García-Aznar, and M. Doblaré, "Modeling mechanosensing and its effect on the migration and proliferation of adherent cells.," *Acta Biomaterialia* **4**, 613–621 (2008).

[109] D. E. Ingber, "Tensegrity i. cell structure and hierarchical systems biology," *Journal of Cell Science* **116**(7), 1157–1173 (2003).

[110] D. E. Ingber, N. Wang, and D. Stamenović, "Tensegrity, cellular biophysics, and the mechanics of living systems," *Reports on Progress in Physics* **77**(4), 046603 (2014).

[111] B. Fabry, G. N. Maksym, J. P. Butler, M. Glogauer, D. Navajas, and J. J. Fredberg, "Scaling the microrheology of living cells," *Physical Review Letters* **87**(14), 148102 (2001).

[112] J. Alcaraz, L. Buscemi, M. Grabulosa, X. Trepat, B. Fabry, R. Farré, and D. Navajas, "Microrheology of human lung epithelial cells measured by atomic force microscopy," *Biophysical Journal* **84**(3), 2071–2079 (2003).

[113] G. Lenormand, E. Millet, B. Fabry, J. P. Butler, and J. J. Fredberg, "Linearity and time-scale invariance of the creep function in living cells," *Journal of The Royal Society Interface* **1**(1), 91–97 (2004).

[114] N. Desprat, A. Richert, J. Simeon, and A. Asnacios, "Creep function of a single living cell," *Biophysical Journal* **88**(3), 2224–2233 (2005).

[115] B. D. Hoffman, G. Massiera, K. M. Van Citters, and J. C. Crocker, "The consensus mechanics of cultured mammalian cells," *Proceedings of the National Academy of Sciences* **103**(27), 10259–10264 (2006).

[116] F. Gallet, D. Arcizet, P. Bohec, and A. Richert, "Power spectrum of out-of-equilibrium forces in living cells: amplitude and frequency dependence," *Soft Matter* **5**(15), 2947–2953 (2009).

[117] E. Zhou, S. Quek, and C. Lim, "Power-law rheology analysis of cells undergoing micropipette aspiration," *Biomechanics and Modeling in Mechanobiology* **9**(5), 563–572 (2010).

[118] C. TanjaáMierke *et al.*, "Nonlinear viscoelasticity of adherent cells is controlled by cytoskeletal tension," *Soft Matter* **7**(7), 3127–3132 (2011).

[119] J. L. Tan, J. Tien, D. M. Pirone, D. S. Gray, K. Bhadriraju, and C. S. Chen, "Cells lying on a bed of microneedles: an approach to isolate mechanical force," *Proceedings of the National Academy of Sciences* **100**(4), 1484–1489 (2003).

[120] K. Suffoletto, N. Ye, F. Meng, D. Verma, and S. Z. Hua, "Intracellular forces during guided cell growth on micropatterns using fret measurement," *Journal of Biomechanics* (2015).

[121] D. Mitrossilis, J. Fouchard, D. Pereira, F. Postic, A. Richert, M. Saint-Jean, and A. Asnacios, "Real-time single-cell response to stiffness," *Proceedings of the National Academy of Sciences* **107**(38), 16518–16523 (2010).

[122] C. C. DuFort, M. J. Paszek, and V. M. Weaver, "Balancing forces: architectural control of mechanotransduction.," *Nature Reviews. Molecular Cell Biology* **12**, 308–319 (2011).

[123] J. Fouchard, D. Mitrossilis, and A. Asnacios, "Acto-myosin based response to stiffness and rigidity sensing.," *Cell Adh Migr* **5**(1), 16–19 (2011).

[124] A. Buxboim, I. L. Ivanovska, and D. E. Discher, "Matrix elasticity, cytoskeletal forces and physics of the nucleus: how deeply do cells 'feel' outside and in?," *Journal of Cell Science* **123**, 297–308 (2010).

[125] P. A. Janmey and D. A. Weitz, "Dealing with mechanics: mechanisms of force transduction in cells.," *Trends in Biochemical Sciences* **29**, 364–370 (2004).

[126] S. W. Moore, P. Roca-Cusachs, and M. P. Sheetz, "Stretchy proteins on stretchy substrates: the important elements of integrin-mediated rigidity sensing.," *Developmental Cell* **19**, 194–206 (2010).

[127] I. Delon and N. H. Brown, "Integrins and the actin cytoskeleton.," *Current Opinion in Cell Biology* **19**, 43–50 (2007).

[128] A. D. Bershadsky, N. Q. Balaban, and B. Geiger, "Adhesion-dependent cell mechanosensitivity," *Annual Review of Cell Biology* **19**(1), 677–695 (2003).

[129] N. Q. Balaban, U. S. Schwarz, D. Riveline, P. Goichberg, G. Tzur, I. Sabanay, D. Mahalu, S. Safran, A. Bershadsky, L. Addadi, and B. Geiger, "Force and focal adhesion assembly: a close relationship studied using elastic micropatterned substrates.," *Nature Cell Biology* **3**, 466–472 (2001).

[130] A. Elosegui-Artola, E. Bazellières, M. D. Allen, I. Andreu, R. Oria, R. Sunyer, J. J. Gomm, J. F. Marshall, J. L. Jones, X. Trepat, and P. Roca-Cusachs, "Rigidity sensing and adaptation through regulation of integrin types.," *Nature Materials* **13**, 631–637 (2014).

[131] C. Borau, R. D. Kamm, and J. M. García-Aznar, "A time-dependent phenomenological model for cell mechano-sensing.," *Biomech Model Mechanobiol* **13**, 451–462 (2014).

[132] J. Étienne, J. Fouchard, D. Mitrossilis, N. Bufi, P. Durand-Smet, and A. Asnacios, "Cells as liquid motors: mechanosensitivity emerges from collective dynamics of actomyosin cortex.," *Proceedings of the National Academy of Sciences* **112**, 2740–2745 (2015).

[133] J. Eyckmans, T. Boudou, X. Yu, and C. S. Chen, "A hitchhiker's guide to mechanobiology.," *Developmental Cell* **21**, 35–47 (2011).

[134] A. B. Chambliss, S. B. Khatau, N. Erdenberger, D. K. Robinson, D. Hodzic, G. D. Longmore, and D. Wirtz, "The linc-anchored actin cap connects the extracellular milieu to the nucleus for ultrafast mechanotransduction.," *Sci Rep* **3**, 1087 (2013).

[135] G. R. Fedorchak, A. Kaminski, and J. Lammerding, "Cellular mechanosensing: getting to the nucleus of it all.," *Progress in Biophysics and Molecular Biology* **115**, 76–92 (2014).

[136] B. L. Ricca, G. Venugopalan, and D. A. Fletcher, "To pull or be pulled: parsing the multiple modes of mechanotransduction.," *Current Opinion in Cell Biology* **25**, 558–564 (2013).

[137] J. Vincent, *Structural biomaterials*, Princeton University Press (2012).

[138] M. L. Williams, "Structural analysis of viscoelastic materials," *AIAA journal* **2**(5), 785–808 (1964).

[139] C. Lim, E. Zhou, and S. Quek, "Mechanical models for living cellsóa review," *Journal of Biomechanics* **39**(2), 195–216 (2006).

[140] W. N. Findley, J. S. Lai, and K. Onaran, *Creep and Relaxation of Nonlinear Viscoelastic Materials*, Dover Publications Inc. (1990).

[141] B. D. Hoffman and J. C. Crocker, "Cell mechanics: dissecting the physical responses of cells to force.," *Annual Review of Biomedical Engineering* **11**, 259–288 (2009).

[142] B. Fabry, G. N. Maksym, J. P. Butler, M. Glogauer, D. Navajas, N. A. Taback, E. J. Millet, and J. J. Fredberg, "Time scale and other invariants of integrative mechanical behavior in living cells," *Physical Review E* **68**(4), 041914 (2003).

[143] D. Icard-Arcizet, O. Cardoso, A. Richert, and S. Hénon, "Cell stiffening in response to external stress is correlated to actin recruitment.," *Biophysical Journal* **94**, 2906–2913 (2008).

[144] M. Balland, N. Desprat, D. Icard, S. Féréol, A. Asnacios, J. Browaeys, S. Hénon, and F. Gallet, "Power laws in microrheology experiments on living cells: Comparative analysis and modeling," *Physical Review E* **74**(2), 021911 (2006).

[145] X. Trepat, G. Lenormand, and J. J. Fredberg, "Universality in cell mechanics," *Soft Matter* **4**(9), 1750–1759 (2008).

[146] A. Asnacios, "Real-time single-cell response to stiffness," *Proceedings of the National Academy of Sciences* **107**(38), 1651816523Mogilner (2010).

[147] E. Moeendarbary, *Time-dependent mechanics of living cells*. PhD thesis, UCL (University College London) (2013).

[148] P. Sollich, "Rheological constitutive equation for model of soft glassy materials," *Physical Review E* **58**(1), 738–759 (1998).

[149] E. H. Zhou, X. Trepat, C. Y. Park, G. Lenormand, M. N. Oliver, S. M. Mijailovich, C. Hardin, D. A. Weitz, J. P. Butler, and J. J. Fredberg, "Universal behavior of the osmotically compressed cell and its analogy to the colloidal glass transition.," *Proceedings of the National Academy of Sciences of the United States of America* **106**, 10632–10637 (2009).

[150] D. Heinrich and E. Sackmann, "Active mechanical stabilization of the viscoplastic intracellular space of Dictyostelia cells by microtubule-actin crosstalk," *Acta Biomaterialia* **2**, 619–631 (2006).

[151] D. Arcizet, B. Meier, E. Sackmann, J. O. Rädler, and D. Heinrich, "Temporal analysis of active and passive transport in living cells," *Physical Review Letters* **101**(December), 248103 (2008).

[152] M. Otten, A. Nandi, D. Arcizet, M. Gorelashvili, B. Lindner, and D. Heinrich, "Local motion analysis reveals impact of the dynamic cytoskeleton on intracellular subdiffusion," *Biophysical Journal* **102**(4), 758–767 (2012).

[153] S. Guo, M. Gao, X. Xiong, Y. J. Wang, X. Wang, P. Sheng, and P. Tong, "Direct measurement of friction of a fluctuating contact line," *Physical Review Letters* **111**(2), 026101 (2013).

[154] G. Binnig, C. F. Quate, and C. Gerber, "Atomic force microscope," *Physical Review Letters* **56**(9), 930 (1986).

[155] Y. L. Lyubchenko and L. S. Shlyakhtenko, "Visualization of supercoiled dna with atomic force microscopy in situ," *Proceedings of the National Academy of Sciences* **94**(2), 496–501 (1997).

[156] A. J. Engler, F. Rehfeldt, S. Sen, and D. E. Discher, "Microtissue elasticity: measurements by atomic force microscopy and its influence on cell differentiation," *Methods in Cell Biology* **83**, 521–545 (2007).

[157] J. L. Hutter and J. Bechhoefer, "Calibration of atomic-force microscope tips," *Review of Scientific Instruments* **64**(7), 1868–1873 (1993).

[158] R. W. Stark, T. Drobek, and W. M. Heckl, "Thermomechanical noise of a free v-shaped cantilever for atomic-force microscopy," *Ultramicroscopy* **86**(1), 207–215 (2001).

[159] H.-J. Butt and M. Jaschke, "Calculation of thermal noise in atomic force microscopy," *Nanotechnology* **6**(1), 1 (1995).

[160] B. Laperrousaz, S. Jeanpierre, K. Sagorny, T. Voeltzel, S. Ramas, B. Kaniewski, M. Ffrench, S. Salesse, F. E. Nicolini, and V. Maguer-Satta, "Primitive cml cell expansion relies on abnormal levels of bmps provided by the niche and on bmprib overexpression," *Blood* **122**(23), 3767–3777 (2013).

[161] A. Arneodo, B. Audit, N. Decoster, J.-F. Muzy, and C. Vaillant, "Wavelet based multifractal formalism: applications to dna sequences, satellite images of the cloud structure, and stock market data," in *The science of Disasters*, 26–102, Springer (2002).

[162] J.-F. Muzy, E. Bacry, and A. Arneodo, "The multifractal formalism revisited with wavelets," *International Journal of Bifurcation and Chaos* **4**(02), 245–302 (1994).

[163] S. Mallat and W. L. Hwang, "Singularity detection and processing with wavelets," *Information Theory, IEEE Transactions on* **38**(2), 617–643 (1992).

[164] S. Digiuni, A. Berne-Dedieu, C. Martinez-Torres, J. Szecsi, M. Bendahmane, A. Arneodo, and F. Argoul, "Single cell wall nonlinear mechanics revealed by a multiscale analysis of afm force-indentation curves," *Biophysical Journal* **108**(9), 2235–2248 (2015).

[165] D. J. Müller and Y. F. Dufrêne, "Atomic force microscopy as a multifunctional molecular toolbox in nanobiotechnology.," *Nature Nanotechnology* **3**, 261–269 (2008).

[166] A. F. Oberhauser, P. K. Hansma, M. Carrion-Vazquez, and J. M. Fernandez, "Stepwise unfolding of titin under force-clamp atomic force microscopy.," *Proceedings of the National Academy of Sciences of the United States of America* **98**, 468–472 (2001).

[167] M. Rief, M. Gautel, F. Oesterhelt, J. M. Fernandez, and H. E. Gaub, "Reversible unfolding of individual titin immunoglobulin domains by AFM.," *Science* **276**, 1109–1112 (1997).

[168] A. E. X. Brown, R. I. Litvinov, D. E. Discher, and J. W. Weisel, "Forced unfolding of coiled-coils in fibrinogen by single-molecule AFM.," *Biophysical Journal* **92**, L39–L41 (2007).

[169] P. Milani, G. Chevereau, C. Vaillant, B. Audit, Z. Haftek-Terreau, M. Marilley, P. Bouvet, F. Argoul, and A. Arneodo, "Nucleosome positioning by genomic excluding-energy barriers.," *Proceedings of the National Academy of Sciences of the United States of America* **106**(52), 22257–22262 (2009).

[170] F. Montel, H. Menoni, M. Castelnovo, J. Bednar, S. Dimitrov, D. Angelov, and C. Faivre-Moskalenko, "The dynamics of individual nucleosomes controls the chromatin condensation pathway: direct atomic force microscopy visualization of variant chromatin.," *Biophysical Journal* **97**, 544–553 (2009).

[171] J. Moukhtar, C. Faivre-Moskalenko, P. Milani, B. Audit, C. Vaillant, E. Fontaine, F. Mongelard, G. Lavorel, P. St-Jean, P. Bouvet, F. Argoul, and A. Arneodo, "Effect of genomic long-range correlations on DNA persistence length: from theory to single molecule experiments.," *The Journal of Physical Chemistry B* **114**(15), 5125–5143 (2010).

[172] P. Hinterdorfer, "Molecular recognition studies using the atomic force microscope," *Methods in Cell Biology* **68**, 115–139 (2002).

[173] Z. Deng, V. Lulevich, F. T. Liu, and G. Y. Liu, "Applications of atomic force microscopy in biophysical chemistry of cells," *Journal of Physical Chemistry B* **114**(18), 5971–5982 (2010).

[174] M. Radmacher, M. Fritz, C. M. Kacher, J. P. Cleveland, and P. K. Hansma, "Measuring the viscoelastic properties of human platelets with the atomic force microscope," *Biophysical Journal* **70**(1), 556–567 (1996).

[175] M. Prass, K. Jacobson, A. Mogilner, and M. Radmacher, "Direct measurement of the lamellipodial protrusive force in a migrating cell.," *The Journal of Cell Biology* **174**, 767–772 (2006).

[176] C. Rotsch, F. Braet, E. Wisse, and M. Radmacher, "AFM imaging and elasticity measurements on living rat liver macrophages.," *Cell Biology International* **21**, 685–696 (1997).

[177] M. J. Rosenbluth, W. A. Lam, and D. A. Fletcher, "Force microscopy of nonadherent cells: a comparison of leukemia cell deformability," *Biophysical Journal* **90**(8), 2994–3003 (2006).

[178] C. Rotsch, K. Jacobson, and M. Radmacher, "Dimensional and mechanical dynamics of active and stable edges in motile fibroblasts investigated by using atomic force microscopy.," *Proceedings of the National Academy of Sciences of the United States of America* **96**, 921–926 (1999).

[179] R. Matzke, K. Jacobson, and M. Radmacher, "Direct, high-resolution measurement of furrow stiffening during division of adherent cells.," *Nature Cell Biology* **3**(June), 607–610 (2001).

[180] S. E. Cross, Y.-S. Jin, J. Rao, and J. K. Gimzewski, "Nanomechanical analysis of cells from cancer patients.," *Nature Nanotechnology* **2**, 780–783 (2007).

[181] P. Milani, M. Gholamirad, J. Traas, A. Arnéodo, A. Boudaoud, F. Argoul, and O. Hamant, "In vivo analysis of local wall stiffness at the shoot apical meristem in arabidopsis using atomic force microscopy," *The Plant Journal* **67**(6), 1116–1123 (2011).

[182] W. L. Wang and S. J. Hu, "Modal response and frequency shift of the cantilever in a noncontact atomic force microscope," *Applied Physics Letters* **87**(18), 183506 (2005).

[183] H. Hertz, "On the contact of elastic solids," *J. Reine Angew. Math* **92**(156-171), 110 (1881).

[184] I. N. Sneddon, "The relation between load and penetration in the axisymmetric boussinesq problem for a punch of arbitrary profile," *International Journal of Engineering Science* **3**(1), 47–57 (1965).

[185] F. Rico, P. Roca-Cusachs, N. Gavara, R. Farré, M. Rotger, and D. Navajas, "Probing mechanical properties of living cells by atomic force microscopy with blunted pyramidal cantilever tips," *Physical Review E* **72**(2), 021914 (2005).

[186] Y.-T. Cheng and C.-M. Cheng, "Scaling, dimensional analysis, and indentation measurements," *Materials Science and Engineering: R: Reports* **44**(4), 91–149 (2004).

[187] J. E. Sader, "Frequency response of cantilever beams immersed in viscous fluids with applications to the atomic force microscope," *Journal of Applied Physics* **84**(1), 64–76 (1998).

[188] D. Vella, A. Ajdari, A. Vaziri, and A. Boudaoud, "The indentation of pressurized elastic shells: from polymeric capsules to yeast cells.," *Journal of the Royal Society, Interface / the Royal Society* **9**, 448–55 (2012).

[189] B. Laperrousaz, *Rôle du microenvironnement dans le maintien et la ré sistance des cellules souches leucémiques de la Leucémie Myéloïde Chronique voie BMP et contraintes mécaniques.* PhD thesis, École Normale Supérieure de Lyon (2015).

[190] B. Laperrousaz, L. Berguiga, F. E. Nicolini, C. Martinez-Torres, A. Arneodo, V. Maguer-Satta, and F. Argoul, "Nano-indentation of normal and transformed immature cells reveals alterations of their strain-to-stress responses.".

[191] J. R. McWhirter and J. Wang, "Activation of tyrosinase kinase and microfilament-binding functions of c-abl by bcr sequences in bcr/abl fusion proteins.," *Molecular and Cellular Biology* **11**(3), 1553–1565 (1991).

[192] R. S. Frank, "Time-dependent alterations in the deformability of human neutrophils in response to chemotactic activation," *Blood* **76**(12), 2606–2612 (1990).

[193] J. R. McWhirter and J. Wang, "An actin-binding function contributes to transformation by the bcr-abl oncoprotein of philadelphia chromosome-positive human leukemias.," *The EMBO Journal* **12**(4), 1533 (1993).

[194] D. Choquet, D. P. Felsenfeld, and M. P. Sheetz, "Extracellular matrix rigidity causes strengthening of integrin–cytoskeleton linkages," *Cell* **88**(1), 39–48 (1997).

[195] A. Bergman and K. Zygourakis, "Migration of lymphocytes on fibronectin-coated surfaces: temporal evolution of migratory parameters," *Biomaterials* **20**(23), 2235–2244 (1999).

[196] G. Giannone, B. J. Dubin-Thaler, H.-G. Döbereiner, N. Kieffer, A. R. Bresnick, and M. P. Sheetz, "Periodic lamellipodial contractions correlate with rearward actin waves," *Cell* **116**(3), 431–443 (2004).

[197] G. Salbreux, J.-F. Joanny, J. Prost, and P. Pullarkat, "Shape oscillations of non-adhering fibroblast cells," *Physical Biology* **4**(4), 268 (2007).

[198] M. Kapustina, T. C. Elston, and K. Jacobson, "Compression and dilation of the membrane-cortex layer generates rapid changes in cell shape," *The Journal of Cell Biology* **200**(1), 95–108 (2013).

[199] J. E. Sader, "Susceptibility of atomic force microscope cantilevers to lateral forces," *Review of Scientific Instruments* **74**(4), 2438–2443 (2003).

[200] J. E. Sader and R. C. Sader, "Susceptibility of atomic force microscope cantilevers to lateral forces: Experimental verification," *Applied Physics Letters* **83**(15), 3195–3197 (2003).

[201] T. G. Mason, "Estimating the viscoelastic moduli of complex fluids using the generalized Stokes-Einstein equation," *Rheologica Acta* **39**(4), 371–378 (2000).

[202] H. Ma, J. Jimenez, and R. Rajagopalan, "Brownian Fluctuation Spectroscopy Using Atomic Force Microscopes," *Langmuir* **16**(5), 2254–2261 (2000).

[203] J. J. Fredberg and D. Stamenović, "On the imperfect elasticity of lung tissue.," *Journal of Applied Physiology* **67**, 2408–19 (1989).

[204] H. Iwai, C. Fang-Yen, G. Popescu, A. Wax, K. Badizadegan, R. R. Dasari, and M. S. Feld, "Quantitative phase imaging using actively stabilized phase-shifting low-coherence interferometry," *Optics Letters* **29**(20), 2399–2401 (2004).

[205] G. Popescu, L. P. Deflores, J. C. Vaughan, K. Badizadegan, H. Iwai, R. R. Dasari, and M. S. Feld, "Fourier phase microscopy for investigation of biological structures and dynamics," *Optics Letters* **29**(21), 2503–2505 (2004).

[206] T. Ikeda, G. Popescu, R. R. Dasari, and M. S. Feld, "Hilbert phase microscopy for investigating fast dynamics in transparent systems," *Optics Letters* **30**(10), 1165–1167 (2005).

[207] C. Mann, L. Yu, C.-M. Lo, and M. Kim, "High-resolution quantitative phase-contrast microscopy by digital holography," *Optics Express* **13**(22), 8693–8698 (2005).

[208] P. Marquet, B. Rappaz, P. J. Magistretti, E. Cuche, Y. Emery, T. Colomb, and C. Depeursinge, "Digital holographic microscopy: a noninvasive contrast imaging technique allowing quantitative visualization of living cells with subwavelength axial accuracy," *Optics Letters* **30**(5), 468–470 (2005).

[209] G. Popescu, T. Ikeda, R. R. Dasari, and M. S. Feld, "Diffraction phase microscopy for quantifying cell structure and dynamics," *Optics Letters* **31**(6), 775–777 (2006).

[210] K. J. Chalut, W. J. Brown, and A. Wax, "Quantitative phase microscopy with asynchronous digital holography," *Optics Express* **15**(6), 3047–3052 (2007).

[211] G. Popescu, "Quantitative phase imaging of nanoscale cell structure and dynamics," *Methods in Cell Biology* **90**, 87–115 (2008).

[212] P. Bon, G. Maucort, B. Wattellier, and S. Monneret, "Quadriwave lateral shearing interferometry for quantitative phase microscopy of living cells," *Optics Express* **17**(15), 13080–13094 (2009).

[213] D. Fu, W. Choi, Y. Sung, Z. Yaqoob, R. R. Dasari, and M. Feld, "Quantitative dispersion microscopy," *Biomedical Optics Express* **1**(2), 347–353 (2010).

[214] Z. Wang, L. Millet, M. Mir, H. Ding, S. Unarunotai, J. Rogers, M. U. Gillette, and G. Popescu, "Spatial light interference microscopy (slim)," *Optics Express* **19**(2), 1016–1026 (2011).

[215] B. Bhaduri, H. Pham, M. Mir, and G. Popescu, "Diffraction phase microscopy with white light," *Optics Letters* **37**(6), 1094–1096 (2012).

[216] P. Bon, J. Savatier, M. Merlin, B. Wattellier, and S. Monneret, "Optical detection and measurement of living cell morphometric features with single-shot quantitative phase microscopy," *Journal of Biomedical Optics* **17**(7), 0760041–0760047 (2012).

[217] M. Mir, B. Bhaduri, R. Wang, R. Zhu, and G. Popescu, "Quantitative phase imaging," *Progress in Optics* **57**, 133–217 (2012).

[218] F. Zernike, "Phase contrast, a new method for the microscopic observation of transparent objects," *Physica* **9**(7), 686–698 (1942).

[219] D. Gabor *et al.*, "A new microscopic principle," *Nature* **161**(4098), 777–778 (1948).

[220] B. Bhaduri, C. Edwards, H. Pham, R. Zhou, T. H. Nguyen, L. L. Goddard, and G. Popescu, "Diffraction phase microscopy: principles and applications in materials and life sciences," *Advances in Optics and Photonics* **6**(1), 57–119 (2014).

[221] Y. Park, M. Diez-Silva, G. Popescu, G. Lykotrafitis, W. Choi, M. S. Feld, and S. Suresh, "Refractive index maps and membrane dynamics of human red blood cells parasitized by plasmodium falciparum," *Proceedings of the National Academy of Sciences* **105**(37), 13730–13735 (2008).

[222] G. Popescu, Y. Park, W. Choi, R. R. Dasari, M. S. Feld, and K. Badizadegan, "Imaging red blood cell dynamics by quantitative phase microscopy," *Blood Cells, Molecules, and Diseases* **41**(1), 10–16 (2008).

[223] H. V. Pham, B. Bhaduri, K. Tangella, C. Best-Popescu, and G. Popescu, "Real time blood testing using quantitative phase imaging," *PLoS One* **8**(2), e55676 (2013).

[224] F. Charrière, A. Marian, F. Montfort, J. Kuehn, T. Colomb, E. Cuche, P. Marquet, and C. Depeursinge, "Cell refractive index tomography by digital holographic microscopy," *Optics Letters* **31**(2), 178–180 (2006).

[225] Y. Park, T. Yamauchi, W. Choi, R. Dasari, and M. S. Feld, "Spectroscopic phase microscopy for quantifying hemoglobin concentrations in intact red blood cells," *Optics Letters* **34**(23), 3668–3670 (2009).

[226] H. Pham, B. Bhaduri, H. Ding, and G. Popescu, "Spectroscopic diffraction phase microscopy," *Optics Letters* **37**(16), 3438–3440 (2012).

[227] B. Rappaz, P. Marquet, E. Cuche, Y. Emery, C. Depeursinge, and P. Magistretti, "Measurement of the integral refractive index and dynamic cell morphometry of living cells with digital holographic microscopy," *Optics Express* **13**(23), 9361–9373 (2005).

[228] C. Martinez-Torres, L. Berguiga, L. Streppa, E. Boyer-Provera, L. Schaeffer, J. Elezgaray, A. Arneodo, and F. Argoul, "Diffraction phase microscopy: retrieving phase contours on living cells with a wavelet-based space-scale analysis.," *Journal of Biomedical Optics* **19**, 36007 (2014).

[229] H. V. Pham, C. Edwards, L. L. Goddard, and G. Popescu, "Fast phase reconstruction in white light diffraction phase microscopy," *Applied Optics* **52**, A97–101 (2013).

[230] J. Morlet, G. Arenss, E. Fourgeau, and D. Giard, "Wave propagation and sampling theory-Part I: Complex signal and scattering in multilayered media," *Geophysics* **47**(2), 203–221 (1982).

[231] J.-P. Antoine, R. Murenzi, P. Vandergheynst, and S. T. Ali, *Two-dimensional wavelets and their relatives*, Cambridge University Press (2004).

[232] L. Berguiga, E. Boyer-Provera, C. Martinez-Torres, J. Elezgaray, A. Arneodo, and F. Argoul, "Guided wave microscopy: mastering the inverse problem," *Optics Letters* **38**(21), 4269–4272 (2013).

[233] C. B. Walsh and E. I. Franses, "Ultrathin pmma films spin-coated from toluene solutions," *Thin Solid Films* **429**(1), 71–76 (2003).

[234] E. Bedrosian, "A product theorem for hilbert transforms," (1962).

[235] R. Barer, "Interference microscopy and mass determination," *Nature* **169**, 366–367 (1952).

[236] N. T. Shaked, L. L. Satterwhite, N. Bursac, and A. Wax, "Whole-cell-analysis of live cardiomyocytes using wide-field interferometric phase microscopy," *Biomedical Optics Express* **1**(2), 706–719 (2010).

[237] P. Girshovitz and N. T. Shaked, "Generalized cell morphological parameters based on interferometric phase microscopy and their application to cell life cycle characterization," *Biomedical Optics Express* **3**(8), 1757–1773 (2012).

[238] B. Bhaduri, D. Wickland, R. Wang, V. Chan, R. Bashir, and G. Popescu, "Cardiomyocyte imaging using real-time spatial light interference microscopy (slim)," *PLoS One* **8**(2), e56930 (2013).

[239] S. Mallat and S. Zhong, "Characterization of signals from multiscale edges," *IEEE Transactions on Pattern Analysis & Machine Intelligence* (7), 710–732 (1992).

[240] A. Arneodo, N. Decoster, and S. Roux, "A wavelet-based method for multifractal image analysis. i. methodology and test applications on isotropic and anisotropic random rough surfaces," *The European Physical Journal B-Condensed Matter and Complex Systems* **15**(3), 567–600 (2000).

[241] A. Arneodo, N. Decoster, P. Kestener, and S. Roux, "A wavelet-based method for multifractal image analysis: from theoretical concepts to experimental applications," *Advances in Imaging and Electron Physics* (126), 1–92 (2003).

[242] J. Canny, "A computational approach to edge detection," *Pattern Analysis and Machine Intelligence, IEEE Transactions on* (6), 679–698 (1986).

[243] T. Roland, A. Khalil, A. Tanenbaum, L. Berguiga, P. Delichère, L. Bonneviot, J. Elezgaray, A. Arneodo, and F. Argoul, "Revisiting the physical processes of vapodeposited thin gold films on chemically modified glass by atomic force and surface plasmon microscopies," *Surface Science* **603**(22), 3307–3320 (2009).

[244] N. Decoster, *Analyse multifractale d'images de surface rugueuses á l'aide de la transformation en ondelettes*. PhD thesis, Université de Bordeaux I (1999).

[245] A. Thaer, "The refractive index and dry mass distribution of mammalian erythrocytes," *Journal of Microscopy* **89**(2), 237–250 (1969).

[246] A. Roggan, M. Friebel, K. Dörschel, A. Hahn, and G. Muller, "Optical properties of circulating human blood in the wavelength range 400-2500 nm," *Journal of Biomedical Optics* **4**(1), 36–46 (1999).

[247] S. V. Tsinopoulos and D. Polyzos, "Scattering of he–ne laser light by an average-sized red blood cell," *Applied Optics* **38**(25), 5499–5510 (1999).

[248] Y. Fung and P. Tong, "Theory of the sphering of red blood cells," *Biophysical Journal* **8**(2), 175 (1968).

[249] Y.-C. Fung, *Biomechanics: mechanical properties of living tissues*, Springer Science & Business Media (2013).

[250] S. Wang, L. Xue, J. Lai, and Z. Li, "Three-dimensional refractive index reconstruction of red blood cells with one-dimensional moving based on local plane wave approximation," *Journal of Optics* **14**(6), 065301 (2012).

[251] R. Blowers, E. M. Clarkson, and M. Maizels, "Flicker phenomenon in human erythrocytes," *The Journal of Physiology* **113**(2-3), 228–239 (1951).

[252] P. Canham and A. C. Burton, "Distribution of size and shape in populations of normal human red cells," *Circulation Research* **22**(3), 405–422 (1968).

[253] F. Brochard and J. Lennon, "Frequency spectrum of the flicker phenomenon in erythrocytes," *Journal de Physique* **36**(11), 1035–1047 (1975).

[254] M. Wortis and R. Mukhopadhyay, "Stomatocyte–discocyte–echinocyte sequence of the human red blood cell: Evidence for the bilayer–couple hypothesis from membrane mechanics," *Proceedings of the National Academy of Sciences* **99**(26), 16766–16769 (2002).

[255] A. Raman, S. Trigueros, A. Cartagena, A. Stevenson, M. Susilo, E. Nauman, and S. A. Contera, "Mapping nanomechanical properties of live cells using multi-harmonic atomic force microscopy," *Nature Nanotechnology* **6**(12), 809–814 (2011).

[256] H. E. Broxmeyer, M. Etienne-Julan, A. Gotoh, S. E. Braun, L. Lu, S. Cooper, G.-S. Feng, X. J. Li, and R. J. Chan, "Hematopoietic colony formation from human growth factor-dependent tf1 cells and human cord blood myeloid progenitor cells depends on shp2 phosphatase function," *Stem Cellse and Development* **22**(6), 998–1006 (2012).

[257] S. Salesse and C. M. Verfaillie, "Mechanisms underlying abnormal trafficking and expansion of malignant progenitors in cml: Bcr/abl-induced defects in integrin function in cml," *Oncogene* **21**(56), 8605–8611 (2002).

[258] J. Evans, W. Gratzer, N. Mohandas, K. Parker, and J. Sleep, "Fluctuations of the red blood cell membrane : relation to mechanical properties and lack of ATP dependence," *Biophysical Journal* **94**(10), 4134–4144 (2008).

[259] N. Gov and S. Safran, "Red blood cell membrane fluctuations and shape controlled by atp-induced cytoskeletal defects," *Biophysical Journal* **88**(3), 1859–1874 (2005).

[260] D. A. Fedosov, B. Caswell, and G. E. Karniadakis, "A multiscale red blood cell model with accurate mechanics, rheology, and dynamics," *Biophysical Journal* **98**(10), 2215–2225 (2010).

[261] Y. Z. Yoon, J. Kotar, A. T. Brown, and P. Cicuta, "Red blood cell dynamics: from spontaneous fluctuations to non-linear response," *Soft Matter* **7**(5), 2042–2051 (2011).

[262] T. Betz, M. Lenz, J.-F. Joanny, and C. Sykes, "Atp-dependent mechanics of red blood cells," *Proceedings of the National Academy of Sciences* **106**(36), 15320–15325 (2009).

Appendix A

Multi-scale analysis of AFM force-indentation curves.

Biophysical Journal Volume 108 May 2015 2235–2248

Article

Single Cell Wall Nonlinear Mechanics Revealed by a Multiscale Analysis of AFM Force-Indentation Curves

Simona Digiuni,[1] Annik Berne-Dedieu,[2] Cristina Martinez-Torres,[1] Judit Szecsi,[2] Mohammed Bendahmane,[2] Alain Arneodo,[1] and Françoise Argoul[1,*]

[1]Centre National de la Recherche Scientifique UMR5672, Laboratoire de Physique, Ecole Normale Supérieure de Lyon, Université de Lyon I, France; and [2]Centre National de la Recherche Scientifique UMR5667, Laboratoire de Reproduction et de Développement des Plantes, Ecole Normale Supérieure de Lyon, Université de Lyon I, France

ABSTRACT Individual plant cells are rather complex mechanical objects. Despite the fact that their wall mechanical strength may be weakened by comparison with their original tissue template, they nevertheless retain some generic properties of the mother tissue, namely the viscoelasticity and the shape of their walls, which are driven by their internal hydrostatic turgor pressure. This viscoelastic behavior, which affects the power-law response of these cells when indented by an atomic force cantilever with a pyramidal tip, is also very sensitive to the culture media. To our knowledge, we develop here an original analyzing method, based on a multiscale decomposition of force-indentation curves, that reveals and quantifies for the first time the nonlinearity of the mechanical response of living single plant cells upon mechanical deformation. Further comparing the nonlinear strain responses of these isolated cells in three different media, we reveal an alteration of their linear bending elastic regime in both hyper- and hypotonic conditions.

INTRODUCTION

A plant cell wall is a composite polymeric structure made of very stiff and high-persistence-length cellulose microfibrils coated with heteroglycans (hemicelluloses such as xyloglucan), which are themselves embedded in a dense, hydrated matrix of various neutral and acidic polysaccharides with protein scaffolds. This maintains the cell wall's cohesion (1–3). Although mammalian cells also have a cross-linked actin network cortex that coats the internal plasma membrane and acts as a physical barrier for the penetration of sharp cantilevers, a much wider variety of mechanical properties can be achieved by plant cells as related to the tissue function and its environment. For instance, creep, stress relaxation, and hysteresis of load-retract curves all reflect the complex viscoelastic behavior of plant cell walls, apart from the fact that this property may also gradually change from inside to outside, depending on the aging of the cell (4). The morphology and growth behavior of a plant cell is driven by the hydrostatic turgor pressure that pushes and stretches the wall by way of its cellulosic matrix relaxation. Typical turgor pressures in plants are ~0.3–1.0 MPa, which is a range that translates to between 10 and 100 MPa of tensile stress in the walls (5). This tensile stress within the wall is a function of the cell curvature, the wall thickness H_w, and the pressure drop across the wall (6). Different methods have been designed over the past decades to characterize the single-cell-wall elastic modulus through global compression (7,8) or bending strain (9) experiments. The mechanical properties of single plant cells were also tracked down locally, with nanotipped indentation systems provided by an atomic force microscope (AFM) (10–17) or by cellular force microscopes (18,19).

The mechanical characterization of a single plant cell with an AFM cantilever depends on the tip shape. As for animal cells, large spherical indenters are better suited to capture the internal pressure of the cell, whereas sharp conical or pyramidal tips are more appropriate for characterizing the local mechanics of the wall (15,17). This latter tip geometry has been chosen in this work to study single-cell-wall mechanics from *Arabidopsis thaliana* root calli. Working with single plant cells of small size makes AFM measurements trickier for two reasons (15): the first one is due to the very low adhesion and spreading of these cells on solid surfaces traditionally used for animal cells. The second one is the lack of knowledge of both cell-wall thickness and tension in single cells. Moreover, classical analysis of AFM force curves requires a good determination of the contact point at the surface of the cell—not always easy to achieve. To help solving these issues, we develop here an original wavelet-based analysis of the force-indentation curves that reveals a succession of power-law mechanical responses encountered by the AFM cantilever during the cell penetration by the cantilever tip. These power-law responses include an intermediate regime of interest that accounts for the wall stretching and/or bending from which we can extract information about cell-wall thickness and tension. We show that this wavelet-based analysis does

Submitted June 23, 2014, and accepted for publication February 12, 2015.

*Correspondence: fargoul@ens-lyon.fr

Editor: Jennifer Curtis.

0006-3495/15/05/2235/14 $2.00

http://dx.doi.org/10.1016/j.bpj.2015.02.024

not need the knowledge of the contact point to efficiently capture nonlinear departures from the expected linear behavior for an elastic shell of a turgescent cell. Beyond investigating the statistical distributions of the cell-wall effective tension and maximum sustainable stress upon penetration, we also develop a much deeper insight on the mechanics of single plant cells, comparing turgescent cells with hypo- and hyperosmotic culture media cells. It appears from these experiments that when the turgor pressure is reduced (hypertonic medium), the wall tension decreases and even if the whole cell shape seems to be conserved, the cell-wall mechanics is damaged. When increasing the turgor pressure (hypotonic medium), the stretching of the cell wall also changes its viscoelastic response, splitting the mechanical response into two new regimes, below and above the original scaling regime that was observed with turgescent cells. Both hyper- and hypotonic media produce a decrease of single-cell effective tension. We further show that the cell-wall mechanical responses vary dramatically from cell to cell and from point to point on single cells, and we illustrate this inhomogeneous distribution on the surface of these cells by cellulose fluorescence staining.

MATERIALS AND METHODS

Single cell preparation

Single cells were separated from undifferentiated calli derived from *A. thaliana Wassilewskija* (WS-2) 35S GFP-MBD (green fluorescent protein microtubule binding domain marker) plants (14,20). Calli were grown on 4.4 g/L of MSARI-modified medium (Murashige & Skoog media with vitamins, Cat. No. M0222), 30 g/L of sucrose (Cat. No. S08069), KOH, and plant agar (Cat. No. P1001) from Duchefa Biochemie, Amsterdam, The Netherlands; and 500 mg/L of MES (Cat. No. M8250), 0.5 mg/L of 2,4D (Cat. No. D7299), 2 mg/L of IAA (Cat. No. I2886), and 7 g/L 2iPRiboside (Cat. No. D7257) from Sigma-Aldrich (Saint-Quentin Fallavier, France), pH 5.8 at 25°C and transferred every 15–20 days. Three-to-four callus pieces were placed in MS solution containing 4.4 g/L of Murashige & Skoog media with vitamins (Cat. No. M0222) and 30 g/L sucrose (Cat. No. S0809) from Duchefa Biochemie (Haarlem, The Netherlands), and 500 mg/L of MES (Cat. No. M8250; Sigma-Aldrich), pH 5.8 with KOH. After 4 h of constant agitation at 200 rpm, the cells were filtered with a 100-μm nylon mesh. The cells in MS solution were then allowed to settle down on petri dishes precoated with poly-L-lysine (50 μg/mL) and placed under the AFM microscope. Once isolated from their tissues, these cells acquire different morphologies, transitioning from spherical to tubular shapes. For the purpose of analysis, we preferentially selected cells with spherical shapes (Fig. 1 *a*) and performed the force-indentation experiments at the cell centers to prevent a lateral slipping while indenting. To generate hyperosmotic stress, 1 mL of a 1 mol/L mannitol solution was added to 5 mL of MS solution containing the cells to produce the cell plasmolysis. On the opposite, hypoosmotic stress was generated by the addition of 2 mL water to 5 mL of MS solution containing the cells.

Atomic force microscopy

Force curves on isolated cells were recorded with two different systems: a Bioscope Catalyst (Bruker, Palaiseau, France and Coventry, UK) mounted on a fluorescent macroscope and a CellHesion 15–200-μm motorized stage

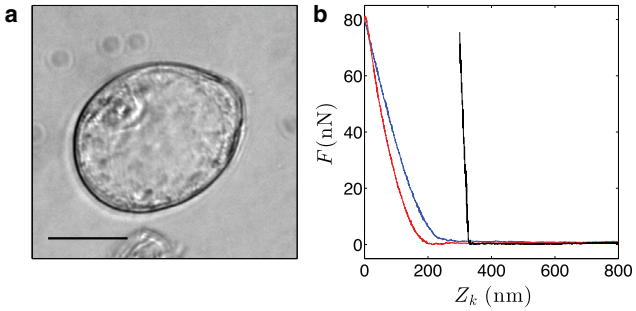

FIGURE 1 (*a*) Bright-field microscopy of a single cell from *A. thaliana* root callus; the scale bar is 25 μm. (*b*) Untreated force curves recorded in liquid on the bottom of a petri dish (*black line*) and on a single cell: (*blue line*) loading force curve; (*red*) unloading curve. The slope of the black line corresponds to the cantilever spring constant k; this slope k is used to correct the force curves (see text). To see this figure in color, go online.

(JPK Instruments, Berlin, Germany) mounted on an inverted microscope in contact mode. We used model No. MPP-12220 triangular shape cantilevers with a nominal spring constant of $k = 5$ N/m (Bruker) with a sweeping velocity of 1 μm/s. Force curves recorded on the bottom of a petri dish containing the MS solution were used to calibrate the deflection sensitivity of the cantilever in liquid. The effective spring constant k of these cantilevers was estimated in between 2 and 3 N/m by directly recording their free fluctuations in MS solution, computing their power spectrum distribution, and fitting these curves with Lorentzian distributions (21–23).

Force-displacement curves were reconstructed from AFM cantilever deflection signals recorded during the decrease of the vertical position Z_k of the cantilever with respect to the sample surface Z_s. When the tip of the cantilever comes precisely into cell contact without being deflected (zero contact force), $Z_k = Z_{k0}$. Once the cell is deformed by the cantilever $Z_k < Z_{k0}$, the difference $\Delta Z_k = Z_{k0} - Z_k$ is given by the sum of the cell deformation $\delta_C = h_{C0} - h_C$ and the ratio of the force F over the cantilever spring constant k (24) as

$$Z_{k0} - Z_k = h_{C_0} - h_C + F/k. \quad (1)$$

A typical set of force curves (approach curve in *blue* and retraction curve in *red*) is shown in Fig. 1 *b*. On the right side of these curves, the cantilever is not yet in contact with the cell, so the force F does not change. When the cantilever comes into contact with the cell surface, the force curve abruptly changes its curvature and increases progressively as the cell is deformed by the penetration of the cantilever tip. The nominal spring constant of the cantilever ($k = 5$ nN/nm) was chosen large enough for the cantilever deflection to be small compared to the cell deformation. This is illustrated by the black force curve in Fig. 1 *b* recorded on a stiff glass coverslip, it corresponds to the correction term $\delta_k = F/k$ in Eq. 1. The loading (*blue*) and unloading (*red*) force curves do not overlap in Fig. 1 *b*, suggesting a partial viscous-loss during this single cell indentation (12,13,25). This slight discrepancy of loading and unloading force curves has been observed in all experiments performed in this work. In the sequel of this article, we will exclusively focus on the loading force curves.

We collected 3457 force curves from 92 *A. thaliana* cells in three different media (60 cells in MS solution, 20 cells in MS solution + mannitol and 12 cells in MS solution + water). We checked that the cantilever stiffness was chosen adequately to be much larger (at least three times) than the cell rigidity. All the curves were corrected, taking into account the cantilever stiffness. When the range of the indentation length (Z_k) was <150 nm, we kept the force curves with a large enough (>0.3 in $\log_{10} s\omega_0$) scaling domain for the computation of the β-exponent (obtained by plotting $T_{g(2)}[F](Z_{kM}, S)$ along the WT maxima line $Z_{kM}(s)$, as described below).

Confocal microscopy

Single cells in MS solution were stained using Pontamine Fast Scarlet 4B (Aldrich Rare Chemicals Library S479896; Sigma-Aldrich,) according to Anderson et al. (4). GFP and Pontamine Fast Scarlet 4B signals were detected using a model No. LSM700 confocal microscope (Zeiss, Jena, Germany) equipped with a 488-nm laser (to detect GFP signal) and a 555-nm laser (to detect Pontamine fast scarlet signal). Z-confocal series were recorded using a 40× water immersion objective and a 500-nm step size. The images and the three-dimensional z-stack projection were analyzed using the software IMAGEJ (National Institutes of Health, Bethesda, MD).

RESULTS

A wavelet-based method to analyze force-indentation curves

The continuous wavelet transform (WT) is a mathematical technique introduced in signal analysis in the 1980s (26). Since then, it has been the subject of considerable theoretical developments and practical applications in many domains (27–31). In particular in the context of this study, the WT has been applied to characterize AFM images of rough surfaces (32) and to image living cells via diffraction phase microscopy (33). It has proved very efficient to estimate scaling exponents and multifractal spectra (34–38). Within the norm $\mathscr{L}^1$, the one-dimensional WT of a signal $F(x)$ reads

$$W_\psi[F](b,s) = \frac{1}{s}\int_{-\infty}^{\infty} F(x)\psi^*\left(\frac{x-b}{s}\right)dx, \qquad (2)$$

where b is a position and s (>0) is a scale parameter (see the Supporting Material for further explanation).

The interest of the WT method is twofold. The first advantage is to use the same smoothing function to filter out the experimental background noise and to compute first- and second-order derivatives with the same smoothing characteristic scale. The second advantage relies on the powerfulness of the WT to detect singularities in a signal (29,30,34,35) and to quantify their force via the estimate of the local Hölder exponent from the behavior across scales of the WT modulus maxima (WTMM) (29–31,34–38). If the wavelet has a compact support, it is straightforward to show that the WT of F, $W_\psi[F](x_0, s)$, depends upon the values of $F(x)$ in a neighborhood of x_0 of size proportional to the scale s. More generally, for any admissible analyzing wavelet ψ, one can show that if $F(x)$ behaves as $(x - x_0)^h$ in the neighborhood of x_0, then the WT of F behaves as a power law of the scale with the exponent h (34,35):

$$\left|W_\psi[F](x_0,s)\right| \propto As^h. \qquad (3)$$

This relation defines how $|W_\psi\ [F](x_0, s)|$ decays when the scale s goes to zero. From the WT, we can therefore recover the local Hölder exponent of the function F, via a simple linear regression fit in a logarithmic representation.

In this study, we use modified versions of the definition (Eq. 2) of the WT that give directly a measure of F in nanoNewtons, dF/dZ in nN/nm and d^2F/dZ^2 in Pascal, once smoothed by a Gaussian window ($g^{(0)}(x)$) of width s,

$$T_{g^{(0)}}[F](b,s) = W_{g^{(0)}}[F](b,s), \qquad (4)$$

$$T_{g^{(1)}}[F](b,s) = \frac{1}{s}W_{g^{(1)}}[F](b,s), \qquad (5)$$

$$T_{g^{(2)}}[F](b,s) = \frac{1}{s^2}W_{g^{(2)}}[F](b,s), \qquad (6)$$

where $g^{(1)}(x)$ and $g^{(2)}(x)$ are the first- and second-order derivatives of $g^{(0)}(x)$ (Supporting Material). Then the local power-law exponent extracted from the WT (Eq. 3) is shifted by -1 or -2, for the first- and second-order derivatives, respectively:

$$T_{g^{(i)}}[F](x_0,s) \propto As^{h-i}. \qquad (7)$$

For illustration, let us consider a piecewise linear function F (Fig. 2 *a*):

$$\begin{aligned} F(Z_k) &= \alpha Z_k \quad \text{for } Z_k < Z_0, \\ F(Z_k) &= 0 \quad \text{for } Z_k \geq Z_0, \end{aligned} \qquad (8)$$

with $\alpha > 0$. This function is continuous, but its first derivative is discontinuous (jumping from α to 0) at $Z_k = Z_0$ and its second derivative is a Dirac delta distribution. In Fig. 2 are

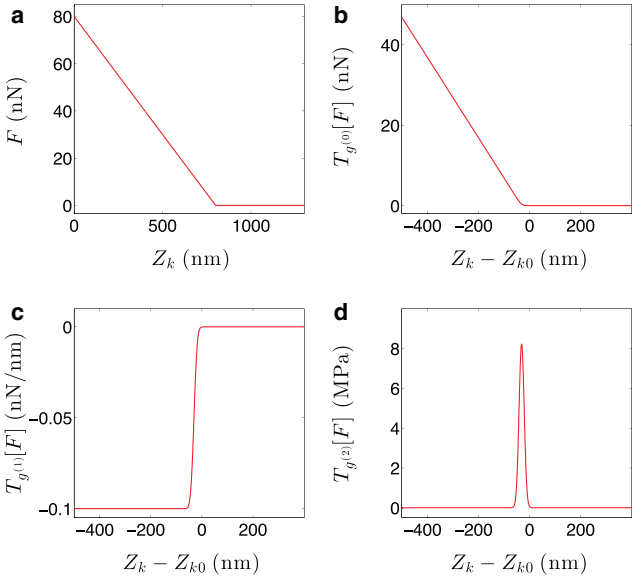

FIGURE 2 Computation of the first and second derivatives of a piecewise linear function using the WT method with a Gaussian function ($sw_0 = 10$ nm). (*a*) The original force curve. (*b*) $T_{g(0)}[F](Z_k - Z_{k0}, s = 1)$, where Z_{k0} corresponds to $T_{\text{contact}} = 10^{-4}$ nN/nm (see text). (*c*) $T_{g(1)}[F](Z_k - Z_{k0}, s = 1)$ in nN/nm. (*d*) $T_{g(2)}[F](Z_k - Z_{k0}, s = 1)$ in MPa. To see this figure in color, go online.

illustrated the two WTs of F computed at the scale $s = 1$ in a $w_0 = 10$ nm unit, using Eqs. 5 (Fig. 2 *c*) and 6 (Fig. 2 *d*), respectively. The value w_0 is a constant value that corresponds to the minimum wavelet size used in this study ($s = 1$). The jump in the first derivative of F and the sharp peak (Dirac) in the second derivative of F at $Z_k = Z_0$ are smoothed by the Gaussian of width $sw_0 = 10$ nm. In this theoretical example, we perfectly know the contact point $Z_{k0} = Z_0$, which is a crucial issue in experimental situations. Indeed the determination of Z_{k0} is a major limitation that groups working on AFM have been facing for more than a decade in their interpretations of experimental noisy force-indentation curves (14,15,39–43). The wavelet-based analysis that we propose here allows us to overcome this difficulty, by simultaneous smoothing out the noise and thresholding the force curve slope $T_{g(1)}[F](Z, s = 1)$ at the value T_{contact} beyond the contact defined at Z_{k0}:

$$T_{g^{(1)}}[F](Z_{k0}, s = 1) = T_{\text{contact}}. \quad (9)$$

For the piecewise linear model in Fig. 2, we used $T_{\text{connect}} = -10^{-4}$ nN/nm, leading to a value of Z_{k0} slightly above Z_0 because the center of the jump in $T_{g(1)}[F]$ in Fig. 2 *c* and the position of the peak in $T_{g(2)}[F]$ in Fig. 2 *d* are slightly shifted toward negative $Z_k - Z_{k0}$ values.

To estimate the Hölder exponent of F at the discontinuity point Z_{k0} of dF/dZ, we simply need to plot $T_{g(2)}[F](Z_{kM}, s)$ along the WT maxima line $Z_{kM}(s)$ (Fig. 3). Fig. 3 *a* shows the color-coded image of $T_{g(2)}[F](b,s)$ in the (b,s) half-plane, together with the so-called maxima line (plotted in *red*) defined by the WTMM obtained at each scale s (34,35). Along the maxima line, we should recover the predicted scaling law $T_{g(2)}[F](Z_{kM}, s) \propto s^{\beta}$ with $\beta = h - 2 = -1$ (Eq. 7). This is verified in Fig. 3 *c*, when plotting $T_{g(2)}[F](Z_{kM}, s)$ versus sw_0 in a logarithmic representation where, by linear regression fit, we get an estimate of the exponent $\beta = -1.002 \pm 0.005$, consistent with the theoretical prediction for a Dirac delta distribution. The scaling law $T_{g(2)}[F](Z_{kM}, s) \propto s^{-1}$ is actually observed over the whole range of scales $10 < sw_0 < 800$ nm. Let us point out that when fitting instead $\log_{10} T_{g(0)}[F](Z_{k0} - Z_k)$ versus $\log_{10}[Z_{k0} - Z_k]$ as commonly performed in the literature (39,41), we do not recover correctly a slope $h = +1$ due to the sensitivity of this curve to the choice of the contact point Z_{k0}. For instance, taking Z_{k0} such that $|T_{g(1)}[F](Z_{k0}, s = 1) = -10^{-4}|$ nN/nm (Fig. 3 *b*), we do not get nice scaling and the expected $h = +1$ exponent is only guessed at very large indentations. Because the WTMM method amounts to tracing the local singularity across scales without a priori knowledge of the contact point Z_{k0}, where the maxima line is expected to converge in the limit $s \to 0^+$, and without any need of precisely defining this contact point, it proves to be very efficient to estimate quantitatively the local Hölder exponent $h = \beta + 2 = 1$ (Fig. 3 *c*).

WTMM characterization of force-indentation curve models

Description of typical AFM force curves

Four force curves captured with the AFM on single plant cells isolated from *A. thaliana* calli are shown in Fig. 4 *a*. In this example, we have selected four different responses taken from two cells (*green* and *red*) at two different positions (*continuous* and *dotted-dashed lines*) to underline the inter- and intracellular variability that we have commonly observed in our single plant cell experiments. Similarly to the piecewise linear model in Fig. 2 *c*, when increasing indentation, the first derivative of these force curves (Fig. 4 *c*), computed with Eq. 5 for $sw_0 = 10$ nm, decreases sharply from zero to reach a plateau. The flatter this plateau, the closer the Hölder exponent to 1. The occurrence of a plateau means that there is a whole range of Z values where $F(Z)$ behaves linearly. When this plateau occurs, its value $T_{g(1)}[F] = -k_E$ provides an estimate of an effective tension of the cell wall in nN/nm (the dimension of a surface stress) at the measurement point. However, for most cells, there is not a strictly constant plateau of $T_{g(1)}[F]$, so we have used instead the second derivative of F to compute an effective stiffness parameter for these cells. Within the linear response theory, k_E is proportional to E (the wall Young modulus) times the wall thickness H_w. The width and the height of the jump from zero to this plateau varies from cell to cell but also with the position of the indentation point on a given cell. The widening of the jump in $T_{g(1)}[F]$ is

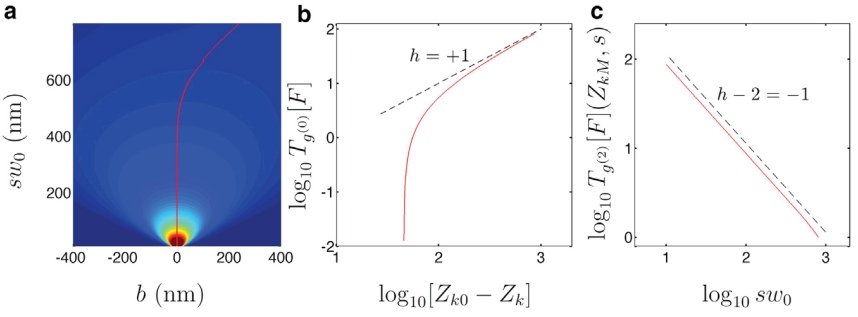

FIGURE 3 (*a*) WT representation $T_{g(2)}[F]$ of the piecewise linear function shown in Fig. 2 *a*. The color map is chosen from 0 (*dark blue*) to 2 MPa (*dark red*). (*Red line*) WT modulus maxima. (*b*) $\text{Log}_{10} T_{g(0)}[F](Z_{k0} - Z_k)$ versus $\log_{10}[Z_k - Z_{k0}]$. (*Dashed line*) Slope $h = +1$. (*c*) Plot of $\log_{10} T_{g(2)}[F](Z_{kM}, s)$ versus $\log_{10}(sw_0)$, on the WT modulus maxima line. (*Dashed line*) Slope $\beta = h - 2 = -1$. To see this figure in color, go online.

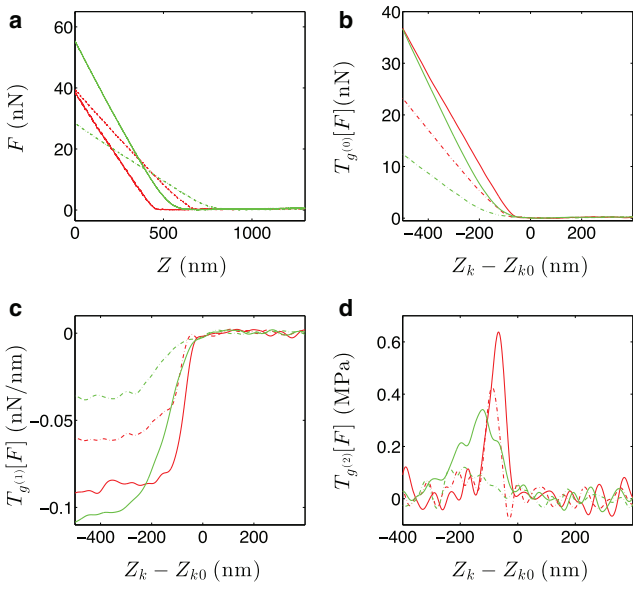

FIGURE 4 Experimental force curves (approach) collected on two different cells. (*a*) Force-indentation curves. (*b*) Plot of $T_{g(0)}[F]$ versus $Z_k - Z_{k0}$. The value Z_{k0} corresponds to $T_{\text{contact}} = -10^{-3}$ nN/nm (Eq. 9). (*c*) Plot of $T_{g(1)}[F]$ versus $Z_k - Z_{k0}$. (*d*) Plot of $T_{g(2)}[F]$ versus $Z_k - Z_{k0}$. (*Continuous* and *dotted-dashed red curves*, *continuous* and *dotted-dash green curves*, respectively) The same cell, but taken with the AFM tip at different positions. The smoothing scale is $s = 1$ ($sw_0 = 10$ nm). To see this figure in color, go online.

correlated to the penetrability of the cell wall by the tip. It can be quantified by looking at $T_{g(2)}[F]$ versus $Z_k - Z_{k0}$ (Eq. 6) (Fig. 2 *d*), which displays a peak positioned at the contact point whose (half) width gives an indication of the thickness of the cell wall and its height quantifies the maximum sustainable pressure upon penetration of the wall by the cantilever tip. We can therefore recover an effective wall stiffness with the product of the local maxima of $T_{g(2)}[F]$ times the scale at which it is estimated. Because the wall has a finite thickness, and because its mechanical strength may vary during its indentation, following this peak along the WTMM maxima line from large to small scales (Fig. 3 *a*) will allow us to evidence and quantify locally changes in the wall effective stiffness k_E. According to the wall thickness, the range of indentations of the wall will be smaller or larger and the maximum sustainable wall indentation will be attained earlier or later. From Fig. 4, *c* and *d*, we therefore conclude that the wall of the cell coded in dotted-dashed green is softer than the one of the cell coded in dotted-dashed red, and the continuous green curve suggests that the wall thickness penetrated by the tip is ~100 nm (half the width of the jump).

Models of mechanical responses of a walled-cell

During its progression into the cell, the sharp pyramidal tip of the AFM cantilever penetrates first into the cell wall with a minor modification of its curvature (Regime A, Fig. 5 *a*)

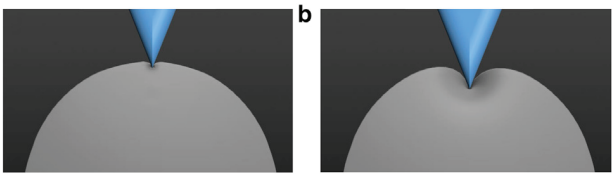

FIGURE 5 Sketch of the indentation of the cell wall by a pyramidal shape tip. (*a*) The tip penetrates the wall without noticeably changing its curvature (Regime A). (*b*) For a deeper indentation, the wall curvature is modified by the pyramidal tip (Regime B). To see this figure in color, go online.

and then bends the cell wall, acting on a thin viscoelastic shell (Regime B, Fig. 5 *b*). For a given deflection of the cantilever (the contact force), the total displacement of the AFM piezo transducer is the sum of the cantilever deflection $\delta_k = F/k$, the depth of penetration of the tip inside the wall δ_p, and the deformation (change of curvature) of the wall δ_b. We use the first derivative of the force curve, computed with the wavelet transform and Eq. 1, to subtract the cantilever deflection term and recover a simple equation for the total indentation δ_C of the cell:

$$\delta_C(F) = [Z_{k_0} - Z_k]_{\text{corr}} = \delta_p(F) + \delta_b(F). \tag{10}$$

Regime A: penetration of the cantilever tip inside the cell wall (*shallow indentations*). The relation $\delta_p(F)$ depends on the shape of the cantilever tip. With the pyramidal shape cantilevers used in this work, we must consider two regimes for the tip penetration inside the wall because the tip is not infinitely sharp and has a finite curvature radius r_t. Roughly speaking, when the indentation is limited to $\delta_p \lesssim r_t$, the shape of the tip can be approximated by a hemisphere and when the indentation increases beyond r_t ($\delta_p \gtrsim r_t$), the cantilever must rather be considered as a square pyramid. These two geometries give force-indentation power laws known, respectively, as Hertz (44) and Sneddon (45) equations.

For $\delta_p \lesssim r_t$ (Hertz),

$$F(\delta_p) = \left[\frac{4E\sqrt{r_t}}{3(1-\nu^2)}\right]\delta_p^{3/2}. \tag{11}$$

In the limit $\delta_p >> r_t$ (Sneddon), and assuming that $\delta_p < H_w$,

$$F(\delta_p) = \left[\frac{\tan(\theta)E}{\sqrt{2}(1-\nu^2)}\right]\delta_p^2, \tag{12}$$

where E is the Young modulus of the wall, ν is the Poisson ratio, and θ is half the tip angle. These formulae predict that if the wall is soft enough for being penetrated by the cantilever tip, we should first observe a power law$\delta^{3/2}$ followed by a power law δ^2, assuming that the wall is thick enough ($H_w >> r_t$). A complete solution of the transition from sphere to pyramid has already been reported in

Rico et al. (46). Because the wall has a finite thickness H_w, the first power law $F(\delta_p) \sim {\delta_p}^{3/2}$ is more likely observed in the experiments.

Regime B: global deformation of the cell wall (*stretching and bending*). Assuming that the wall thickness is <1/10 the cell radius, the theory of spherical shells predicts a linear behavior for $F(\delta_b)$, when the wall Young modulus can be considered as homogeneous in space and invariant during the deformation (47–49). Here we will consider a more general form for $F(\delta_b)$ with a nonlinearity exponent h that will generalize these linear response models to strain-hardening ($h > 1$) or strain-softening ($h < 1$) systems,

$$F(\delta_b) = k_E\, \delta_b^h, \tag{13}$$

where k_E can be considered as an effective tension of the wall.

Piecewise nonlinear model mimicking a force-indentation curve. To guide the interpretation of the experimental force curves, we have generalized the piecewise model discussed above (Eq. 8), to a nonlinear model including a first local penetration regime ($F(\delta_p) \propto {\delta_p}^{3/2}$) and a large-scale deformation regime ($F(\delta_b) \propto {\delta_p}^{h}$):

$$\begin{aligned} F(Z_k) &= 0 && \text{for } Z_k \geq Z_0, \\ F(Z_k) &= A(Z_k - Z_0)^{3/2} && \text{for } Z_1 < Z_k < Z_0 : \text{Regime A}, \\ F(Z_k) &= k_E(Z_k - Z^*)^h && \text{for } Z_k < Z_1 : \text{Regime B}. \end{aligned} \tag{14}$$

The values of A, Z^*, and $F(Z_1)$ are determined as functions of the parameters k_E (effective wall tension or stiffness) and $Z_1 - Z_0$ (wall thickness), by fulfilling the continuity of F and of its first derivative at Z_0 and Z_1. In consistency with the values measured in the experiments reported in Fig. 4, we set $k_E = 0.1$ nN/nm and $Z_0 - Z_1 = 100$ nm. We show in Fig. 6 the three (orders 0, 1, and 2) derivatives of F computed with a smoothing Gaussian wavelet at the scale $s = 1$ with $w_0 = 10$ nm, for three Hölder exponent values: $h = 1.2$ (*green curve*), 1 (*red curve*), and 0.8 (*brown curve*). The occurrence of a plateau in $T_{g(1)}[F]$ (*red curve* in Fig. 6 *c*) at large indentations means that the bending deformation δ_b of the cell wall prevails over the wall tip penetration length δ_p. The curves corresponding to other Hölder exponents differ only in the deformation regime B, because we keep the same term for the penetration regime A (-100 nm $< Z_k - Z_{k0} < 0$). The first-order derivative of F is continuous at $Z_k = Z_1$ but its second-order derivative is discontinuous; the smaller the exponent h, the larger the jump in $T_{g(2)}[F]$ at this transition point Z_1. For $h < 1$, this second derivative abruptly changes its sign when crossing Z_1. Even if the experimental force curves shown in Fig. 4 were selected among the $h > 1$ class responses, we have also observed many cell responses corresponding to $h < 1$.

In this ad hoc model (Eq. 14), we have assumed that the wall deformation is nonlinear for large indentations, which includes the possibility of changes of the cell-wall tension during its deformation. Fitting the force curves to recover the underlying scaling laws is again sensitive to the choice of the contact point. As shown in Fig. 7 *b* for the two force curves of Fig. 6 *a* corresponding to $h = 1$ (*red curve*) and $h = 1.2$ (*green curve*), depending on our choice of the contact point Z_{k0}, the representation of the force curve function in logarithmic scales may be more or less convincing. We choose two different origins Z_{k0} to compute the variable $\delta = |Z_k - Z_{k0}|$ to illustrate the high sensitivity of the reconstruction of these curves (corresponding, respectively, to $T_{\text{contact}} = -10^{-4}$ nN/nm for the *solid curves* and $T_{\text{contact}} = -10^{-3}$ nN/nm for the *dashed curves*). We note that the exponents $h = 1$ and 1.2 can be recognized for indentation $\delta = Z_{k0} = Z_k$ larger than 100 nm, whereas the penetration regime ($\delta^{3/2}$) (Eq. 14) is also visible over a decade $\delta \leq 100$ nm. However, decreasing slightly the contact point Z_{k0} shortens dramatically the range of indentation values where the 3/2 exponent can be estimated. With this noiseless theoretical case, we realize that if, for instance, the threshold criteria on T_{contact} were relaxed further, the shape of the $\log_{10} T_{g(0)}[F](Z_k - Z_{k0}, s = 1)$ curve beyond Z_1 would no longer be fittable by a straight line, meaning that the estimation of the exponent h would become intractable.

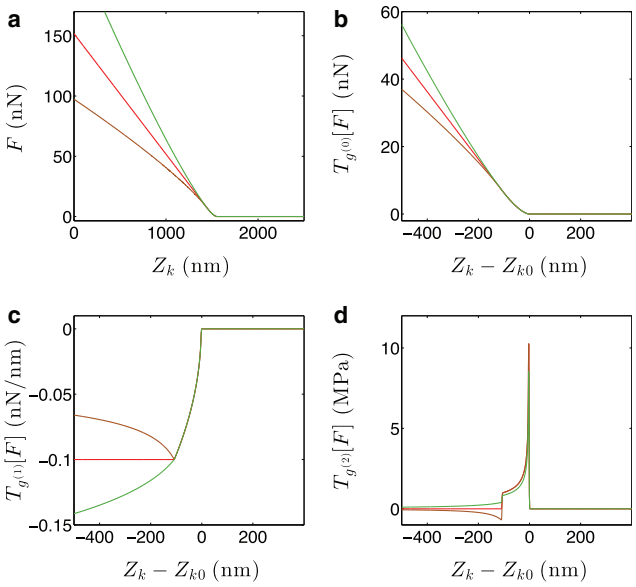

FIGURE 6 Computation of the first and second derivatives of the nonlinear force-curve model (Eq. 14) using the WT method with a Gaussian function ($sw_0 = 1$ nm with $w_0 = 1$ nm). (*Green*, *red*, and *brown curves*) Hölder exponents $h = 1.2$, 1, and 0.8, respectively. (*a*) The original force curves. (*b*) $T_{g(0)}[F](Z_k - Z_{k0}, s = 1)$, Z_{k0} corresponds to $T_{\text{contact}} = -10^{-4}$ nN/nm (see text). (*c*) $T_{g(1)}[F](Z_k - Z_{k0}, s = 1)$ in nN/nm. (*d*) $T_{g(2)}[F](Z_k - Z_{k0}, s = 1)$ in MPa. To see this figure in color, go online.

Wavelet-based multiscale analysis of theoretical force curves

For comparison, Fig. 7, *a* and *c*, show the color-coded space-scale (b,s) representation of $T_{g(2)}[F](Z_k - Z_{k0}, s)$ computed from the same two theoretical force signals in Fig. 6 *a*

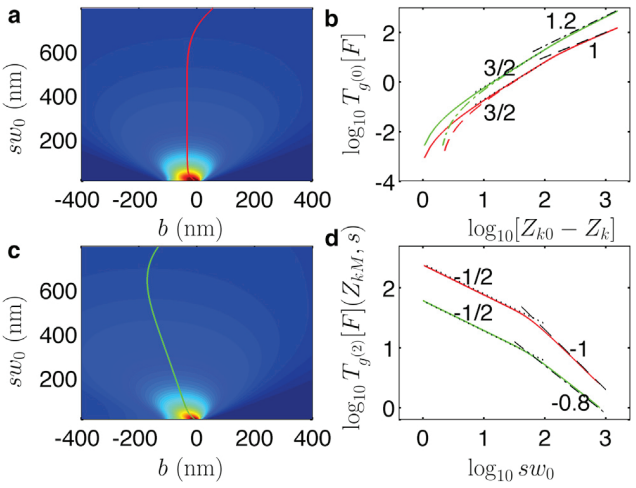

FIGURE 7 Wavelet-based analysis of two theoretical forces curves. (*a* and *c*) Color-coded representation (from 0, *dark blue* to 2 MPa, *red*) of $T_{g(2)}[F](Z_k - Z_{k0}, s)$ computed from two of the force curves in Fig. 6 *a*, corresponding to the Hölder exponents $h = 1$ (*a*) and $h = 1.2$ (*c*). The WTMM line is coded with the same color as the original force curve. (*b*) $\mathrm{Log}_{10}T_{g(0)}[F](Z_k - Z_{k0}, s = 1)$ versus $\log(\delta) = \log(Z_{k0} - Z_k)$ with $T_{\mathrm{contact}} = -10^{-4}$ nN/nm (*solid curves*) and $T_{\mathrm{connect}} = -10^{-3}$ nN/nm (*dashed curves*). (*Black-dashed*, *dashed-dotted*, and *dotted straight lines*) Slopes 1, 1.2, and 3/2 corresponding to the scaling behavior $F \propto \delta$, $F \propto \delta^{1.2}$, and $F \propto \delta^{3/2}$, respectively. (*d*) Logarithmic representation of $T_{g(2)}[F]$ versus scale sw_0 along the WT maxima lines shown in (*a*) and (*c*). (*Black dashed*, *dotted-dashed*, and *dotted straight lines*) Scaling behavior of $T_{g(2)}[F] \propto s^{-1}$, $s^{-0.8}$, and $s^{-1/2}$, respectively. To see this figure in color, go online.

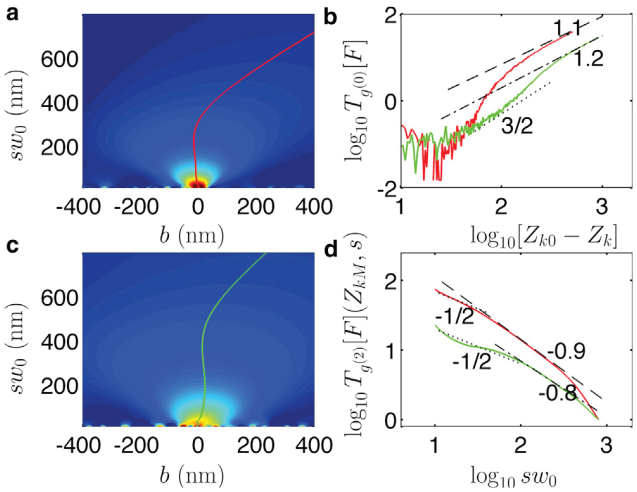

FIGURE 8 Wavelet-based analysis of two experimental force curves. (*a* and *c*) Color-coded representation (from 0, *dark blue* to *red*, 500 kPa (*a*) and 150 kPa (*c*)) of $T_{g(2)}[F](b,s)$ computed from two force curves of Fig. 4 *a* with the same color and line coding. (*b*) $\mathrm{Log}(\delta) = \log_{10}T_{g(0)}[F](Z_k - Z_{k0}, s = 1)$ versus $\log(\delta) = \log(Z_{k0} - Z_k)$ with $T_{\mathrm{contact}} = -5.510^{-3}$ nN/nm. (*Black dashed*, *dashed-dotted*, and *dotted straight lines*) Slopes 1.1, 1.2, and 3/2 corresponding to the scaling behavior $F \propto \delta^{1.1}$, $F \propto \delta^{1.2}$, and $F \propto \delta^{3/2}$, respectively. (*d*) Logarithmic representation of $T_{g(2)}[F]$ versus scale sw_0 along the WTMM lines shown in (*a*) and (*c*). (*Black dashed*, *dotted-dashed*, and *dotted straight lines*) Scaling behavior: $T_{g(2)}[F] \propto s^{-0.9}$, $s^{-0.8}$, and $s^{-1/2}$, respectively. To see this figure in color, go online.

corresponding to the exponent values $h = 1$ (*red curve*) and $h = 1.2$ (*green curve*). The local maxima line of $T_{g(2)}[F](Z_{k0} - Z_k, s)$ points toward the point Z_{kM} of maximum stress of the tip of the cantilever with the shell cortex when the scale sw_0 tends to 1 nm (in the experiments we cannot afford such a small scale, and we will limit our scale analysis to 10 nm). The color code is the same in Fig. 7, *a* and *c*; the larger the *h*, the larger the force for a given deformation and the weaker the divergence of $T_{g(2)}[F](Z_{k0} - Z_k, s)$ when *s* tends to zero. As shown in Fig. 7 *d*, not only are the large-scale power laws expected from the deformation regimes B ($T_{g(2)}[F] \propto s^{-1}$ (and $s^{-0.8}$) well recognized now, but also the scaling regime ($s^{-1/2}$) at low scales. This new wavelet-based approach allows us to recover not only the correct scaling exponents but also the whole interval of scales where these scaling laws are expected to be fulfilled. This gives us confidence in the chance to resolve these two scaling domains $s^{-1/2}$ and s^{β} with $\beta = h - 2$ (Eq. 7) in experimental situations.

Wavelet-based multiscale analysis of experimental force-indentation curves

Turgescent cells

As a first experimental application of our wavelet-based methodology, we report in Fig. 8 the results of a similar analysis of two force curves shown in Fig. 4. Note that the color-coding range of $T_{g(2)}[F](b,s)$ in Fig. 8 *a* is 3.3 times larger than in Fig. 8 *c* because the latter cell (*green line*) is softer than the former (*red line*). Similarly to the theoretical case discussed just above, we can detect a WTMM line (coded with the same color as the force curve) pointing to the maximum stress at Z_{kM} when $sw_0 \rightarrow 10$ nm. We again compare in Fig. 8, *b* and *d*, the scaling behavior of the force-indentation curves and of the WTMM along the maxima lines, respectively. The affordable scaling regime B of $T_{g(0)}[F](Z_k - Z_{k0}, s = 1)$ in Fig. 8 *b* is shifted toward larger indentations (>400 nm) for the green curve and is barely identifiable in the red curve. This distortion of the curve is typically what we anticipated in the theoretical modeling. Enhanced by the presence of noise, the practical incapacity to have a precise estimation of Z_{k0} impairs the characterization of the power-law regime. At low indentations, the shape of the red force-indentation curve misses completely the first penetration regime, and we cannot therefore have any estimation of the cross-over scale in between the low and large indentation regimes (Eq. 14). The green curve seems more favorable, because we can delineate a low indentation range with the scaling law $F \propto \delta^{3/2}$, although it is hindered by the experimental noise. Even though we suspect that this green curve behaves with a power law $F \propto \delta^{1/2}$ at larger indentations, it is again impossible to trust the cross-over indentation scale (~400 nm) where this power-law seems to arise. The analysis with the WTMM lines (Fig. 8 *d*) gives

a much clearer picture of the two indentation regimes involved in these two force curves. We have plotted dashed and dotted-dashed straight lines with slopes $\beta = -0.9$ (*red curve*) and $\beta = -0.8$ (*green curve*) to highlight the range of scales sw_0 where these power-law behavior values of $h = \beta + 2 = 1.1$ and 1.2 appear, respectively. At scales $sw_0 > 100$ nm (respectively, 65 nm) for the green (respectively, *red*) curve, the maxima line enters a power-law regime outlined with a dashed line in Fig. 8 *d*. The minimum scale where this scaling law occurs (noted as $\min(sw_0)$ in the following figures) is very important for this study, because it provides an estimate of how far the cell wall is penetrated by the tip, i.e., a measure of its softness. The experimental examples reported in Fig. 8 confirm that the WTMM method is very efficient to 1) reveal and delimit the range of scales over which scaling operates and 2) estimate the corresponding power-law exponents with good accuracy.

Practically, to compute the exponent $\beta = h - 2$ from the WTMM curves versus sw_0, we do not take a fixed range of scales. For each force curve, we first detect the largest scale range where $\log_{10}[\max(T_{g(2)}[F])1$ versus $\log_{10}(sw_0)$ can be fitted with a linear function within 1% error. Because our experimental force curves are limited in indentation depth, we restrict this scale range from above to the maximum scale $sw_0 < 400$ nm to avoid finite-size effects in the WTMM computation.

Fig. 9 *a* represents the range of sw_0 values where a linear behavior (fixed β) has been detected from a sample of single *A. thaliana* turgescent cells. The corresponding histogram of β-values shown in Fig. 9 *b* is broadly distributed around a mean value ~ -0.9. We did not expect such a result because we thought that when working on single cells extracted from an undifferentiated tissue, the mechanical response would be more homogeneous, and that, for instance, the distribution of β-values would be peaked at ~ -1 (corresponding to $h = 1$). Another important observation is the variability of the range of scales and more importantly of the minimum scale $\min(sw_0)$ where a power-law behavior of the WTMM can be extracted along the maxima lines (Fig. 9 *c*). Note that when β is < -1, the scaling range seriously shrinks down to half a decade, meaning that there is probably not really a scaling law in that case, but instead a global crossover from a first-penetration regime A that extends to larger depths, to a larger-scale regime B that cannot be attained because we are limited in scales. These $\beta < -1$ scaling responses correspond to $h < 1$ (Eq. 13), which is precisely to strain-softening wall domains, where the cell wall may lack cohesion in the cellulose architecture.

This large variability of the mechanical parameters of *A. thaliana* single cells led us to perform confocal fluorescence microscopy to image the distribution of cellulose on the cell cortex (Fig. 10). Fig. 10 *a* is obtained from a confocal section and shows the boundary distribution of cellulose and microtubules underneath. Fig. 10 *b* illustrates the whole surface of the cell, observed from above, where we clearly notice a nonhomogeneous distribution of cellulose. The white arrow points to a hole of cellulose, and the yellow arrows point to external cellulose deposits. If we correlate the mechanical properties of the cell wall to its cellulose content, this image conforms to the wide distribution of β-exponents measured on turgescent cells (Fig. 9 *b*). We also remark in Fig. 10 *a* that the microtubules

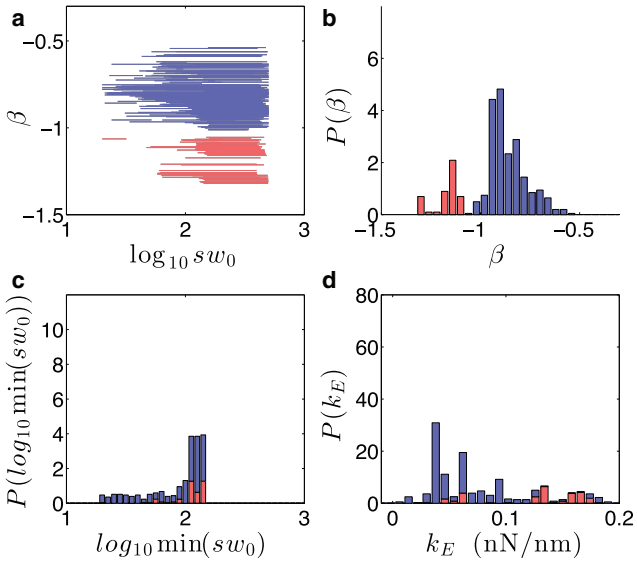

FIGURE 9 Statistical analysis of the mechanical properties of turgescent *A. thaliana* cell walls (2,111 force curves captured on 60 cells). (*a*) β-exponents plotted versus the range of scales sw_0 (in log scale). (*b*) Histogram of β-values. Two intervals of β-values are distinguished with different color codings ($\beta > -1$ ($h > 1$) in *blue*, $\beta < -1$ ($h < 1$) in *red*). (*c*) Stacked histograms of the minimum scale sw_0 (in $\log_{10}$) delimiting the scaling range from below. (*d*) Stacked histograms of effective stiffness k_E coefficient. To see this figure in color, go online.

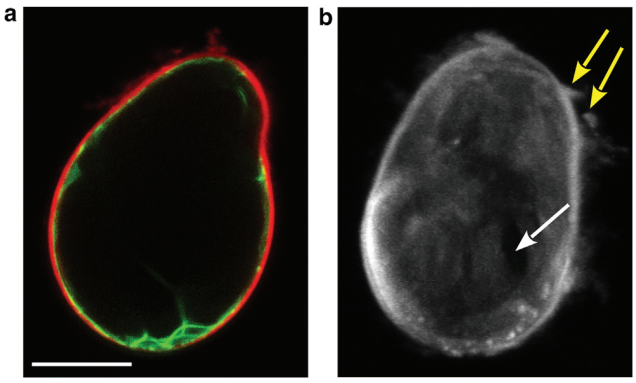

FIGURE 10 Confocal images of turgescent single *A. thaliana* cells. (*a*) Middle section of a cell expressing 35S:GFP-MBD (*green*) that marks microtubules, and stained with Pontamine Fast Scarlet 4B (*red*) that marks cellulose. (*b*) Three-dimensional z-stack projection (IMAGEJ software; National Institutes of Health) of a half cell stained with Pontamine Fast Scarlet 4B (*gray*). (*White arrow*) Region with less cellulose; (*yellow arrows*) irregularities of the cell wall. Scale bar, 20 μm. To see this figure in color, go online.

are not distributed over the periphery of this cell wall but, instead, strictly confined to it bottom part. These fluorescence images (Fig. 10) corroborate our suspicion concerning the heterogeneity in mechanical properties of turgescent plant cells.

We choose two-color-coding in Fig. 9, *a* and *b*, to distinguish β-exponents below (in *red*) and above (in *blue*) -1, and trace to which effective wall stiffness these part of the β-histograms (Fig. 9 *b*) correspond. The histograms of the effective stiffness k_E in Fig. 9 *d* show that the force curves of turgescent cells with β-exponents smaller than -1 ($h < 1$) are stiffer than those with β-exponents larger than -1 ($h > 1$). The value k_E is computed for each force curve from the second derivative modulus maximum $T_{g(2)}$ where the scaling law with exponent β is detected; this wavelet maximum modulus is then multiplied by the wavelet width at this scale to get an effective stiffness in nN/nm. Fig. 9 *d* shows that the distribution of k_E values is limited to a bounded interval, $k_E < 0.2$ nN/nm. Clearly, the upper bound of this interval of k_E values is far below the nominal spring constant of the cantilever (~5 nN/nm), suggesting that this maximum effective wall tension is a characteristic of our 60-cell sample, including eight different pools of cells. The observed variability of k_E is a strong characteristic of these cells. It results not only from variations in the Young modulus, but also from the thickness of their walls. Again the fluorescence images in Fig. 10 support this observation and suggest that the coefficient k_E commonly used to quantify the cell-wall rigidity is not the most appropriate parameter to separate the different cell domains corresponding to strain-hardening ($\beta > -1$, $h > 1$), neutral ($\beta = -1$, $h = 1$), and strain-softening ($\beta < -1$, $h < 1$) situations. Computing a standard deviation on k_E is not relevant either, because we do not have a Gaussian distribution for k_E (Fig. 9 *d*). The β-distribution above -1 bears a stronger resemblance to a Gaussian distribution (Fig. 9 *b*), which suggests that whatever the stiffness of the different wall domains may be, the ability of the cell to change its strain response during indentation (strain-softening, neutral or strain-hardening) is a better indicator of healthy turgescent cells when combined with their effective stiffness.

The histogram of β-values in Fig. 9 *b* led us to the conclusion that these single turgescent cells extracted from *A. thaliana* calli respond to a mechanical stress through a great variability of strain functions. Direct evidence on how these mechanical properties are distributed in space are obtained by mapping the cell by a grid of force curves, as shown in Fig. 11. We captured $10 \times 10 = 100$ force curves on a 10×10 μm^2 grid from a single turgescent cell (Fig. 11 *a*) and we reconstructed in Fig. 11, *b–d*, the maps of the three quantities—the Hölder exponent h, the minimum scale sw_0 delimiting the scaling range of the WTMM line from below, and the effective stiffness k_E, respectively. The map of Hölder exponents in Fig. 11 *b*

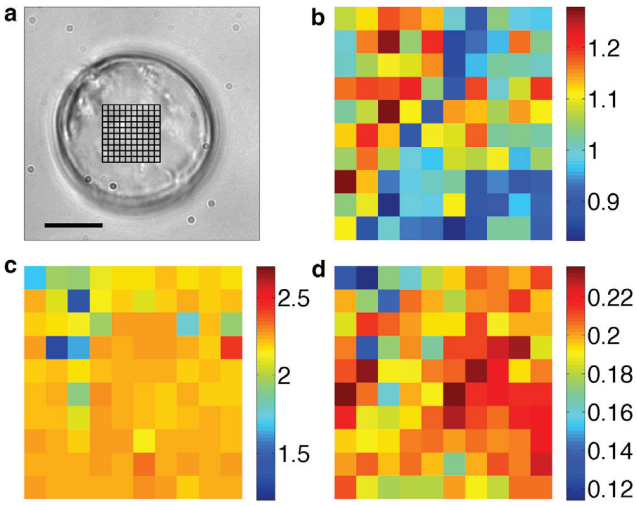

FIGURE 11 Two-dimensional maps of the three quantities $h = 2 + \beta$ (*b*), minimum scale sw_0 (in $\log_{10}$) delimiting the scaling regime s^β of the WTMM along the maxima line (*c*) and the effective wall stiffness k_E (in nN/nm) (*d*) captured from a single turgescent cell shown in (*a*). One-hundred force curves were recorded from a 10×10 μm^2 grid, superimposed to the bright-field microscopy image of this cell in (*a*). Scale bar, 10 μm. To see this figure in color, go online.

shows that this cell wall has a strong heterogeneity of strain responses, from $h = 0.8$ to $h = 1.3$, with the upper-left corner behaving rather like a strain-stiffening domain (*red* and *dark red squares*), and the diagonal of the map and the lower-right corner behaving rather like strain-softening zones (*blue squares*). In between these domains, we also have neutral strain responses (*light-green squares*). This strong variability is not reflected on the minimum scale sw_0 that serves to delimit the WTMM scaling range (Fig. 11 *c*), suggesting that the tip penetration does not change much in this example as an indication that the thickness of the wall does not vary significantly. The map of effective stiffness k_E shows two patches with higher stiffness (*dark red* $>$ 0.2 nN/nm) separated by a diagonal line (*light green-blue*) corresponding to k_E values at ~0.18 nN/nm. The spatial distribution of k_E correlates quite well to h, large k_E values corresponding to large h values, meaning that the regions where the cell wall is stiff also have the propensity to stiffen even further upon deformation (strain-stiffening regions). On the opposite, the softer regions would have less ability to sustain the deformation (strain-softening regions). The corresponding histograms obtained from these 100 force curves can be found in Fig. S2 in the Supporting Material. From the histogram of β-values (Fig. S2 *b*), we see that this cell has a range of Hölder exponents centered at $h \simeq 1.1$ ($\beta \simeq -0.9$), with a narrower distribution than the one previously obtained in Fig. 9 *b*. The peak in the histogram of $\min(sw_0)$ in Fig. S2 *c* is much finer than in Fig. 9 *c*, and confirms that the penetration of this cell is not changing much over the considered grid surface. Finally, the distribution of wall tension k_E values is globally shifted

to higher values, and somewhat peaked in the interval 0.18–0.20 nN/nm. As already visible in Fig. 11 *d*, the variability of k_E can be considered negligible as compared to the variability of the Hölder exponent. This observation indeed makes sense because the shape of a turgescent cell is completely determined by the mechanical property of its wall. If this shape does not change rapidly in time (which is actually what we observe on the systems we are considering in this study), the wall should be locally at equilibrium and its tension should not change dramatically on the cell surface. The variability of these cell responses comes from the richness of their strain responses that ultimately would maintain a stability of the wall tension despite some local variations of the wall's Young modulus. This Young modulus would be directly proportional to the tightness and compactness of the network of cellulose fibrils.

This variability cannot be explained solely by the separation process of the tissue into single cells, performed by a gentle and smooth agitation. Fig. S3 shows a three-dimensional reconstructed confocal image of the cellulose patches of a piece of *A. thaliana* root callus. This image shows that the calli are constituted by a disorganized agglomeration of cells with a cellulose-rich matrix surrounding them. This staining confirms that, at this stage, there are already patches of cell walls with highly variable cellulose contents. This strongly suggests that the inhomogeneity of the cell wall cellulose fibrils is an intrinsic property of these undifferentiated cells, which is maintained during the cell separation process. The inhomogeneity of this living tissue makes a direct estimation of the wall thickness by electron microscopy a difficult task. Nevertheless, we succeeded in capturing scanning electron microscopy images on frozen root callus samples, untreated and unstained to avoid any alteration of their wall structure. Fig. S4 brings additional evidence of the strong variability of the wall thickness (highlighted with *colored stars*). From both these characterizing methods, we can only conclude that the wall thickness of root callus ranges in between 100 and 1000 nm. However, this estimation cannot be extrapolated to the single cells isolated from the callus tissue.

Plasmolyzed cells

To push further the mechanical characterization of these single plant cells, we have tested two different media—one with a higher osmotic pressure (addition of a polyol: mannitol) and the other with a lower osmotic pressure (dilution with water). The characterization of hyperosmotic cells is reported in Fig. 12. The range of scales where the exponent β can be retrieved with 1% error is dramatically reduced (Fig. 12 *a*). The difference with turgescent cells is impressive; the β-exponent distribution is shifted to higher β-values with a small percentage of β-values <-0.9 (Fig. 12 *b*). The $\beta < -1$ responses have completely disappeared. The fact that β is increasing beyond -0.9 is a strong indication of strain-hardening responses. Indeed the

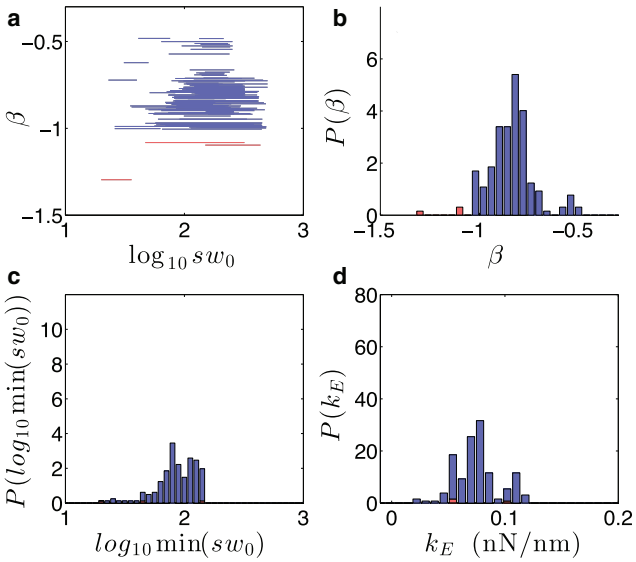

FIGURE 12 Statistical analysis of the mechanical properties of *A. thaliana* single cell walls under hypertonic conditions (900 force curves captured on 20 cells; for details, see Materials and Methods). (*a*) β-exponents plotted versus the range of scales sw_0 (in log scale). (*b*) Histogram of β-values. Two intervals of β-values have been distinguished with different color codings as in Fig. 9. (*c*) Stacked histograms of the minimum scale sw_0 (in $\log_{10}$) delimiting the scaling range from below. (*d*) Stacked histograms of effective stiffness k_E coefficient. To see this figure in color, go online.

plasmolysis of the cells changes drastically the way they adapt to a mechanical stress. The minimum scale values sw_0 are now grouped at ~100 nm (Fig. 12 *c*). The effective tension coefficient k_E is globally decreased (Fig. 12 *d*), meaning that these cells behave as softer cells. Thus, if the thickness of the wall penetrable by the tip increases, its Young modulus must decrease—likely resulting in a decrease of k_E. But this variation of k_E is not very large, and cannot be used as a good criteria for comparing turgescent from plasmolyzed cells. A more discriminating criteria turns out to be the β-exponent and the range of scales where it can be detected, which, a posteriori, contributes to validate the multiscale analysis performed with the WTMM method.

Cytolyzed cells

Finally, the characterization of cells in hypoosmotic media (Fig. 13) is also very instructive. We may consider that this hypoosmotic media pushes the internal turgor pressure to higher values, and thus increases the tension of their walls or destabilizes them if there is a local rupture. The WTMM scaling analysis brings into light an amazing result: β-values ~-0.9 (mild strain-hardening responses) are diminished whereas the probability of neutral and strain-softening responses ($\beta \in [-1.2;1]$) is increased (Fig. 13 *b*). The range of β-values is actually split in two separate β-ranges, which can be made visible on the surface of these cytolyzed cells with fluorescence staining of

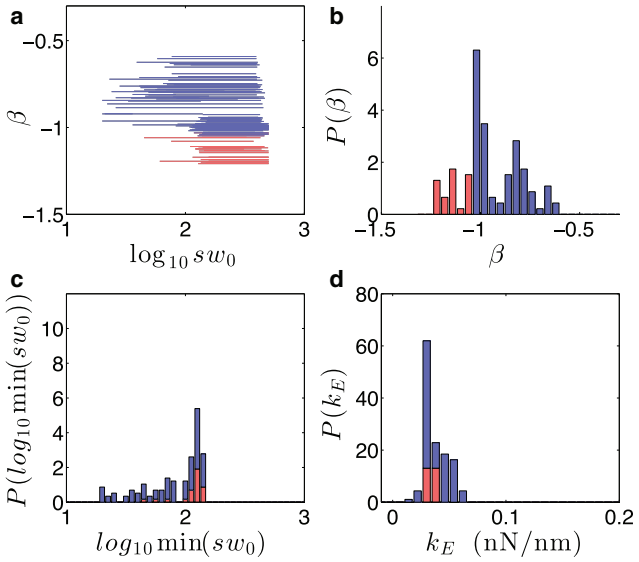

FIGURE 13 Statistical analysis of the mechanical properties of cytolyzed *A. thaliana* cell walls (446 force curves captured on 12 cells; for details, see Materials and Methods). (*a*) β-exponents plotted versus the range of scales sw_0 (in log scale). (*b*) Histogram of β-values. Two intervals of β-values have been distinguished with different color codings as in Fig. 9. (*c*) Stacked histograms of the minimum scale sw_0 (in $\log_{10}$) delimiting the scaling range from below. (*d*) Stacked histograms of effective stiffness k_E coefficient. To see this figure in color, go online.

cellulose (Fig. S5). On the one hand, there may be a reinforcement of stronger, strain-hardening domains; on the other hand, an enlargement of the weaker strain-softening domains may result from stretching-induced damage. The variability of the minimum of sw_0 for the strain-softening domains is actually wider than for turgescent cells (Fig. 13 *c*). The histogram of effective tensions k_E (Fig. 13 *d*) shows a global decrease, with a mean value ~0.03 nN/nm, with the smaller k_E values corresponding to smaller β-exponent values (strain-softening domains).

DISCUSSION

The walls of plant cells vary dramatically in their cellulose fiber composition with plant type. More recently the hierarchical structure of plant materials (3,50–52) has raised increasing interest among botanists and biologists to explain the wide range of their mechanical properties. In this article, we show that on a single plant cell, we have already a whole variety of mechanical behavior that will likely be used by the plant for further development. This high variability requires a broader view of the mechanics of shells. Let us review the energy terms involved in a shell indentation by a sharp cantilever. At shallow indentations (Regime A), the models of Hertz (Eq. 11) and Sneddon (Eq. 12) are frequently used to extrapolate the Young's modulus to characterize cell-wall stiffness in plant cells (14,15,17,53). When the tip of the cantilever penetrates further into the cell wall, a larger deformation occurs that may stretch and bend the wall on larger scales (Regime B) (Fig. 5). The stretching energy per unit surface for a homogeneous expansion of a sphere of radius R reads (54)

$$E_{\text{stretch}} \propto K_S \left(\frac{d}{R}\right)^2, \tag{15}$$

where A is the stretched surface, d is the displacement of an elementary surface, and K_S is the stretching modulus, $K_S = EH_w/(1-\nu^2)$. The bending energy per unit surface is

$$E_{\text{bend}} \propto K_B \left(\frac{d}{R^2}\right)^2, \tag{16}$$

where K_B is the bending modulus,

$$K_B = \frac{1}{12} K_S H_w^2 = EH_w^3/\left(12\left(1-\nu^2\right)\right). \tag{17}$$

The ratio of the stretching over the bending energies scales therefore as

$$\frac{E_{\text{stretch}}}{E_{\text{bend}}} \propto \left(\frac{R}{H_w}\right)^2. \tag{18}$$

When the local radius of curvature R is less than the wall thickness H_w, the bending energy is not negligible as compared to the stretching energy. We can therefore suspect that both these energies will impact the wall response. If the cell wall is very stiff (large Young modulus E), the tip of the cantilever will not penetrate very far inside the wall and the wall will instead flatten and curve on large radius R (Fig. 5 *b*), because it will cost much less to bend ($E_{\text{bend}} \propto EH_w/R^2 \times H_w^2/R^2$) than to stretch ($E_{\text{stretch}} \propto EH_w/R^2$) the wall. The first regime A will therefore be very short in penetration length, and the range of scales sw_0 for computing β will be larger. It is typically what is observed for β-exponents larger than -1 for the turgescent cells. For this set of responses, $h > 1$ means that the force implied for the cell deformation increases faster than expected for a linear response, and the deformation of the cell wall is less and less easy (strain-hardening). This may be explained by the fact that the wall texture and mechanics is not constant over its thickness, with two (or more) layers of different mechanical responses; to prevent wall deformations that are too large, the inner layer could be stiffer than the outer layer (15,50). On the other hand, if the wall Young modulus is comparatively low, the cantilever tip will penetrate deeper inside the wall, and the energy cost for bending it will be much higher than for stretching. The range of scale sw_0 where the WTMM behaves as a power law will be shifted to larger scales, and it will be more difficult to have a correct estimation of the scaling exponent β. There is a set of responses of turgescent cells that give a β-exponent smaller than -1 ($h < 1$), where the range of sw_0 is markedly diminished (both from below and above) (Fig. 9 *b*). The wall domains corresponding to these responses are probably much

softer, and their penetration by the tip is easier than expected for a linear regime; we can call them "strain-softening" domains.

Note that although the heterogeneity of the mechanical properties of plant cell walls was guessed in previous works (14,15), the presence of strain-hardening and strain-softening domains, to our knowledge, has never been remarked upon before. From the histogram of k_E values and the range of sw_0, we can give an estimation of an effective cell wall Young's modulus $E \sim k_1/\langle sw_0 \rangle$: $E \sim 0.49 \pm 0.25$ MPa for the turgescent cells, $E \sim 0.32 \pm 0.18$ MPa for the hypertonic cells, and $E \sim 0.16 \pm 0.12$ MPa for the hypotonic cells. These estimations of E are in quite good agreement with other AFM force curve studies on isolated single cells with sharp pyramidal tips (15,17). However, they are three orders-of-magnitude lower than those obtained from whole tissues such as leaves, for instance (7,16,19,53), suggesting either that the cell wall structure is very different or that beyond the wall of each cell, there are additional layers that reinforce the whole tissue to maintain its cohesion. We must also remark that the sharp tip indenter used in this work allows very local measurements that do not modify the cellulose fiber network over long distances. This can therefore explain why this local perturbation leads to much lower elastic modulus estimations. Note also that we are working with undifferentiated call cells that have not yet achieved the rigidity required by a whole tissue.

The loss of a wide β-scaling range is observed in plasmolyzed cells (hypertonic mannitol medium) (Fig. 12). These cells lose their wall bendability and elasticity, typically as inflated balls (Fig. S5, *a* and *b*). The effective tension k_E, which is related to EH_w in that case, is comparatively lower in plasmolyzed cells than in turgescent cells. If one keep computing the exponent β on a very narrow range of scales, despite the lack of convincing scaling law, its shift to larger values (closer to zero) is the signature of some further increase of the h exponent, revealing again a strain-hardening of these cells and the inhomogeneity of their wall. It is also important to note that the plasmolyzed cells lack completely the original $\beta = -1$ ($h = 1$) behavior of the turgescent cells, confirming a strong modification of their bending elasticity. Finally, when the cells are submitted to a hypotonic media (Figs. 13 and S5, *c* and *d*), their internal water pressure is increased, which strongly modifies their normal turgescent response and likely destabilizes the wall mechanics. The fact that we recover a scaling range that extends to values <100 nm (compared to plasmolyzed cells) means that these cells keep their ability to bend on large domains (as long as such large homogeneous domains exist). However, they lose the range of β-exponents in between -1 and -0.9, to keep only the strain-hardening ($\beta > -0.8$, $h > 1.2$) and the strain-softening ($\beta < -1$, $h < 0.9$) responses. Is it precisely the intermediate regime of β-values close to -0.9 (only observed in turgescent cells) that would be the most active and the easiest to remodel upon a mechanical stress? We note also in Fig. 13 *b* that, contrarily to turgescent cells, a nonnegligible fraction of cytolyzed cells behave as purely elastic shells ($\beta = -1$). Finally, the collapse of the effective stiffness k_E of cytolyzed cells could point out their progressive destabilization under higher internal turgor pressure.

CONCLUSION

We have elaborated on an original approach to study the mechanics of single plant cells, based on a multiscale decomposition of force-indentation curves collected from an atomic-force microscope. We have shown that the mechanical characteristics of living cells usually embodied in their Young moduli are not sufficient to capture the complexity of deformation response of walled-cells. It is therefore necessary to develop new methods that help understanding of the nonlinearities of these responses. The wavelet transform modulus maxima method has been adapted here to quantify these nonlinearities on single cells, isolated from *A. thaliana* calli, and examined in iso-, hyper-, or hypotonic conditions. We have shown that the well-known elastic response of plant cell walls is strongly challenged by our methodology, which reveals that only a finite percentage of cytolyzed cells can behave as purely elastic shells (bending elasticity). This study also illuminates the necessity of considering their nonlinear response via the computation of the nonlinear exponent h, providing additional information to the commonly used Young's modulus estimation. This could also help in distinguishing cell domains that have stronger remodeling ability under a mechanical stress.

SUPPORTING MATERIAL

Supporting Materials and Methods and five figures are available at http://www.biophysj.org/biophysj/supplemental/S0006-3495(15)00221-0.

ACKNOWLEDGMENTS

We are very grateful to T. Muller and A. Duprat from JPK Instruments for their exclusive support on the installation of CellHesion system in our laboratory. We also thank A. Asnacios, L. Berguiga, K. Berthet, A. Boudaoud, P. Durand-Smet, and O. Hamant for very fruitful discussions.

This work has been supported by Agence Nationale de la Recherche grants No. ANR-10-BLAN-1516, ANR 10-BLANC-1615, and ANR-11 IDEX-0007-02 with the PRES-University of Lyon.

REFERENCES

1. Fry, S. C. 2004. Primary cell wall metabolism: tracking the careers of wall polymers in living plant cells. *New Phytol.* 161:641–675.
2. Burgert, I. 2006. Exploring the micromechanical design of plant cell walls. *Am. J. Bot.* 93:1391–1401.
3. Geitmann, A. 2010. Mechanical modeling and structural analysis of the primary plant cell wall. *Curr. Opin. Plant Biol.* 13:693–699.

4. Anderson, C. T., A. Carroll, …, C. Somerville. 2010. Real-time imaging of cellulose reorientation during cell wall expansion in *Arabidopsis* roots. *Plant Physiol.* 152:787–796.
5. Wei, C., and P. M. Lintilhac. 2007. Loss of stability: a new look at the physics of cell wall behavior during plant cell growth. *Plant Physiol.* 145:763–772.
6. Carpita, N. C. 1985. Tensile strength of cell walls of living cells. *Plant Physiol.* 79:485–488.
7. Wang, C. X., L. Wang, and C. R. Thomas. 2004. Modeling the mechanical properties of single suspension-cultured tomato cells. *Ann. Bot. (Lond.).* 93:443–453.
8. Geitmann, A. 2006. Experimental approaches used to quantify physical parameters at cellular and subcellular levels. *Am. J. Bot.* 93:1380–1390.
9. Nezhad, A. S., M. Naghavi, …, A. Geitmann. 2013. Quantification of the Young's modulus of the primary plant cell wall using Bending-Lab-On-Chip (BLOC). *Lab Chip.* 13:2599–2608.
10. Arnoldi, M., C. M. Kacher, …, M. Fritz. 1998. Elastic properties of the cell wall of *Magnetospirillum gryphiswaldense* investigated by atomic force microscopy. *Appl. Phys. A Mater. Sci. Process.* 66:613–617.
11. Arnoldi, M., M. Fritz, …, A. Boulbitch. 2000. Bacterial turgor pressure can be measured by atomic force microscopy. *Phys. Rev. E Stat. Phys. Plasmas Fluids Relat. Interdiscip. Topics.* 62:1034–1044.
12. Parre, E., and A. Geitmann. 2005. More than a leak sealant. The mechanical properties of callose in pollen tubes. *Plant Physiol.* 137:274–286.
13. Parre, E., and A. Geitmann. 2005. Pectin and the role of the physical properties of the cell wall in pollen tube growth of *Solanum chacoense*. *Planta.* 220:582–592.
14. Milani, P., M. Gholamirad, …, O. Hamant. 2011. In vivo analysis of local wall stiffness at the shoot apical meristem in *Arabidopsis* using atomic force microscopy. *Plant J.* 67:1116–1123.
15. Radotić, K., C. Roduit, …, S. Kasas. 2012. Atomic force microscopy stiffness tomography on living *Arabidopsis thaliana* cells reveals the mechanical properties of surface and deep cell-wall layers during growth. *Biophys. J.* 103:386–394.
16. Forouzesh, E., A. Goel, …, J. A. Turner. 2013. In vivo extraction of *Arabidopsis* cell turgor pressure using nanoindentation in conjunction with finite element modeling. *Plant J.* 73:509–520.
17. Zdunek, A., and A. Kurenda. 2013. Determination of the elastic properties of tomato fruit cells with an atomic force microscope. *Sensors (Basel).* 13:12175–12191.
18. Yang, S., and M. T. A. Saif. 2008. Microfabricated force sensors and their applications in the study of cell mechanical response. *Exp. Mech.* 49:135–151.
19. Routier-Kierzkowska, A.-L., A. Weber, …, R. S. Smith. 2012. Cellular force microscopy for in vivo measurements of plant tissue mechanics. *Plant Physiol.* 158:1514–1522.
20. Mathur, J., and C. Koncz. 1998. Callus culture and regeneration. *Methods Mol. Biol.* 82:31–34.
21. Sader, J. E., I. Larson, …, L. R. White. 1995. Method for the calibration of atomic force microscope cantilevers. *Rev. Sci. Instrum.* 66:3789–3798.
22. Sader, J. E., J. A. Sanelli, …, E. J. Bieske. 2012. Spring constant calibration of atomic force microscope cantilevers of arbitrary shape. *Rev. Sci. Instrum.* 83:103705.
23. Sader, J. E., M. Yousefi, and J. R. Friend. 2014. Uncertainty in least-squares fits to the thermal noise spectra of nanomechanical resonators with applications to the atomic force microscope. *Rev. Sci. Instrum.* 85:025104.
24. Cappella, B., and G. Dietler. 1999. Force-distance curves by atomic force microscopy. *Surf. Sci. Rep.* 34:1–104.
25. Radmacher, M., M. Fritz, …, P. K. Hansma. 1996. Measuring the viscoelastic properties of human platelets with the atomic force microscope. *Biophys. J.* 70:556–567.
26. Grossmann, A., and J. Morlet. 1984. Decomposition of Hardy functions into square integrable wavelets of constant shape. *SIAM J. Math. Anal.* 15:723–736.
27. Y. Meyer, editor 1992. Wavelets and their Applications. Springer, Berlin, Germany.
28. Daubechies, I. 1992. Ten Lecture on Wavelets. SIAM, Philadelphia, PA.
29. Mallat, S. 1998. A Wavelet Tour of Signal Processing. Academic Press, New York.
30. Arneodo, A., B. Audit, …, C. Vaillant. 2002. Wavelet-based multifractal formalism: application to DNA sequences, satellite images of the cloud structure, and stock market data. *In* The Science of Disasters: Climate Disruptions, Heart Attacks, and Market Crashes. A. Bunde, J. Kropp, and H. J. Schellnhuber, editors. Springer, Berlin, Germany, pp. 26–102.
31. Arneodo, A., C. Vaillant, …, C. Thermes. 2011. Multi-scale coding of genomic information: from DNA sequence to genome structure and function. *Phys. Rep.* 498:45–188.
32. Roland, T., A. Khalil, …, F. Argoul. 2009. Revisiting the physical processes of vapodeposited thin gold films on chemically modified glass by atomic force and surface plasmon microscopies. *Surf. Sci.* 603:3307–3320.
33. Martinez-Torres, C., L. Berguiga, …, F. Argoul. 2014. Diffraction phase microscopy: retrieving phase contours on living cells with a wavelet-based space-scale analysis. *J. Biomed. Opt.* 19:36007.
34. Mallat, S., and W. L. Hwang. 1992. Singularity detection and processing with wavelets. *IEEE Trans. Inf. Theory.* 38:617–643.
35. Muzy, J. F., E. Bacry, and A. Arneodo. 1994. The multifractal formalism revisited with wavelets. *Int. J. Bifurcat. Chaos.* 4:245–302.
36. Delour, J., J. F. Muzy, and A. Arneodo. 2001. Intermittency of 1D velocity spatial profiles in turbulence: a magnitude cumulant analysis. *Eur. Phys. J. B.* 23:243–248.
37. Audit, B., E. Bacry, …, A. Arneodo. 2002. Wavelet-based estimators of scaling behavior. *IEEE Trans. Inf. Theory.* 48:2938–2954.
38. Arneodo, A., B. Audit, and P. Kestener. 2008. Wavelet-based multifractal analysis. *Scholarpedia.* 3:4103.
39. Domke, J., and M. Radmacher. 1998. Measuring the elastic properties of thin polymer films with the atomic force microscope. *Langmuir.* 14:3320–3325.
40. A-Hassan, E., W. F. Heinz, …, J. H. Hoh. 1998. Relative microelastic mapping of living cells by atomic force microscopy. *Biophys. J.* 74:1564–1578.
41. Crick, S. L., and F. C.-P. Yin. 2007. Assessing micromechanical properties of cells with atomic force microscopy: importance of the contact point. *Biomech. Model. Mechanobiol.* 6:199–210.
42. Carl, P., and H. Schillers. 2008. Elasticity measurement of living cells with an atomic force microscope: data acquisition and processing. *Pflugers Arch.* 457:551–559.
43. Gavara, N., and R. S. Chadwick. 2012. Determination of the elastic moduli of thin samples and adherent cells using conical atomic force microscope tips. *Nat. Nanotechnol.* 7:733–736.
44. Hertz, H. 1881. About the contact of solid elastic bodies [Über die berührung fester elastischer Körper]. *J. Reine Angew. Math.* 92:156–171.
45. Sneddon, I. N. 1965. The relation between load and penetration in the axisymmetric Boussinesq problem for a punch of arbitrary profile. *Int. J. Eng. Sci.* 3:47–57.
46. Rico, F., P. Roca-Cusachs, …, D. Navajas. 2005. Probing mechanical properties of living cells by atomic force microscopy with blunted pyramidal cantilever tips. *Phys. Rev. E Stat. Nonlin. Soft Matter Phys.* 72:021914.
47. Rosenbluth, M. J., W. A. Lam, and D. A. Fletcher. 2006. Force microscopy of nonadherent cells: a comparison of leukemia cell deformability. *Biophys. J.* 90:2994–3003.

48. Vella, D., A. Ajdari, …, A. Boudaoud. 2012. The indentation of pressurized elastic shells: from polymeric capsules to yeast cells. *J. R. Soc. Interface.* 9:448–455.

49. Vaziri, A., and A. Gopinath. 2008. Cell and biomolecular mechanics in silico. *Nat. Mater.* 7:15–23.

50. Gibson, L. J. 2012. The hierarchical structure and mechanics of plant materials. *J. R. Soc. Interface.* 9:2749–2766.

51. Geitmann, A. 2006. Plant and fungal cytomechanics: quantifying and modeling cellular architecture. *Can. J. Bot.* 84:1–13.

52. Beauzamy, L., N. Nakayama, and A. Boudaoud. 2014. Flowers under pressure: ins and outs of turgor regulation in development. *Ann. Bot. (Lond.).* 114:1517–1533.

53. Hayot, C. M., E. Forouzesh, …, J. A. Turner. 2012. Viscoelastic properties of cell walls of single living plant cells determined by dynamic nanoindentation. *J. Exp. Bot.* 63:2525–2540.

54. Fery, A., and R. Weinkamer. 2007. Mechanical properties of micro- and nanocapsules: single-capsule measurements. *Polymer (Guildf.).* 48: 7221–7235.

SUPPLEMENTARY MATERIAL
for
Single cell wall nonlinear mechanics revealed by a multi-scale analysis of AFM force-indentation curves
S. Diguini et al

Complement for the wavelet transformation method

A typical analyzing wavelet $\psi(x)$, that is admissible (of null integral) is the second derivative of a Gaussian $g^{(0)}(x) = e^{-x^2/2}$, also called the Mexican hat wavelet:

$$g^{(2)}(x) = -\frac{d^2}{dx^2} g^{(0)}(x) = e^{-x^2/2}(1 - x^2) \; . \tag{18}$$

Via two integrations by part, we get that the WT $W_{g^{(2)}}[F](b, s)$ of F with the second derivative of a Gaussian wavelet at scale s is nothing but (up to a multiplicative coefficient s^2) the second derivative of a smoothed version $W_{g^{(0)}}[F](b, s)$ of F by a Gaussian function at scale s:

$$W_{g^{(2)}}[F](b, s) = s^2 \frac{d^2}{db^2} W_{g^{(0)}}[F](b, s) \; . \tag{19}$$

Note that we can derive a similar relation with the first derivative of F. Given that $g^{(1)}(x) = -\frac{d}{dx} g^{(0)}(x) = x e^{-x^2/2}$ [30, 31, 35]:

$$W_{g^{(1)}}[F](b, s) = s \frac{d}{db} W_{g^{(0)}}[F](b, s) \; . \tag{20}$$

Let us point out that the validity of the WT definition (Eq. (2)) was further proved for distributions including Dirac distributions [34, 35].

Working recipe for the wavelet transformation computation

Here we describe the different computation steps of the wavelet transform modulus maxima lines and the scaling exponent β, following the four panels of Supplementary Fig. 1.

(a) We take the force curve signal $F(Z)$ on the investigated $[Z_{min},\ Z_{max}]$ indentation interval, together with the Gaussian $g^{(0)}(Z)$ and its second order derivative $g^{(2)}(Z)$ at different scales.

The numerical code for implementing and computing the wavelet transform $T_{g^{(2)}}[F](b, s)$ is given just below as a matlab script for those who would be interested to test this method. Note that for logarithmic analysis of the modulus maxima curves and extraction of the scaling exponent β it is best to use a geometric series of s values. We take in this study $w_0 = 10$ nm and $[s_{min} = 1,\ s_{max} = 80$ nm], which gives a scale varying in between $s_{min} w_0 = 10$ nm and $s_{max} w_0 = 800$ nm. Given Ns the number of scales to be computed, the index i of scales $s w_0$ varies in between 1 and Ns. For each scale we repeat the wavelet transform computation.

```
for i=1:Ns
    s(i) = exp(log(max_scale/min_scale)*(i-1)/Ns);
% l2 is half the length of the force curve signal
    l2 = uint64(length(Z)/2);
% Zmedium is the  middle of the [Zmin, Zmax] positions recorded in the experiment
    Zmedium = Z(l2);
% SQ_Z is the scaled quantity that will appear inside the exponential in g0 and in g2
    SQ_Z = ((Z-Zmedium).*(Z-Zmedium))/(s(i)*s(i)*w0^2);
% if the first derivative g1 of g0 needs also to be computed, their the variable Z needs also to
% be rescaled
    Z_norm = (Z-Zmedium)./(s(i)*w0);
    Eexp_term=exp(-SQ_Z./2);  % for g(0)
    E2 = (SQ_Z - 1)/(s(i)*s(i)*w0*w0);   % for g(2)
% Normalisation of the Gaussian  (order 0) function
    Mo0=Eexp_term/sum(Eexp_term);
% Mo0 is g(0)
    Mo2 = Mo0.*E2;
% Mo2 is the second order g(2) analyzing wavelet (second derivative of a Gaussian)
```

```
% To compute the wavelet transform, we fast fourier transform the wavelet and the force curve Fc
    Mo2fft = fft(Mo2);
    Fcfft = fft(Fc);
 % finally for each scale of index i, we inverse fourier transform the product Mo2fft.Fcfft
 % to retrieve the wavelet transform:
     CWT(1:length(Z),i) = ifft(Mo2fft.*FCfft);
 % CWT corresponds to what we have noted T g(2) [F] (b,s) in the text,  the first index
 % corresponds to the space variable b and the second index corresponds to  the scale parameter s
end
```

The length of the signals to be fast Fourier transformed should be taken as a power law of two to avoid automatic zero-padding by the fft subroutine.

(b) Once the wavelet $T_{g^{(2)}}[F](b,s)$ is computed, we look for the local positive maxima of this wavelet transform. These local maxima are pointed out by circles in Supplementary Fig. 1b.

(c) Along the WT maxima line, defined by linking the maxima across scales, the wavelet transform behaves as a divergent function of the scale parameter s when s tends to zero because we have normalized it on purpose (Eq. (6)) (Supplementary Fig. 1c).

(d) Finally we plot the logarithm of the wavelet transform $T_{g^{(2)}}[F]$ along the maxima line versus the logarithm of s. In this representation, the range of scales where the curve can be approximated by a straight line of slope β is estimated by a linear regression fit. In this example $\beta = -0.93$.

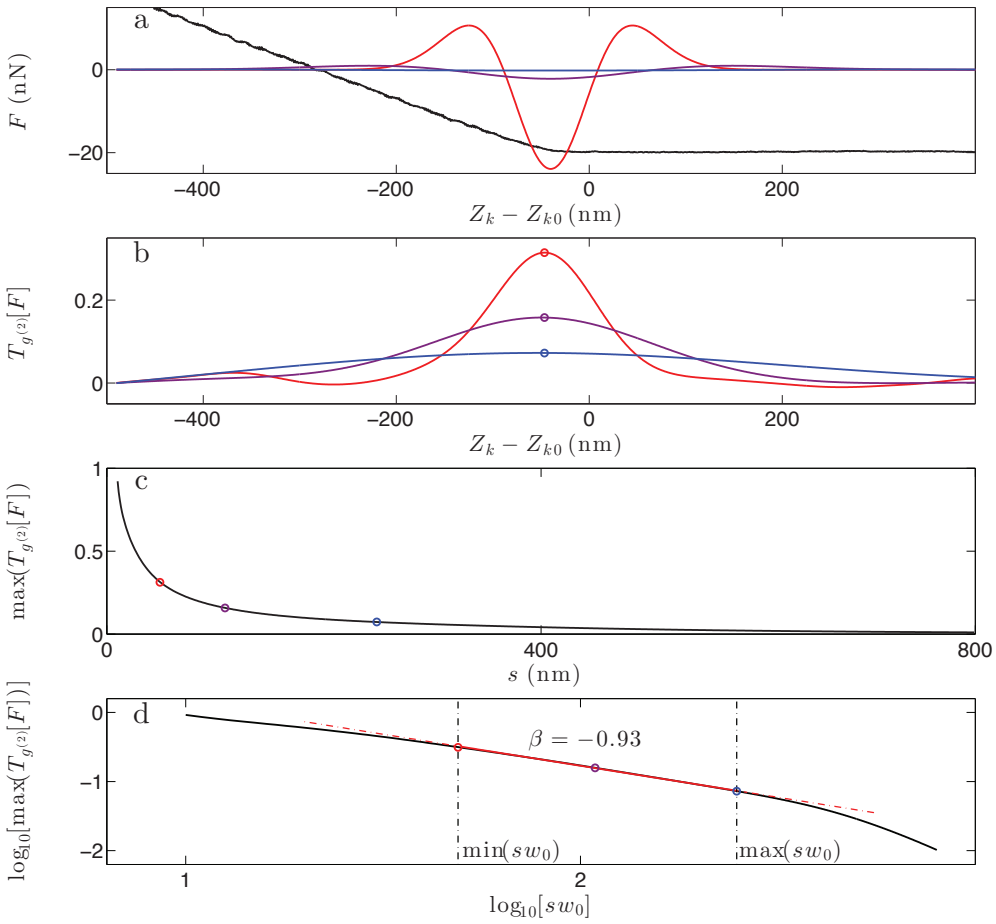

Figure S1: Subsequent computation steps of the scaling exponent β. (a) A typical force curve (black) with the analyzing wavelet g^2 (Eq. (18)) represented for three values of the scale parameter: $s = 4.9$ (red), 10.8 (purple) and 24.9 (blue)). (b) Second derivative of the force curve $T_{g^{(2)}}[F]$ computed with the wavelet transform method (Eq. (6)), for the three scales defined in (a). On each curve, the maximum is outlined by a colored circle; the position and amplitude of this maximum are saved for further analysis. (c) Plot of the wavelet transform $T_{g^{(2)}}[F]$ along the maxima line versus the scale parameter s. (d) Logarithmic plot of the wavelet transform $T_{g^{(2)}}[F]$ along the maxima line versus the scale parameter s. In this representation, the range of scales where the curve can be approximated by a straight line of slope β is estimated by a linear regression fit. In this example $\beta = -0.93$

Appendix B

Passive cell rheology with thermally excited AFM

Passive microrheology of soft materials with atomic force microscopy: a wavelet-based spectral analysis

C. Martinez-Torres,[1] A. Arneodo,[1] L. Streppa,[1] P. Argoul,[2] and F. Argoul[1]
[1)] *UMR5672, CNRS, Laboratoire de Physique, Ecole Normale Supérieure de Lyon, 46 Allée d'Italie, Université de Lyon, Lyon, France*
[2)] *Laboratoire Navier (ENPC/IFSTTAR/CNRS), Université Paris-Est, Ecole des Ponts ParisTech, 6 & 8 av. Blaise Pascal, Champs sur Marne, France*

(Dated: 15 October 2015)

Compared to active microrheology where a known force or modulation is periodically imposed to a soft material, passive microrheology relies on the spectral analysis of the spontaneous motion of tracers inherent or external to the material. Passive microrheology studies of soft or living materials with atomic force microscopy (AFM) cantilever tips are rather rare because, in the spectral densities, the rheological response of the materials is hardly distinguishable from other sources of random or periodic perturbations. To circumvent this difficulty, we propose here a wavelet-based decomposition of AFM cantilever tip fluctuations and we show that when applying this multi-scale method to soft polymer layers and to living myoblasts, the structural damping exponents of these soft materials can be retrieved.

Keywords: atomic force microscopy, spectral density, soft-glassy materials, wavelet transform analysis, scale invariance

Local stiffness and internal friction of soft materials (passive or active such as living cells) have lately been addressed at the nanoscale thanks to the development of pico- to nano-Newton force sensing systems and of nanometer resolution position detection devices[1]. AFM is one of these methods, where a sharply tipped flexible cantilever is indented inside a material to extract its local viscoelasticity from the shift and spreading of the cantilever spectral resonance modes[2–4]. However, these estimations are limited to rather narrow frequency bands surrounding the cantilever resonance modes or their higher harmonics. Spectral decomposition of cantilever fluctuations in contact with soft living tissues in the low frequency range has more rarely been explored. The few attempts which can be found in the litterature were performed with small amplitude harmonic excitations (50 nm) of the sample position driven by a piezo-translator, in the 0.1 to 100 Hz frequency range, for a small and finite number of frequencies[5,6]. Whereas passive (driven by thermal fluctuations) microrheology has been performed for the past two decades by a variety of techniques capturing micro-probe spatial fluctuations[7], it has not been applied yet to AFM cantilever fluctuations. The limitation of AFM-based passive rheology in the low frequency range comes from the mixing of the background vibrations of the liquid chamber with the cantilever fluctuations given by the rheological response of the material which are difficult to disentangle by standard FFT-based spectral averaging methods. In this work, we show that in quasi-stationary situations, these limitations can be circumvented using a wavelet-based spectral analysis of micro-cantilever fluctuations under passive excitation. Two experimental applications to passive polymer layers and living adherent myoblast cells are reported.

Based on the generalized Stokes-Einstein relation (GSER) and associated generalizing assumptions[8], passive microrheology of soft materials enables the extraction of the frequency-dependent complex modulus $G(\omega)$ which is common to a large class of soft materials (foams, emulsions, slurries, cells)[9–11]. The observed scaling laws are explained by a characteristic structural disorder and the metastability of these materials which are embodied under the name of "soft glassy materials" or structural damping model[12]. Their complex shear modulus behaves as:

$$G(\omega) = G_0 \left(\frac{\omega}{\omega_0}\right)^{\alpha} (1 + i\overline{\eta}) \cos\left(\frac{\alpha\pi}{2}\right), \qquad (1)$$

with $\overline{\eta} = \tan(\alpha\pi/2)$ the structural damping coefficient[13], $\omega = 2\pi f$ the radian frequency and α a scaling exponent. G_0 and ω_0 are material dependent scaling factors for stiffness and frequency and $G(\omega) = G'(\omega) + iG''(\omega)$, where $G'(\omega)$ is the storage modulus and $G''(\omega)$ the loss modulus ($i^2 = -1$). An additional viscous term $i\omega\mu$ can be added to Eq. (1) to include a linear viscous regime at high frequency. Eq. (1) was established from fractional calculus[13,14] to interpolate between purely elastic ($\alpha = 0$) and purely viscous ($\alpha = 1$) behaviours. When α tends towards 0, the energy dissipated within a cycle is independent of the frequency[15] and is proportional to the deformation amplitude ε_m^2: $\Delta_{cycle} = G_0(\pi^2\alpha/2)\,\varepsilon_m^2$.

The local deflection signals of an AFM cantilever are produced by different sources of fluctuations. At high frequencies, the hydrodynamic coupling of the cantilever with the surrounding liquid is exciting its resonance modes. At low frequencies, the cantilever captures the acoustic vibrations of the chamber, but also the local random deformations of the material it is in contact with. Each time the material in contact with the cantilever tip breaks locally, or changes its ridigity by fluctuations, the cantilever tip is displaced vertically by δz. In AFM experiments, the cantilever tip is not completely immersed

in the viscoelastic medium, so the continuum approach of Stokes equations must be modified to take into account different boundary conditions. The linearized Hertz-Sneddon[16] equation defines the viscoelastic compliance of the material as proportional to the ratio of the infinitesimal displacement of the tip $\delta z(\omega) = h(\omega) - h_0$ inside the media and the cantilever deflection change $\delta d(\omega)$:

$$\chi(\omega) = \frac{1}{G(\omega)} = \frac{8\tan\theta}{\pi(1-\nu)} \frac{h_0\ \delta z(\omega)}{k_c\ \delta d(\omega)}\ , \tag{2}$$

where θ is the half cone tip angle ($\sim 15°$), h_0 the mean depth of indentation of the tip, ν the Poisson ratio and k_c the stiffness constant of the cantilever.

Within the same approximations as those used in GSER[8], the spectral density $\mathcal{E}_z(\omega)$ of the vertical tip position z can be computed by Fourier transforming its autocovariance function $C_z(\tau)$. $\mathcal{E}_z(\omega)$ is related to the imaginary part $\chi''(\omega)$ of the medium surrounding the tip[17]:

$$\mathcal{E}_z(\omega) = \widehat{C}_z(\omega) = \int_{-\infty}^{\infty} C_z(\tau) e^{-i\omega\tau} d\tau = -\frac{bk_BT\chi''(\omega)}{h_0}\ , \tag{3}$$

where $\widehat{C}_z(\omega)$ denotes the Fourier transform of $C_z(\tau)$. $C_z(\tau) = \mathbb{E}\{z(t)z(t+\tau)\}$ is even and integrable over $\mathbb{R}$ and decreases fast enough to zero as $\tau \to \infty$. $\mathbb{E}\{u\}$ is the expectation of u. h_0 is a characteristic indentation depth depending of the loading force and the viscoelasticity of the sample, k_B is the Boltzmann constant and $b = \pi(1-\nu)/(8\tan\theta)$. When the complex modulus behaves as in Eq. (1), then

$$\mathcal{E}_z(\omega) \propto \omega^{-\alpha}\ . \tag{4}$$

Thus, the spectral density $\mathcal{E}_z(\omega)$ gives access to the imaginary part $\chi''(\omega)$ of $\chi(\omega)$ and its real part $\chi'(\omega)$ can be obtained by the Kramers-Kronig transformation[18]:

$$\chi'(\omega) = \frac{2}{\pi}\mathbb{P}\int_0^{\infty} \frac{\zeta\ \chi''(\zeta)}{\zeta^2 - \omega^2}\ d\zeta\ , \tag{5}$$

where $\mathbb{P}$ stands for *Cauchy principal value*. $G(\omega)$ is then obtained by inverting $\chi(\omega)$ (Eq. (2)).

As illustrated in Fig. 1, the spectral density[19] of AFM micro-cantilever fluctuations exhibits two different behaviours: at high frequencies we observe the cantilever resonance modes with a characteristic Lorentzian shape, and at low frequencies (from 150 to 10 kHz in air, and from 10 to 1 kHz in liquid) the spectrum looks similar to white or coloured noise spectra. From the least square fits of the resonance modes, mechanical parameters of the cantilever (stiffness, quality factor, resonance frequency, damping) are usually retrieved[21?] . The grey (resp. black) FFT-based spectra plotted in Fig. 1 are computed by FFT transform of the z signals captured at 2.5 MHz rate for 2 s (5 10^6 points), without averaging (resp. averaging in log-log scales over frequency windows $\Delta\log_{10}\omega = 0.003$). It comes out from these two periodograms that without averaging it is impossible to retrieve the shape of the resonance peaks. But let us point

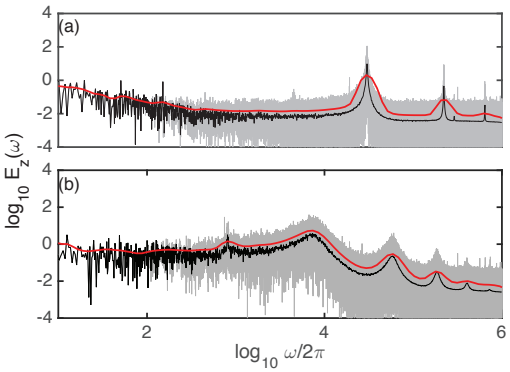

FIG. 1. **Comparison of FFT-based spectra $\mathcal{E}_z(\omega)$ and wavelet-based spectra $\mathcal{E}_{z,CWT}(\omega)$ of free cantilever fluctuations in two different media**. (a) Air. (b) Liquid aqueous chamber. The curves correspond to raw FFT (grey), averaged FFT (black) and wavelet-based (red) spectra. The wavelet scale $a = \omega_0/\omega$.

out that the averaging is much less efficient at low frequency due to the finite length of the z signal. Outside the resonance regions, these spectra collect a combination of external sources of noise or vibrations which increase considerably in liquid chambers (Fig. 1(b)) when the cantilever tip is approached to the chamber bottom wall. In the contact limit, the cantilever is used as a local vibration sensor and no more as a vibrating structure with intrinsic resonance modes[20].

Separating all these sources of fluctuations is a rather tricky problem at low frequencies[22]. The main drawbacks of FFT-based spectral densities are amplified when scaling laws must be retrieved. Only a sub-interval of the frequencies can actually be used for the linear fit (in a logarithmic representation). The continuous wavelet transform (CWT) is a time-frequency technique that turns out to be very helpful for smoothing the power spectra[19]. The CWT is defined by a convolution integral proposed in the early eighties by A. Grossmann *et al.*[23,24], using L^2 normalization:

$$T_z(b,a) = \frac{1}{\sqrt{a}}\int_{-\infty}^{\infty} \overline{\psi}\left(\frac{t-b}{a}\right) z(t)dt\ . \tag{6}$$

$T_z(b,a)$ contains information on the signal z at the scale $a = \omega_0/\omega$ around the point b, ω_0 is a reference frequency. We choose for this study the complex-valued Cauchy analyzing wavelet of order n[15,25]: $\psi(t) = \psi_n(t) = (i/(t+i))^{(n+1)}$ with $n = 31$. The variance of $T_z(b,a)$ can be written as an integral[19]:

$$\mathbb{E}\{|T_z(b,a)|^2\} = \frac{a}{2\pi}\int_{-\infty}^{\infty} \mathcal{E}_z(\omega)|\hat{\psi}(a\omega)|^2 d\omega\ , \tag{7}$$

$$= \frac{1}{2\pi}\int_{-\infty}^{\infty} \mathcal{E}_z(\frac{\omega}{a})|\hat{\psi}(\omega)|^2 d\omega\ . \tag{8}$$

From the variance of $T_z(b,a)$, the wavelet spectral function is defined as:

$$\mathcal{E}_{z,CWT}(a) = \frac{1}{\|\psi\|^2}\mathbb{E}\{|T_z(b,a)|^2\}\ . \tag{9}$$

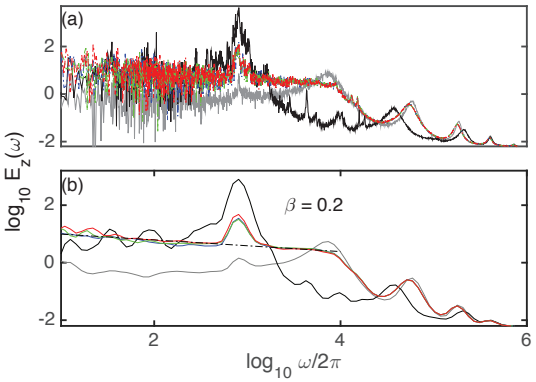

FIG. 2. **Comparison of FFT-based spectra $\mathcal{E}_z(\omega)$ and wavelet spectra $\mathcal{E}_{z,CWT}(\omega)$ of cantilever fluctuations in contact with PDMS thin layers.** (a) FFT-based spectra. (b) Wavelet-based spectra. Grey: free cantilever in liquid, black: cantilever in hard contact with glass (1 nN contact force), blue, (resp. green and red): cantilever in contact with a PDMS thin layer with 0.5 nN (resp. 1 and 2 nN) contact force.

For a white noise z of common variance σ^2, $\mathcal{E}_{z,CWT}(a) = \sigma^2$ does not depend on the scale a. If the wavelet is chosen such that $\|\psi\|^2 = 1$, the wavelet spectrum function yields an unbiased estimator of spectral power laws. For instance, if $\mathcal{E}_z(\omega) \sim \omega^{-\beta}$ for $\omega \in \Omega = [\omega_1, \omega_2]$, then for a given interval $[a_1 = \omega_0/\omega_2, a_2 = \omega_0/\omega_1]$, $\mathcal{E}_{z,CWT}(a) \sim a^\beta = (\omega/\omega_0)^{-\beta}$. The wavelet spectra of free cantilever fluctuations are plotted in red over the FFT-based spectra (averaged in black, non averaged in grey) in Fig. 1(a) and (b) and follow very closely the shape of the cantilever resonance peaks.

The advantage of the wavelet method is to get rid of fluctuations more efficiently than FFT-averaging at low frequencies (because the wavelet averaging window size depends on the scale) and to facilitate the characterization of the out of resonance behaviour when the cantilever comes in contact with a soft material. This is illustrated in Fig. 2 where we compare $\mathcal{E}_z$ and $\mathcal{E}_{z,CWT}$ on five different spectra; the grey line corresponds to a free cantilever in liquid, the black line to the same cantilever tip in hard contact with a glass coverslip, and the blue, green and red spectra are obtained when the cantilever tip is in contact with a soft PDMS layer[26]. The noticeable drawback of the wavelet method is the widening of the cantilever resonance modes but their maxima are correctly estimated. The five spectra shown in Fig. 2 reveal some interesting features. When the cantilever is oscillating freely in the liquid chamber (grey curve of Fig. 2(b)), the wavelet spectrum from $f = \omega/2\pi = 10$ Hz to $f = 1$ kHz is much lower than when the cantilever is pressed on the bottom coverslip (black curve), and this spectrum changes very little with the frequency ω, reminiscent of an uncorrelated white noise. When the cantilever is placed in contact with the bottom chamber coverslip (black curve), the background vibrations of the liquid chamber are amplified, the largest one emerges around $f = 800$ Hz. The spectral density of the cantilever fluctuations when it is pressed on a soft layer (PDMS) is drastically different at low frequency (< 8 kHz) from that obtained for the same cantilever in contact with a solid coverslip, in particular the chamber vibration peak is partly damped by the PDMS layer. Its higher frequency resonance modes are slightly shifted to lower frequencies (order 2 mode: from $f = 59$ kHz to $f = 53.4$ kHz, order 3 mode: from $f = 187$ kHz to $f = 179$ kHz), and its broader resonance peak at 7.3 kHz is flattened in its leftmost part to make place to a flat curve (power-law behaviour). The slope of this line gives an exponent $\beta = 0.2$, the hallmark of a coloured noise signal with persistent correlations[27–29]. From the slope β, the exponent α of Eq. (1) can be estimated, in the low frequency limit ($\omega \to 0$), as $\alpha = \beta = 0.2$. This value of α is characteristic of a viscoelastic material with a more pronounced elasticity than viscosity. Let us point out that this exponent does not change much when increasing the loading force; at this depth of indentation (less than a few micrometers) the material complex modulus is robustly estimated over the range of loading forces considered.

Finally we have performed the same spectral analysis of the cantilever thermal fluctuations when pressed inside a living myoblast (C2C12 cell)[26]. Fig. 3(a) shows consecutive approach (red) - retract (green) force curves recorded above the nucleus of the adherent myoblast cell shown in Fig. 3(b). We report in Fig. 3(c,d) the comparison of FFT-based spectra $\mathcal{E}_z(\omega)$ with the wavelet-based spectra $\mathcal{E}_{z,CWT}(\omega)$ for a free cantilever in culture media (grey) and for the same cantilever indented inside the cell, above its nucleus, for three loading forces 0.44 (blue), 1.1 (green) and 2.2 nN (red). Similarly to the PDMS layer, we observe a drastic flattening of the spectra, just below the first resonance mode of the cantilever ($f \sim 7\ kHz$) when the cantilever is pressed on the cell. We note also that the FFT-based spectrum of the free cantilever in the culture medium containing motile adherent and floating non adherent cells (Fig. 3(c)) is much more noisy than the spectrum recorded in pure water (Figs 1(a) and 2(a)). The presence of cells inside the chamber introduces extra hydrodynamic perturbations that interact with the background vibration modes of the chamber. The wavelet-based spectra are again much smoother (Fig. 3(d)) and the characteristic scaling behavior of structural damping material model emerges again in the lower frequency range (< 6 kHz), with a β exponent that significantly increases with the loading force. The corresponding α values are 0.23 (low load) and 0.38 (higher load) as an indicator of some increase of the viscous component when the cantilever is pressed deeper inside the cell, closer to the nucleus. These cells are much softer than the PDMS layer ($G \sim 480 \pm 50$ Pa), however, when sensed at low loads, their cytoskeleton (including the cell cortex) keeps a rather high elastic to viscous proportion in their response to stress. For deeper indentations, the increase of α suggests that these deeper zones (related to nucleus responses) are more viscous than the outer parts. It is interesting to note that the three spec-

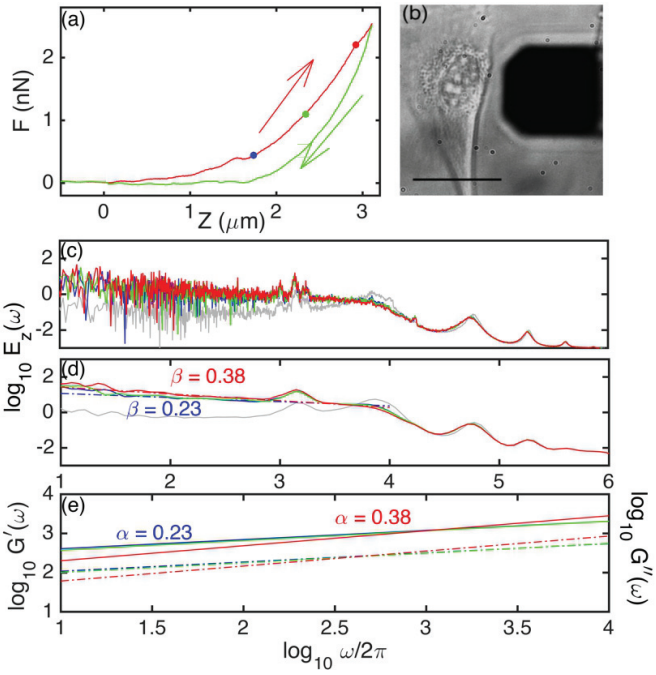

FIG. 3. **Comparison of FFT-based spectra and wavelet spectra of AFM cantilever fluctuations in pressed within a living myoblast.** (a) Approach (red) -retract (green) force curves captured on a living C2C12 myoblast cell. (b) Transmission image of the myoblast cell (left) with the cantilever (right) before the scan. Scale bar: 30 μm. (c) Averaged FFT-based spectra. (d) Wavelet-based spectra. (e) Corresponding storage $G'(\omega)$ (plain lines) and loss $G''(\omega)$ (dashed lines) moduli computed with the GSER and Kramers Kronig integral. Grey: free cantilever in liquid, blue: (resp. green and red): cantilever in contact with a C2C12 myoblast cell with 0.44 nN (resp. 1.1 and 2.2 nN) loading force.

tra intersect around the frequency $f = 1$ kHz, suggesting that the cantilever fluctuations do not depend on the loading force, as the signature of the ability of the cell to robustly respond to a stress independently of its magnitude. Around $f = 1$ kHz, the energy dissipated inside the cell does not vary with the load.

The values of α estimated at low loads with our passive AFM rheology method are very close to those measured with other techniques with adherent cells[11] ($\alpha \sim 0.26$ for myoblasts, $\alpha \sim 0.22$ for macrophages, $\alpha \sim 0.2$ for fibroblasts). It seems that this exponent α would be an invariant of adherent cells, independently of their static shear modulus G_0. Then, using Eqs. (2) and (5), we can compute the storage $G'(\omega)$ and loss $G''(\omega)$ moduli of this myoblast cell for the three loading forces (Fig. 3(e)). We note that at frequencies lower that 1 kHz, the complex moduli of the cell (real and imaginary parts) are larger for shallow indentation depths (targeting the cytoskeleton) than for deep indentations (contacting the nucleus), whereas at larger frequencies this behaviour is inverted, the deeper indentations giving larger complex moduli. This observation is very interesting since it suggests that the elasticity and viscosity parameters of a cell depend on both the speed at which it is stressed (the higher the frequency, the faster the strain) and the depth of sensing. It also points out the importance of performing spectral studies that would allow us to investigate larger spectral ranges. Our study shows that in the acoustic frequency range (from 10 Hz to 20 kHz), the cell behaves as a material with a broad range of delay times and that the distribution of these delays behaves as a power law.

We have shown in this work that AFM can be used for passive rheologic characterization of soft samples (polymers, living cells) thanks to a wavelet-based computation of spectral density of AFM micro-cantilever fluctuations. This method is fast since from a single fluctuation signal, the elastic and viscous characteristics of the sample can be obtained without need of modulating periodically the sample height for a finite set of frequencies. The advantage of AFM, as compared to other particle tracing methods, is to provide some estimate of the low frequency shear modulus G_0 from force indentation curves and to adapt the range of loading forces to investigate the rheology of soft materials. Furthermore, the possibility to work with cantilevers with different stiffnesses should also allow to enlarge further the frequency range for passive rheology. Indeed the full performance of this time-frequency decomposition was not used in this work, since we computed a time-averaged variance of the wavelet transform coefficients. To perform a rheological characterization of slowly varying systems, like migrating or dividing cells, a time-frequency decomposition of the complex shear modulus would be very helpful. This work is under progress

We are very thankful to L. Schaeffer and L. Berguiga for fruitful discussions. This work was supported by the French Agency for Research (ANR-11 IDEX-0007-02 - PRES-University of Lyon). The scholarships of C.M.T. and L.S. have been supported respectively by CONACyT (Mexico) and AFM-Téléthon.

[1] G. Bao and S. Suresh, Nat. Mat. **2**, 715 (2003).
[2] M. Radmacher and R.W. Tillmann and H. E. Gaub, Biophys. J. **64**, 735 (1993).
[3] R. Garcia and R. Perez, Surf. Sci. Rep. **47**, 197 (2002).
[4] N. Ploscariu and R. Szoszkiewicz, Appl. Phys. Lett. **103**, 263702 (2013).
[5] J. Alcaraz, L. Buscemi, M. Grabulosa, X. Trepat, B. Fabry, R. Farré and D. Navajas, Biophys. J. **84**, 2071 (2003).
[6] P. Roca-Cusachs, I. Almendros, R. Sunyer, N. Gavara, R. Farre and D. Navajas, Biophys. J. **91** 3508 (2006).
[7] T. M. Squires and T. G. Mason, Ann. Rev. Fluid Mech. **42**, 413 (2010).
[8] T. G. Mason and D. A. Weitz, Phys. Rev. Lett. **74**, 1250 (1995).
[9] F. Gittes, B. Schnurr, P. D. Olmsted, F. C. MacKintosh and C. F. Schmidt, Phys. Rev. Lett. **79**, 3286 (1997).
[10] B. Fabry, G. N. Maksym, J. P. Butler, M. Glogauer, D. Navajas, N.A. Taback, E.J. Millet and J. J. Fredberg, Phys. Rev. E **68**, 041914 (2003).
[11] M. Balland, N. Desprat, D. Icard, S. Féréol, A. Asnacios, J. Browaeys, S. Hénon and F. Gallet, Phys. Rev. E **74**, 021911 (2006).
[12] P. Sollich, Phys. Rev. E **58**, 738 (1998).
[13] R. L. Bagley and P. J. Torvik, J. Rheol. **30**, 133 (1986).
[14] L. Garibaldi, *Viscoelastic Material Damping Technology* (Becchis Osiride, Torino, 1996).
[15] P. Argoul, *Quelques réflexions sur l'identification de paramètres*

en dynamique des matériaux et des structures. HDR, Lyon I University, https://tel.archives-ouvertes.fr/tel-00364431 (2004)
[16] I. N. Sneddon, Int. J. Eng. Sci. **3**, 47 (1965).
[17] T.G. Mason, Rheol. Acta **39**, 371 (2000).
[18] N. Pottier, *Physique Statistique Hors d'Equilibre* (CNRS Edition, Paris, 2007).
[19] R.A. Carmona, W.L. Hwang and B. Torrésani, *Practical Time-Frequency Analysis* (Academic Press, San Diego, 1998).
[20] J. L. Hutter and J. Bechhoefer, Rev. Sci. Instrum. **64**, 1868 (1993).
[21] J. W. M. Chon, P. Mulvaney, J. E. Sader, J. Appl. Phys. **87**, 3978 (2000).
[22] T. P. Le and P. Argoul, Mech. Sys. Signal Proc. **52-23**, 29 (2014).
[23] A. Grossmann and J. Morlet, SIAM J. Math. Anal. **15**, 723 (1984).
[24] J. M. Combes, A. Grossmann and P. Tchamitchian, *Wavelets. Time-Frequency Methods and Phase Space* (Springer-Verlag, Berlin, 1990).
[25] P. Argoul, T. P. Le, Mech. Sys. Signal Proc. **17**, 243 (2003).
[26] See supplementary material at http://dx.doi.org/.... for a more detailed description of materials and methods, polymer layers preparation, cell culture and other data.
[27] J.F. Muzy, E. Bacry and A. Arneodo, Int. J. of Bifurc. Chaos **4**, 245 (1994).
[28] A. Arneodo, E. Bacry and J. F. Muzy, Physica A **213**, 232 (1995).
[29] B. Audit, E. Bacry, J. F. Muzy and A. Arneodo, IEEE Trans. Info. Theory **48**, 1938 (2002).

Passive microrheology of soft materials with atomic force microscopy: a wavelet-based spectral analysis

C. Martinez Torres, A. Arneodo, L. Streppa, P. Argoul and F. Argoul

Materials and Methods

AFM measurements The AFM experiments are performed with JPK CellHesion 200 system (JPK, Berlin), mounted on an inverted microscope. Transparent pyramidal tip cantilevers with rectangular section (qp-Cont from Nanosensors, Neufchatel, Switzerland) with a nominal spring constant 0.1 nN/nm are used. Prior to each experiment, the deflection sensitivity of the cantilever is estimated on fused silica and the cantilever spring constant is calibrated by the thermal noise method[1,2], the deflection set-point and feedback control gains are chosen for optimum signal to noise ratio. Approach-retract force curves (Fig. 3(a)) are recorded at 1 μ/s for a fixed force set-point (2 nN) on each sample.

The cantilever deflection raw signals are recorded separately from AFM CellHesion electronics with a high-speed acquisition board, at a frequency of 2.5 MHz in segments of 2 s. For measurements in liquid, distilled water or culture medium (2 ml) is poured into petri dishes with a glass bottom. Once the cantilever reaches the contact loading force with the sample, its fluctuations are recorded. The set of following forces 0.5 nN / 1 nN / 2 nN for PDMS and 0.44 nN / 1.1 nN / 2.2 nN for myoblasts are tested on different samples. We consider the cantilever as free when it is far enough from the bottom surface of the chamber, typically when the FFT spectrum no longer changes (for larger distances than the cantilever length 200-300 μm).

Preparation of the PDMS layers RTV615 silicone rubber compounds (purchased from Momentive Performance Materials) are mixed in a 20:1 ratio (agent A : agent B), and poured in a medium sized petri dish to reach a gel thickness of about 2 mm. The gel is cured at 70°C during 18 h, and let to rest at room temperature for 4 h before AFM experiments. The mean quasi-static shear modulus of these PDMS layers is estimated by fitting indentation curves with the Sneddon model[3], to the value $G_0 = 14 \pm 2$ kPa (1 μm indentation depth and 1 μm/s scan velocity).

Cell cultures C2C12 mouse cells (ATCC CRL-1772TM) are grown in high glucose (4.5 g/L) Dulbeccos modified Eagle medium (DMEM - GE Healthcare Life Science) supplemented with 20% fetal bovine serum (GE Healthcare Life Science) and 1% antibiotics (penicillin/streptamicine - Sigma Aldrich). Adherent myoblasts on cleaned glass bottom petri dishes are maintained at 37°C and 5% CO_2, until they reach 60% confluence before rapidly transferred to the AFM (Fig. 3(b)) for mechanical tests at room temperature. The quasi-static shear modulus of these adherent myoblasts is estimated by fitting indentation curves (Fig. 3(a)) with the Sneddon model[3], to the value $G_0 = 480 \pm 50$ Pa above the nuclear zone and $G_0 = 500 \pm 35$ Pa above the cytoskeleton zone. The Young modulus is given by the relation: $E = 2G_0(1 - \nu)$ with ν the Poisson's ratio.

REFERENCES

[1]J. L. Hutter and J. Bechhoefer, Rev. Sci. Instrum. **64**, 1868 (1993).

[2]J.L. Sader, Journal of Applied Physics **84**(1), 64-76 (1998)

[3]I.N. Sneddon, International Journal of Engineering Science **3**(638), 47 (1965)

Appendix C

Wavelet-based analysis to retrieve the phase from DPM images.

Journal of Biomedical Optics 19(3), 036007 (March 2014)

Diffraction phase microscopy: retrieving phase contours on living cells with a wavelet-based space-scale analysis

Cristina Martinez-Torres,[a] Lotfi Berguiga,[b] Laura Streppa,[a,c] Elise Boyer-Provera,[a] Laurent Schaeffer,[c] Juan Elezgaray,[d] Alain Arneodo,[a] and Françoise Argoul[a,*]
[a]Université de Lyon, CNRS UMR5672, ENS de Lyon, 69007 France
[b]Université de Lyon, CNRS USR3010, ENS de Lyon, 69007 France
[c]Université de Lyon, CNRS UMR5239, ENS de Lyon, 69007 France
[d]Université Bordeaux 1-ENITAB, CNRS UMR 5248, Pessac, 33600 France

Abstract. We propose a two-dimensional (2-D) space-scale analysis of fringe patterns collected from a diffraction phase microscope based on the 2-D Morlet wavelet transform. We show that the adaptation of a ridge detection method with anisotropic 2-D Morlet mother wavelets is more efficient for analyzing cellular and high refractive index contrast objects than Fourier filtering methods since it can separate phase from intensity modulations. We compare the performance of this ridge detection method on theoretical and experimental images of polymer microbeads and experimental images collected from living myoblasts. [DOI: 10.1117/1.JBO.19.3.036007]

Keywords: quantitative phase imaging; diffraction phase microscopy; continuous wavelet transform; space-scale analysis; interferometry.

Paper 130776RR received Oct. 29, 2013; revised manuscript received Jan. 28, 2014; accepted for publication Jan. 30, 2014; published online Mar. 10, 2014.

1 Introduction

During the past century, the attraction of biophysicists for observing and characterizing living matter at cellular and subcellular levels has been the prime mover for developing sophisticated microscopic devices. Even if the concept of diffraction-limited imaging and interferometry principles[1] was established for a long time, the actual development of microscopic devices based on interferometric contrast was achieved in the first part of the 20th century by Zernike[2] and Nomarski and Weill[3] and further developed by Gabor,[4] who pioneered the principle of holographic microscopy. Retrieving a phase information from the light transmitted through transparent objects, like living cells, has benefited from the development of coherent sources, optoelectronic polarizing tools, and fast and sensible cameras in the second part of the 20th century. It is nowadays quite straightforward to design a compact, highly sensitive phase microscope that can follow in real time the dynamics of cells. In the last decade, different teams[5–13] have played a major role in disseminating the concepts of quantitative phase microscopy (QPM) among the optical and biophysical community. They have applied this technique to the real-time characterization of cellular dynamics and their alteration in cases of diseases.[6,13–16]

Other approaches that do not rely on interferometric principles have also been proposed to circumvent the constraint of high degree of coherence. They rather start from a principle of electromagnetic energy conservation, written as the divergence of the wave flow vector being equal to zero.[17–21] The technique of transport of intensity is valid only for weak defocus and reduces to a differential equation for field propagation.[22,23] This method is interesting for partially coherent illumination such as given by broadband polychromatic sources. For thick samples, three-dimensional computation is required.[24]

The principle of diffraction phase microscopy (DPM) introduced by Popescu and coauthors[25–27] relies on both off-axis and common-path principles in combination with fast acquisition rate and high temporal sensitivity. The interference patterns produced by a DPM system correspond to the superimposition of a simple carrier fringe pattern, given, for instance, by a diffraction grating, with the image of the object through the objective lens. To retrieve the phase image associated with the sample object, different methods have been proposed, including Hilbert transform followed by phase unwrapping,[28,29] derivative methods,[30] and Fourier filtering to avoid unwrapping problems.[31] All these phase retrieval algorithms rely on the assumption that the object phase does not alter the fringe carrier pattern, allowing a quasi one-dimensional analysis of interference patterns. To improve this approach and delineate more precisely the validity of this assumption, we propose here to generalize Fourier filtering methods using a two-dimensional (2-D) space-scale analysis based on Morlet wavelet transform.[32] We first introduce the DPM principle and illustrate it on simple physical objects, such as micron-size particles. We then describe the space-scale analysis and the possibility to measure directly the phase of the interference pattern from the detection of the ridges of the Morlet wavelet transform of the original image. Finally, we illustrate this method on living myoblasts, showing that both the modulus and the phase of the interference pattern can be retrieved.

*Address all correspondence to: Françoise Argoul, E-mail: fargoul@ens-lyon.fr

2 Modeling the QPM System Response and Its Space-Scale Analysis

Popescu and coauthors[25–27] designed an elegant QPM by introducing an amplitude diffraction grating in the image plane of an inverted microscope to generate multiple diffraction orders containing the full spatial information about the transparent object crossed by the light beam. This QPM setup, inspired from this principle, was assembled in our laboratory. It is described in the Sec. 7 and illustrated in Fig. 1. After the transmission grating G, the zeroth- (U_0) and first-order (U_1) components of the diffracted beams are separated in the conjugated Fourier plane of the image plane of the microscope. Then, the zeroth order is low-pass filtered with a spatial filter and recombined with the first order, thanks to a second Fourier lens L_2 to give a spatially modulated interference image $I(x,y)$ similar to the one shown in Fig. 2(a), captured from a glass coverslip covered by a scratched polymer layer. The vertical fringes of this image have a frequency f_g that is related to the grating period; they superimpose to the object phase image. We propose here a method based on a 2-D continuous wavelet transform (CWT) to retrieve the object phase information from this type of image.

The intensity map $I(x,y)$ recorded on the CMOS camera is directly proportional to the modulus square of the electric field at this point.

$$I(\vec{x}) = |U_0 + U_1|^2(\vec{x}) = [|U_0|^2 + |U_1|^2 + U_0U_1^* + U_0^*U_1](\vec{x}). \quad (1)$$

If f_g is the spatial frequency of the grating, the phase difference between U_1 and U_0 includes both the grating and the object phase information: $\Phi(\vec{x}) = f_g x + \phi(\vec{x})$, with $\vec{x} = (x,y)$. This gives a synthetic form of $I(\vec{x})$.

$$I(\vec{x}) = P(\vec{x}) + Q(\vec{x})\cos[f_g x + \phi(\vec{x})]. \quad (2)$$

$\phi(\vec{x})$ is the phase due to the object transmission at location $\vec{x}$. $P(\vec{x})$ and $Q(\vec{x})$ are real valued; they correspond, respectively, to the background and modulation intensities at location $\vec{x}$. One common assumption is that $P(\vec{x})$ and $Q(\vec{x})$ vary much slower than $\phi(\vec{x})$. The local frequencies of the signal U can be computed in both directions x and y from the partial derivatives of the phase $\phi(\vec{x})$.

$$f_x(\vec{x}) = f_g + \partial[\phi(\vec{x})]/\partial x, \quad (3)$$

$$f_y(\vec{x}) = \partial[\phi(\vec{x})]/\partial y. \quad (4)$$

These equations can be rewritten in the vectorial form.

$$\begin{bmatrix} f_x \\ f_y \end{bmatrix} = \vec{\nabla}[f_g x + \phi(\vec{x})]. \quad (5)$$

Equation (3) shows that the local frequency in x may deviate from the carrier frequency f_g depending on the strength of the phase derivative with respect to x, the steeper $\phi(\vec{x})$, the larger this deviation.

By a simple computation, assuming that we are characterizing a homogeneous object of thickness d and index n imbedded in a continuum medium of index n_0, we can approximate the optical path change Δp_o at the center of the object with the relation $\Delta p_o \sim d(n - n_0)$ and $\Delta\phi = 2\pi\Delta p_o/\lambda$. Assuming that the microscope can achieve a 10^{-2} rad phase sensitivity, this gives the possibility to detect objects of thickness $10^{-2}\lambda/(2\pi\Delta n)$, which for a refractive index drop of 0.2 and wavelength $\lambda = 532$ nm gives a sensitivity to objects with thickness down to 4 nm, along the optical axis.

The practical treatment of interference fringe patterns often assumes that the background and the fringe modulation intensities as well as the phase vary slowly across the fringe pattern.[33,34] This may no longer be true when the fringe pattern is produced by a highly diffracting object, such as a highly structured living cell, for instance, with thickness of several micrometers. A living cell is not a homogeneous medium, but is made of compartments surrounded by lipid membranes with high refractive index (plasmic membrane, nuclear membrane, Golgi apparatus, mitochondrial network) and highly dynamic proteic fiber network (cytoskeleton, nuclear matrix). This situation requires a method that is able to capture the spatial variation of the local frequencies f_x and f_y, without being biased by the spatial dependence of the fringe amplitude $Q(\vec{x})$ [Eq. (2)]. The wavelet transform offers this possibility since it allows a decomposition of a signal (uni- or multidimensional) into atoms

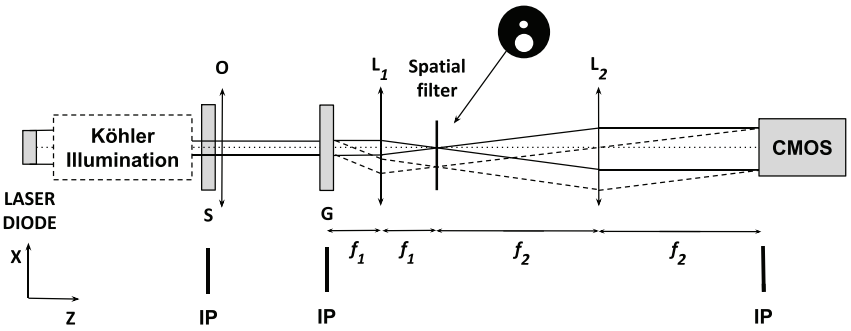

Fig. 1 Quantitative phase microscopy (QPM) setup. A transmission grating (G), positioned at the image plane (IP) of the microscope objective lens (O), is used for beam division into a central beam (order 0) and two symmetric beams (order 1) with respect to the optical axis. A spatial filter is placed at the Fourier plane of the lens L_1 to select the first-order beam (imaging field) and to low-pass filter the zeroth-order beam.[25–27] The two beams are recombined with the lens L_2 and the interferogram is recorded on a CMOS camera.

(wavelets) that are well localized in space and frequency.[35] The CWT is a mathematical technique introduced in signal analysis in the early 1980s.[36,37] Since then, it has been the subject of considerable theoretical developments and practical applications in a wide variety of fields.[38–54] An optical wavelet device has also been designed that performs the CWT, thanks to Fourier optics principles.[55,56] We choose here a 2-D Morlet wavelet[32] because it is particularly well suited for time (or space) frequency analysis.

3 Phase Map Reconstruction Using the CWT

Phase stepping and Fourier transform methods have been proposed in the 1980s for interferogram analysis in one and two dimensions.[33,57] These methods, however, assume that the coefficients $P(\vec{x})$ and $Q(\vec{x})$ vary slowly over one fringe cycle, so they can be treated as constants. To our knowledge, the first attempt to use a wavelet transform as a processing tool with white-light interferometry dates back to 1997.[58] Since then many teams have used this tool with success, in one dimension[59–67] as well as in two dimensions.[68–75]

More than a simple signal filtering tool, the wavelet transform analysis can also offer the possibility of a direct computation of the phase of the interferometry image, thanks to a wavelet transform ridge detection algorithm.[59–62,64,66,67,75]

The 2-D CWT of an interferogram $I(\vec{x})$ with $\vec{x} = (x, y)$ is defined as[52]

$$W_\Psi(\vec{b}, a, \theta) = a^\eta \int_{\Re^2} I(\vec{x}) \Psi^*[a^{-1} r_\theta(\vec{x} - \vec{b})] d^2\vec{x}. \quad (6)$$

$W_\Psi(\vec{b}, a, \theta)$ is the wavelet transform coefficient, at position $\vec{b}$, scale parameter a, and rotation angle θ. $\vec{b} = (b_x, b_y)$ is a 2-D translation parameter describing the position of the wavelet, $a > 0$ is the scale dilation parameter (nondimensioned), θ is a rotation parameter, $\mathbf{r}_\theta$ is the 2×2 rotation operator matrix, Ψ is the mother wavelet, Ψ^* is the complex conjugate of Ψ, and η is a normalization exponent. In Fourier space, the wavelet transform reads as

$$W_\Psi(\vec{b}, a, \theta) = a^\eta \int_{\Re^2} \hat{I}(\vec{k}) e^{i\vec{b}\cdot\vec{k}} \hat{\Psi}^*[a r_{-\theta}(\vec{k})] d^2\vec{x}. \quad (7)$$

The symbol $\hat{}$ denotes the Fourier transformation. A typical mother wavelet commonly used to detect localized and oriented features is the 2-D Morlet wavelet.[52]

$$\Psi_M(\vec{x}) = e^{i\vec{k}_0\cdot\vec{x}} e^{-\frac{1}{2}|A\vec{x}|^2} - e^{-\frac{1}{2}|A^{-1}\vec{k}_0|^2 - \frac{1}{2}|A\vec{x}|^2}, \quad (8)$$

$$\hat{\Psi}_M(\vec{k}) = \sqrt{\varepsilon}[e^{-\frac{1}{2}|A^{-1}(\vec{k}-\vec{k}_0)|^2} - e^{-\frac{1}{2}|A^{-1}\vec{k}_0|^2 - \frac{1}{2}|A^{-1}\vec{k}|^2}]. \quad (9)$$

The parameter k_0 is the wave vector and $A = diag[1, \varepsilon^{1/2}]$ is a 2×2 anisotropic matrix ($\varepsilon \geq 1$).

We use here this anisotropic 2-D continuous Morlet wavelet transform, with anisotropy factor ϵ, to extract the phase of a fringe pattern obtained with the QPM, such as shown in Fig. 2(a). The correction terms in Eqs. (8) and (9) enforce the admissibility condition $\hat{\Psi}_M(\vec{0}) = 0$. However, they are numerically negligible for $|k_0| \geq 5.6$, and one usually drops them. Putting $\varepsilon = 1$ and removing the correction terms gives the Gabor function.

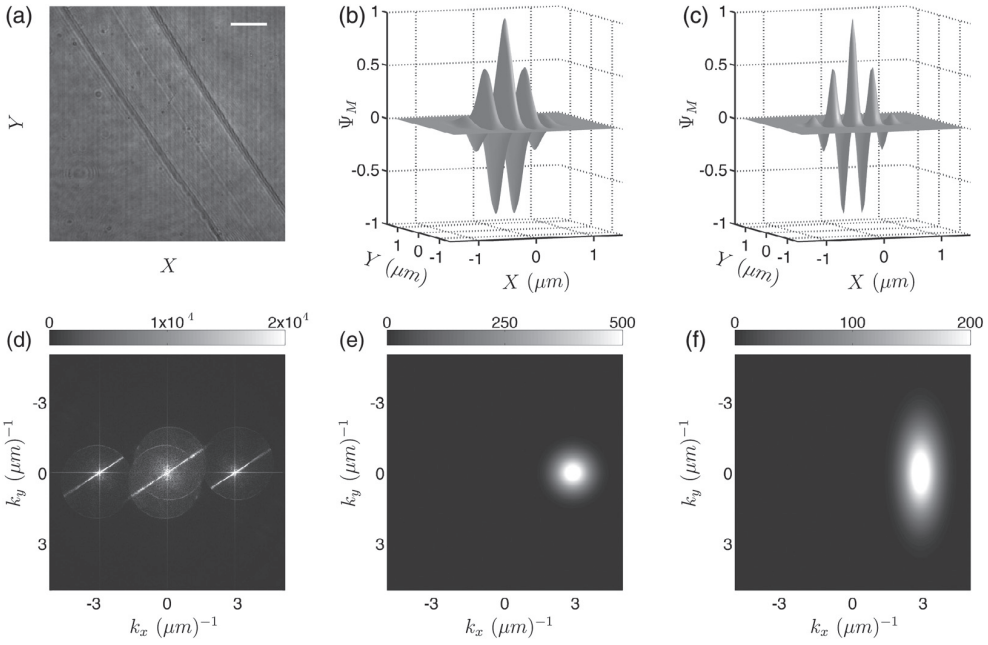

Fig. 2 (a) Untreated QPM image of a glass coverslip coated with polymer layer including a scratch in the diagonal direction. The scale bar is 10 μm. (b) Real part of the symmetric two-dimensional (2-D) Morlet wavelet Ψ_M with $\epsilon = 1$. (c) Real part of the anisotropic two-dimensional Morlet wavelet Ψ_M, with $\epsilon = 10$. (d), (e), and (f) modulus of the 2-D Fourier transforms of (a), (b), and (c), respectively, coded with a gray colormap.

$$\Psi_G(\vec{x}) = \exp(i\vec{k}_0 \cdot \vec{x}) \exp\left(-\frac{1}{2}|\vec{x}|^2\right). \quad (10)$$

The Morlet wavelet is a complex function; the modulus of the truncated Morlet wavelet (without the correction term) is a Gaussian, elongated in the x direction if $\varepsilon > 1$, and its phase is constant along the direction orthogonal to $\vec{k}_0$, and linear in $\vec{x}$, mod$(2\pi/|k_0|)$, along the direction of $\vec{k}_0$. As compared to the 1-D case, the additional feature of the 2-D Morlet (or Gabor) wavelet function is its inherent directivity, entirely contained in its phase. This turns to be a crucial advantage for studying objects with directional properties. Indeed, since the wavelet transform [Eq. (6)] is a convolution product of the fringe pattern with the dilated wavelet, we see that the wavelet transform smoothes the image in all directions, but detects the sharp transitions in the direction perpendicular to $\vec{k}_0$. In Fourier space, the effective support (footprint) of the function $\hat{\Psi}_M$ is an ellipse centered at $\vec{k}_0$ and elongated in the k_y direction. In Figs. 2(b) and 2(c) we show two Morlet wavelets computed for $\vec{k}_0 = (5.6, 0)$, and $\varepsilon = 1$ and $\varepsilon = 10$, respectively; their Fourier transforms are shown in Figs. 2(e) and 2(f). Since the ratio of the axes is equal to $\sqrt{\varepsilon}$, the cone of the wavelet in Fourier space elongates along k_y direction as ε increases. This wavelet preferentially detects edges perpendicular to the y-direction (i.e., parallel to $\vec{k}_0$), and its angular selectivity increases with $\vec{k}_0$ and with the anisotropy ε. For the optical image shown in Fig. 2(a) recorded with the QPM from a glass coverslip coated with a scratched polymer layer, the best selectivity is achieved with $\vec{k}_0$ perpendicular to the long axis of the ellipse in $\vec{k} - space$, that is $\vec{k}_0 = (k_0, 0)$. We show in Fig. 2(d) the modulus of the Fourier transform of the fringe image shown in Fig. 2(a). The Morlet wavelet selects the right part of this Fourier transform by performing a band-pass filtering around the grating frequency. The advantage of taking a smooth wavelet and not a simply circular window in Fourier space[31] is not only to avoid the introduction of artificial oscillations produced by the sharp boundary of such a window, but also to have the ability to use the mathematical formalism of wavelet analysis, for instance, the ridge detection method.[52] The Morlet wavelet Ψ_M is then written as

$$\Psi_M(\vec{x}) = \exp\left[-\frac{1}{2}(x^2 + \varepsilon y^2)\right][\exp(ik_0 x) - \exp(-k_0^2/2)]. \quad (11)$$

We notice the general form of the truncated Morlet wavelet.

$$\Psi_M(\vec{x}) = V_\Psi(\vec{x}) \exp[i\phi_\Psi(\vec{x})], \qquad \phi_\Psi(\vec{x}) = k_0 x, \quad (12)$$

where $V_\Psi(\vec{x})$ is an anisotropic Gaussian function and ϕ_Ψ is the phase of the wavelet.

The ridge of the wavelet transform can be computed at each spatial point $\vec{x}$; it corresponds to a scale $a_r(\vec{b})$ such that the local derivative of the wavelet phase ϕ_Ψ compensates the local derivative of the object phase ϕ.

$$f_g \vec{\nabla}(x, 0) + \vec{\nabla}\phi(\vec{x}) - \vec{\nabla}\phi_\Psi[a_r^{-1}(\vec{b}) r_\theta(\vec{x} - \vec{b})] = 0. \quad (13)$$

If we consider only the modulated part of the fringe pattern $Q(\vec{x}) \exp[i\phi(\vec{x})]$ (complex form), we can derive the equation for its Morlet CWT, given that $Q(\vec{b})$ changes slowly compared to the phase of the fringes; the rotation angle is fixed, $\theta = 0$. It is important to note here that the choice of $\eta = 2$ (norm $\mathcal{L}^1$)[52,63,64,74] makes this computation straightforward.

$$W_\Psi(\vec{b}, a) = \frac{\hat{\Psi}_M\{a[f_g(1,0) + \vec{\nabla}\phi(\vec{b})]\}}{C(\vec{b}, a)} Q(\vec{b}) e^{i\phi(\vec{b})}, \quad (14)$$

up to a correction term $C(\vec{b}, a)$ that depends on the local variations of the phase $\phi(\vec{x})$ and the modulation amplitude $Q(\vec{x})$ of the optical signal on the ridge skeleton. Note that this correction term is constant in the approximation of a slow spatial variation $Q(\vec{b})$. Equation (14) is a local equation describing the shape of the wavelet transform in the vicinity of the scale $a_r(\vec{b})$ that maximizes its modulus; this shape is Gaussian because $\hat{\Psi}_M$ is a Gaussian function.

Hence, from Eq. (9), the maxima of the modulus of the CWT correspond to the wavelet ridge skeleton, where the optical phase ϕ produced by the object fulfills the equation

$$\vec{k}_0 / a_r(\vec{b}) = f_g(1, 0) + \vec{\nabla}\phi(\vec{b}). \quad (15)$$

It can be demonstrated analytically that this ridge detection method is independent of the modulation intensity $Q(\vec{x})$ [Eq. (2)] of the original fringe pattern (as long as the fringes are detectable) using the properties of Gaussian functions in real and Fourier spaces. This result can be intuitively understood because the ridge detection method boils down to the computation of the position of a local maxima of the wavelet transform with the scale parameter a, whatever the value of this maxima. The modulus of the wavelet transform on the ridge skeleton reads

$$W_\Psi[\vec{b}, a_r(\vec{b})] = \frac{\hat{\Psi}_M(\vec{k}_0)}{C[\vec{b}, a_r(\vec{b})]} Q(\vec{b}) e^{i\phi(\vec{b})}. \quad (16)$$

According to Eq. (16), we could straightforwardly compute $\phi(\vec{b})$ from the phase of the wavelet transform $W_\Psi[\vec{b}, a_r(\vec{b})]$, without using the derivative form of Eq. (15). This is not true when the variations of the phase and their amplitude modulations are too fast compared to f_g, giving a complex value to $C[\vec{b}, a_r(\vec{b})]$. In that case, Eq. (15) must be preferred. We also note that the modulus of the wavelet transform on the ridge follows the fringe amplitude modulation $Q(\vec{b})$. As a general remark, this wavelet-based method intrinsically eliminates background intensity variations $P(\vec{x})$ that do not affect the fringe pattern modulations.

4 Validation of the CWT Ridge Detection Method on Latex Microbeads

We discuss the efficiency of the 2-D CWT ridge detection method on a model system made of a microbead particle (radius $R = 5$ μm) with refractive index $n_b = 1.59$ surrounded by a matching index oil $n_0 = 1.5167$. Figure 3(a) shows the fringe pattern computed with Eq. (2) for the 2-D phase of the bead.

$$\phi(\vec{x}) = [4\pi(n_b - n_0)\sqrt{R^2 - (\vec{x} - \vec{x}_c)^2}]/\lambda, \quad (17)$$

where $\vec{x}_c$ corresponds to the projection of the center of the bead in the (X, Y) plane. This bead is a good model of the experimental fringe patterns that will be presented later on. It is a good guide for defining the optimum wavelet parameters for

retrieving the phase from a fringe pattern. We observe in Fig. 3 (a) that on the border of the bead there is a breakdown of the fringe continuity because the phase derivative is not continuous at these points, which makes the phase computation harder. Figures 3(b) and 3(c) [respectively, Figs. 3(d) and 3(e)] show a gray-coded representation of the modulus of the 2-D CWT on the horizontal (respectively, vertical) section shown in Fig. 3(a). The 2-D CWT of the horizontal section [Figs. 3(b) and 3(c)] shows a strong deformation of the ridge $a_r(b_x)$ when entering and exiting the bead. This is also visible on the fringe pattern [Fig. 3(a)] since on the left side of the bead the fringes are compressed (smaller scale a), whereas on the right side they are dilated (larger scale a). Close to the border of the bead, $|W_\Psi(.,a)|$ is no longer a single humped Gaussian function (reflecting the shape of the modulus of the wavelet) since two maxima appear, corresponding to the existence of two local frequencies slightly splitted apart from the carrier fringe frequency f_g, corresponding to $a = 1$ here. When the anisotropy of the 2-D Morlet wavelet is increased [see Fig. 3(c)], the ridge detection is more acurate, improving the detection of the border of the bead. The improvement provided by an anisotropic wavelet is more visible on the 2-D CWT analysis of a vertical section, shown in Figs. 3(d) and 3(e). $|W_\Psi(b_y,a)|$ keeps its single humped shape, except in a close neighborhood of the bead border, where it vanishes. This evanescence of the $|W_\Psi(.,a)|$ curves prevents a precise determination of the scale a_r where it is maximum. With an anisotropic 2-D Morlet wavelet ($\epsilon = 10$), this vanishing is more localized in b_y and damped [Fig. 3(e)]. The evanescence of the wavelet transform modulus maxima curves is explained by a rapid shift of the fringes along the axis X and their summation by the wavelet transform, since its width is ~5.6 fringe periods along X. The 2-D CWT with a Morlet analyzing wavelet is, therefore, particularly suited for the detection of fringe compression or dilation along the X direction. It is less efficient to detect the shift of fringes along X, especially with curved fringes. From this 2-D CWT analysis, we can propose three methods for phase retrieval.

- 1. The first method uses the 2-D Morlet wavelet as a Fourier filter, with a fixed scale $a = 1$ corresponding to the grating fringe modulation f_g; it does not use the ridge detection. We will call it the Fourier filtering method 1.
- 2. The second method uses the 2-D CWT ridge detection method to compute the phase derivative of the fringe pattern, described by Eq. (15), and makes an integration of this derivative along X. We will call it the ridge integral method 2.
- 3. The third method uses the 2-D CWT ridge detection method to compute the new complex quantity $W_\Psi[b, a_r(\vec{b})]$ on the ridge and takes its argument to compute the phase [Eq. (16)]. We will call it the ridge argument method 3.

Figure 4 compares these three methods for phase retrieval on the bead model, for two values of the anisotropy factor ϵ. Figures 4(a) and 4(b) show the phase extracted with a simple Fourier filtering of the fringe pattern, using a Morlet wavelet at fixed scale a. This method does not succeed to recover the theoretical phase whatever ϵ because on the border of the bead, the local frequency of the fringes is too far from the fringe carrier f_g, and it is, therefore, impossible to estimate their phase correctly. Figures 4(c) and 4(d) show the ridge integral method 2 on this bead model. In that case, the theoretical phase can be estimated correctly on the central part of the bead, but computation errors remain on the top and bottom borders of the bead, which come from the difficulty to capture the local CWT modulus maxima position when this modulus vanishes. With method 2, the phase is computed by integration of the gradient $\vec{\nabla}\phi(\vec{b})$ along the axis b_x, which produces an accumulation of the errors on $\phi(\vec{x})$ on the right side of the bead. However, switching from isotropic [Fig. 4(c) and $\epsilon = 1$] to anisotropic wavelet [Fig. 4(d) and $\epsilon = 10$] corrects the errors on the top and the bottom borders of the bead, but the integration errors remain. To improve this aspect, a higher resolution in the modulus maxima detection method is necessary at the expense of computation time. Note, however, that if the fringe pattern is very noisy, method 2 avoids the unwrapping of the phase and may stabilize the computation of the phase. Figures 4(e) and 4(f) show the ridge argument method 3. This method is still sensitive to fringe discontinuities [Fig. 4(e)] on the top and the bottom borders of

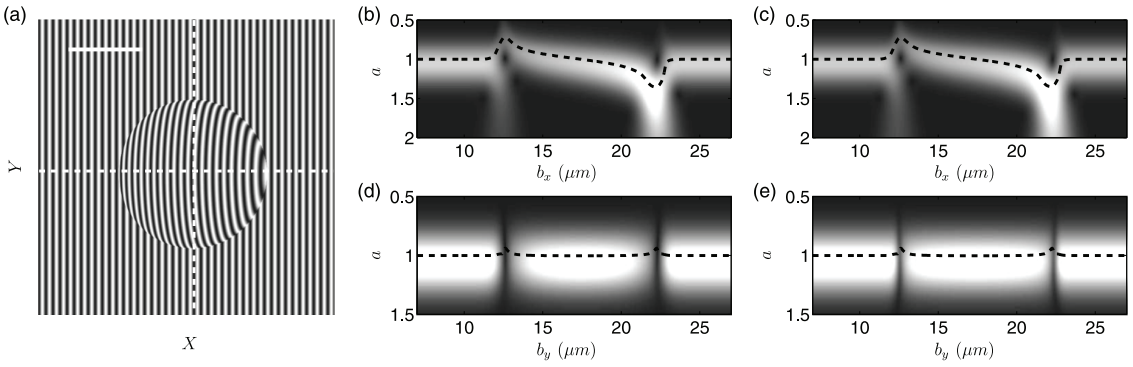

Fig. 3 (a) Theoretical QPM intensity image of a transparent micro-bead, computed with Eqs. (2) and (17). The scale bar is 5 μm. (b) and (d) Modulus of the 2-D continuous wavelet transform (CWT) on the horizontal (fixed Y) section shown in (a) by a white dashed line. (c) and (e) Modulus of the 2-D CWT on the vertical (fixed X) section shown in (a) by a white dashed line. (b) and (d) have been computed with an isotropic 2-D Morlet wavelet ($\epsilon = 1$). (c) and (e) have been computed with an anisotropic 2-D Morlet wavelet ($\epsilon = 10$). $a = 1$ corresponds to the fringe frequency f_g. The dashed black lines outline the $a_r(\vec{b})$ ridge functions. The gray coding is identical for all CWT modulus images, from zero (black) to 0.8 (white).

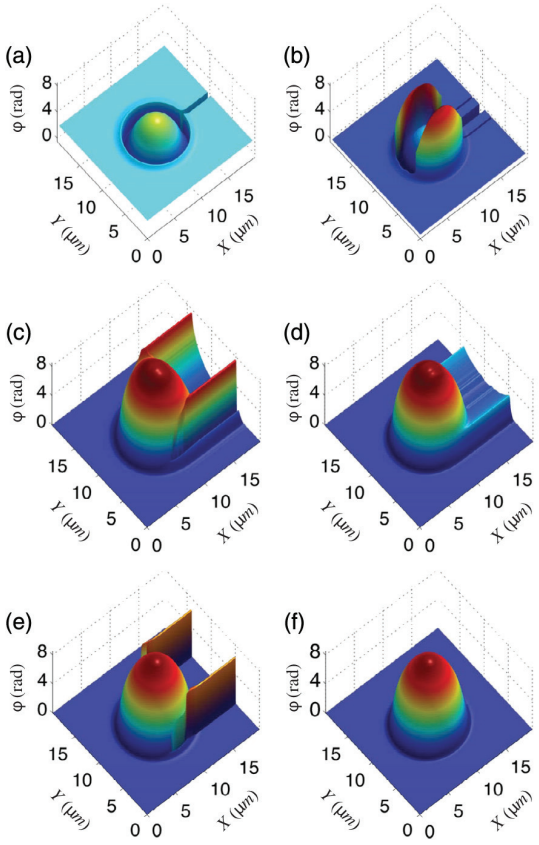

Fig. 4 Three-dimensional (3-D) representation of the reconstructed phases from the fringe pattern of Fig. 3(a) with methods 1 [(a) and (b)], 2 [(c) and (d)], and 3 [(e) and (f)]. (a), (c), and (e) are computed with the isotropic Morlet wavelet ($\epsilon = 1$). (b), (d), and (f) are computed with the anisotropic Morlet wavelet ($\epsilon = 10$). The phase ϕ is given in radians.

the bead. With an anisotropic wavelet ($\epsilon = 10$), this method succeeds to reproduce the theoretical phase with a 10^{-3} relative error on the phase. The possibility to adjust the anisotropy of the wavelet is, therefore, important for analyzing phase discontinuities; it has never been reported in that context.

To compare with the bead model, we have imaged a 5 μm radius latex microbead with the QPM and applied the 2-D anisotropic CWT ($\epsilon = 10$) to analyze the experimental fringe pattern shown in Fig. 5(a). Unlike the theoretical model, the fringe intensity modulation in the QPM is no longer constant, see the horizontal section plotted in black in Fig. 5(b). This intensity modulation is produced by the light scattering by the bead. As established by Bedrosian,[76] when this modulation contains frequencies that overlap with the fringe carrier frequency f_g, the extraction of the phase with the Hilbert method is biased and leads to a false estimation. Indeed, from the Hilbert transform of the term $Q(\vec{x})\cos[f_g x + \phi(\vec{x})]$ in Eq. (2), we would like to recover a function like $Q(\vec{x})\sin[f_g x + \phi(\vec{x})]$ from which the phase could be computed straightforwardly. Bedrosian's theorem shows that this is workable only if the amplitude modulation $Q(\vec{x})$ does not contain frequencies that mix with the carrier frequency f_g. This condition is not experimentally satisfied as illustrated in Fig. 5(b). In that case, when using the ridge detection, the CWT offers the advantage of leading to a measure of the frequency from the ridge that considerably reduces the effects of fringe modulation amplitude on phase retrieval [Eq. (15)]. In Fig. 5(c), we show the modulus of the 2-D CWT $|W_\Psi(b_x, a)|$ on the horizontal section shown in Fig. 5(a). The ridge $a_r(\vec{b})$ plotted in Fig. 5(c) with a black line is very similar to the theoretical curve shown in Fig. 3(c). The real part of the CWT computed on the ridge shown in Fig. 5(d) is very impressive when compared to the original image [Fig. 5(a)]. It looks as if the major intensity modulations of the original images were damped out to keep only the fringe distorsion, from which the phase is computed. The same section of Fig. 5(d) is plotted in gray in Fig. 5(b). The efficiency of the wavelet transform is well illustrated in this example. Figure 5(e) shows the modulus $|W_\Psi[\vec{b}, a_r(\vec{b})]|$ computed on the ridge of the 2-D CWT on this latex microbead; it is coded in gray from minimum (black) to maximum (white). Figure 5(f) gives a 2-D gray-coded image of the phase derivative $\partial\phi(\vec{b})/\partial b$ of the CWT on the ridge, and Fig. 5(g) shows the three-dimensional (3-D) representation of the phase $\phi(\vec{x})$ computed from the ridge of the CWT with method 3. The modulus of the 2-D CWT on the ridge preserves the intensity of the original fringe image, whereas this intensity modulation disappears completely on the phase derivative $\partial\phi(\vec{b})/\partial b$. We also note that as for the bead model, the anisotropic Morlet wavelet allows a very nice detection of the phase derivative. The 3-D picture of the phase in Fig. 5(g) is very appealing since it not only detects perfectly the phase drop due to this bead and reproduces the theoretical prediction, but also delineates some defects of the beads that are visible as phase irregularities on the surface of the bead. We have estimated the standard deviation of the background phase on this image of ~0.25 rad.

5 Application of the CWT Phase Retrieval Method to Living Cell Imaging

We illustrate the performance of the CWT phase retrieval method on a murine myoblast cell line C2C12, which can be differentiated to give rise to plurinucleate syncytia (the myotubes) by fusion. We will focus here on undifferentiated C2C12 cell monolayers. Figure 6 reports the 2-D CWT ridge analysis of a QPM image of a nonadherent myoblast that is progressively rounding and will detach from the glass to enter mitosis.[77] The characteristic organization of the microtubule-actin cytoskeleton with stress fibers has disappeared, the cell is round, and it is no longer possible to delineate a nice nuclear contour inside this cell. However, this spherical shape is interesting because it allows us to perform the same parametrization of the phase map as we have done previously for spherical particles. Compared to the previous example of the microbead in Sec. 4, we observe on Fig. 6(a) that besides scattering effects on the border of the bead, the internal structure of the cell also produces intensity modulations of the fringes that may make the analysis more complex. We have plotted in Fig. 6(b) a profile of the fringe image selected on the white dashed section of Fig. 6(a) (black curve), which can be compared to the corresponding profile of the real part of the 2-D CWT ridge on the same section. Similar to the example of Fig. 5, the CWT ridge analysis regularizes the fringe intensity modulation. Figure 6(c) reports the modulus of the 2-D CWT $|W_\Psi(b_x, a)|$ on the horizontal section shown in Fig. 6(a). The ridge $a_r(\vec{b})$ plotted in Fig. 6(c) with a black line is reminiscent of the one shown in Fig. 5(c). The real part of the CWT computed on the ridge shown in Fig. 6(d) when compared to the original QPM image [Fig. 6(a)] definitely flattens the intensity

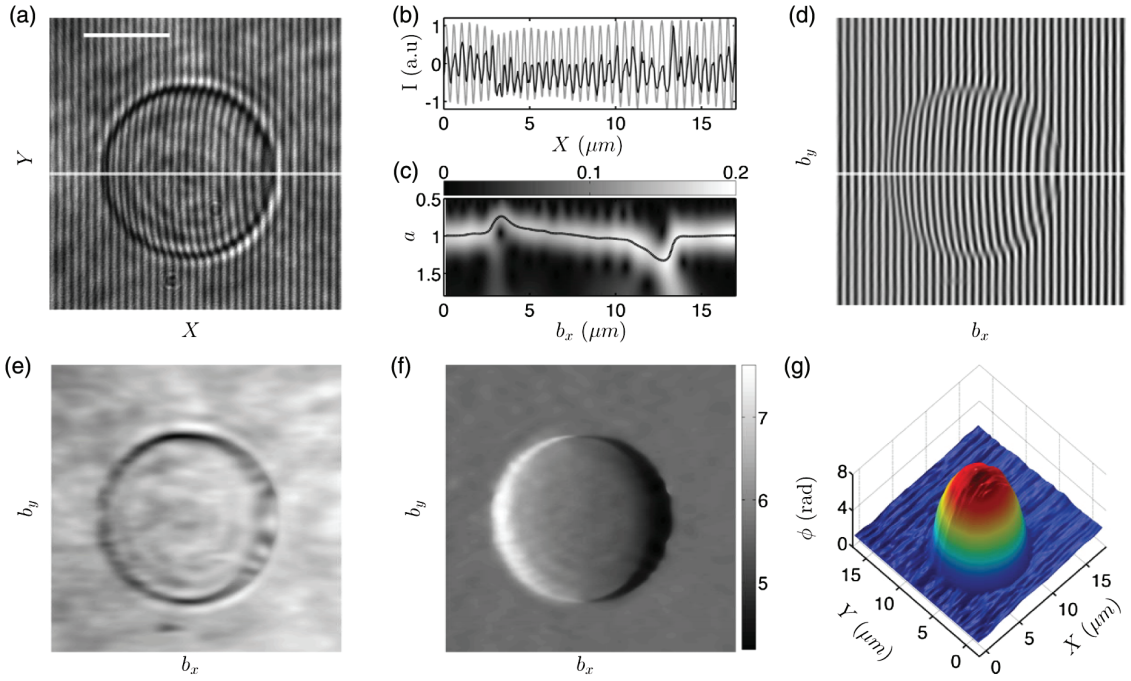

Fig. 5 2-D CWT analysis of an experimental QPM fringe pattern captured from a 5 μm radius latex microbead embedded in glass index matching oil. (a) The untreated QPM image. The scale bar is 5 μm. (b) Intensity profile (black line) of the section marked with a white dashed line in (a). The gray line corresponds to the real part of the CWT ridge computed on this section. (c) Gray coded modulus of the 2-D CWT on the horizontal section shown in (a). The ridge $a_r(\vec{b})$ is plotted with a black line. (d) Real part of the CWT computed on the ridge. (e) Modulus of the 2-D CWT computed on the ridge. (f) $\partial\phi(\vec{b})/\partial x$ computed from the ridge [Eq. (15)]. (g) 3-D representation of phase computed from the fringe pattern of (a) with method 3. The anisotropic Morlet wavelet ($\epsilon = 10$) is used for this analysis. The gray coding is done from black (minimum) to white (maximum).

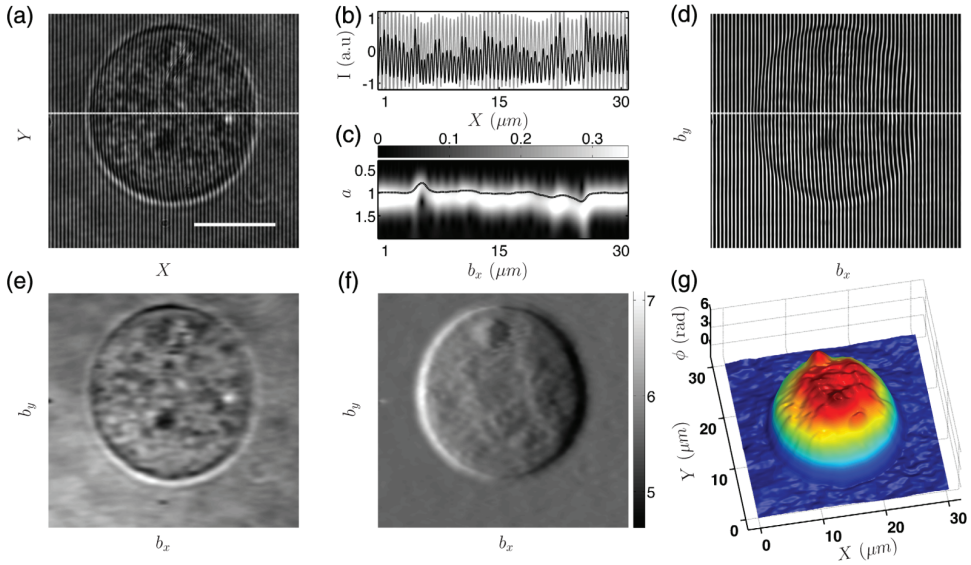

Fig. 6 2-D CWT analysis of a QPM fringe pattern collected from a round myoblast. (a) The untreated QPM image. The scale bar is 10 μm. (b) Intensity profile (black line) of the section marked with a white dashed line in (a). The gray line corresponds to the real part of the CWT ridge computed on this section. (c) Gray coded modulus of the 2-D CWT on the horizontal section shown in (a). The ridge $a_r(\vec{b})$ is plotted with a black line. (d) Real part of the CWT computed on the ridge. (e) Modulus of the CWT computed on the ridge. (f) $\partial\phi(\vec{b})/\partial x$ computed from the ridge of the CWT. (g) 3-D representation of phase computed from the fringe pattern shown in (a) with method 3. The anisotropic Morlet wavelet ($\epsilon = 10$) is used for this analysis. The gray coding is done from black (minimum) to white (maximum).

modulations. Figure 6(e) shows the modulus $|W_\Psi[\vec{b}, a_r(\vec{b})]|$ computed on the ridge of 2-D CWT; it is coded in gray from minimum (black) to maximum (white). The intensity modulation that remains in Fig. 6(e) is eliminated in the derivative of the phase shown in Fig. 6(f) (ridge method 2). Finally, using method 3, we reconstruct a 3-D profile of the phase of this myoblast in Fig. 6(g). This representation confirms the round shape of this cell in the third direction Z and points out a central part where smaller objects are identified, which may be attributed to condensed chromosomes. We use the same model as proposed for a spherical bead as a first approximation to extract the mean refractive index of this cell and delineate one of the protruding object and its refractive index. The interpolation of the whole cell by a spherical phase shape [Eq. (17)] is reported in Fig. 7. This interpolation leads to an estimation of the overall refractive index of the cell as $n_c = 1.36 \pm 0.005$, given that the buffer refractive index is $n_0 = 1.33$. Moreover, subtracting this mean spherical phase contour from the total phase contour (see Fig. 7), we can also compute the phase drop of the small spherical object that pops up on the upper part of the cell and estimate its index to be 1.4 ± 0.005.

In Fig. 8, we show the image of an adherent myoblast cell, where we can recognize thin lamellipodia extensions that exhibit filopodia projections on the leading edge: a characteristic pattern of cell motility. It has been shown in the literature that differentiation and fusion of myoblasts into multinucleated myotubes is accompanied by a dramatic reorganization of the Golgi complex.[78] Here we rather have the classic compact juxtanuclear Golgi complex of an undifferentiated myoblast that we can recognize as small granular objects on both the derivative of the phase ϕ reported in Fig. 8(c) and on the phase ϕ shown in a 3-D representation in Fig. 8(d). The phase response of this adherent cell is different from that shown for the round cell [Fig. 6(g)]; the nucleus looks more like a phase plateau, flattened by the mechanical tractions of the lamellipodia. On the border of the nucleus, the QPM detects a necklace of phase droplets and a central part with higher phase [Figs. 8(c) and 8(d)]. At this stage, it is difficult to conclude if these small bodies are essentially Golgi complex or a combination of perinuclear organelles as rough and smooth endoplasmic reticulum, Golgi, vesicles, and mitochondrial network.

6 Summary

We have shown that a wavelet-based space-scale analysis can be used to decode the fringe images recorded from living cells with a QPM. The implementation of the ridge detection method is more successful than Fourier filtering methods when imaging cellular and high refractive index contrast objects since it can discriminate intensity from phase changes. This technique has been applied to undifferentiated myoblast cells and revealed internal structures of these cells, which were confirmed by fluorescence imaging. This microscope is coupled to a high-speed camera, and we hope in the near future that besides capturing the optical phase changes produced by the cell internal structures, the record of the dynamics of these internal bodies will provide a complementary way to distinguish these structures without the need of fluorescence staining.

7 Materials and Methods

7.1 *Quantitative Phase Microscope*

A low-coherence laser diode (Thorlabs, GmbH, Germany, $\lambda = 532$ nm) is used as a light source and is directed to the sample (S) using Köhler illumination, such that the field at the image plane (IP) is spatially coherent over the entire field of view (Fig. 1). Different diffraction orders are then created with a transmission grating (G) (70 grooves/mm) localized at the IP of the microscope equipped with an objective (O) 40× (Olympus, France, SPlan40, N.A. = 0.7). A spatial filter (Thorlabs, custom-made) is placed at the Fourier plane of lens L_1 to select the first-order beam (imaging field) and to low-pass filter the zeroth-order beam (reference). The spatial filter has been designed with two circular apertures with diameters of 15 μm and 2 mm. The two beams are recombined using a second Fourier lens (L_2), and the resulting interferogram is recorded as an image of 2048 × 2048 pixels with a CMOS camera (Hamamatsu, Japan, ORCA-Flash 4.0). The $4f$ lens system adds a 5× magnification ($f_1 = 50$ nm, $f_2 = 250$ mm).

7.2 *Polymer Layer Preparation*

A solution of 10% poly(methyl methacrylate) (PMMA, Sigma-Aldrich, France) in toluene was spin coated over a glass coverslip at a speed of 1000 rpm during 50 s. A time of 10 s is fixed to reach the nominal speed. After coating, the film was annealed for 1 h at 140°C. Prior to imaging, a portion of the PMMA layer was removed with a scalpel.

7.3 *Polystyrene Beads Preparation*

1 μL of an aqueous solution containing polystyrene beads (FLUKA 72986) was diluted in 10 mL of deionized water.

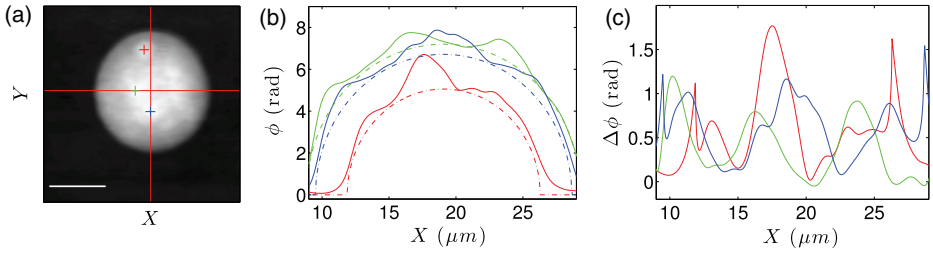

Fig. 7 Decomposition into spherical phase shapes of the myoblast phase map shown in Fig. 6. (a) The original 2-D phase map computed from the fringe pattern with ridge method 3. The gray coding is done from black (minimum) to white (maximum). (b) Horizontal sections corresponding to the colored crosses shown in (a) and their spherical phase contour envelope [Eq. (17)] in dashed line. (c) The subtraction of the original phase map with the spherical phase contour envelopes, revealing other phase contours of smaller objects, inside the cell. The red curve can again be parametrized by a spherical phase contour to estimate the index of this small protruding object, marked with a red cross in (a).

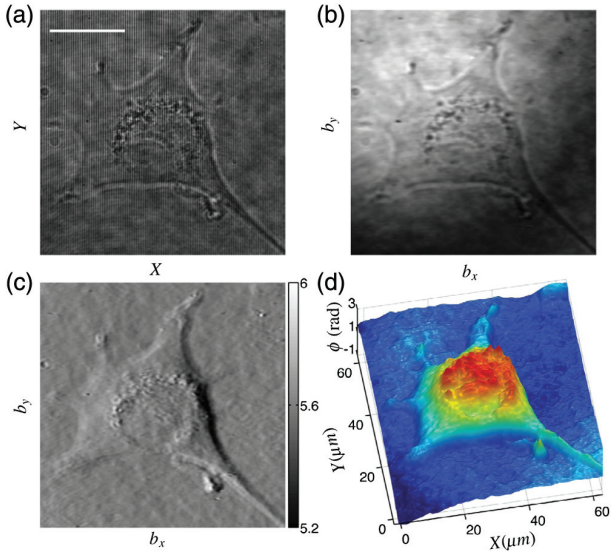

Fig. 8 2-D CWT analysis of a QPM fringe pattern collected from an adherent myoblast. (a) The untreated QPM image. The scale bar is 20 μm. (b) Modulus of the CWT computed on the ridge. (c) $\partial\phi(\vec{b})/\partial x$. (d) 3-D representation of phase computed from the fringe pattern in (a) with method 3. The anisotropic Morlet wavelet ($\epsilon = 10$) is used for this analysis. The gray coding is done from black (minimum) to white (maximum).

250 μL of the dilution were deposited on a small petri dish with a glass window and let overnight in an oven at 70°C to dry. Before imaging, 500 μL of glass index matching oil were added.

7.4 *Cell Culture*

C2C12 mouse cells (ATCC number CRL-1772™) were grown in high glucose (4.5 g/L) Dulbecco's modified Eagle medium [(DMEM), GE Healthcare Life Science, Dominique Dutscher, France] supplemented with 20% fetal bovine serum GE Healthcare Life Science and 1% antibiotics (penicillin/streptamicine). Adherent myoblasts on 50 mm petri dishes with a glass bottom of 0.17 mm thickness were maintained at 37°C and 5% CO_2 up to 60% confluence until they were used. The glass surface was not treated to enhance cell adhesion. The growth medium was replaced by phosphate buffered saline solution before imaging. No further sample preparation was required.

Acknowledgments

We are indebted to Centre National de la Recherche Scientifique, Ecole Normale Supérieure de Lyon, Lyon Science Transfert (projet L659), Région Rhône Alpes (CIBLE Program 2011), INSERM (AAP Physique Cancer 2012), and the French Agency for Research (ANR-AA-PPPP-005, EMMA 2011) for their financial support. C.M.T. is very grateful to the National Council of Science and Technology (CONACyT, Mexico) for supporting her PhD scholarship. L.S. is very thankful to the Association Française Contre les Myopathies, AFM-Téléthon, for supporting her PhD scholarship.

References

1. M. Born and E. Wolf, *Principles of Optics: Electromagnetic Theory of Propagation, Interference and Diffraction of Light*, 7th ed., Cambridge University Press, Cambridge (1999).
2. F. Zernike, "How I discovered phase contrast," *Science* **121**(3141), 345–349 (1955).
3. G. Nomarski and A. R. Weill, "Application à la métallographie des méthodes interférentielles à deux ondes polarisées," *Revue de Métallurgie* **2**, 121–128 (1955).
4. A. D. Gabor, "Microscopy by reconstructed wave-fronts," *Proc. R. Soc. Lon. A* **197**(1051), 454–487 (1949).
5. B. Rappaz et al., "Measurement of the integral refractive index and dynamic cell morphometry of living cells with digital holographic microscopy," *Opt. Express* **13**(23), 9361–9373 (2005).
6. L. Yu et al., "Digital holographic microscopy for quantitative cell dynamic evaluation during laser microsurgery," *Opt. Express* **17**(14), 12031–12038 (2009).
7. V. P. Tychinsky and A. N. Tikhonov, "Interference microscopy in cell biophysics. 1. Principles and methodological aspects of coherent phase microscopy," *Cell Biochem. Biophys.* **58**(3), 107–116 (2010).
8. G. Popescu, *Quantitative Phase Imaging of Cells and Tissues*, McGraw Hill, New York (2011).
9. N. Cardenas, S. Kumar, and S. Mohanty, "Dynamics of cellular response to hypotonic stimulation revealed by quantitative phase microscopy and multi-fractal detrended fluctuation analysis," *Appl. Phys. Lett.* **101**(20), 203702 (2012).
10. N. T. Shaked, "Quantitative phase microscopy of biological samples using a portable interferometer," *Opt. Lett.* **37**(11), 2016–2018 (2012).
11. N. Sugiyama et al., "Label-free characterization of living human induced pluripotent stem cells by subcellular topographic imaging technique using full-field quantitative phase microscopy coupled with interference reflection microscopy," *Biomed. Opt. Express* **3**(9), 2175–2183 (2012).
12. P. Bon, B. Wattellier, and S. Monneret, "Modeling quantitative phase image formation under tilted illuminations," *Opt. Lett.* **37**(10), 1718–1720 (2012).
13. P. Bon et al., "Optical detection and measurement of living cell morphometric features with single-shot quantitative phase microscopy," *J. Biomed. Opt.* **17**(7), 076004 (2012).
14. V. Tychinsky, "The metabolic component of cellular refractivity and its importance for optical cytometry," *J. Biophotonics* **2**(8–9), 494–504 (2009).
15. Y. Park et al., "Measurement of red blood cell mechanics during morphological changes," *Proc. Natl. Acad. Sci. U. S. A.* **107**(15), 6731–6836 (2010).
16. Y. Park et al., "Metabolic remodeling of the human red blood cell membrane," *Proc. Natl. Acad. Sci. U. S. A.* **107**(4), 1289–1294 (2010).
17. T. E. Gureyev, A. Roberts, and K. A. Nugent, "Phase retrieval with the transport-of-intensity equation: matrix solution with use of Zernike polynomials," *J. Opt. Soc. Am. A* **12**(9), 1932–1941 (1995).
18. T. E. Gureyev, A. Roberts, and K. A. Nugent, "Partially coherent fields, the transport-of-intensity equation, and phase uniqueness," *J. Opt. Soc. Am. A* **12**(9), 1942–1946 (1995).
19. S. Bajt et al., "Quantitative phase-sensitive imaging in a transmission electron microscope," *Ultramicroscopy* **83**(1–2), 67–73 (2000).
20. M. R. Teague, "Image formation in terms of the transport equation," *J. Opt. Soc. Am. A* **2**(11), 2019–2026 (1985).
21. G. Ade, "On the validity of the transport equation for the intensity in optics," *Opt. Commun.* **52**(5), 307–310 (1985).
22. M. Beleggia et al., "On the transport of intensity technique for phase retrieval," *Ultramicroscopy* **102**(1), 37–49 (2004).
23. A. Barty et al., "Quantitative optical phase microscopy," *Opt. Lett.* **23**(11), 817–819 (1998).
24. C. J. Bellair et al., "Quantitative phase amplitude microscopy IV: imaging thick specimens," *J. Microsc.* **214**(Pt 1), 62–69 (2004).
25. G. Popescu et al., "Diffraction phase microscopy for quantifying cell structure and dynamics," *Opt. Lett.* **31**(6), 775–777 (2006).
26. Y. Park et al., "Diffraction phase and fluorescence microscopy," *Opt. Express* **14**(18), 8263–8268 (2006).
27. B. Bhaduri et al., "Diffraction phase microscopy with white light," *Opt. Lett.* **37**(6), 1094–1096 (2012).
28. T. Ikeda et al., "Hilbert phase microscopy for investigating fast dynamics in transparent systems," *Opt. Lett.* **30**(10), 1165–1167 (2005).

29. H. V. Pham et al., "Real time blood testing using quantitative phase imaging," *PloS One* **8**(2), e55676 (2013).
30. B. Bhaduri and G. Popescu, "Derivative method for phase retrieval in off-axis quantitative phase imaging," *Opt. Lett.* **37**(11), 1868–1870 (2012).
31. H. V. Pham et al., "Fast phase reconstruction in white light diffraction phase microscopy," *Appl. Opt.* **52**(1), A97–101 (2013).
32. J. Morlet et al., "Wave propagation and sampling theory—Part II: Sampling theory and complex waves," *Geophysics* **47**(2), 222–236 (1982).
33. M. Takeda, H. Ina, and S. Kobayashi, "Fourier-transform method of fringe-pattern analysis for computer-based topography and interferometry," *J. Opt. Soc. Am.* **72**(1), 156–160 (1982).
34. C. Roddier and F. Roddier, "Interferogram analysis using Fourier transform techniques," *Appl. Opt.* **26**(9), 1668–16673 (1987).
35. P. Flandrin, *Time-Frequency / Time-Scale Analysis*, Academic Press, New York (1999).
36. P. Goupillaud, A. Grossmann, and J. Morlet, "Cycle-octave and related transforms in seismic signal analysis," *Geoexploration* **23**(1), 85–102 (1984).
37. A. Grossmann and J. Morlet, "Decomposition of Hardy functions into square integrable wavelets of constant shape," *SIAM J. Math. Anal.* **15**(4), 723–736 (1984).
38. J. M. Combes, A. Grossmann, and P. Tchamitchian, Eds., *Wavelets*, Springer, Berlin (1989).
39. I. Daubechies, *Ten Lecture on Wavelets*, SIAM, Philadelphia (1992).
40. Y. Meyer, Ed., *Wavelets and Their Applications*, Springer, Berlin (1992).
41. M. B. Ruskai et al., Eds., *Wavelets and Their Applications*, Jones and Bartlett, Boston (1992).
42. P. Flandrin, *Temps-Fréquence*, Hermès, Paris (1993).
43. Y. Meyer and S. Roques, Eds., *Progress in Wavelets Analysis and Applications*, Editions Frontières, Gif-sur-Yvette (1993).
44. A. Arneodo et al., *Ondelettes, Multifractales et Turbulences: de l'ADN aux croissances cristallines*, Diderot Editeur, Art et Sciences, Paris (1995).
45. A. Arneodo, E. Bacry, and J. F. Muzy, "The thermodynamics of fractals revisited with wavelets," *Physica A* **213**(1–2), 232–275 (1995).
46. G. Erlebacher, M. Y. Hussaini, and L. M. Jameson, Eds., *Wavelets: Theory and Applications*, Oxford University Press, Oxford (1996).
47. S. Mallat, *A Wavelet Tour of Signal Processing*, Academic Press, New York (1998).
48. B. Torresani, *Analyse Continue par Ondelettes*, Editions de Physique, Les Ulis (1998).
49. A. Arneodo, N. Decoster, and S. Roux, "A wavelet-based method for multifractal image analysis. I. Methodology and test applications on isotropic and anisotropic random rough surfaces," *Eur. Phys. J. B* **15**(3), 567–600 (2000).
50. A. Arneodo et al., "A wavelet-based method for multifractal image analysis: from theoretical concepts to experimental applications," *Adv. Imaging Electron Phys.* **126**, 1–92 (2003).
51. P. Kestener and A. Arneodo, "Generalizing the wavelet-based multifractal formalism to random vector fields: application to three-dimensional turbulence velocity and vorticity data," *Phys. Rev. Lett.* **93**(4), 044501 (2004).
52. J. P. Antoine et al., *Two-Dimensional Wavelets and Their Relatives*, Cambridge University Press, Cambridge, United Kingdom (2004).
53. A. Arneodo, B. Audit, and P. Kestener, "Wavelet-based multifractal analysis," *Scholarpedia* **3**(3), 4103 (2008).
54. A. Arneodo et al., "Multi-scale coding of genomic information: from DNA sequence to genome structure and function," *Phys. Rep.* **498**(2–3), 45–188 (2011).
55. E. Freysz et al., "Optical wavelet transform of fractal aggregates," *Phys. Rev. Lett.* **64**(7), 745–748 (1990).
56. J. F. Muzy et al., "Optical-diffraction measurement of fractal dimensions and $f(\alpha)$ spectrum," *Phys. Rev. A* **45**(12), 8961–8964 (1992).
57. W. W. Macy, "Two-dimensional fringe-pattern analysis," *Appl. Opt.* **22**(23), 3898–3901 (1983).
58. P. Sandoz, "Wavelet transform as a processing tool in white-light interferometry," *Opt. Lett.* **22**(14), 1065–1067 (1997).
59. P. Tomassini et al., "Analyzing laser plasma interferograms with a continuous wavelet transform ridge extraction technique: the method," *Appl. Opt.* **40**(35), 6561–6568 (2001).
60. J. Zhong and J. Weng, "Spatial carrier-fringe pattern analysis by means of wavelet transform: wavelet transform profilometry," *Appl. Opt.* **43**(26), 4993–4998 (2004).
61. H. Liu, "Experimental verification of improvement of phase shifting Moiré interferometry using wavelet-based image processing," *Opt. Eng.* **43**(5), 1206–1214 (2004).
62. J. Zhong and J. Weng, "Phase retrieval of optical fringe pattern from the ridge of a wavelet transform," *Opt. Lett.* **30**(19), 2560–2562 (2005).
63. Z. Wang and H. Ma, "Advanced continuous wavelet transform algorithm for digital interferogram analysis and processing," *Opt. Eng.* **45**(4), 045601 (2006).
64. S. Li, X. Su, and W. Chen, "Wavelet ridge techniques in optical fringe pattern analysis," *J. Opt. Soc. Am. A* **27**(6), 1245–1254 (2010).
65. M. A. Gdeisat et al., "Spatial and temporal carrier fringe pattern demodulation using the one-dimensional continuous wavelet transform: recent progress, challenges, and suggested developments," *Opt. Lasers Eng.* **47**(12), 1348–1361 (2009).
66. R. Oven, "Extraction of phase derivative data from interferometer images using a continuous wavelet transform to determine two-dimensional refractive index profiles," *Appl. Opt.* **49**(22), 4228–4236 (2010).
67. Z. Zhang et al., "Comparison of Fourier transform, windowed Fourier transform, and wavelet transform methods for phase calculation at discontinuities in fringe projection profilometry," *Opt. Lasers Eng.* **50**(8), 1152–1160 (2012).
68. M. A. Gdeisat, D. R. Burton, and M. J. Lalor, "Spatial carrier fringe pattern demodulation by use of a two-dimensional continuous wavelet transform," *Appl. Opt.* **45**(34), 8722–8732 (2006).
69. Q. Kemao, "Two-dimensional windowed Fourier transform for fringe pattern analysis: principles, applications and implementations," *Opt. Lasers Eng.* **45**(2), 304–317 (2007).
70. A. Federico and G. H. Kaufmann, "Phase retrieval of singular scalar light fields using a two-dimensional directional wavelet transform and a spatial carrier," *Appl. Opt.* **47**(28), 5201–5207 (2008).
71. H. Niu, C. Quan, and C. Tay, "Phase retrieval of speckle fringe pattern with carriers using 2D wavelet transform," *Opt. Lasers Eng.* **47**(12), 1334–1339 (2009).
72. S. Li, X. Su, and W. Chen, "Spatial carrier fringe pattern phase demodulation by use of a two-dimensional real wavelet," *Appl. Opt.* **48**(36), 6893–6906 (2009).
73. K. Pokorski and K. Patorski, "Visualization of additive-type Moiré and time-average fringe patterns using the continuous wavelet transform," *Appl. Opt.* **49**(19), 3640–3651 (2010).
74. J. Ma et al., "Two-dimensional continuous wavelet transform for phase determination of complex interferograms," *Appl. Opt.* **50**(16), 2425–2430 (2011).
75. K. Pokorski and K. Patorski, "Separation of complex fringe patterns using two-dimensional continuous wavelet transform," *Appl. Opt.* **51**(35), 8433–8439 (2012).
76. E. Bedrosian, "Product theorem for Hilbert transforms," *Proc. IEEE* **51**, 868–869 (1963).
77. B. Städler, T. M. Blättler, and A. Franco-Obregón, "Time-lapse imaging of in vitro myogenesis using atomic force microscopy," *J. Microsc.* **237**(1), 63–69 (2010).
78. E. Ralston, "Changes in architecture of the Golgi complex and other subcellular organelles during myogenesis." *J. Cell Biol.* **120**(2), 399–409 (1993).

Cristina Martinez-Torres obtained a BSc in biophysics from the Autonomous University of San Luis Potosi, Mexico. During her undergraduate studies, she was involved in several research groups, working in topics such as bioinformatics, cellular biology, biophysics, optical engineering, and atomic physics. Currently, she is a PhD student in the group of Françoise Argoul at the Ecole Normale Suprieure de Lyon, France, where she studies cell dynamics.

Lotfi Berguiga received his PhD in physics from the University of Burgundy in France in 2001, where he worked in near field optics. Since 2004, he has worked at the Ecole Normale Suprieure de

Lyon, where he has investigated surface plasmon microscopy. Since 2007, he has worked as research engineer at the French National Centre for Scientific Research, and his research interests include development of new techniques of microscopy applied to cell biology.

Laura Streppa obtained her MSc with honors in biomolecular research from University of Urbino "Carlo Bo" and performed three years compulsory and volunteer internship in different laboratories (microbiology, molecular biology, biochemistry, and physics). She is currently a first-year PhD student at PHAST of Lyon. Her thesis, titled "Biomechanical study of neuromuscular junction and its impact in myopathies," is supported by AFM Telethon and is a collaboration between Laboratory of Physics and LMBC of ENS.

Elise Boyer-Provera graduated in optics and industrial visual systems from the Engineering School of Telecom in Saint Etienne in 2010. After a three-year training in the private company Thales Angenieux, she was hired as an engineer at Ecole Normale Suprieure de Lyon to develop original microscopy devices based on surface plasmon microscopy and quantitative phase microscopy.

Laurent Schaeffer obtained his PhD thesis in molecular biology in 1995 from the University of Strasbourg, France. He is presently the head of the Center of Cell Biotechnology of Lyon Hospitals and the director of the Laboratory of Molecular Biology of the Cell in ENS Lyon. He currently studies the mechanisms that control muscle and neuromuscular junction formation and maintenance with a special focus on the control of muscle gene expression by neural cues.

Juan Elezgaray is a senior researcher at CNRS, in the unit CBMN (UMR 5248, Pessac, France). He received his PhD in theoretical physics from Paris 6 University in 1989. He has held a permanent position at CNRS since 1989. His scientific interests are focused on modeling biologically motivated systems, from proteins to DNA; he also develops optics-related modeling.

Alain Arneodo got his thesis in elementary particle physics from the University of Nice, France, in 1978. He is the director of research at CNRS and has published over 200 peer-reviewed papers. His scientific contribution encompasses many fields of modern physics, including statistical mechanics, dynamical systems theory, fully developed turbulence, the mathematics of fractals and multifractals, signal and image processing, wavelet transform analysis, and its applications in physics, geophysics, astrophysics, chemistry, biology, and finance.

Françoise Argoul received her PhD from the University of Bordeaux in 1986. She is director of research at CNRS and has coauthored over 110 peer-reviewed papers. She manages a research program in Laboratory of Physics of Ecole Normale Superieure of Lyon, devoted to the experimental characterization of the mechanical and genomic response of cellular systems under external stress and to the role of mechanical and dynamical parameters on the modification of cellular mechanims.

Appendix D

Detection of internal boundaries from optical path difference gradients.

Journal of Biomedical Optics 20(9), 096005 (September 2015)

Deciphering the internal complexity of living cells with quantitative phase microscopy: a multiscale approach

Cristina Martinez-Torres,[a,b] Bastien Laperrousaz,[a,b,c] Lotfi Berguiga,[b,d] Elise Boyer-Provera,[a,b] Juan Elezgaray,[e] Franck E. Nicolini,[b,c,f] Veronique Maguer-Satta,[b,c] Alain Arneodo,[a,b] and Françoise Argoul[a,b,*]

[a]CNRS UMR5672, Laboratoire de Physique, Ecole Normale Supérieure de Lyon, 46 Allée d'Italie, 69007 Lyon, France
[b]Université de Lyon 1, 43 Boulevard du 11 Novembre 1918, 69100 Villeurbanne, France
[c]CNRS UMR5286, INSERM U1052, Centre de Recherche en Cancérologie de Lyon, 28 rue Laennec, 69008 Lyon, France
[d]CNRS USR3010, Laboratoire Joliot-Curie, Ecole Normale Supérieure de Lyon, 46 Allée d'Italie, 69007 Lyon, France
[e]CNRS UMR5248, Institut de Chimie et Biologie des Membranes et des Nano-objets, Allée de Geoffroy St Hilaire, 33600 Pessac, France
[f]Hospices Civils de Lyon, Hematology Department, Centre Hospitalier Lyon Sud, 165 Chemin du Grand Revoyet, 69495 Pierre Bénite, France

Abstract. The distribution of refractive indices (RIs) of a living cell contributes in a nonintuitive manner to its optical phase image and quite rarely can be inverted to recover its internal structure. The interpretation of the quantitative phase images of living cells remains a difficult task because (1) we still have very little knowledge on the impact of its internal macromolecular complexes on the local RI and (2) phase changes produced by light propagation through the sample are mixed with diffraction effects by the internal cell bodies. We propose to implement a two-dimensional wavelet-based contour chain detection method to distinguish internal boundaries based on their greatest optical path difference gradients. These contour chains correspond to the highest image phase contrast and follow the local RI inhomogeneities linked to the intracellular structural intricacy. Their statistics and spatial distribution are the morphological indicators suited for comparing cells of different origins and/or to follow their transformation in pathologic situations. We use this method to compare nonadherent blood cells from primary and laboratory culture origins and to assess the internal transformation of hematopoietic stem cells by the transduction of the BCR-ABL oncogene responsible for the chronic myelogenous leukemia. [DOI: 10.1117/1.JBO.20.9.096005]

Keywords: quantitative phase microscopy; cellular complexity; wavelet transform; contour detection; refractive index.

Paper 150441R received Jun. 30, 2015; accepted for publication Jul. 31, 2015; published online Sep. 3, 2015.

1 Introduction

During the last several decades, identification of the physical properties of single living cells has been a subject of considerable interest for cytopathology diagnoses.[1–5] In particular, quantitative optical microscopic methods[3,6,7] have shown that the refractive index (RI) of a cell can be used as an indicator for cell transformation in cancer processes. By offering the possibility of recovering the global and local RIs of a living cell without any *a priori* treatment by staining agents,[8–12] the development of quantitative phase microscopy (QPM) techniques is likely to shed a new light on the internal organization of different cell types.[1,3,7,8,13–20] In addition to the measurements of the averaged RIs over the whole cells, the intracellular distribution of RIs revealed by QPM provides quantitative information concerning the internal heterogeneous complexity of living cells.[8–12,21]

In recent years, cell imaging has seen the emergence of diverse microscopic setups suitable for living cell morphology capture.[1,9,17,20,22,23] Among them, diffraction phase microscopy (DPM)[23–25] has become a powerful tool for real-time analysis of single cell morphology and the alteration of cells in diverse pathologies.[20,23,26] However, with the exception of enucleated mature red blood cells (RBCs), whose RI can be presupposed as homogeneous (at the resolution of optical microscopy), the extraction of RIs from phase images often requires the use of rather complex algorithms. Converting the optical phase computed from the images of a QPM to an RI distribution in three dimensions (3-D) is quite impossible with a single wavelength measurement. Two-wavelength microscopes have been proposed to circumvent this limitation.[27] In some conditions, it is possible to include the effect of diffraction in the reconstruction process of high-resolution 3-D images throughout the entire sample volume.[7,28,29] More recently, elegant and relatively simple and low-cost methods have been proposed[30–32] for tomographic reconstruction of living cells. When the 3-D shape of the cell can be established *a priori*, the computation of RIs from phase images is then possible. Nonadherent cells in liquid generally adopt a spherical shape, which facilitates the inversion problem. We will use this assumption in this study for the characterization of blood cells.

Here, we aim at developing an original method for the detection of optical path difference (OPD) contours from living cells. The underlying idea is to look for local maxima of the OPD derivative in the two-dimensional (2-D) optical phase image. These maxima define interface chains where the RI and/or the cell shape vary abruptly and can be considered as domain boundaries. Even if we do not know *a priori* which is the prominent variation (RI or thickness) at each maximum, the connectivity of these maxima provides a direct access to the complexity of the cell interior. Because living cells are made of crowded macromolecules which may condensate or dilute at some stages

*Address all correspondence to: Françoise Argoul, E-mail: fargoul@ens-lyon.fr

1083-3668/2015/$25.00 © 2015 SPIE

of their lifespan, to assist global processes, such as growth, chromatin condensation, cell division, invasion, apoptosis, and migration, their internal structure bears a rather high level of complexity. Our study shows that except in some rare cases (RBCs), living blood cells are not partitioned into subdomains by isotropic and smooth contours, but rather look like randomly distributed contours with a broad distribution of lengths.

2 Materials and Methods

2.1 *Diffraction Phase Microscope*

Our DPM (Fig. 1) is directly inspired from the system published in Ref. 24. This interference microscope combines both off-axis and common-path interferometry techniques to produce fringe patterns [Fig. 1(a)] from which the phase images [Fig. 1(d)] can be reconstructed. The optical system is very compact and stable and does not require an expensive laser source [for instance, a laser-diode (Thorlabs, GmbH, Germany) with a wavelength $\lambda = 532$ nm]. It can be coupled to a fast image recording system (e.g., a CMOS camera, Hamamatsu, Japan, ORCA-Flash 4.0) with a 2048×2048 pixel grid. A Köhler illumination[33] is required to obtain an extremely even illumination and to avoid any perturbation of the sample image by the image of the light source at the image plane (IP) [Fig. 1(f)]. The interferences are obtained by combining a transmission grating (G) (110 grooves/mm), localized at the IP of the microscope, with a spatial filter (Thorlabs, custom-made) placed at the Fourier plane of lens L_1 that selects the first-order beam (imaging field) created by the grating and low-pass filters the zeroth-order beam (reference). The two beams are recombined through a second Fourier lens L_2. This $4f$ lens system adds a 5.9× magnification ($f_1 = 25.4$ mm, $f_2 = 150$ mm). The spatial filter consists of two circular apertures with diameters of 1 and 15 μm [Fig. 1(f)]. The objective lens (O) 40× (Olympus, SPlan40, NA = 0.7) allows a field of view of 75 μm. Prior to image capture, 65 μL of the solution containing the cells are poured between two glass coverslips glued by a Gene Frame Seal (Thermo Scientific AB-0577). Images are captured on the CMOS camera within the next 15 min of preparation at room temperature $T \sim 22$°C. A reference image of the background next to the area containing the cell is also recorded for each image.

2.2 *Cell Culture*

2.2.1 *Hematopoietic cell line model*

The immature CD34+ TF1 cell line (ATCC CRL-2003) was maintained at 1×10^5 cells/mL in RPMI-1640 medium, 10% fetal calf serum, and granulocyte macrophage colony-stimulating factor (10 ng/mL) (Sandoz Pharmaceuticals). Engineered TF1-GFP and TF1-BCR-ABL-GFP cell lines were obtained by transduction with a murine stem cell virus-based retroviral vector, encoding either the enhanced green fluorescent protein (EGFP) cDNA alone as a control or the BCR/ABL-cDNA upstream from an IRES-eGFP sequence, as described in Ref. 34. EGFP+ TF1 cells were sorted using a Becton Dickinson FACSAria. For imaging, 65 μL of the solution were poured between two glass coverslips glued by a Gene Frame (ThermoScientific). The images were taken from two different

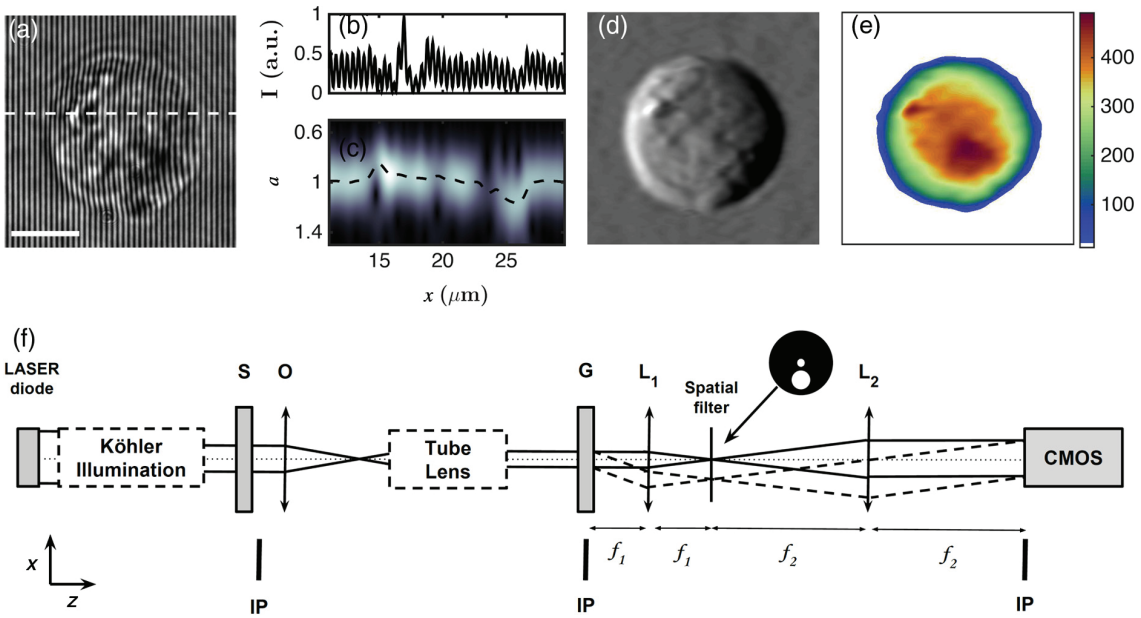

Fig. 1 Diffraction phase microscopy (DPM) principle: (a) untreated DPM image of a nonadherent immature myeloid cell (TF1-GFP). Scale bar: 5 μm; (b) intensity profile of the section marked with a white dashed line in (a); (c) space-scale representation of the modulus of the wavelet transform (WT) $|\mathbf{T}_\Psi[I]|(b, a)$ of the section shown in (b); with a black dashed line we distinguish the wavelet transform modulus maxima (WTMM) profile. Note that we label the horizontal axis with the same variable x to align the two signals (image section and WT), in that representation $b = x$; (d) $\partial\phi(\mathbf{b})/\partial x$ computed for each line of the original phase image with the method illustrated in (c), the gray coding spans the interval [−2.7 to 5.4] rad/μm; (e) color-coded optical path difference (OPD) $\Phi = \phi\lambda/2\pi$ (in nm) computed from the arguments $A_\Psi[I](\mathbf{b}, a^*)$ of the WT at the scale a^* corresponding to a maximum of its modulus; and (f) DPM optical setup (see text).

cell batches per cell line type (TF1-GFP or TF1-BCR-ABL-GFP), and the total numbers of cells analyzed were 298 TF1-BCR-ABL-GFP (short name: TF1-BA) cells and 263 TF1-GFP cells.

2.2.2 *Human primary cells (nucleated immature cells and red blood cells)*

After informed consent in accordance with the Declaration of Helsinki and local ethics committee bylaws (from the Délégation à la recherche clinique des Hospices Civils de Lyon, Lyon, France), peripheral blood and bone marrow samples were obtained from chronic myelogeneous leukemia patients. Mononuclear cells were separated using a Ficoll gradient (Bio-Whittaker) and were then subjected to CD34 immunomagnetic separation (Stemcell Technologies). The purity of the CD34+-enriched fraction was checked by flow cytometry and was over 95% on average.

3 Diffraction Phase Microscopy Image Analysis with a Wavelet-Based Multiscale Analyzing Method

3.1 *Diffraction Phase Microscopy Principle for Cell Imaging*

DPM[23–25] allows a fast, nonintrusive, and high-sensitive measurement of the OPD produced by a transparent object embedded inside a homogeneous medium. The DPM optical setup sketched in Fig. 1(f) produces 2-D images with parallel fringe patterns [Fig. 1(a)] corresponding to a periodic modulation of the intensity:

$$I(\mathbf{x}) = P(\mathbf{x}) + Q(\mathbf{x})\cos[f_g x + \phi(\mathbf{x})], \tag{1}$$

where $\phi(\mathbf{x})$ is the optical phase due to light transmission through the object at point $\mathbf{x} = (x, y)$, $P(\mathbf{x})$ and $Q(\mathbf{x})$ are, respectively, the unmodulated and modulated intensities at the same point of the image, and f_g is the spatial frequency of the diffraction grating. One common assumption is that $P(\mathbf{x})$ and $Q(\mathbf{x})$ vary much more slowly than $\phi(\mathbf{x})$.[9,17,20,23,26] However, this is rarely the case with thick spherical cells, since they produce modulations of both the optical phase ϕ and the amplitude Q [Figs. 1(a) and 1(b)]. To circumvent this difficulty, we computed the ridges [wavelet transform modulus maxima (WTMM) lines] from the wavelet transform (WT) of the fringe image with a 2-D anisotropic Morlet analyzing wavelet.[35–40] The implementation of this method on DPM has been recently published[36] and shown to surpass more traditional Hilbert methods[41] when the amplitude modulation $Q(\mathbf{x})$ spans the frequencies that mix with the carrier frequency (f_g). In Fig. 1(c), we show the space-scale representation of the WT modulus computed from the horizontal section [Fig. 1(b)] of the fringe image in Fig. 1(a) ($a = 1$ corresponds to the fringe carrier frequency). The black dashed line outlines the position of the WTMM line. The scale a of the WTMM is proportional to the inverse of the derivative of the object phase $\{\partial[f_g x + \phi(\mathbf{x})]/\partial x\}$ and directly gives the image of the phase derivative shown in Fig. 1(d). The optical phase ϕ at position $\mathbf{x}$ is given by the integral:

$$\phi(\mathbf{x}) = \frac{2\pi}{\lambda}\int_{z_m(\mathbf{x})}^{z_M(\mathbf{x})} \Delta n(\mathbf{x}, z)\mathrm{d}z, \tag{2}$$

where λ is the illumination wavelength, $\Delta n = n - n_0$ is the difference between the RIs of the object (n) and the external medium (n_0), and z_M (respectively, z_m) is the upper (respectively, lower) bound of the object at position $\mathbf{x}$. The total thickness of the object at point $\mathbf{x}$ is $h(\mathbf{x}) = z_M(\mathbf{x}) - z_m(\mathbf{x})$. The recovery of $\Delta n(\mathbf{x})$ from the phase map $\phi(\mathbf{x})$ amounts to solving an inverse problem.[21,42] This is quite difficult without any assumption on the topography of the object, except in the case where the internal RI of the object is constant. This actually occurs for RBCs, for which we will be able to recover the shape of the cell from its fringe pattern[26] (see below). Nucleated cells involve a much more heterogeneous internal structure that requires a more complex reconstruction algorithm. Given that the optical phase ϕ depends on the illumination wavelength, in practice it is more convenient to work with the OPD: $\Phi = \phi\lambda/2\pi$. The OPD is equivalent to the retardation path length of the light after crossing the cell. According to Eq. (2), the OPD function is the integral on the RI drop through the cell whose limits of integration depend on the point $\mathbf{x}$:

$$\begin{aligned}\Phi(\mathbf{x}) &= \int_{z_m(\mathbf{x})}^{z_M(\mathbf{x})} \Delta n(\mathbf{x}, z)\mathrm{d}z = [\Delta N(\mathbf{x}, z)]_{z_m(\mathbf{x})}^{z_M(\mathbf{x})} \\ &= \Delta N(\mathbf{x}, z_M) - \Delta N(\mathbf{x}, z_m),\end{aligned} \tag{3}$$

where $\Delta N(\mathbf{x}, z)$ is the integral function of $\Delta n(\mathbf{x}, z)$. For example, if $\Delta n(\mathbf{x}, z) = \mathrm{C}^{st}$, $\Delta N(\mathbf{x}, z) = C^{st} z + B$ is a linear function of the variable z and $\Phi(\mathbf{x}) = \mathrm{C}^{st}[z_M(\mathbf{x}) - z_m(\mathbf{x})] = \mathrm{C}^{st} h(\mathbf{x})$. The OPD function precisely follows the shape of the object and its derivative is proportional to the derivative of its thickness h at each point $\mathbf{x}$. In general, the derivative of Φ along a radial coordinate of the (x, y) plane results from both RI and topography variations:

$$\frac{\partial\Phi(\mathbf{x})}{\partial r} = \frac{\partial\Delta N(\mathbf{x}, z_M)}{\partial r} - \frac{\partial\Delta N(\mathbf{x}, z_m)}{\partial r}. \tag{4}$$

If Δn is an integrable function, the two integral values $\Delta N(\mathbf{x}, z_M)$ and $\Delta N(\mathbf{x}, z_m)$ exist and their derivatives with respect to r can be computed. The boundary of the object is precisely defined by an abrupt change in the RI slope at the interface between the interior and the exterior media. Because domain boundaries in biological matter are not very sharp, we will rather consider them as transitory zones with a sharpness described by the gradient of the OPD. The local maxima of this OPD spatial gradient will follow the boundary zones wherever they can be detected (external and internal). If we consider that the object is made of the assembly of different internal structures with RI variations, we will apply the same assumption as above for the domain boundary detection. The main difficulty will, therefore, be to correctly compute these spatial gradients and extract local maxima lines. If the maxima lines are closed, we will infer the existence of well-defined internal structures with a quite homogeneous composition. On the contrary, if the maxima lines are unclosed and randomly distributed curves, we will rather infer a more complex organization of the internal structure of the considered object.

3.2 *Diffraction Phase Microscopy Analysis of Model Spherical Cells*

Let us first consider as a theoretical example, a spherical object of radius R with a radial RI function varying from n_0 (the outer medium) to n_C (at the center of the sphere):

$$\Delta n(\mathbf{x}, z) = \begin{cases} |(R-r)/R|^{\alpha}\Delta n_C & \text{for } r \le R, \\ 0 & \text{for } r > R, \end{cases} \quad (5)$$

with $r = \sqrt{x^2+y^2+z^2}$ the radial distance, $\Delta n_C = n_C - n_0$, and α a real positive exponent. We consider only the positive values of z [the object is symmetric in respect to the equatorial plane (x, y)]. The boundaries of the sphere at position $\mathbf{x}$ are such that $x^2 + y^2 \le R^2$ are

$$z_m(\mathbf{x}) = -\sqrt{R^2 - (x^2+y^2)} \quad \text{and}$$
$$z_M(\mathbf{x}) = \sqrt{R^2 - (x^2+y^2)}. \quad (6)$$

Centering the three vector bases ($\vec{e}_x$, $\vec{e}_y$, and $\vec{e}_z$) at the center of the sphere ($x_C = 0$, $y_C = 0$, and $z_C = 0$), we plot in Fig. 2(a) the RI profile along the x ($y = 0$) axis in green for different values of the exponent α in Eq. (5), namely $\alpha = 0$ (solid line), 0.25 (dashed-dotted line), 0.5 (dotted line), and superimposed to the sphere height profile (black dashed-dotted line).

The OPD of this spherical object at position $\mathbf{x}$ with $x^2 + y^2 \le R^2$ is given by

$$\Phi(\mathbf{x}) = \Delta n_C \int_{-\sqrt{R^2-(x^2+y^2)}}^{\sqrt{R^2-(x^2+y^2)}} \left| \left(R - \sqrt{x^2+y^2+z^2} \right)/R \right|^{\alpha} \mathrm{d}z. \quad (7)$$

The three OPD functions corresponding to $\alpha = 0$, 0.25, and 0.5 are plotted in green in Fig. 2(b) with the same line style as in Fig. 2(a). When the RI is increasing monotonously from the border to the center of the sphere, the OPD $\Phi(x, y = y_C)$ retains a global single humped shape, with a nonlinearity that depends on the exponent α. The local maxima of the first derivative of the OPD functions with respect to x are close to the position of the sphere's border. Note also that the OPD functions are symmetrical with respect to the center of the sphere, retaining the centrosymmetry of the object. In that example, we have computed the first derivative of the OPD with a smoothing first derivative of a Gaussian function, as further used in the experimental situations reported hereafter. Thus, the slight shift of the maxima of the red curves $\partial\Phi/\partial x$ from the sphere borders (dashed blue line) is due to the smoothing scale of this Gaussian filtering.

To mimic an internal variation of the RI, we have constructed another structure with the same outer spherical shape, but containing an internal concentric spherical shell with a higher RI, the boundary of which also varyies smoothly with the radius r:

$$\Delta n(\mathbf{x}, z) = \begin{cases} [|f(r)|^{\alpha} + \{\cos[2\pi f(r)] - 1\}^2/6]\Delta n_C & \text{for } r \le R, \\ 0 & \text{for } r > R, \end{cases} \quad (8)$$

where $f(r) = [R - \sqrt{x^2+y^2+z^2})/R]$. As shown in Fig. 2(c), the corresponding RI profiles for $\alpha = 0$, 0.25 and 0.5 bear two supplementary local maxima at $x = -2$ μm and 2 μm, which are superimposed to the smoothly increasing profile [similar to those in Fig. 2(a)]. The corresponding Φ and $\partial\Phi/\partial x$ profiles plotted in Fig. 2(d) are very instructive, since they show that the combination of both the spherical shape and nonmonotonous RI profiles may lead to an unexpected behavior. In the situation

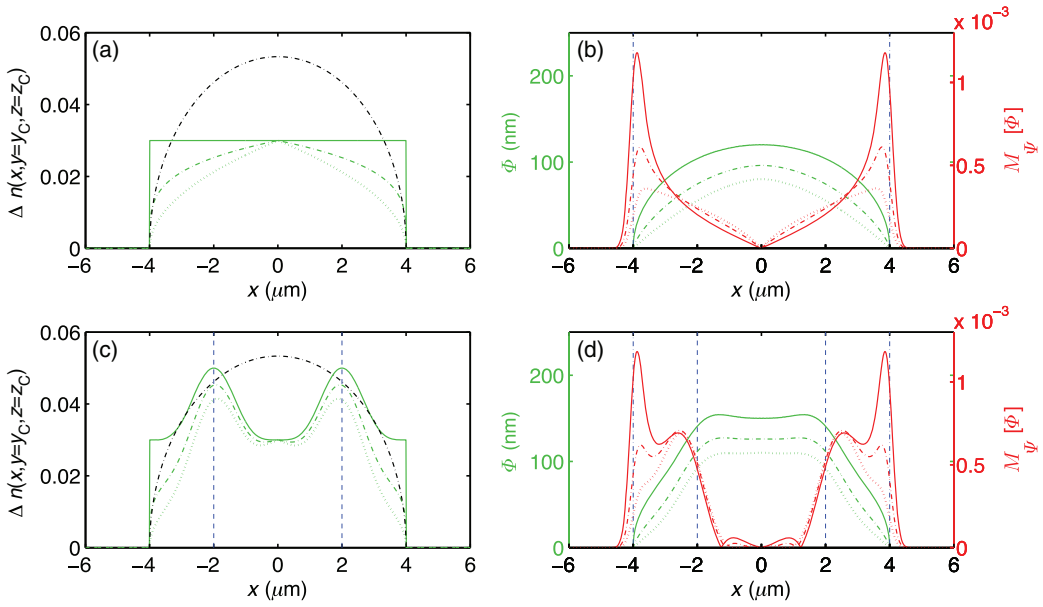

Fig. 2 OPD and OPD derivative functions for spherical shell models with radial RI profiles: (a) monotonously increasing (or constant) RI profiles $\Delta n(x, y = y_C, z = z_C)$ (from the border to the center) given by Eq. (5); (b) corresponding $\Phi(x)$ (green lines) and $\partial\Phi/\partial x$ (red lines) computed from the profiles in (a), using the first derivative of the Gaussian function as smoothing analysing wavelet (see text); (c) nonmonotonously increasing RI profiles $\Delta n(x, y = y_C, z = z_C)$ described by Eq. (8); and (d) $\Phi(x)$ (green lines) and $\partial\Phi/\partial x$ (red lines) computed as before from the profiles in (c). $\alpha = 0$ (respectively 0.25 and 0.5) is plotted with a green solid (respectively dashed-dotted and dotted) line. The underlying sphere shape is reported with a black dashed-dotted line. $x_C = 0$, $y_C = 0$, and $z_C = 0$ correspond to the center of the sphere.

shown here, not only the underlying object spherical shape is smeared out, but the local maxima of the index profile are also strongly damped, giving place to a quasi OPD plateau in the middle interval [−2 μm, 2 μm]; the higher α is, the flatter this plateau.

From this last model, we conclude that trusting the OPD isocontours to delineate regions of different RIs from a reconstructed phase image may be totally misleading even though we can still recover some information on the boundary (internal and external) properties with the computation of the local derivative of the OPD function.

3.3 *Multiscale Method Based on the Continuous Two-Dimensional Wavelet Transform*

Given that the OPD images are 2-D, computation of the derivatives must be performed along both directions $\mathbf{x}$ and $\mathbf{y}$ and ideally we must also include in the computation the possibility to smooth out the enhanced noise that could come from the derivative procedure. As originally noticed by Mallat and coworkers,[43,44] the 2-D WT[45–47] can be used to revisit Canny's multiscale edge detector.[48] The principle of this analysis is to smooth the image by convolving it with a filter and then to compute the gradient of the smoothed image. Let us consider the two wavelets defined respectively as the partial derivatives with respect to x and y of a 2-D smoothing function $\psi(\mathbf{x})$:

$$\Psi_1 = \frac{\partial \psi(\mathbf{x})}{\partial x} \quad \text{and} \quad \Psi_2 = \frac{\partial \psi(\mathbf{x})}{\partial y}. \tag{9}$$

The smoothing function ψ must be well localized (around $x = y = 0$), isotropic, and dependent on the modulus of $\mathbf{x}$ only. The Gaussian function is the mostly used function that fulfills these conditions:

$$\psi(\mathbf{x}) = e^{-(x^2+y^2)/2}. \tag{10}$$

The WT of any 2-D function $\Phi(\mathbf{x})$ [which is embedded in $L^2(\Re)$] with respect to the analyzing wavelets $\mathbf{\Psi} = (\Psi_1, \Psi_2)$ has two components and can be expressed in a vectorial form:

$$\mathbf{T_\Psi}[\Phi](\mathbf{b}, a) = \left\{ \begin{array}{l} T_{\Psi_1}[\Phi] = a^{-2} \int \mathrm{d}^2 x \Psi_1[a^{-1}(x - \mathbf{b})]\Phi(x) \\ T_{\Psi_2}[\Phi] = a^{-2} \int \mathrm{d}^2 x \Psi_2[a^{-1}(x - \mathbf{b})]\Phi(x) \end{array} \right\}. \tag{11}$$

By a straightforward integration by parts,[45] this 2-D WT can be rewritten as

$$\begin{aligned} \mathbf{T_\Psi}[\Phi](\mathbf{b}, a) &= a^{-2}\nabla \left\{ \int \mathrm{d}^2 x \psi[a^{-1}(x - \mathbf{b})]\Phi(x) \right\} \\ &= \nabla \{T_\psi[\Phi](\mathbf{b}, a)\} = \nabla\{\psi_{b,a} * \Phi\}. \end{aligned} \tag{12}$$

If $\psi(\mathbf{x})$ is a smoothing filter like the Gaussian function [Eq. (10)], then Eq. (12) amounts to the computation of the gradient vector of $\Phi(\mathbf{x})$ smoothed by dilated versions $\psi(a^{-1}\mathbf{x})$ of this filter. If $\psi(\mathbf{x})$ has some vanishing moments, then $T_\psi[\Phi](\mathbf{b}, a)$ in Eq. (12) is the continuous 2-D wavelet (C2DWT) of $\Phi(\mathbf{x})$,[35] provided that $\psi(\mathbf{x})$ is an isotropic analyzing wavelet. Further on, we will compute the 2-D WT modulus $\mathcal{M}_\Psi[\Phi](\mathbf{b}, a)$ and its argument $\mathcal{A}_\Psi[\Phi](\mathbf{b}, a)$:

$$\begin{aligned} \mathcal{M}_\Psi[\Phi](\mathbf{b}, a) &= |\mathbf{T_\Psi}[\Phi](\mathbf{b}, a)|, \\ &= \{[T_{\Psi_1}[\Phi](\mathbf{b}, a)]^2 + [T_{\Psi_2}[\Phi](\mathbf{b}, a)]^2\}^{1/2}, \end{aligned} \tag{13}$$

and

$$\mathcal{A}_\Psi[\Phi](\mathbf{b}, a) = \mathrm{Arg}[T_{\Psi_1}[\Phi](\mathbf{b}, a) + iT_{\Psi_2}[\Phi](\mathbf{b}, a)]. \tag{14}$$

In practice, at a given scale a, we first compute the 2-D fast Fourier transform (FFT) of Ψ_1 and Ψ_2 and we multiply these images by the FFT of Φ: $\tilde{\Psi}_1 \cdot \tilde{\Phi}$ and $\tilde{\Psi}_2 \cdot \tilde{\Phi}$ and from the inverse FFT of these products, we get the WTs $T_{\Psi_1}[\Phi]$ and $T_{\Psi_2}[\Phi]$. We then identify the so-called WTMM as the points $\mathbf{b}$, where the modulus $\mathcal{M}_\Psi[\Phi](\mathbf{b}, a)$ is locally maximum for a given scale a^*. To increase the resolution of this local maxima detection, we transform the pixelated images into radial representations. To switch from Cartesian to cylindrical geometry, we interpolate the WT argument and modulus on 1440 radial axes crossing the center of the cell with an angular shift of $\delta\theta = 4.410^{-3}$ rad. On each of these rotating axes with θ varying from 0 to 2π, we interpolate each pixelated image along the radial variable r with a spatial resolution $\mathrm{d}r = 1.8$ nm. This allows a very acute determination of both the local angle θ and the argument $\mathcal{A}_\Psi$ of the WT vector. From the radial coordinates of the WTMMs, we reconstruct maxima chains as 2-D curves made of a sequence of neighboring points (distant of less than $2r\delta\theta$).

When the maxima chain is circular [Fig. 3(a)] and the WT vector $\mathbf{T_\Psi}[\Phi](\mathbf{b}, a)$ is oriented outward [blue arrows in Fig. 3(a)], the argument of the WT is equal to the radial angle θ, $\Delta\theta = \mathcal{A}_\Psi[\Phi]_{\mathrm{WTMM}} - \theta = 0$ [Fig. 3(b), blue circles]. If the WT vector is oriented inward [magenta arrows in [Fig. 3(a)], the argument is equal to π [Fig. 3(b), magenta circles]. If instead

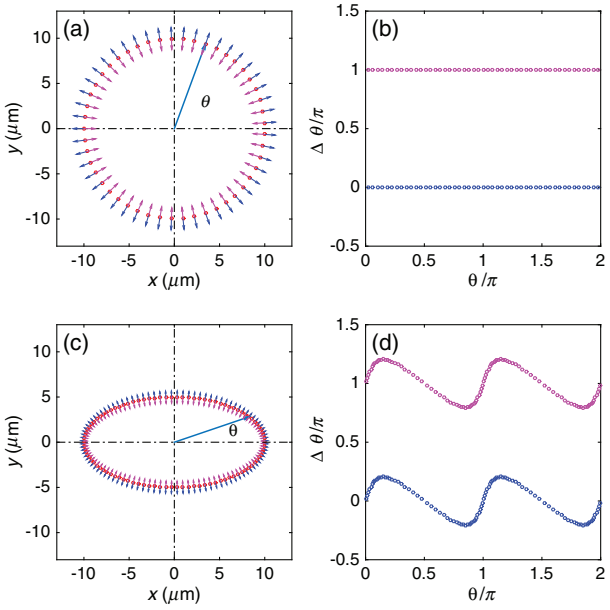

Fig. 3 WT argument for a spheroid and an ellipsoid cell model: (a) circular chain model with outward (respectively inward) WT vectors $[\mathbf{T_\Psi}[\Phi](\mathbf{r}, a)]$; (b) $\Delta\theta = \mathcal{A}_\Psi[\Phi]_{\mathrm{WTMM}} - \theta$ on the WTMM chain line in (a); (c) ellipsoidal chain model with outward and inward wavelet vectors; and (d) $\Delta\theta = \mathcal{A}_\Psi[\Phi]_{\mathrm{WTMM}} - \theta$ on the WTMM chain line in (c). The outward (respectively inward) vectors in (a) and (c) correspond to blue (respectively magenta) circles in (b) and (d).

we take an ellipsoidal-shaped maxima chain [Fig. 3(c)], the argument of the WT is no longer a constant function versus the angle θ. Again we consider the two cases of outward WT vector [blue arrows in Fig. 3(c) and blue circles in Fig. 3(d)] and inward WT vector [magenta arrows in Fig. 3(c) and magenta circles in Fig. 3(d)]. It is important to note that when the WTMM chain deviates from a circular contour, the angle difference $\Delta\theta$ may oscillate versus the radial angle θ, with alternating increasing ($\theta < 0.15\pi$) and decreasing ($0.15\pi < \theta < 0.85\pi$) intervals in Fig. 3(d). The flatter the shape of the chain, the larger the slope of these curves (in absolute values). The positive slopes of $\Delta\theta$ versus θ curves (which may reach vertical lines) correspond to highly curved chains (compared with a circle), whereas the negative slopes correspond to flatter chains (compared with a circle).

3.4 *Wavelet-Based Analysis of Model Spherical Cells with Noise*

We illustrate the WTMM method for detecting the local maxima chains from noisy data, taking again the previous model of a spherical object with an internal spherical shell of higher RI [Eq. (8)], adding a white noise term to the RI function before computing the OPD image:

$$\Delta n(\mathbf{x}, z) = \begin{cases} \{|f(r)|^{\alpha} + \{\cos[2\pi f(r)] - 1\}^2/6 + \zeta\}\Delta n_C & \text{for } r \le R, \\ \zeta & \text{for } r > R \end{cases}. \tag{15}$$

ζ is a uniformly distributed random variable (MATLAB random generator rand) in the $[-1/10, 1/10]$ interval, giving a standard deviation of ζ that we fix to 2.8%. We report in Fig. 4 the WT modulus and the local WTMM for two scales a of the analyzing wavelet computed from the noisy shell model [Eq. (15)]. From the OPD image [Fig. 4(d)] and its x-section through the central point ($x = x_C$, $y = y_C$) [Fig. 4(a), green line], we do not see much difference from the noise-free profile in Fig. 2(d). However, when computing the derivative with a small value of the scale parameter a [red curve in Fig. 4(a) and 2-D image of Fig. 4(b)], we notice that the background white noise that we have added to the RI introduces fluctuations that dramatically perturb the detection of the local maxima of the WT modulus [Fig. 4(c)]. To circumvent this problem, we follow a strategy recommended in Ref. 49 which amounts to increasing the scale parameter a until the number of local maxima chains no longer changes and their structure becomes more regular and robust. In that simple theoretical example, by simply increasing the scale a by a factor of 5 [Fig. 4(e)], we get the three expected maxima chain lines corresponding respectively to the outer boundary and the two (internal and external) boundaries on the internal concentric shell of a higher RI [Fig. 4(f)]. In this example, once the scale a is chosen correctly to smooth down the background noise, the maxima lines predicted by the model are recovered.

4 Application of the Wavelet Transform Modulus Maxima Method to Diffraction Phase Microscopy Images of Living Cells

To test the WTMM detection of phase boundary contours on DPM images of living cells, we first considered RBCs as an example of anucleated cells with an almost homogeneous cytoplasm (RI $\sim 1.401 \pm 0.006$)[50–52] with a high concentration of hemoglobin. The shape of healthy, unstressed RBCs has been fully described in the literature[26,52–55] with a biconcave equation

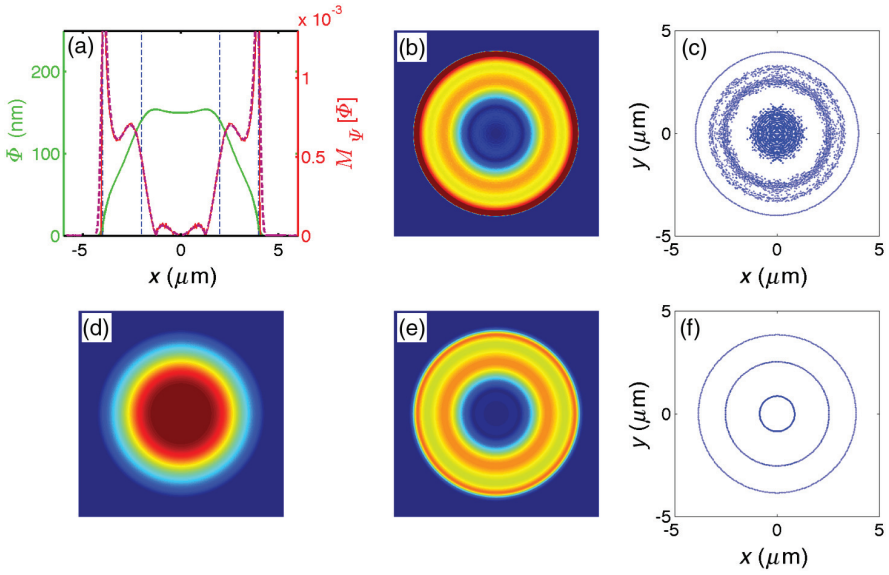

Fig. 4 WTMM chain line detection from the OPD of a spherical cell model with noise: (a) OPD $\Phi(x)$ (green line) computed from model [Eq. (15)] for $\alpha = 0.25$ and its WT modulus $\mathscr{M}_{\Psi}[\Phi](b, a)$ estimated for two scales $a = 2$ (red) and 10 (magenta dashed line); (b) two-dimensional (2-D) color-coded image of $\mathscr{M}_{\Psi}[\Phi]$ for $a = 2$, color coded from dark blue to red in the interval [0, 0.001]; (c) local maxima of $\mathscr{M}_{\Psi}[\Phi]$ for $a = 2$; (d) 2-D color-coded representation of Φ (in the interval [0, 133 nm]), computed from model [Eq. (15)]; (e) 2-D color-coded image of $\mathscr{M}_{\Psi}[\Phi]$ for $a = 10$, color coded in the interval [0, 0.001]; and (f) local maxima of $\mathscr{M}_{\Psi}[\Phi]$ for $a = 10$.

for their thickness h versus the radial coordinate r, as observed experimentally in isotonic buffers:

$$h(r) = z_M - z_m = \left[1 - \left(\frac{2r}{d}\right)^2\right]^{1/2} \times \left[0.72 + 4.512\left(\frac{2r}{d}\right)^2 - 3.426\left(\frac{2r}{d}\right)^4\right]. \quad (16)$$

4.1 *Red Blood Cells*

A typical healthy RBC has a maximum and minimum thicknesses of 2.84 and 1.44 μm, respectively, and a diameter $d = 7.5 \pm 0.5$ μm. We recognize in Fig. 5(a) the characteristic OPD "donut" shape of a RBC,[26,55] with a central hole and cylindrical symmetry. This example is particularly interesting to test the performance of WTMM detection method, as shown in Figs. 5(b)–5(d). Figure 5(c) shows the corresponding sections of Φ (green) and $\mathcal{M}_\Psi[\Phi]$ (red) along the x direction, taken at the barycenter of the cell. The experimental green profile in Fig. 5(c) is in very good agreement with the biconcave shape (black line) predicted by Eq. (16). This method detects two WTMM chains, one exterior and one interior. Note that the exterior WTMM chain is color coded in hot (red to brown red) colors in Fig. 5(d) as an indicator of larger modulus values than the interior WTMM chain coded in cold (dark blue to blue) colors. The plot of the argument of the WT $\mathcal{A}_\Psi[\Phi]$ versus θ along each of the two WTMM chains shows a clear separation of the two chains [Fig. 5(e)]. The exterior chain corresponds roughly to the diagonal (red to brown red color) and the interior chain is globally shifted from the diagonal by π. This shift corresponds simply to the inward direction of the wavelet vector (as already illustrated in Fig. 3). The two plots of the evolution of $\Delta\theta = \mathcal{A}_\Psi[\Phi] - \theta$ in Fig. 5(f) for each WTMM chain confirm the reversal of the direction of the wavelet vector from the outer to the inner WTMM chain. Indeed this vector gives the direction of the steepest descent of the WT modulus. More interestingly, we note that the fluctuations of $\Delta\theta$ on the inner chain are much larger than on the outer chain, meaning a more irregular shape (loss of circularity) distribution of the internal part of this cell. Given the predicted minimal thickness of a RBC,[26,52–55] $h_{\min} \sim 1.44$ μm, we can use the averaged Φ values in the hole of this RBC $\Phi_{\min} = 90 \pm 5$ nm $= h_{\min}\Delta n$ to estimate the RI drop: $\Delta n = 0.063 \pm 0.004$, leading to the following estimate of the RBC RI: $n = 1.333 + 0.063 = 1.396 \pm 0.004$.

4.2 *Primary Immature Blood Cells*

We consider now spherical mononucleated immature blood cells (nonadherent). These CD34+ cells are sorted from the bone marrow or peripheral blood by the CD34 antigen; they are a mixture of hematopoietic stem and progenitor cells with various degrees of maturity. In healthy conditions, these cells remain mostly in the bone marrow. In chronic myeloid leukemia (CML), these immature cells can also be found in the blood. These cells have a rather high nuclear:cytoplasmic ratio (N:C) in the interphase.[56–58] This ratio indicates the maturity of the cell; for example for immature leukocytes, it may reach 4:1.[59] If we assume that the nucleus is a concentric sphere (which can be applied to CD34+ cells) of the cell of radius R_N, a 4:1 N:C would give $R_N = (4/5)^{1/3} \cdot R_C \sim 0.93R_C$ (R_C is the cell radius). If $R_C = 4$ μm, this would give $R_N = 3.7$ μm, leaving only a 300-nm distance in between the outer cytoplasmic and the inner nuclear membranes. Such a large nucleus should not be distinguishable from the outer membrane shell in our microscope device, since one fringe produced by the grating is too thick ~400 nm (in the scale of the cell). If the N:C ratio drops to 3:1, the radius of the nucleus decreases only by 70 nm, which should also be undetectable with our optical setup. The impact of the nucleus should, therefore, only be visible on the amplitude of the OPD Φ and/or its derivative. However, we should be able to detect

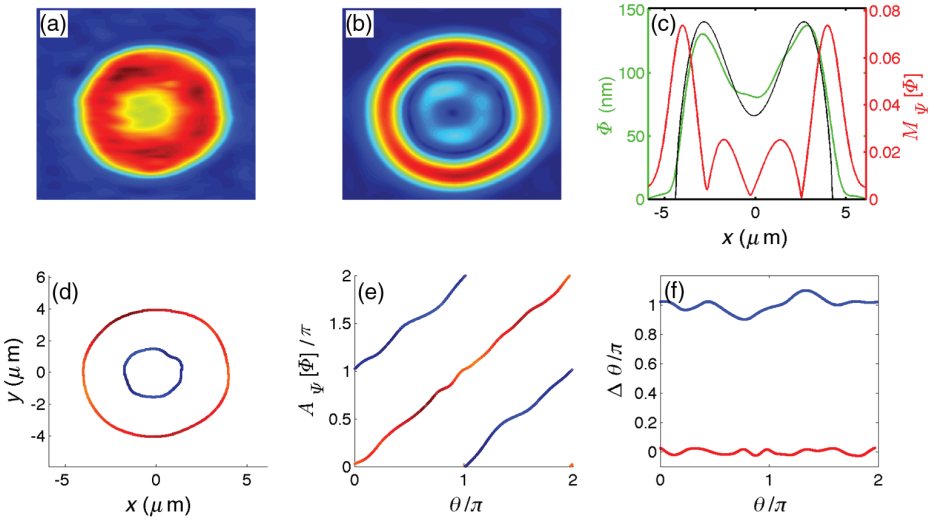

Fig. 5 WTMM chain detection from the OPD of a living red blood cell (RBC): (a) OPD phase image, color coded from dark blue ($\Phi = 0$ nm) to brown red ($\Phi = 163$ nm); (b) $\mathcal{M}_\Psi[\Phi](\mathbf{b}, a)$ for $a = 15$, color coded in the interval [0, 0.09]; (c) horizontal sections through the barycenter of the cell of the OPD Φ (green line) and of $\mathcal{M}_\Psi[\Phi]$ (red line). The black line corresponds to the biconcave shape predicted by Eq. (16); (d) WTMM chains of the RBC cell shown in (a), color coded according to the value of $\mathcal{M}_\Psi[\Phi]$; (e) plot of the argument $\mathcal{A}_\Psi[\Phi]_{\text{WTMM}}$ of the WTMM chains versus θ [same color coding as in (d)]; and (f) plot of $\Delta\theta = \mathcal{A}_\Psi[\Phi]_{\text{WTMM}} - \theta$ versus θ.

internal structures of the nuclei on this type of cells. Figure 6 illustrates the WTMM boundary detection on a rounded nonadherent living CD34+ cell. The outer boundary of this spherical cell is detected straightforwardly by the maxima chain with maximum mean $\langle \mathcal{M}_\Psi[\Phi]_{\mathrm{WTMM}} \rangle$. While the external contour of the cell is very circular [$\mathcal{A}_\Psi[\Phi]_{\mathrm{WTMM}}$ versus θ is a straight line in Fig. 6(e)], with few fluctuations [Fig. 6(f)], the internal shape of Φ [Fig. 6(a)] presents a single slightly off-centered small bump, leading to the conical shape of the Φ profile in Fig. 6(c) (green line). If we fit the outer part of this Φ profile by the prediction for a homogeneous sphere with radius $R_C = 4.5 \pm 0.08$ μm [$\alpha = 0$ in Eq. (7)]:

$$\Phi(x) = 2\Delta n_C \sqrt{R^2 - (x^2 + y^2)}, \tag{17}$$

we get the following estimate for its internal index: $n = 1.365 \pm 0.004$ [black line in Fig. 6(c)]. Another way to obtain an estimate of the internal cell index is to compute the optical path volume (OPV):

$$\mathrm{OPV} = \int_{y_m}^{y_M} \int_{x_m}^{x_M} \int_{z_m(x)}^{z_M(x)} \Delta n(x, y, z) \mathrm{d}z \, \mathrm{d}x \, \mathrm{d}y. \tag{18}$$

For the discretized Φ images, we simply compute

$$\mathrm{OPV} = \mathcal{S}_{xy} \sum_{\mathrm{intra}} \mathrm{OPD}, \tag{19}$$

where $\mathcal{S}_{xy}$ is the area of a pixel. For a homogeneous sphere with RI drop Δn, the OPV is that of an oblate ellipsoid with height $R\Delta n_C$ (z direction) and radius R in the (x, y) plane:

$$\mathrm{OPV} = \frac{4}{3} \pi R_C^3 \Delta n_C = V_S \Delta n_C, \tag{20}$$

with V_S the formal volume of the perfect spherical cell of the same radius R_C. From the OPD image of Fig. 6(a), we obtain OPV $= 13.84$ μm^3, which with $R_C = 4.5$ μm leads to $\Delta n_C = 0.0365 \pm 0.005$ and thus to a cell averaged RI $n = 1.369 \pm 0.005$. This estimation is better when matching the averaged cell RI than the above estimation obtained from a single $\Phi(x)$ profile since it embraces the whole cell phase topography. Globally, we can conclude from this example that this primary blood cell has an average RI which is not much larger than what is known for eukaryotic cell cytoplasmic zones.[60] This OPV is an interesting quantity that will help us comparing different cells. In particular, by dividing this OPV [Eq. (20)] by the projected area of the cell to the power 3/2: $S_C^{3/2} = (\sum_{\mathrm{intra}} S_{xy})^{3/2}$, we get a dimensionless quantity that can be computed to compare adherent and nonadherent cells:

$$\langle \Delta_{n,\mathrm{eff}} \rangle = \begin{cases} 3\sqrt{4\pi} & \mathrm{OPV}/S_C^{3/2} \\ \Delta n_C, & \text{for spherical cells} \end{cases}. \tag{21}$$

This quantity gives the same prediction for the cell RI as previously estimated, if the cell is spherical. If the cell is not spherical, this quantity provides some estimate of the effective density of the cell and its flattening under adhesion; the flatter the cell the smaller $\langle \Delta_{n,\mathrm{eff}} \rangle$ gets.

The small off-centered dome of the CD34+ cell shown in Fig. 6 corresponds to a higher density zone of the nucleus which is mainly detectable by the WTMM method on its border oriented toward the center of the cell image (computed from the center of mass of the projected shadow of the cell image onto the **x** plane, where its gradient is stronger). The outer contour of this small dome is shrouded in the nuclear-extracellular borders and is hardly detectable due to a limited number of fringes per micrometer.

It is interesting to compare this WTMM analysis of a domed CD34+ cell with a flatter CD34+ cell from the same bone marrow sample (Fig. 7). This new cell has an average radius of 5.53 ± 0.18 μm and is only 23% larger than the previous CD34+ cell (Fig. 6). Its OPD topography is drastically different, since its internal nucleus is more inhomogeneous with a larger

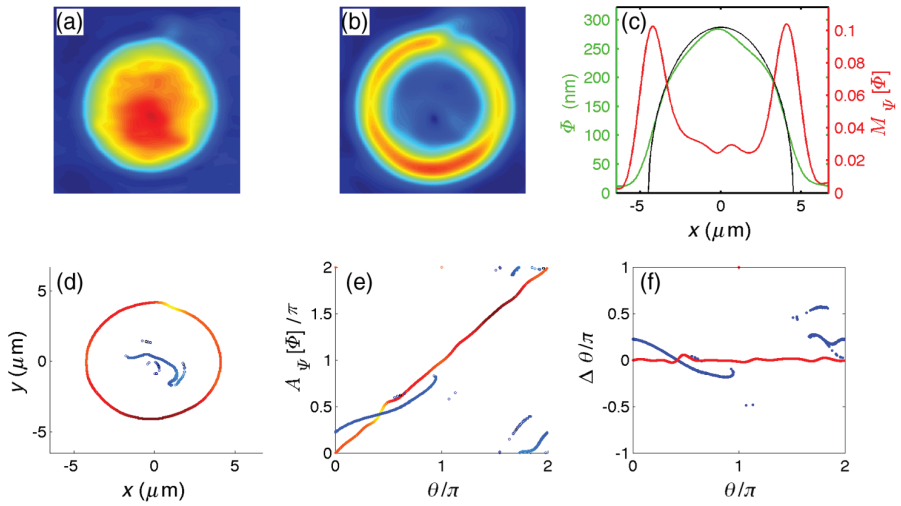

Fig. 6 WTMM method analysis of the OPD of a living domed CD34+ cell: (a) OPD phase image, color coded from dark blue ($\Phi = 0$ nm) to brown red ($\Phi = 320$ nm); (b) $\mathscr{M}_\Psi[\Phi](\mathbf{b}, a)$ for $a = 15$, color coded in the interval [0, 0.16]; (c) horizontal sections through the barycenter of the cell of the OPD Φ (green line) and of $\mathscr{M}_\Psi[\Phi]$ (red line). The black line corresponds to the OPD profile for a homogeneous sphere with radius 4.5 μm and index $n = 1.365$; (d) WTMM chains of the CD34+ cell shown in (a), color coded according to the value of $\mathscr{M}_\Psi[\Phi]$; (e) plot of the argument $\mathscr{A}_\Psi[\Phi]_{\mathrm{WTMM}}$ of the WTMM chains versus θ [same color coding as in (d)]; and (f) plot of $\Delta\theta = \mathscr{A}_\Psi[\Phi]_{\mathrm{WTMM}} - \theta$ versus θ.

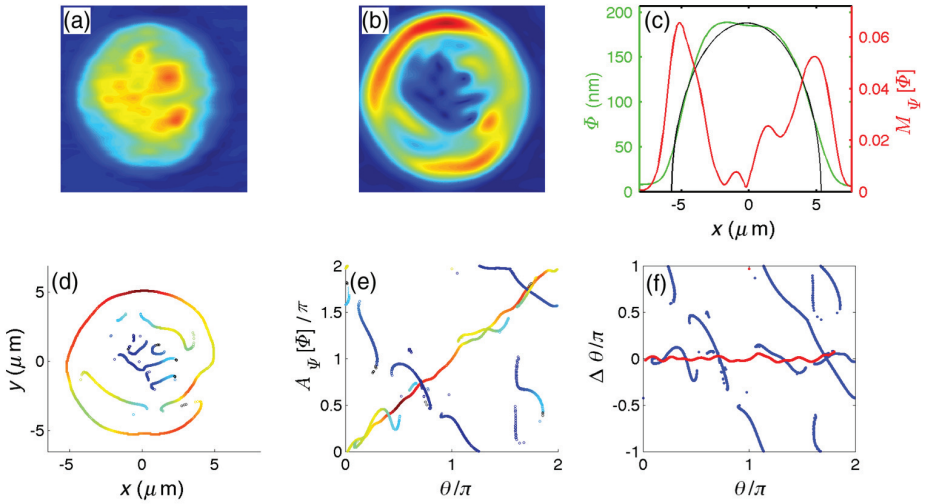

Fig. 7 WTMM method analysis of the OPD of a living flattened shape CD34+ cell: (a) OPD phase image, color coded from dark blue ($\Phi = 0$ nm) to brown red ($\Phi = 230$ nm); (b) $\mathscr{M}_\Psi[\Phi](\mathbf{b}, a)$ for $a = 15$, color coded in the interval [0, 0.092]; (c) horizontal sections through the barycenter of the cell of the OPD Φ (green line) and of $\mathscr{M}_\Psi[\Phi]$ (red line). The black line corresponds to the OPD profile for a homogeneous sphere with radius 5.53 μm and index $n = 1.35$; (d) WTMM chains of the CD34+ cell shown in (a), color coded according to the value of $\mathscr{M}_\Psi[\Phi]$; (e) plot of the argument $\mathscr{A}_\Psi[\Phi]_{\text{WTMM}}$ of the WTMM chains versus θ [same color coding as in (d)]; and (f) plot of $\Delta\theta = \mathscr{A}_\Psi[\Phi]_{\text{WTMM}} - \theta$ versus θ.

set of WTMM chains. One may wonder if this roughening of the internal core of the cell could be accounted for by its larger size, which would facilitate the local maxima detection. Actually, the threshold for local maxima detection is chosen to be small enough (1×10^{-3}) to collect all the local events given the wavelet scale a. The occurrence of these WTMM chains is really reflecting a modification of the internal structure of the cell. Another way to confirm this transformation is to compare the OPVs: in that latter case, OPV $= 13.3$ μm^3, which, surprisingly, is very close to the OPV of the previous CD34+ cell. According to Eq. (20), if we divide the OPV by the volume of the ideal sphere with the same radius $R_C = 5.53$ μm ($V_S = 708$ μm^3), we get an average RI drop: $\Delta n_C = 0.0188 \pm 0.005$, leading to a much smaller averaged RI of the cell: $n_C = 1.352 \pm 0.005$. Since the OPV remains invariant, we know that the total material of the cell is not changed. This means that its apparent surface and its internal structure have changed, possibly due to a local condensation of the intranuclear material. Since we did not stain the nucleus to avoid any alteration of the cell with an external agent that could also modify the interferometric measure, we cannot conclusivelydetermine this possibility. Further experiments could be needed to confirm this hypothesis, in particular by following the transformation of a living cell during a whole division cycle.

4.3 *Cell Models for Hematopoietic Stem Cells*

Primary CD34+ cells are much more difficult to maintain alive than laboratory cell lines. We used the TF1 cell line as a model of immature CD34+ cells, because it displays clonogenic ability similar to human bone marrow CD34+ cells and is able to differentiate into myeloid lineages.[61] As compared with a wild-type or GFP-transduced TF1 cells, BCR-ABL-transduced (CML oncogene) TF1 cells (TF1-BCR-ABL) increase their transcriptional levels of BCR-ABL and ABL.[34] These cells could bring information on the impact of BCR-ABL oncogene transduction on immature cells. Figure 8 shows the results of the WTMM analysis of the OPD of a nontransformed (control) TF1-GFP cell. Immediately, we notice that the size of this cell ($R_C = 8.22 \pm 0.2$ μm) is definitely larger than that of the CD34+ primary cells. This cell looks rather homogeneous in its composition because we do not detect so many WTMM chains. The parametrization of the OPD section [Fig. 8(c)] and the computation of the OPV $= 76$ μm lead to a mean RI, $n_C = 1.363 \pm 0.004$, which is not very far from the one estimated for the first domed CD34+ cell (Fig. 6). It seems that even if this cell has significantly increased its size compared with primary cells, its optical properties are not very different. In the sampling of these control and transformed cells, we have observed very drastic changes, as illustrated in Fig. 9, for the TF1-GFP-BCR-ABL cell line whose morphology is dramatically different from the TF1-GFP cell shown in Fig. 8. This type of transformation occurs in less than 10% of the cells transduced by the BCR-ABL oncogene, but since it is accompanied by a drastic reorganization of the cytoskeleton, we think it is important to show how the QPM-WTMM method can interpret and quantify this transformation. BCR-ABL has previously been demonstrated to bind actin filaments (F-actin),[62] one of the major force transducers in cellular adhesion and motility,[63] and to induce its redistribution into punctate, juxtanuclear aggregates,[64] implying a reorganization of the whole cytoskeleton. In Fig. 9, we immediately notice that the cell radius has increased by a factor $\sim 3/2$. The number of chains detected by the WTMM method has also increased by a factor ~ 5 (we count only the chains with a length larger than 100 nm, as smaller chain detection may be spoiled by background noise). The mean RI of this TF1-GFP-BCR-ABL cell, computed from the OPV$/V_S$ ratio [Eq. (20)], is not distinguishable from the mean RI of the previous TF1-GFP cell. When comparing Figs. 8(b) and 8(c) and 9(b) and 9(c), we realize that the difference between the 2-D OPD derivatives of control and cancer cells is higher in the inner cell structures ($\mathcal{M}_\Psi[\Phi] = 0.011 \pm 0.009$ for TF1-GFP

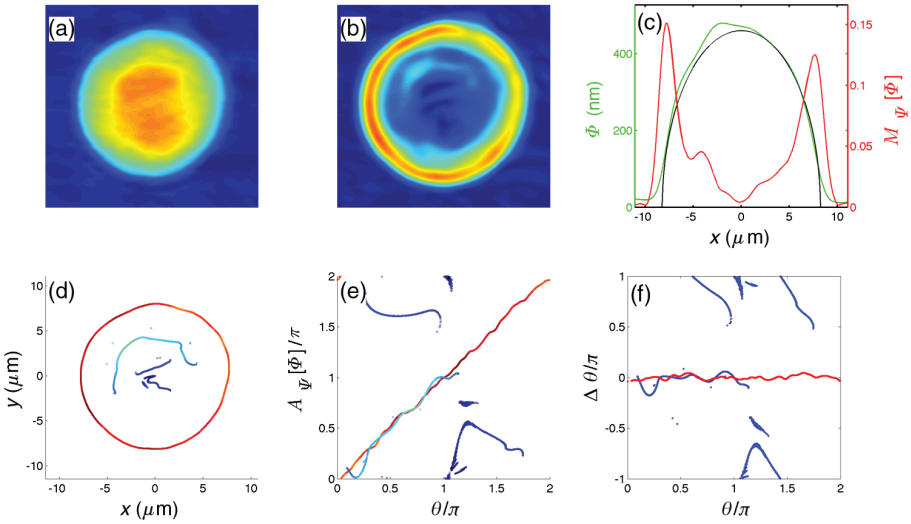

Fig. 8 WTMM method analysis of the OPD of a living hematopoietic model cell TF1-GFP: (a) OPD phase image, color coded from dark blue ($\Phi = 0$ nm) to brown red ($\Phi = 507$ nm); (b) $\mathscr{M}_\psi[\Phi](\mathbf{b}, a)$ for $a = 15$, color coded in the interval [0, 0.2]; (c) horizontal sections through the barycenter of the cell of the OPD Φ (green line) and of $\mathscr{M}_\Psi[\Phi]$ (red line). The black line corresponds to the OPD profile for a homogeneous sphere with radius 8.22 μm and index $n = 1.363$; (d) WTMM chains of the TF1-GFP cell shown in (a), color coded according to the value of $\mathscr{M}_\Psi[\Phi]$; (e) plot of the argument $\mathscr{A}_\Psi[\Phi]_{\text{WTMM}}$ of the WTMM chains versus θ [same color coding as in (d)]; and (f) plot of $\Delta\theta = \mathscr{A}_\Psi[\Phi]_{\text{WTMM}} - \theta$ versus θ.

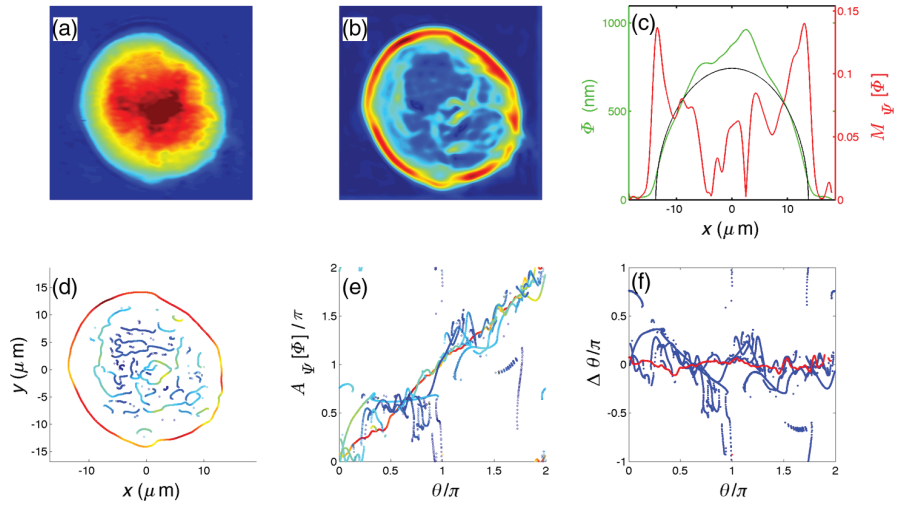

Fig. 9 WTMM method analysis of the OPD of a living TF1-BCR-ABL cell: (a) OPD phase image, color coded from dark blue ($\Phi = 0$ nm) to brown red ($\Phi = 1050$ nm); (b) $\mathscr{M}_\Psi[\Phi](\mathbf{b}, a)$ for $a = 15$, color coded in the interval [0, 0.2]; (c) horizontal sections through the barycenter of the cell of the OPD Φ (green line) and of $\mathscr{M}_\Psi[\Phi]$ (red line). The black line corresponds to the OPD profile for a homogeneous sphere with radius 13.77 μm and index $n = 1.36$; (d) WTMM chains of the TF1-GFP-BCR-ABL cell shown in (a), color coded according to the value of $\mathscr{M}_\Psi[\Phi]$; (e) plot of the argument $\mathscr{A}_\Psi[\Phi]_{\text{WTMM}}$ of the WTMM chains versus θ [same color coding as in (d)]; and (f) plot of $\Delta\theta = \mathscr{A}_\Psi[\Phi]_{\text{WTMM}} - \theta$ versus θ.

cell and 0.035 ± 0.02 for TF1-GFP-BCR-ABL cell) than along the outer contour ($\mathcal{M}_\Psi[\Phi] = 0.061 \pm 0.047$ for TF1-GFP cell and 0.07 ± 0.0085 for TF1-GFP-BCR-ABL cell). This internal reorganization of the TF1-GFP-BCR-ABL is also visible on the higher dispersion of the WT arguments [Figs. 8(e) and 8(f) and 9(e) and 9(f)]. If this preliminary discussion on these two cells does not allow us to make general conclusions on the transformation of TF1 cells upon BCR-ABL oncogen transduction, it simply illustrates the fact that the internal structure of these cells may appear very different through QPM analysis.

We repeated this analysis on two large sets of TF1-GFP (294) and TF1-GFP-BCR-ABL (216) cells, and we computed the statistical distributions of the mean radius of the outer chain, the OPV, the mean RI drop [computed from Eq. (20)], the angle difference $\Delta\theta$, the number of chains per cells, and the chain length (Fig. 10). The cell radius distribution is clearly shifted

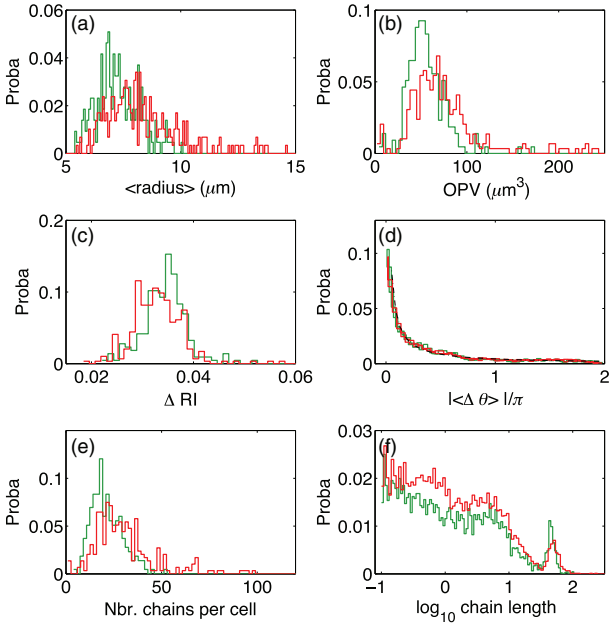

Fig. 10 Statistical analysis of cell structural parameters from the WTMM analysis of the OPD of control and cancer cell lines: (a) distribution of mean cell radius, estimated from the outermost contour WTMM chain; (b) distributions of OPVs computed from Eq. (19); (c) distributions of RI drops computed from Eq. (20); (d) distribution of $\Delta\theta$ values; (e) distribution of the numbers of chains per cell; $\overline{N_C} = 21 \pm 7$ for TF1-GFP cells and $\overline{N_C} = 30 \pm 9$ for TF1-GFP-BCR-ABL cells; and (f) distribution of chain lengths ($\log_{10}$ of the length in μm). The green (respectively red) lines are obtained from a set of 294 (respectively 216) TF1-GFP (respectively TF1-GFP-BCR-ABL) cells.

and spread to larger values with $\overline{R_C} = 7.2 \pm 1.2$ μm for the TF1-GFP cells and $\overline{R_C} = 8.2 \pm 2.1$ μm for the TF1-GFP-BCR-ABL cells. The OPV follows the same trend with $\overline{\mathrm{OPV}} = 56 \pm 3$ μm^3 for the TF1-GFP cells and $\overline{\mathrm{OPV}} = 89 \pm 5$ μm^3 for the TF1-GFP-BCR-ABL cells (we use the error of the mean for these quantities). Again, we note that the OPV values are much more dispersed for the transformed cells. The oncogene transduction seems to increase the variability of the cell structural properties. One more surprising result is that the mean RI drop (inner to outer media) of these cells is slightly decreasing from 0.0351 ± 0.0075 to 0.0331 ± 0.019, suggesting that the apparent swelling of the TF1-GFP-BCR-ABL cells is not followed by an adapted increase of the intracellular concentration of proteins to keep the mean RI invariant. The distribution of angle differences $\Delta\theta$ follows a power law distribution $P(\Delta\theta) \propto |\Delta\theta|^{-\alpha}$, with $\alpha = 1$. The fact that the shape of this distribution does not change when switching from control to oncogene-transduced TF1 cell means that the statistics of angular orientation of the maxima chains are not immediately impacted by the cell transformation. In contrast, the number of chains per cell is affected by oncogene transduction. The median value of the two distributions in Fig. 10(e) increases from 21 to 30 chains per cell (considering only the chains of length larger than 100 nm). Again, we observe that the distribution of these chain numbers for TF1-GFP-BCR-ABL cells is more spread out than for control TF1-GFP cells. The distribution of length of these chains (above 100 nm) follows a smoothly decreasing (logarithmic decrease) function for chains smaller than 5 μm, which drops rapidly to zero for larger chains. The peak popping up around 45 μm corresponds to the outer chain length, and the slight flattening and shifting to higher values of this peak for transduced TF1-GFP-BCR-ABL cells mean that the circumference of these cells increases (as their radius) and is more variable than for nontransformed cells. This observation corroborates our previous remarks on the cell radius distribution.

5 Conclusions

The interpretation of quantitative phase images of living cells and their inversion for recovering index profiles is a very tough task, since a living cell is rarely a homogeneous media, and even worse its internal bodies (cytoskeletal networks of filaments, endoplasmic reticulum, golgi, mitochondrial network, and intranuclear structures) are not invariant during the cell cycle. It is, therefore, very difficult to predict a well-established distribution of the RIs of a living cell. For instance, the integrated RI values over the cell thickness extracted from the phase images are not systematically organized along closed domains, strongly challenging traditional interpretation of phase images by phase isocontours. When the phase profiles are not monotonous nor smooth functions, the derivatives of the phase may display local maxima that reflect a local change of RI or the topography of the cells. We show here that the detection of these local maxima may help us deciphering the internal complexity of living cells. The introduction of the WTMM method to detect the maxima of the derivative of the phase allows a robust and automatized reconstruction of their outer and inner boundary chains. From these chains, morphological and global RI characterizations of living blood cells can be performed. The reported comparison of the results obtained for erythrocytes, primary immature hematopoietic (CD34+), and model (TF1) cells provides a good survey of the efficiency of this method to distinguish healthy from cancer cells. In particular, this study suggests that the RI and its intracell roughening may serve as a quantitative marker for cancer cell detection.

Acknowledgments

We are very thankful to Centre National de la Recherche Scientifique, Ecole Normale Supérieure de Lyon, Lyon Science Transfert (project L659), Région Rhône Alpes (CIBLE Program 2011), INSERM (AAP Physique Cancer 2012), and the French Agency for Research (ANR-AA-PPPP-005, EMMA 2011, ANR-11 IDEX-0007-02 with the PRES-University of Lyon) for their financial support. C.M.T. is very grateful to the National Council of Science and Technology (CONACyT, Mexico) for supporting her PhD scholarship.

References

1. N. Lue et al., "Live cell refractometry using microfluidic devices," *Opt. Lett.* **31**, 2759–2761 (2006).
2. C. Brunner, A. Niendorf, and J. A. Käs, "Passive and active single-cell biomechanics: a new perspective in cancer diagnosis," *Soft Matter* **5**, 2171–2178 (2009).
3. G. Popescu, "Random and deterministic transport in live cells quantified by SLIM," in *OSA: BODA/NTM/OMP/OTA*, p. 1 (2011).
4. D. K. Kang et al., "Droplet microfluidics for single-molecule and single-cell analysis in cancer research, diagnosis and therapy," *Trends Anal. Chem.* **58**, 145–153 (2014).
5. A. Grünberger, W. Wiechert, and D. Kohlheyer, "Single-cell microfluidics: opportunity for bioprocess development," *Curr. Opin. Biotechnol.* **29**, 15–23 (2014).
6. G. Popescu, *Quantitative Phase Imaging of Cells and Tissues*, McGraw Hill, New York (2011).

7. K. Lee et al., "Quantitative phase imaging techniques for the study of cell pathophysiology: from principles to applications," *Sensors* **13**(4), 4170–4191 (2013).
8. C. L. Curl et al., "Refractive index measurement in viable cells using quantitative phase-amplitude microscopy and confocal microscopy," *Cytometry, Part A* **65**, 88–92 (2005).
9. B. Rappaz et al., "Measurement of the integral refractive index and dynamic cell morphometry of living cells with digital holographic microscopy," *Opt. Express* **13**, 9361–9373 (2005).
10. W. Choi et al., "Tomographic phase microscopy," *Nat. Methods* **4**(9), 717–719 (2007).
11. W. J. Choi et al., "Full-field optical coherence microscopy for identifying live cancer cells by quantitative measurement of refractive index distribution," *Opt. Express* **18**(22), 23285–23295 (2010).
12. T. Yamauchi et al., "Low-coherent quantitative phase microscope for nanometer-scale measurement of living cells morphology," *Opt. Express* **16**, 12227–12238 (2008).
13. V. Backman et al., "Detection of preinvasive cancer cells," *Nature* **406**, 35–36 (2000).
14. X. Liang et al., "Determining refractive index of single living cell using an integrated microchip," *Sens. Actuators, A* **133**, 349–354 (2007).
15. Y. Park et al., "Refractive index maps and membrane dynamics of human red blood cells parasitized by Plasmodium falciparum," *Proc. Natl. Acad. Sci. U. S. A.* **105**, 13730–13735 (2008).
16. Y. Yanase et al., "Detection of refractive index changes in individual living cells by means of surface plasmon resonance imaging," *Biosens. Bioelectron.* **26**(2), 674–681 (2010).
17. P. Bon, B. Wattellier, and S. Monneret, "Modeling quantitative phase image formation under tilted illuminations," *Opt. Lett.* **37**, 1718–1720 (2012).
18. Y. Yanase et al., "Evaluation of peripheral blood basophil activation by means of surface plasmon resonance imaging," *Biosens. Bioelectron.* **32**(1), 62–68 (2012).
19. D. Morikawa et al., "Detection of swelling of single isolated mitochondrion with optical microscopy," *Biomed. Opt. Express* **5**(3), 848–857 (2014).
20. H. V. Pham et al., "Real time blood testing using quantitative phase imaging," *PLoS One* **8**, e55676 (2013).
21. V. P. Tychinsky et al., "Dissecting eukaryotic cells by coherent phase microscopy: quantitative analysis of quiescent and activated T lymphocytes," *J. Biomed. Opt.* **17**, 076020 (2012).
22. P. Marquet et al., "Digital holographic microscopy: a noninvasive contrast imaging technique allowing quantitative visualization of living cells with subwavelength axial accuracy," *Opt. Lett.* **30**(5), 468–470 (2005).
23. G. Popescu et al., "Diffraction phase microscopy for quantifying cell structure and dynamics," *Opt. Lett.* **31**, 775–777 (2006).
24. Y. Park et al., "Diffraction phase and fluorescence microscopy," *Opt. Express* **14**, 8263–8268 (2006).
25. B. Bhaduri et al., "Diffraction phase microscopy with white light," *Opt. Lett.* **37**, 1094–1096 (2012).
26. Y. Park et al., "Measurement of red blood cell mechanics during morphological changes," *Proc. Natl. Acad. Sci. U. S. A.* **107**, 6731–6836 (2010).
27. B. Rappaz et al., "Simultaneous cell morphometry and refractive index measurement with dual-wavelength digital holographic microscopy and dye-enhanced dispersion of perfusion medium," *Opt. Lett.* **33**, 744–746 (2008).
28. V. Lauer, "New approach to optical diffraction tomography yielding a vector equation of diffraction tomography and a novel tomographic microscope," *J. Microsc.* **205**(2), 165–176 (2002).
29. Y. Sung et al., "Optical diffraction tomography for high resolution live cell imaging," *Opt. Express* **17**(1), 266–277 (2009).
30. R. Fiolka et al., "Simplified approach to diffraction tomography in optical microscopy," *Opt. Express* **17**(15), 12407–12417 (2009).
31. K. Kim et al., "Diffraction optical tomography using a quantitative phase imaging unit," *Opt. Lett.* **39**(24), 6935–6938 (2014).
32. S. Shin et al., "Active illumination using a digital micromirror device for quantitative phase imaging," arXiv:1506.06237 (2015).
33. C. Hammond, "A symmetrical representation of the geometrical optics of the light microscope," *J. Microsc.* **192**(1), 63–68 (1998).
34. B. Laperrousaz et al., "Primitive CML cell expansion relies on abnormal levels of BMPs provided by the niche and on BMPRIb overexpression," *Blood* **122**(23), 3767–3777 (2013).
35. J. P. Antoine et al., *Two-Dimensional Wavelets and their Relatives*, Cambridge University Press, Cambridge, UK (2004).
36. C. Martinez-Torres et al., "Diffraction phase microscopy: retrieving phase contours on living cells with a wavelet-based space-scale analysis," *J. Biomed. Opt.* **19**, 036007 (2014).
37. J. Zhong and J. Weng, "Phase retrieval of optical fringe pattern from the ridge of a wavelet transform," *Opt. Lett.* **30**(19), 2560–2562 (2005).
38. Z. Wang and H. Ma, "Advanced continuous wavelet transform algorithm for digital interferogram analysis and processing," *Opt. Eng.* **45**, 045601 (2006).
39. S. Li, X. Su, and W. Chen, "Wavelet ridge techniques in optical fringe pattern analysis," *J. Opt. Soc. Am. A* **27**(6), 1245–1254 (2010).
40. J. Ma et al., "Two-dimensional continuous wavelet transform for phase determination of complex interferograms," *Appl. Opt.* **50**(16), 2425–2430 (2011).
41. T. Ikeda et al., "Hilbert phase microscopy for investigating fast dynamics in transparent systems," *Opt. Lett.* **30**, 1165–1167 (2005).
42. Y. Sung et al., "Stain-free quantification of chromosomes in live cells using regularized tomographic phase microscopy," *PLoS One* **7**, e49502 (2012).
43. S. Mallat and W. L. Hwang, "Singularity detection and processing with wavelets," *IEEE Trans. Inf. Theory* **38**(2), 617–643 (1992).
44. S. Mallat and S. Zhong, "Characterization of signals from multiscale edges," *IEEE Trans. Pattern Anal. Mach. Intell.* **14**(7), 710–732 (1992).
45. A. Arneodo, N. Decoster, and S. Roux, "A wavelet-based method for multifractal image analysis. I. Methodology and test applications on isotropic and anisotropic random rough surfaces," *Eur. Phys. J. B* **15**(3), 567–600 (2000).
46. N. Decoster, S. G. Roux, and A. Arneodo, "A wavelet-based method for multifractal image analysis. II. Applications to synthetic multifractal rough surfaces," *Eur. Phys. J. B* **15**(4), 739–764 (2000).
47. A. Arneodo et al., "A wavelet-based method for multifractal image analysis: from theoretical concepts to experimental applications," *Adv. Imaging Electron Phys.* **126**, 1–92 (2003).
48. J. Canny, "A computational approach to edge detection," *IEEE Trans. Pattern Anal. Mach. Intell.* **PAMI-8**(6), 679–698 (1986).
49. A. Khalil et al., "Chromosome territories have a highly nonspherical morphology and nonrandom positioning," *Chromosome Res.* **15**(7), 899–916 (2007).
50. A. Thaer, "The refractive index and dry mass distribution of mammalian erythrocytes," *J. Microsc.* **89**(2), 237–250 (1969).
51. A. Roggan et al., "Optical properties of circulating human blood in the wavelength range 400–2500 nm," *J. Biomed. Opt.* **4**(1), 36–46 (1999).
52. S. V. Tsinopoulos and D. Polyzos, "Scattering of He-Ne laser light by an average-sized red blood cell," *Appl. Opt.* **38**(25), 5499–5510 (1999).
53. Y. C. Fung and P. Tong, "Theory of the sphering of red blood cells," *Biophys. J.* **8**, 175–198 (1968).
54. Y. C. Fung, *Biomechanics: Mechanical Properties of Living Tissues*, Springer Verlag, New York (1993).
55. S. Wang et al., "Three-dimensional refractive index reconstruction of red blood cells with one-dimensional moving based on local plane wave approximation," *J. Opt.* **14**, 065301 (2012).
56. P. H. Wiernik, *Adult Leukemia*, BC Decker Inc., Hamilton, London (2001).
57. M. D. Huber and L. Gerace, "The size-wise nucleus: nuclear volume control in eukaryotes," *J. Cell Biol.* **179**(4), 583–584 (2007).
58. D. Zink, A. H. Fischer, and J. A. Nickerson, "Nuclear structure in cancer cells," *Nat. Rev. Cancer* **4**(9), 677–687 (2004).
59. S. Nazlibilek et al., "Automatic segmentation, counting, size determination and classification of white blood cells," *Measurement* **55**, 58–65 (2014).
60. R. Barer, "Refractometry and interferometry of living cells," *J. Opt. Soc. Am.* **47**, 545–556 (1957).
61. H. E. Broxmeyer et al., "Hematopoietic colony formation from human growth factor-dependent TF1 cells and human cord blood myeloid progenitor cells depends on Shp2 phosphatase function," *Stem Cells Dev.* **22**(6), 998–1006 (2012).
62. J. R. McWhirter and J. Y. J. Wang, "Activation of tyrosine kinase and microfilament-binding functions of c-ABL by BCR sequences in BCR-ABL fusion proteins," *Mol. Cell. Biol.* **11**(3), 1553–1565 (1991).
63. R. Salgia et al., "BCR/ABL induces multiple abnormalities of cytoskeletal function," *J. Clin. Invest.* **100**(1), 46–57 (1997).
64. J. R. McWhirter and J. Y. Wang, "An actin-binding function contributes to transformation by the BCR-ABL oncoprotein of Philadelphia chromosome-positive human leukemias," *EMBO J.* **12**, 1533–1546 (1993).

Cristina Martinez-Torres obtained her BSc in biophysics from the Autonomous University of San Luis Potosi, Mexico, in 2011. During her undergraduate studies, she was involved in several research groups, working in topics such as bioinformatics, cellular biology, biophysics, optical engineering, and atomic physics. Currently, she is a PhD student at the ENS Lyon, where she studies the structure and dynamics of single living cells.

Bastien Laperrousaz received his PhD in biology from the Ecole Normale Supérieure of Lyon, France, in 2015, at the interface with the Cancer Research Center of Lyon. He is currently developing microfluidic devices for high-throughput and high-content RNAi screens of 3D tumor structures for biomedical applications at the Institute of Life Sciences Research and Technologies of the Atomic Energy Commission, Grenoble, France. His research interests include cancer stem cell biology, biotechnologies, and biomedical applications.

Lotfi Berguiga received his PhD in physics from the University of Burgundy, Dijon, France, in 2001, where he worked in near field optics. Since 2004, he has worked at the Ecole Normale Superieure de Lyon, where he has investigated surface plasmon microscopy. Since 2007, he has worked as research engineer at the French National Centre for Scientific Research, and his research interests include development of new techniques of microscopy applied to cell biology.

Elise Boyer-Provera graduated in optics and industrial visual systems from the Engineering School of Telecom in Saint Etienne, France, in 2010. After a three-year training in the private company Thales Angenieux, she was hired as an engineer at Ecole Normale Superieure de Lyon to develop original microscopy devices based on surface plasmon microscopy and quantitative phase microscopy.

Juan Elezgaray received his PhD in theoretical physics from University of Paris 6, France, in 1989. Since 1989, he has been a researcher at CNRS. Currently, he works in the UMR 5248 (CBMN) unit in Pessac (France). He has collaborated with Françoise Argoul's team in the development of a surface plasmon microscope. His interests include the modelling of nanooptical systems and DNA nanotechnology.

Franck E. Nicolini got his PhD from University Claude Bernard, Lyon, France in 2001 and his "habilitation for directing research" in human biology in 2004, in the same university. He worked as a hospital practitioner in the hematology department of Pr. J. Reiffers between 1999–2001, mostly focused on CML and autologous and allogeneic stem cell transplant. He is a senior scientist in the Inserm research unit 1042 in Lyon, where he leads with Dr. Maguer-Satta a scientific program of basic scientific research on CML and normal hematopoiesis, mostly focus on the role of the hematopoietic niche in the resistance of CML to TKIs and maintenance of Ph+ stem cells. He has more than 100 original publications and book chapters in the field of hematology, stem cell transplantation and CML, and is or has been a reviewer several times for more than 20 peer-reviewed journals in the field of hematology, and for EHA, EBMT, and ASH meetings.

Véronique Maguer Satta received her PhD in immune-virology at University Claude Bernard of Lyon 1, France (1994). She spent several years in Dr. C. Eaves' laboratory in Vancouver, Canada (1994–1997) to learn normal and leukemic hematopoiesis. Then she joined for one year Pr. Reiffers lab in Bordeaux, France, to explore a clinical approach of research in hematopoieisis. In 1998, she developed her own research group on human hematopoiesis at Inserm U453, Lyon, France. She was recruited by CNRS as a permanent researcher (2002) and promoted research director (2012). She is now directing her research team on "BMPs, tumor niche and cancer stem cells" at the Cancer Research Center of Lyon-CRCL, France.

Alain Arneodo received his thesis in elementary particle physics from the University of Nice, France, in 1978. Then he switched his scientific interests to complex systems. After 20 years in a Bordeaux (France) CNRS laboratory, he moved to ENS Lyon (France) to work at the physics-biology interface. His scientific contribution encompasses many fields of modern physics including statistical mechanics, dynamical systems theory, chaos, fully-developed turbulence, economics, geophysics, the mathematics of fractals and multifractals, fractal growth phenomena, signal and image processing, multiscale analysis based on wavelets.

Françoise Argoul received her PhD from the University of Bordeaux, France, in 1986. She was promoted director of research (CNRS) in 1997 and has coauthored over 130 peer-reviewed papers. She manages a research program in Physics Department of ENS Lyon (France), devoted to the experimental characterization of the mechanical and genomic response of cellular systems under external stress. Her expertise ranges from nonlinear and complex dynamical systems to nanomechanical and optomechanical methods for capturing the dynamics of living systems.